SAKARYA UNIVERSITY
INSTITUTE OF SCIENCE AND TECHNOLOGY

# PROBABILISTIC THREE-DIMENSIONAL FRACTURE MECHANICS AND ITS APPLICATIONS USING FCPAS

**Ph.D. THESIS**

**Mehmet Faruk YAREN**

| | | |
|---|---|---|
| **Department** | : | **COMPUTATIONAL MECHANICS AND MANUFACTURING** |
| **Supervisor** | : | **Prof. Dr. Ali Osman AYHAN** |

**July 2021**

SAKARYA UNIVERSITY
INSTITUTE OF SCIENCE AND TECHNOLOGY

# PROBABILISTIC THREE-DIMENSIONAL FRACTURE MECHANICS AND ITS APPLICATIONS USING FCPAS

## Ph.D. THESIS

**Mehmet Faruk YAREN**

| | | |
|---|---|---|
| **Department** | **:** | **COMPUTATIONAL MECHANICS AND MANUFACTURING** |
| **Supervisor** | **:** | **Prof. Dr. Ali Osman AYHAN** |

**This thesis has been accepted unanimously by the examination committee on 08.07.2021**

**Chairman of The Committee** **Committee Member** **Committee Member**

**Committee Member** **Committee Member**

# DECLARATION

I declare that all the data in this thesis was obtained by myself in academic rules, all visual and written information and results were presented in accordance with academic and ethical rules, there is no distortion in the presented data, in case of utilizing other people’s works they were referenced properly under scientific norms, the data presented in this thesis has not been used in any other thesis in this university or in any other university.

Mehmet Faruk YAREN
08.07.2021

# ACKNOWLEDGMENTS

I would like to express my deepest sincere gratitude to my advisor Prof. Dr. Ali Osman AYHAN who has an important role in the determination of the thesis subject and elaboration of the Ph.D. study. During my study, he was available whenever I needed his valuable knowledge and experience, and it would not be possible to overcome difficulties in the study without his guidance.

The financial support of this research by The Scientific and Technological Research Council of Turkey (TUBITAK) under project no 217M690 is gratefully acknowledged. I am pleased to be a member of this project, which has an excellent team. I wish to thank the member of Sakarya University and researcher in TUBITAK project Dr. Sedat İRİÇ for his supports; especially in manufacturing of the specimens and designing the test setup. I appreciate the contribution of Dr. Oğuzhan DEMİR, a faculty member in Bilecik University and a researcher in TUBITAK project, who was very generous to share his experimental/numerical experiences. Emre KURT, who is a scholarship-student in the project, was very helpful with the detailed discussions we had about my results.  Also, I wish to thank Sakarya University R&D and Application Center for allowing me to use the facilities of the Experimental Fracture Mechanics Lab. I would like to thank Turkish Aerospace Industries Inc. for providing me an opportunity to exchange ideas about the study and especially for suggesting the use of FALSTAFF spectrum in random loading tests.

I wish to express my gratitude for the support and encouragement of my parents and wife. Their understandings and motivation are vital for the completion of this study.

## TABLE OF CONTENTS

CHAPTER 1.

CHAPTER 2.

CHAPTER 3.

# LIST OF SYMBOLS AND ABBREVIATIONS

| | |
|---|---|
| a | : Crack length |
| C - n | : Crack growth constants for Paris-Erdogan Equation |
| $C_{Walker}$ | : Crack growth constants for Walker Equation |
| $C_{Forman}$ | : Crack growth constants for Forman Equation |
| $\Delta K$ | : Stress intensity factor range |
| $\Delta X$, $\Delta Y$, $\Delta Z$ | : Geometric offset of EDM notch in X-Y-Z directions |
| DOE | : Design of Experiment |
| EDM | : Electrical discharge machining |
| FCPAS | : Fracture and Crack Propagation Analysis System |
| $K_{IC}$ | : Fracture toughness |
| $K_I$ , $K_I$ , $K_{III}$ | : Stress intensity factor in Mode-I or Mode-II or Mode-III |
| $K_{OL}$ | : Stress intensity factor generated by overload |
| $K_{th}$ | : Threshold value of stress intensity factor |
| $P_Q$ | : Peak load in fracture toughness tests |
| R | : Stress ratio |
| $R_{SO}$ | : Shut-off ratio |
| SP1, SP2, SP3 | : Random loading spectrums |
| SPPI | : Spectrum Profile Position Index |
| SOL index | : Spectrum overload index |
| SIF | : Stress intensity factor |
| $\sigma_Y$ | : Yield stress |
| $\emptyset_R$ | : Wheeler retardation parameter |
| w | : Width of the specimen |

# LIST OF FIGURES

# LIST OF TABLES

# SUMMARY

Keywords: Probabilistic fatigue crack growth, Fracture mechanics, Monte Carlo simulation

Cracks can be seen in many engineering structures. It is important to determine the mechanical strength and life of the cracked structure or design a mechanical part with a damage tolerance approach. It is hard to determine the remaining life of machine parts exactly, since they include some uncertainties and variations in governing parameters of the problem, such as geometric dimensions and the variability of material properties and loading conditions. Therefore, for such problems, crack growth lives must be estimated by means of probabilistic approaches considering the variables that affect lives.

In this study, for three-dimensional fatigue crack growth problems, a probabilistic crack growth life estimation procedure, which also involves Monte Carlo Simulations, was developed and validated by controlled laboratory experiments. The uncertainty in material properties affecting fatigue crack propagation life was determined using standard Compact Tension (CT) specimens machined from 7075-T6 aluminium alloy. Fatigue crack growth models for constant or variable amplitude loading in the literature were investigated and an improved model has been proposed. The data obtained from two-dimensional crack propagation tests were used in three-dimensional crack propagation simulations. A non-standard specimen made from Aluminium 7075-T6 has been designed for three-dimensional mode-I fatigue surface crack growth tests. Surface crack growth experiments under constant and variable amplitude loads were conducted using this specimen. Fatigue crack growth simulations were also carried out by considering the geometric tolerances of the specimen, the scatter of the fatigue crack growth-related material properties and the variability in loading. Experimental results were compared with simulations for different crack growth models, allowing validation of the proposed probabilistic fatigue crack growth methodology.

# FCPAS KULLANILARAK OLASILIK TEMELLİ ÜÇ-BOYUTLU KIRILMA MEKANİĞİ VE UYGULAMALARI İÇİN PROSEDÜR OLUŞTURULMASI

## ÖZET

Anahtar kelimeler: Olasılık temelli yorulma çatlak ilerlemesi, Kırılma mekaniği, Monte Carlo simulasyonu

Mühendislik yapılarında kullanılan bir çok elamanda çatlaklarla karşılaşılmaktadır. Çatlak içeren yapının mekanik dayanımının ve ömrünün belirlenmesi veya tasarım aşamasındaki bir elemanın hasar toleransı yaklaşımıyla modellenmesi önemlidir. Geometrik toleranslar, malzeme özellikleri gibi belirsizlikler ve yükleme şartlarındaki değişkenliklerden dolayı makina parçaları için kesin bir ömür tahmininde bulunmak zordur. Bu nedenle ömür değerlerini etkileyecek değişkenlikler dikkate alınarak olasılık temelli yaklaşımlarda bulunulmaktadır.

Bu çalışmada, üç boyutlu yorulma çatlak ilerleme problemleri için Monte Carlo simulasyonu ile olasılık temelli ömür tahmin yöntemi oluşturulmuş ve deneylerle doğrulanmıştır. Yorulma çatlak ilerleme ömrünü etkileyen malzeme özelliklerindeki belirsizlik, 7075-T6 alüminyum ile standart Compact Tension numunesi kullanılarak belirlenmiştir. Sabit ve değişken genlikli yükleme altında literatürdeki yorulma çatlak ilerleme modelleri değerlendirilmiş ve iyileştirilmiş model önerilmiştir. İki boyutlu çatlak ilerleme deneylerinde elde edilen veriler üç boyutlu çatlak ilerleme analizlerinde kullanılmıştır. 7075-T6 alüminyum ile standart olmayan ve üç boyutlu mod-I yüzey çatlağı içeren numune tasarlanmıştır. Bu numune ile sabit ve değişken genlikli yükler altında üç boyutlu çatlak ilerleme deneyleri gerçekleştirilmiştir. Numune üzerindeki geometrik toleranslar, malzeme özelliklerindeki saçılımlar ve yükleme şartlarındaki değişkenlikler dikkate alınarak yorulma çatlak ilerleme simulasyonları gerçekleştirilmiştir. Farklı çatlak ilerleme modellerini kullanılarak gerçekleştirilen simulasyon sonuçları deneylerle karşılaştırılmıştır.

# CHAPTER 1. INTRODUCTION

## 1.1. Background of Fracture Mechanics

Cracks can be seen in many engineering applications because of the material defects, design and manufacturing. A structure that includes crack, can be safe under short-term static loading conditions, but in case of fatigue loading, the remaining mechanical life must be re-evaluated. The structure must be investigated to determine whether the crack grows under the applied fatigue loading. If so, the crack growth rates and remaining life must be calculated. Fracture mechanics is a research area that investigates the mechanical strength and remaining lives of cracked structures by using the basic principles of mechanics along with some special approaches. The science of fracture mechanics is vital for sectors such as aviation, space, energy, transportation and defense, which are critical areas in case of damage, since a large number of casualties or high maintenance costs may occur. The importance of fracture mechanic studies is increasing with the developments in aviation, space, nuclear studies, military and defense systems.

In the 15th century, Leonardo Da Vinci noted an inverse relationship between the length and fracture load of the wires produced from the same material and having the same cross-sectional area. Afterward in some studies performed by different scientists, it has been explained that fracture was caused by material defects and there might be more defects in a longer wire [1]. Based on these studies A.A. Griffith has published new studies about fracture theory (1920; 1924) which are known as the first systematic research on fracture mechanics [1]–[3].

During the Second World War years, the USA launched Emergency Ship Building Program. Large numbers of the ships built in this program experienced unexpected damages. Investigation of shipwrecks showed that cracks and gaps occurred during the welding process triggered these catastrophic failures especially when the materials get brittle in cold water. After these findings, researchers focused on Griffith's studies, which had not been popular for years, and research on fracture mechanics has gained pace.

Irvin [4] published his study and he showed the way to apply fracture mechanics theory on engineering problems by using stress intensity factors. Thus, studies on Linear Elastic Fracture Mechanics (LEFM) were accelerated. On the other hand, his approach is not compatible with ductile materials because of the plastic zone on crack tips. For ductile materials, J.R. Rice proposed a new method that calculates the strain energy release rate by using J integral [5].

## 1.2. Probabilistic Fracture Mechanics

The maintenance period of a machine is directly related to the life of its sub-components. Therefore, the life of each component must be evaluated separately. Crack propagation rate of a component for a given load spectrum can be calculated by using the crack growth properties of the material and its geometry. However, external forces predicted for machine parts in the design may be different from those under the operating conditions. Furthermore, load spectrum can be characteristically random such as the loading profile of an airplane. It is difficult to determine an exact life for machine parts due to the variability in material properties and the small changes in the geometry. For this reason, the Probabilistic Fracture Mechanics (PFM) method is needed to express crack growth life by considering the variability of inputs in crack growth life equations such as initial crack size, geometry, material properties and load.

If the number of input variables is more than three, it is recommended to use Monte-Carlo simulation or First/Second Order Reliability Methods (FORM / SORM) approach [6]. Therefore, Monte Carlo simulation method was adopted in this study. This method can be explained simply as determining the distribution of the output values generated by the relation between the output variables and the input variables, which are randomly picked from their distributions. To obtain the probability distribution of the output, a re-calculation process is necessary for each randomly picked input data.

## 1.3. Literature Review

Modeling of crack growth behavior under fatigue loading is very important for safely operating the parts containing cracks. It is known that an unstable fracture occurs when the stress intensity factor reaches the fracture toughness of the material, which can be obtained experimentally including its scattered variation. Variability in material properties, loading conditions, geometrical tolerances and other environmental conditions affect the crack growth rate. For estimating the crack growth life under operating conditions, probabilistic fracture mechanics is generally used.

During the operation of a machine part, the most effective parameter on crack growth life is the loading spectrum. The size of the plastic zone in the crack tip changes and crack growth rate retards due to overload cycles in the loading spectrum.

Early studies related to crack growth focused on constant amplitude loading. The most common fatigue crack growth equation is Paris-Erdogan Equation [7] in the literature owing to its simplicity. This equation can be used in the second region of the crack growth curve and the stress ratio (mean stress effect) is not used. Forman [8], Walker [9], and Newman [10] proposed new models, considering the stress ratio in the calculation of the crack growth rate.

As variable amplitude loading results in variations on plastic zone size on the crack tip, novel approaches with different levels of details addressing this phenomenon were also proposed. Some models in the literature such as Elber [11], Wheeler [12] and Willenborg [13] are based on cycle-by-cycle analysis to investigate the interaction effect in loading profiles. For example, Elber [11] has considered the crack closure effect, while Wheeler [12] and Willenborg [13] have compared plastic zone sizes between loading profiles. Another approach is used in several studies, such as Barsom

[14], Hudson [15], Manjunatha [16] with a more general view on loading spectrum using root mean square. Even though many models have been proposed in the literature, no universal model is proposed which can be applied to all cases due to the challenges arising from different characteristics of variable amplitude loading.

Wheeler [12] determined the crack propagation behavior by comparing the plastic zone size at the crack tip created by the load cycles. If the current plastic zone is in the boundaries of a larger plastic zone that has already occurred and active, a retardation multiplier is added to the equation of Paris-Erdogan. The value of the retardation multiplier is between zero and one. An empirical Wheeler exponent is necessary to calculate the Wheeler retardation multiplier. Wheeler [12] showed that this exponent depended on the material and loading spectrum. The exponent can be found by trial and error, based on the comparison of the calculated life with the experiment. Sheu B.C. [17] experimentally demonstrated that the exponent in the Wheeler model is also dependent on the initial crack length and the overload ratio. A new model based on plastic zone size was proposed by Willenborg [13] with no empirical exponent, and an effective stress intensity factor is identified and substituted in Forman fatigue crack growth equation in the Willenborg model. The crack growth retardation is determined by using the effective stress intensity factor. If the overload ratio is greater than or equal to 2, it yields a mathematical obstacle. This problem has been solved by adding a multiplier in the Modified Willenborg model [18]. The capability of modeling crack growth for underload was enhanced by using a piecewise function, called Generalized Modified Willenborg Model. Further details of models and formulations are given in Section 3.6.

Wheeler and/or Willenborg Models were compared with the experimental results in several studies in the literature. Meggiolaro and Castro [19] calculated the crack propagation life with different models, using the singular and block loading test spectra for two-dimensional crack propagation generated by Zhang S et al. [20]. In their study, the best result was obtained by using the Wheeler Model with a retardation parameter values between %2 and %22 for different load spectrum types.

Xiaoping et al. [21] proposed a piecewise function of stress ratio for the retardation multiplier in the Wheeler Model, and the crack growth curves in different stress ratios were combined to obtain the modified multiplier and exponent. In other words, the Wheeler Model was related to the stress ratio. In the same study, another parameter is added to represent the interaction effects between load profiles. A specimen with a central crack made of 350WT steel was subjected to block loading and results were compared with the tests and showed good accordance.

Crack growth tests of Center Crack Tension (CCT) specimen, made of 2219-T851 aluminum alloy, were performed under random loading by ASTM in 1981. Three loading spectrums were taken from an airplane and the loading values are scaled to specimen levels. Six different studies used this experimental data to estimate crack growth life were published in a single book [22]. In these studies, Multiparameter Yield Zone [23], Modified Elber [24], root mean square [15] and Walker FCG equation in Generalized Willenborg/Chang model were used [25]. The latter model was also used by considering the negative loads to be equal to zero. None of the models were found to be specifically used for random loading since the error in the life estimation changes significantly under different load spectrums. The ratio of the calculated crack growth life to the test results varies from 0.45 to 1.28.

Wu and Ni [26] has performed two-dimensional crack propagation experiments using 2024-T351 aluminum material under constant amplitude. The average and standard deviation values of the distribution of crack length versus the number of cycles were calculated with the data from 30 different tests and it was observed that, as expected, the standard deviation increased with the number of cycles. Using the probability model of Yang and Manning [27], they plotted the cumulative probability distribution compatible with the experimental data.

Monte Carlo Simulation Method is a useful tool for risk assessment in engineering problems. It is based on the iteration of the solution of the problem by using the randomly picked input variables. If the number of samples taken from the variables is sufficient, it gives accurate results but the samples in the Monte Carlo (MC) Method must be independent of each other. The two interrelated material constants, *C* and *n*, are used for calculation of crack growth rate. Selecting these variables as independent in the Monte Carlo Simulation will cause inaccurate results. More detailed explanation of the MC Simulation and sampling process can be found in Annis's work [28]. Farahmand and Abdi [29] has investigated the effect of fracture toughness $K_{1c}$ and $K_{th}$ on crack growth life by using GENPAM,  a computer software for probabilistic material and structural analysis. They used 2219-T87 aluminum alloy, with a fracture toughness and threshold values having variations between 5% to 10%. A shift was observed on fatigue crack growth curves due to variation of the considered material properties.

## 1.4. Objective of The Present Study

Engineering problems contain inherent uncertainties arising from geometric dimensions, material properties (elasticity modulus, thermal conduction, crack propagation properties, etc.) and external loads (load, thermal input, boundary conditions, etc.). The changes in inputs of the problem affect the variability intervals of the output parameters obtained from the solution of the problem. For this reason, the variability of the output parameters is also calculated by using probabilistic approaches.

In this dissertation, it is aimed to develop a computational method in order to determine the variability in fracture parameters and crack propagation rates, considering the variations in load, geometry and material properties using the "Fracture and Crack Propagation Analysis System (FCPAS)".

Design of experiment (DOE) analysis was performed, and a transfer function was obtained to calculate KI SIFs for three-dimensional crack on the Lee James specimen used in tests. To reduce the computation time of DOE analysis, the calculation of the element stiffness matrices in FRAC3D has been parallelized with OpenMP commands and the details are explained in Chapter 2.

In Chapter 3; Two-dimensional crack propagation models were evaluated with the data obtained from the experiments under constant and variable loading to determine the variations in the crack propagation material properties. Three-dimensional crack propagation studies were carried out using the data and experiences obtained from Chapter 3 and the details are explained in Chapter 4. In this context, tests were carried out in different crack propagation test groups with different loading spectrums using non-standard specimen with three-dimensional cracks. In Chapter 5, probabilistic crack growth life predictions were made using Monte Carlo analysis and the results were verified by experiments. A flowchart is given in Figure 1.1.  for the probabilistic crack growth life prediction.

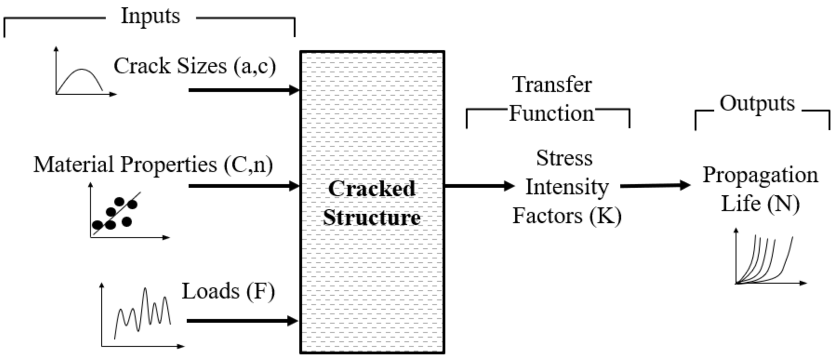

Figure 1.1. A flowchart for the probabilistic crack growth life estimation

# CHAPTER 2. PARALLELIZATION OF FINITE ELEMENT STIFFNESS MATRICES USING OPENMP

In probabilistic studies, a large number of statistical data is required. Since obtaining statistical data by experiments is costly and time-consuming, Design of Experiment (DOE) analyses are generally preferred to create a transfer function to calculate the stress intensity factors (SIF)s as functions of the problem's governing (input) parameters. Monte Carlo (MC) simulations are, then, performed by using the calculated SIFs, and the variations in the input parameters, including the material properties obtained by experiments. In this study, the above procedure is applied and the results of MC simulations are verified with those from the related experiments.

Two DOE tables, including 405 and 288 independent cases for fracture analyses were created by using FCPAS (Fracture and Crack Propagation Analysis System) [30]. Some routines FRAC3D [31], finite element solver of FCPAS, including solver and stress calculation, were parallelized using OpenMP commands in a previous study [32]. However, calculation of the element stiffness matrices and assembling them into the global stiffness matrix were being performed on one processor. In this study, before performing the DOE analyses for the probabilistic simulations, it is planned to reduce the solution time with multiple processors in all calculations by using OpenMP commands in FRAC3D. Further details of the studies using multiple processors will be given in this section. A paper titled "*Implementation of Parallel Computations on 3-D Enriched Finite Elements Used for Fracture Analyses"* [33] was also published using the results in this chapter.

## 2.1. FRAC3D: Finite Element Solver of Fracture and Crack Propagation Analyses System (FCPAS)

The use of numerical methods for engineering problems has increased with the advances in computer technology. These advancements in technology also make it possible to solve fracture mechanics problems easily for complex geometries.

The Finite Element Method (FEM) is one of the most common numerical methods in engineering. Since the FEM performs solutions based on nodes, defining the element type can be considered as the first step. Depending on the element type, element matrices are created to represent the behavior of elements. Then, a global structural matrix is generated by assembling the element matrices. External loads and the boundary conditions are also taken into account in the corresponding matrices and their solutions.

Displacement of an element {u} can be calculated by using the nodal degree of freedom {d} and the shape function matrix [N] of the element. Differentiation of the displacement {u} gives the strains. Strain-nodal displacement matrix [B] is obtained by differentiation of the shape function matrix [N].

$$\{u\} = [N]\{d\} \tag{2.1}$$

$$\{\varepsilon\} = [\partial]\{u\} \text{ yields } \{\varepsilon\} = [B]\{d\} \tag{2.2}$$

$$[B] = [\partial]\{N\} \tag{2.3}$$

Element stiffness matrix in global coordinates can be calculated by using strain-nodal displacement matrix and elastic property matrix [E] according to Equation (2.4). $V_e$ denotes the volume of an element.

$$[k] = \int_{V_e} [B]^T [E][B] \; dV \tag{2.4}$$

Isoparametric formulation of the element stiffness matrix is rewritten in Equation (2.5) in terms of isoparametric coordinates, $\zeta$, $\eta$, $\rho$. Note that the isoparametric coordinates vary between -1 and 1, and the determinant of a Jacobean matrix is added to the equation.

$$[k] = \iiint_{-1}^{1} [B]^T [E][B] \; J \; d\zeta d\eta d\rho \tag{2.5}$$

The conventional type of FEM is not suitable for fracture problems because of the stress singularity problem in the crack tip.  The enriched finite element method is one of the proposed approaches to deal with this obstacle. Strain terms also have singularity. As we approach the crack tip, it takes very high vaules because of the singularity. Therefore, it has high level of change. To be able to captute that high level of change in the strain gradient, more and more integration points are necessary.

FCPAS (Fracture and Crack Propagation Analysis System) [30] is an independent software that uses the enriched finite element method to calculate stress intensity factors (SIFs) along a three-dimensional crack front. A solid model is created in ANSYS and finite element information is taken from ANSYS and converted to FCPAS finite element input file format. In this process, element and node information along the crack front is used to identify enriched elements.

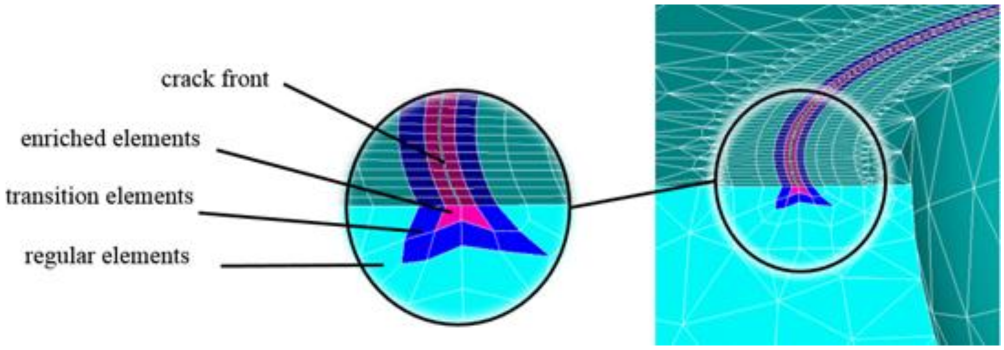

Figure 2.1. Enriched and transition elements along the crack front

In Figure 2.1., the enriched elements at the crack front of a finite element model and the neighboring transition elements are shown. Figure 2.2. shows a representative view of 20-node enriched element that touches the crack front, which is located in three-dimensional space.

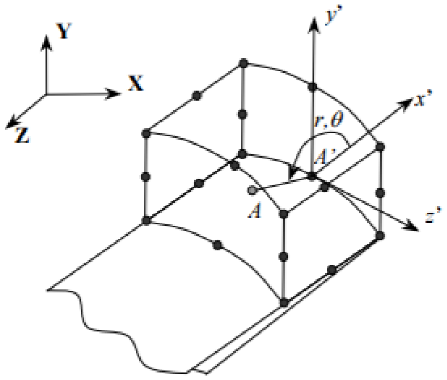

Figure 2.2. 20-node enriched elements on an arbitrarily oriented crack front [31]

$$
\begin{aligned}
u(\xi,\eta,\rho) = \sum_{j=1}^{m} N_j(\xi,\eta,\rho)\,u_j + Z_0(\xi,\eta,\rho)\left(f_u(\xi,\eta,\rho) - \sum_{j=1}^{m} N_j(\xi,\eta,\rho)\,f_{uj}\right)\left(\sum_{i=1}^{ntip} N_i(\Gamma)\,K_I^i\right) \\
+Z_0(\xi,\eta,\rho)\left(g_u(\xi,\eta,\rho) - \sum_{j=1}^{m} N_j(\xi,\eta,\rho)\,g_{uj}\right)\left(\sum_{i=1}^{ntip} N_i(\Gamma)\,K_{II}^i\right) \\
+Z_0(\xi,\eta,\rho)\left(h_u(\xi,\eta,\rho) - \sum_{j=1}^{m} N_j(\xi,\eta,\rho)\,h_{uj}\right)\left(\sum_{i=1}^{ntip} N_i(\Gamma)\,K_{III}^i\right)
\end{aligned}
\tag{2.6}
$$

$$v(\xi,\eta,\rho) = \sum_{j=1}^{m} N_j(\xi,\eta,\rho)\, v_j + Z_0(\xi,\eta,\rho)\left( f_v(\xi,\eta,\rho) - \sum_{j=1}^{m} N_j(\xi,\eta,\rho)\, f_{vj} \right)\left( \sum_{i=1}^{ntip} N_i(\Gamma)\, K_I^i \right)$$
$$+Z_0(\xi,\eta,\rho)\left( g_v(\xi,\eta,\rho) - \sum_{j=1}^{m} N_j(\xi,\eta,\rho)\, g_{vj} \right)\left( \sum_{i=1}^{ntip} N_i(\Gamma)\, K_{II}^i \right)$$
$$+Z_0(\xi,\eta,\rho)\left( h_v(\xi,\eta,\rho) - \sum_{j=1}^{m} N_j(\xi,\eta,\rho)\, h_{vj} \right)\left( \sum_{i=1}^{ntip} N_i(\Gamma)\, K_{III}^i \right) \qquad (2.7)$$

$$w(\xi,\eta,\rho) = \sum_{j=1}^{m} N_j(\xi,\eta,\rho)\, w_j + Z_0(\xi,\eta,\rho)\left( f_w(\xi,\eta,\rho) - \sum_{j=1}^{m} N_j(\xi,\eta,\rho)\, f_{wj} \right)\left( \sum_{i=1}^{ntip} N_i(\Gamma)\, K_I^i \right)$$
$$+Z_0(\xi,\eta,\rho)\left( g_w(\xi,\eta,\rho) - \sum_{j=1}^{m} N_j(\xi,\eta,\rho)\, g_{wj} \right)\left( \sum_{i=1}^{ntip} N_i(\Gamma)\, K_{II}^i \right) \qquad (2.8)$$
$$+Z_0(\xi,\eta,\rho)\left( h_w(\xi,\eta,\rho) - \sum_{j=1}^{m} N_j(\xi,\eta,\rho)\, h_{wj} \right)\left( \sum_{i=1}^{ntip} N_i(\Gamma)\, K_{III}^i \right)$$

Displacement formulation of enriched finite element is written in Eqn. (2.6) to (2.8). $N_j$ denotes the shape function of regular elements according to ξ, η, ρ local coordinates, and nodal displacements are labeled as $u_j$, $v_j$ and $w_j$, respectively. The functions $f_{u\text{-}v\text{-}w}$, $g_{u\text{-}v\text{-}w}$, $h_{u\text{-}v\text{-}w}$ are obtained from the analytically known element of the asymptotic crack tip displacement expression, and represent the mode I, mode II and mode III displacement components transformed from local to a global coordinate system [31]. $Z_0(\xi,\eta,\rho)$ is a function, changing between 0 and 1. Its value is 1 for all enriched finite elements, and 0 for regular elements. There are also transition elements between enriched and regular elements. The value of $Z_0(\xi,\eta,\rho)$ is either 1 or 0 for transition elements depending on neighboring an enriched or regular element. A new term $\sum_{i=1}^{ntip} N_i(\Gamma)\, K_{I,\ II,\ III}^i$ is added to the end of finite element formulation to calculate the SIFs with enriched elements in crack front. $K_{I,\ II,\ III}^i$ indicates the SIFs for any element in crack front under different crack modes. Locally isoparametric coordinate (Γ) changes between -1 and 1. The studies of Ayhan and Nied [31], [34] can be referred for further information about enriched element formulation and their numerical integration.

## 2.2. Calculation of Element Stiffness Matrix by Parallel Computing

In this study, OpenMP directives were used to compute element stiffness matrices in a parallel manner. OpenMP is a shared-memory parallelization method supported by many hardware manufacturers, preparing compilers and libraries compatible with OpenMP. Parallel regions are created between the sentinel *"!$"* in OpenMP code. Since the lines starting with an exclamation mark *"!"* are the command line in normal compilers, the code is read only with OpenMP routines in this region. Thus, serial and parallel regions can be used together in the same code.

Work-sharing and the synchronization between threads are among the most critical issues in parallelizing. Since all threads read/write shared data at the same time, some synchronization problems may occur. For this reason, the variables must be classified as private or shared, carefully.

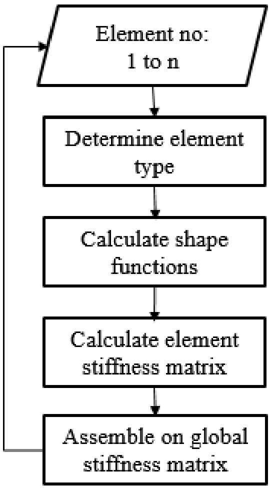

Figure 2.3. Serial processing algorithm

A serial algorithm is given in Figure 2.3. This algorithm calculates an element stiffness matrix using the shape function related to the element type. Then, assembles it into a global stiffness matrix for each element. Note that, high order integral calculation is required for the shape functions of enriched elements, and it is time-consuming as these steps are running for each element one by one in a serial manner.

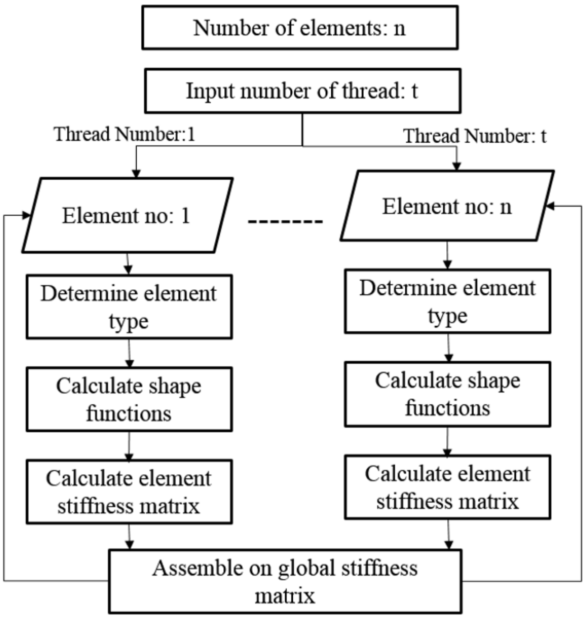

Figure 2.4. Parallel processing algorithm

The calculations of the elements can be performed at the same time by work-sharing as seen in Figure 2.4., so that the total processing time can be shortened. In FCPAS, the shape function is calculated by calling the related subroutine, after determining the element types according to the numbers and locations of nodes. Parallelizing the "Calling a sub-routine" makes it possible to calculate the element stiffness matrix and assemble it in the global stiffness matrix for more than one element at the same time. In order for the same global stiffness matrix is to be reached by each thread, it must be defined as shared. But, at a given time, only one thread must be operating in the global stiffness matrix in order to avoid a reduction problem during the addition of the element stiffness matrix to the global stiffness matrix. Calculation of an element stiffness matrix must be done by only one thread. The corresponding components belonging to the element, such as element load matrix, must be private.

## 2.3. Case Studies and The Results

11 different cases, such as surface crack, edge crack, corner crack and inclined surface crack were analyzed with the serial and parallel version of FCPAS in the same computer (8 GB RAM, i7-4710 2.5 GHz CPU). All cases were in mode-I loading

condition except inclined surface crack that generates mode-I, -II and -III SIFs. Details of the models can be seen in Table 2.1.

Table 2.1. Details of the 11 cases and their comparisons between serial and parallel computing time

| Model No | Number of Elements | Number of Nodes | Enriched Elements | Transition Elements | Element Matrix Calculation & Assembly | | |
|---|---|---|---|---|---|---|---|
| | | | | | Serial [s] | Parallel (2) [s] | % gain |
| 1 | 499 | 3886 | 2 | 6 | 1.82 | 1.27 | 30.2 |
| 2 | 2826 | 20084 | 4 | 12 | 4.43 | 2.82 | 36.3 |
| 3 | 6104 | 34673 | 4 | 12 | 5.87 | 3.52 | 40.0 |
| 4 | 33833 | 62123 | 100 | 300 | 210.12 | 67.58 | 67.9 |
| 5 | 39012 | 71814 | 200 | 400 | 312.87 | 101.99 | 67.3 |
| 6 | 46948 | 91513 | 160 | 480 | 315.55 | 110.99 | 64.8 |
| 7 | 52861 | 106357 | 160 | 480 | 347.65 | 111.0 | 68.1 |
| 8 | 57174 | 117271 | 240 | 720 | 488.79 | 166.34 | 66.0 |
| 9 | 77817 | 143350 | 200 | 600 | 433.00 | 138.85 | 67.9 |
| 10 | 88859 | 195934 | 480 | 1440 | 981.43 | 335.66 | 65.8 |
| 11 | 135186 | 251842 | 602 | 1814 | 1290.17 | 418.11 | 67.6 |

FCPAS writes “wall clock time” of the main calculation processes in a file. The time spent for “Element Matrix Calculation & Assembly” was read from the file and presented in Table 2.1. along with the percentage of saved time for all cases. The total number of elements, number of the enriched and transition elements were given separately. As the total number of enriched and transition elements (non-regular element) increases, the time difference between serial and parallel computing has become significant. Parallel computing is more efficient for a high number of enriched and transition elements since it takes more solution time to calculate the stiffness matrices requiring high order numerical integrations. Figure 2.5. shows the relation between the computation time and the number of non-regular elements.

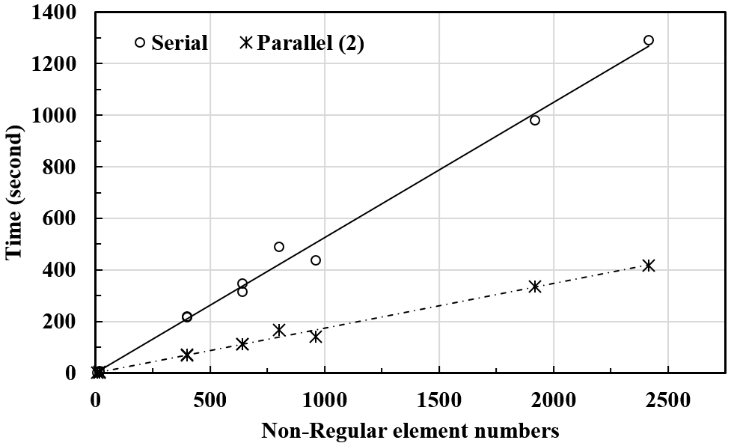

Figure 2.5. Computation time vs total number of non-regular elements

The SIFs were calculated for all cases and the results of parallel processing were verified with the results of serial computing. A detailed view of the model and calculated SIFs are given in Figure 2.6. - Figure 2.11. The cases of 5, 6, 7, 8 and 10 are surface crack in a finite thickness plate with the same aspect ratio and the graph was plotted only for case 5. As seen in Figure 2.6. - Figure 2.11. there is no difference between the results of serial and parallel computing methods.

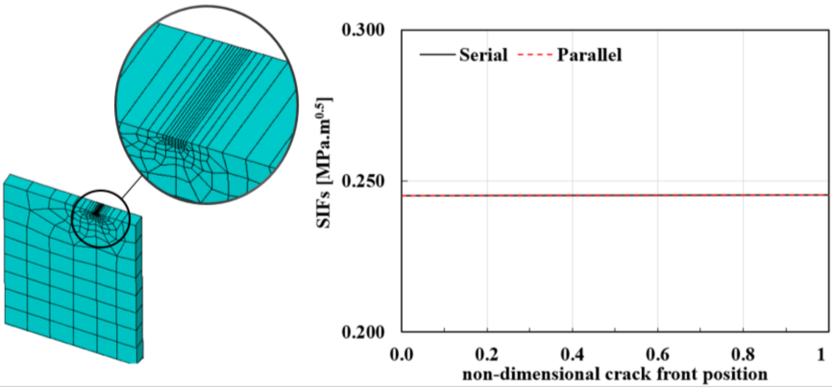

Figure 2.6. Edge crack in a finite thickness plate, a/w = 0.7 (Case 1)

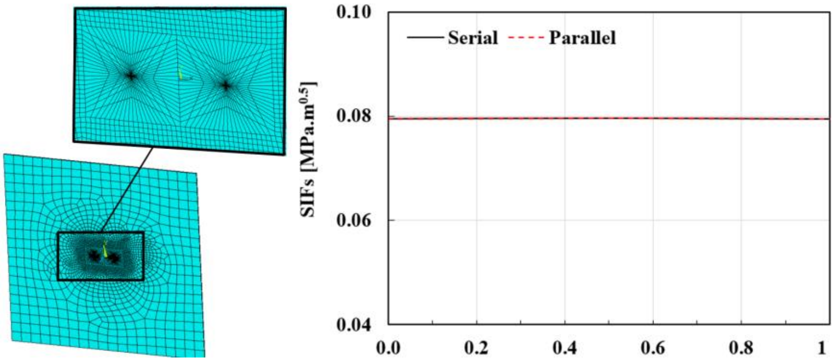

Figure 2.7. Central crack on a functionally graded material (Case 2)

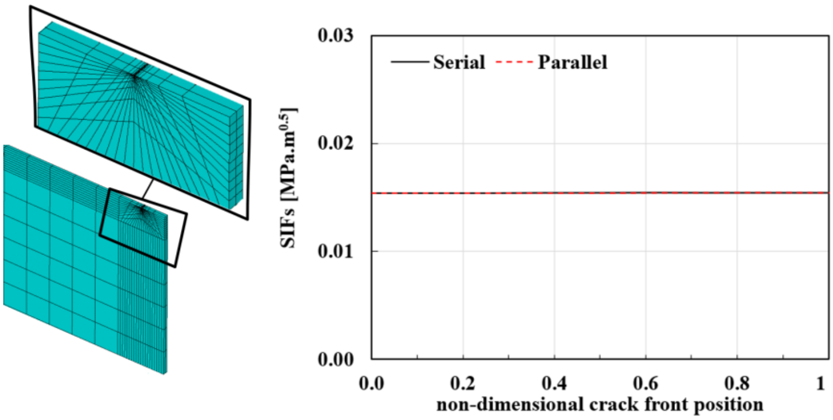

Figure 2.8. Edge crack in a finite thickness plate, a/w = 0.1 (Case 3)

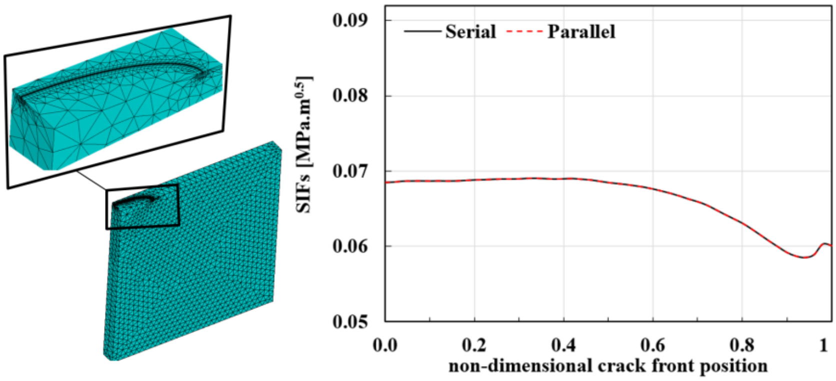

Figure 2.9. Surface crack in a finite thickness plate, a/c = 0.33 (Case 4)

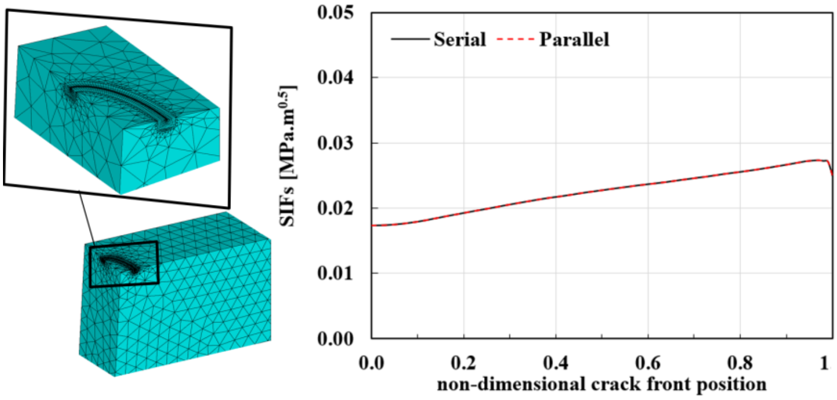

Figure 2.10. Surface crack in a plate, a/c =2 – submodelling (Case 5)

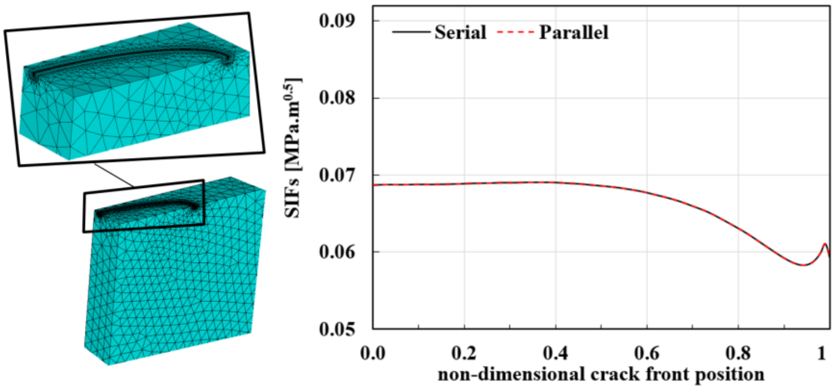

Figure 2.11. Surface crack in a finite thickness plate, a/c = 0.33 (Case 9)

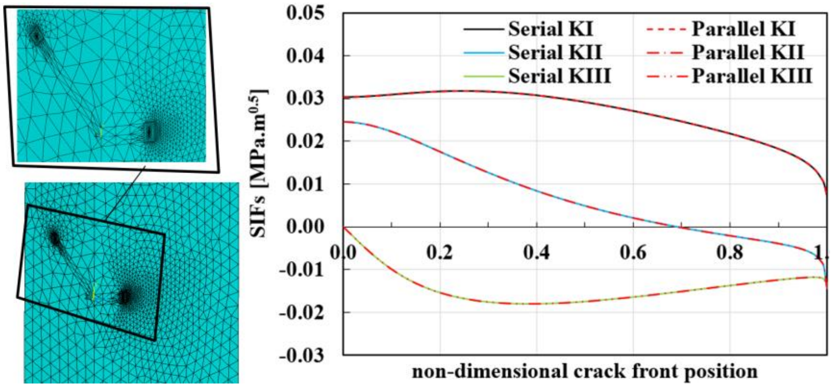

Figure 2.12. Validation model for the inclined surface crack in a finite thickness plate (Case 11)

# CHAPTER 3. PROBABILISTIC FRACTURE MECHANICS STUDIES FOR TWO-DIMENSIONAL FATIGUE CRACK GROWTH PROBLEMS

In this chapter, axial tensile, fracture toughness and crack propagation tests under constant and variable-amplitude loads are discussed for usage in probabilistic fracture mechanics studies. The variabilities of material properties were determined by axial tensile, fracture toughness and constant-amplitude crack propagation tests. Using these data, the variable amplitude loading test results were compared with the existing crack propagation models in the literature and the results were presented.

This chapter has been prepared by using data from the reports of the TUBITAK-funded project, 217M690 “Fracture and Crack Propagation System – Phase 3” [35].

## 3.1. Determination of Variabilities on Fracture and Crack Growth Material Properties

In this section, the variability caused by material properties was experimentally investigated. Certificated hot-rolled 7075-T651 aluminum alloy slabs with a thickness of 30 mm were used in all experiments. The crack orientation is in the direction of L-T. The specimens used in axial tensile or two-dimensional crack growth tests were machined by CNC milling at Sakarya University, Engineering Faculty, Laboratory of Department of Mechanical Engineering. Experiments were done by MTS axial/torsional fatigue test machine in Sakarya University Research, Development and Application Center (SARGEM). The axial tension and the torque capacity of the machine are 100 kN and 1100 Nm, respectively.

## 3.2. Axial Tension Tests

First, axial tension tests were performed to determine the mechanical strength of the material. The yield stresses were obtained as 497, 512 and 507 MPa from three tests with specimens of 90 mm critical length and 5.5 mm thickness. Stress-strain curves of these tests are given in Figure 3.1.

Note: Displacements were measured on the actuator since the aim of the tensile test was to determine yield stress. An axial extensometer was not used.

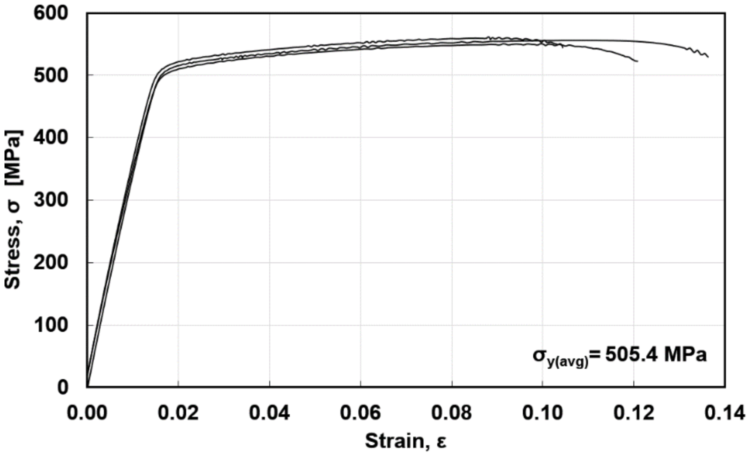

Figure 3.1. Stress-Strain curves for aluminum 7075-T651

After the tensile tests, it was observed that the fracture was in the critical section and was generally perpendicular to the loading direction, as expected for a brittle material under tensile stress. The view of the specimens after tests are given in Figure 3.2.

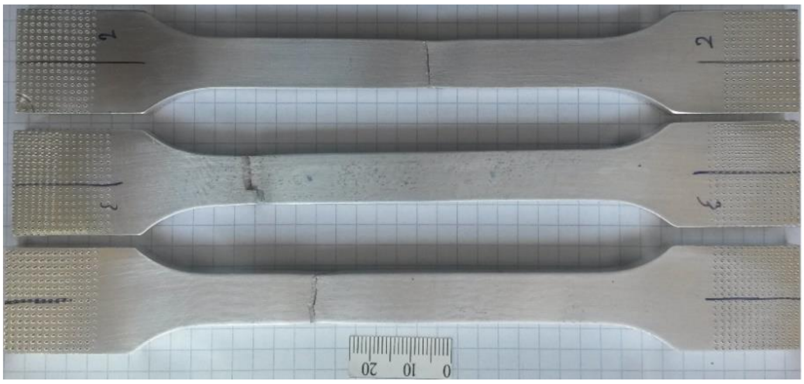

Figure 3.2. View of specimens after tensile testing

### 3.3. Fracture Toughness Tests

29 tests were carried out under the same load conditions to determine the variability of fracture toughness. The 7075-T651 aluminum alloy specimens used in the tests were identical and produced according to ASTM E399-12 standard [36]. The specimens were of 25 mm thickness. The width of the specimen (the distance between the center of the loading pin and back) is 50 mm and the other dimensions that depends on the width according to ASTM E399-12. Technical drawing of the compact tension (CT) specimen is given in Figure 3.3.

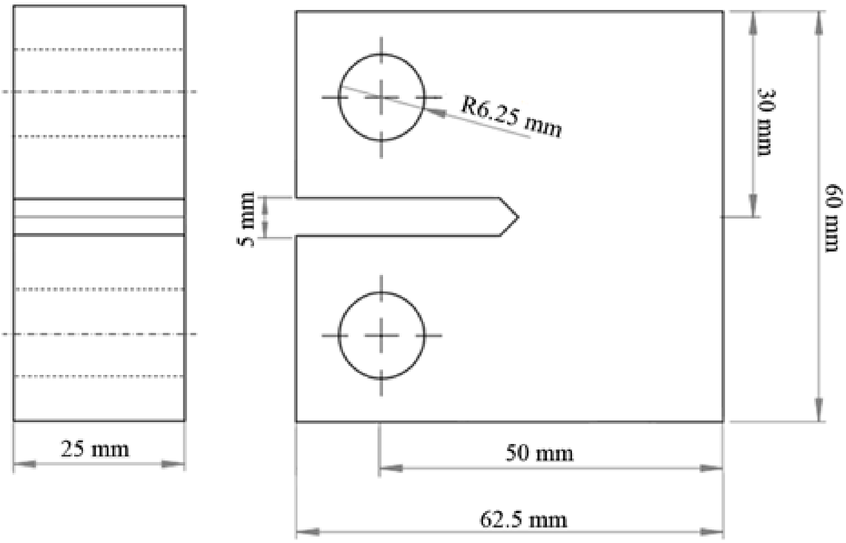

Figure 3.3. Technical drawing of CT specimen

Brief notes related to the ASTM E399-12 standard are given below.

- Specimen thickness B, must be compatible with the inequality B $\geq 2.5\left({}^{K_{IC}}/_{\sigma_y}\right)^2$. Therefore, the thickness value must be greater than 10 mm for aluminum 7075 alloy.
- Specimen width w, must be compatible with the inequality w $\geq 5\left({}^{K_{IC}}/_{\sigma_y}\right)^2$ In this condition, the width must be greater than 16.5 mm for 7075 aluminum alloy.
- The width must be between 2 and 4 times of thickness.

- The applied load cannot be greater than 80% of the fracture toughness while generating the precrack.
- Loading rate must be between 0.55 and 2.75 MPa.m$^{0.5}$/s in fracture toughness test.
- After the fracture toughness test, the crack front must be measured from three different points that are equally spaced along with the thickness. The difference between one of the three points and the average of them cannot be greater than 10%. The symmetry of the specimen can be verified with this condition.

The relation between fracture load and stress intensity factor is empirically given by ASTM E399-12 in Equation 3.1.

$$K_{IC} = \frac{P_Q}{B\sqrt{w}} \frac{\left(2+\frac{a}{w}\right)}{\left(1-\frac{a}{w}\right)^{3/2}} \left[0.866 + 4.64\left(\frac{a}{w}\right) - 13.32\left(\frac{a}{w}\right)^2 + 14.72\left(\frac{a}{w}\right)^3 - 5.6\left(\frac{a}{w}\right)^4\right] \tag{3.1}$$

$P_Q$ is the fracture load and $K_{IC}$ is the fracture toughness, w is the width of the specimen in Eqn. (3.1). $P_Q$ is determined by the trend of the force-displacement curve. Force-displacement curve obtained from the test can be classified into three types as seen in Figure 3.4. and the procedure of determination of $P_Q$ was written in the standard for each type. If the force-displacement curve is not linear, like type-I, a linear line is drawn by using the 95% secant of the curve and the intersection point of two lines is equal to fracture load. Type-II is seen in the tests where a partial fracture occurs on the specimen before fast fracture. Fracture load is equal to the first jump point on the curve. Type-III curve is linear and does not contain any discontinuity during the test, thus the fracture load is the maximum load.

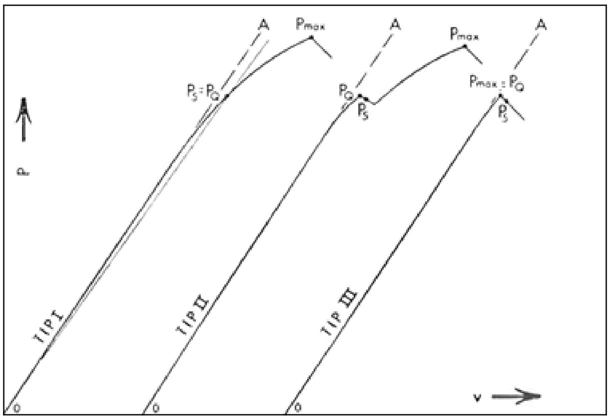

Figure 3.4. Typical force-displacement curves obtained from fracture toughness tests [36]

CT specimens were manufactured in the L-T direction and experimental procedures were determined according to ASTM E-399 as explained above. It is expected that the fracture toughness for 7075-T6 material is about 29 MPa.m$^{0.5}$. The fatigue load was calculated by using Eqn. (3.1) as the half of fracture toughness, and applied to the specimen to generate precrack. The stress ratio (R) of the fatigue load was 0.1. The final length of the precrack was expected to be 25 mm, and half millimetric labels were pasted on the surfaces to measure the crack length during the tests. Two microscope cameras were placed front and back sides of the specimen to monitor the crack growth. Precrack generating process was stopped when the crack reached 25 mm. Note that; this precrack length on surfaces is not the exact dimension used in the calculation of fracture toughness. It is measured on the cracked surface after the fracture test. The experimental setup is given in Figure 3.5.

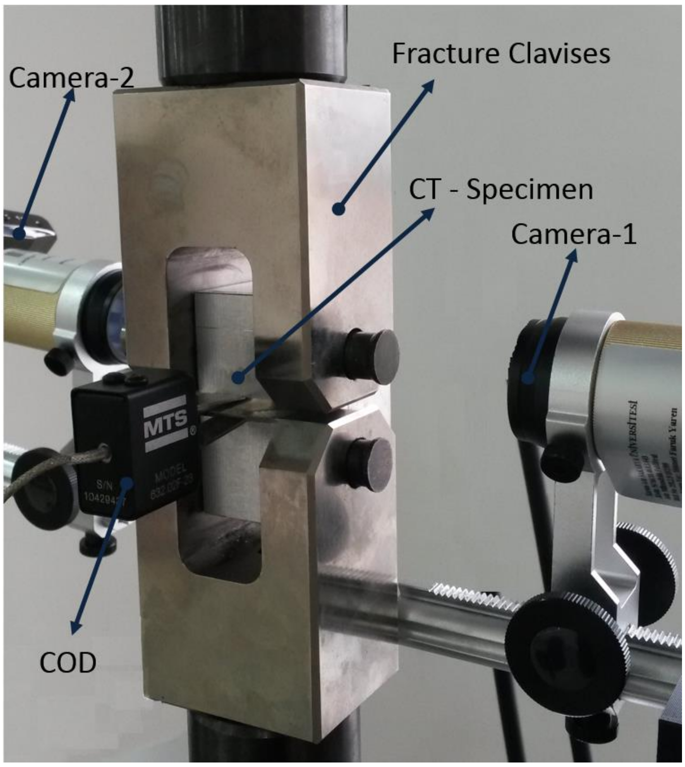

Figure 3.5. Experimental test setup

After the precracking process, axial tension force was applied with a loading rate of 0.6 kN/s and the specimens were fractured. The force-displacement data were recorded during the test. Images were taken from the fracture surfaces and the precrack length was measured from equally divided three different points $a_1$, $a_2$, $a_3$ along with the thickness by using pixel size with Analyzing Digital Images-ADI16 [37] software and the average of three measurements were taken as the precrack length (Analyzing Digital Images-ADI16 software is free for noncommercial use).

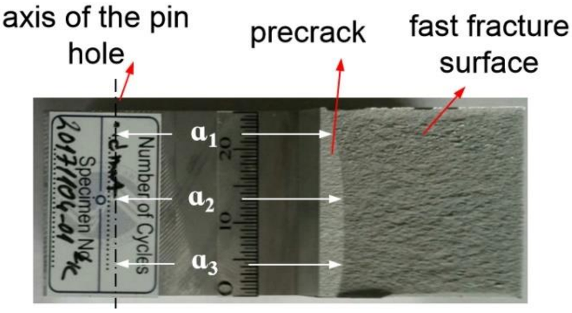

Figure 3.6. Measurement of precrack length on fracture surface

Fracture load $P_Q$ was determined by using the force-displacement curves, obtained from each fracture toughness test. According to Eqn (3.1), fracture toughness was calculated by using the average precrack length. Figure 3.7. is given as an example of force-displacement curves from tests.

29 different fracture toughness tests are listed in Table 3.1. Fracture toughness values $K_{Ic}$ are presented in the last column of the table. The average of $K_{Ic}$ is 29.957 MPa.m$^{0.5}$, and the standard deviation and variance are 1.306 and 1.705, respectively.

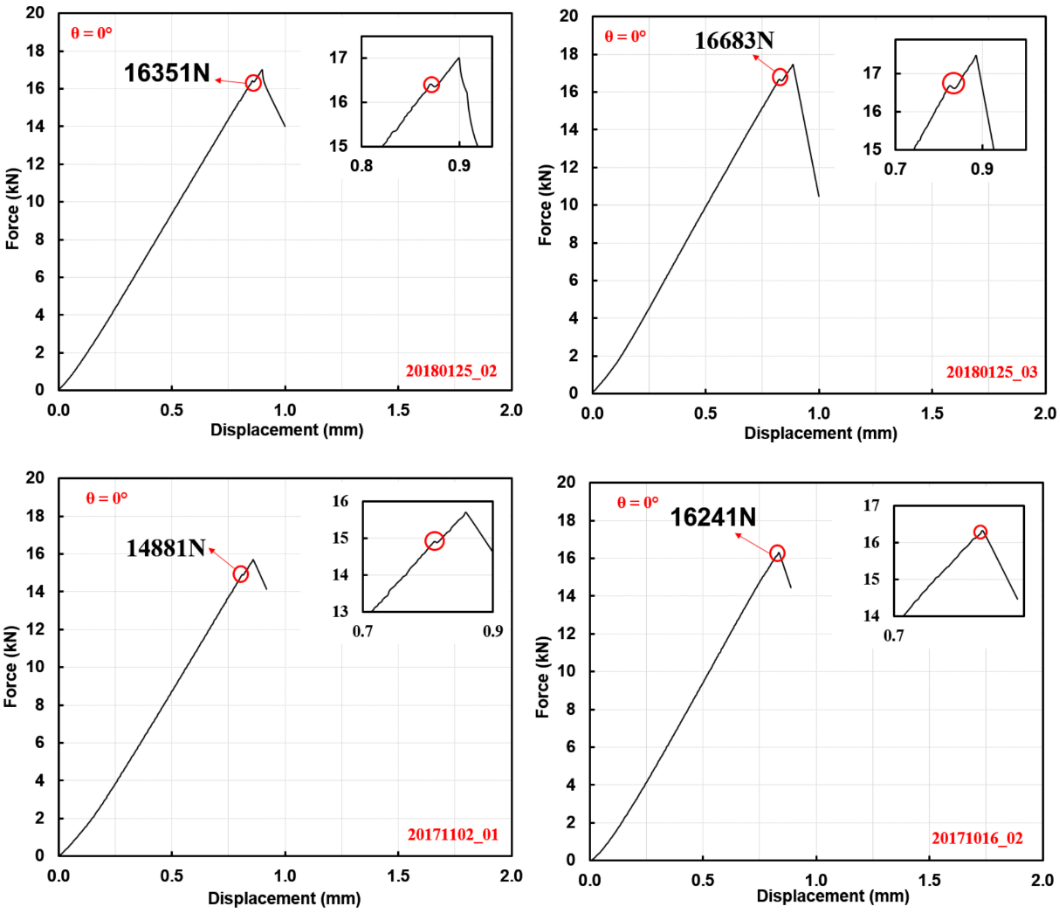

Figure 3.7. Force-displacement curves from some tests and determination of the fracture load

Table 3.1. Detailed information for all of fracture toughness tests

| Specimen Name | Max. Load for Precrack (kN) | $a_1$ (mm) | $a_2$ (mm) | $a_3$ (mm) | $a_{(avg)}$ (mm) | $P_Q$ (kN) | $K_{IC}$ MPa.m$^{0.5}$ |
|---|---|---|---|---|---|---|---|
| 20171011_01 | 7.2 | 26.080 | 26.580 | 26.700 | 26.453 | 15.99 | 30.290 |
| 20171011_02 | 7.2 | 26.540 | 26.700 | 26.140 | 26.460 | 14.34 | 27.181 |
| 20171012_01 | 7.2 | 26.720 | 27.490 | 27.550 | 27.253 | 14.45 | 28.892 |
| 20171016_01 | 7.2 | 26.170 | 25.970 | 25.670 | 25.937 | 16.52 | 30.277 |
| 20171016_02 | 7.2 | 26.710 | 26.460 | 26.290 | 26.487 | 16.24 | 30.842 |
| 20171027_01 | 5.0 | 26.590 | 26.860 | 26.480 | 26.643 | 15.45 | 29.650 |
| 20171102_01 | 6.0 | 26.550 | 27.100 | 26.950 | 26.867 | 14.88 | 28.980 |
| 20171104_01 | 5.6 | 25.960 | 26.620 | 26.600 | 26.393 | 14.88 | 28.080 |
| 20171123_01 | 5.6 | 27.700 | 27.430 | 26.630 | 27.253 | 13.81 | 27.606 |
| 20171127_02 | 6.0 | 27.300 | 26.770 | 26.370 | 26.813 | 15.77 | 30.594 |
| 20171207_02 | 6.0 | 26.030 | 26.410 | 26.820 | 26.420 | 16.14 | 30.519 |
| 20171212_01 | 6.0 | 25.970 | 26.300 | 26.790 | 26.353 | 14.83 | 27.920 |
| 20171212_02 | 5.8 | 27.610 | 27.110 | 26.570 | 27.097 | 15.26 | 30.186 |
| 20180110_01 | 6.2 | 26.630 | 26.570 | 26.060 | 26.420 | 15.20 | 28.745 |
| 20180117_01 | 6.2 | 27.060 | 26.900 | 26.340 | 26.767 | 16.05 | 31.055 |
| 20180124_01 | 6.2 | 26.740 | 26.450 | 26.740 | 26.643 | 16.49 | 31.636 |
| 20180124_02 | 6.2 | 26.410 | 26.350 | 26.660 | 26.473 | 16.61 | 31.521 |
| 20180124_04 | 6.2 | 25.910 | 26.180 | 26.350 | 26.147 | 16.85 | 31.291 |
| 20180125_02 | 6.4 | 25.670 | 26.050 | 26.610 | 26.110 | 16.35 | 30.299 |
| 20180125_03 | 6.4 | 26.270 | 25.800 | 25.870 | 25.980 | 16.68 | 30.657 |
| 20180125_04 | 6.4 | 25.580 | 25.550 | 26.080 | 25.737 | 17.08 | 30.894 |
| 20180212_01 | 7.0 | 26.500 | 26.440 | 26.630 | 26.523 | 16.71 | 31.810 |
| 20180212_02 | 7.0 | 26.600 | 27.320 | 26.870 | 26.930 | 15.52 | 30.349 |
| 20180213_01 | 7.0 | 26.530 | 27.250 | 27.320 | 27.033 | 14.55 | 28.652 |
| 20180213_02 | 7.0 | 26.950 | 27.270 | 26.770 | 26.997 | 15.32 | 30.090 |
| 20180213_03 | 7.0 | 25.670 | 25.840 | 26.250 | 25.920 | 16.90 | 30.935 |
| 20180214_01 | 7.0 | 26.600 | 27.040 | 26.930 | 26.857 | 14.51 | 28.244 |
| 20180214_02 | 7.0 | 26.080 | 25.700 | 26.100 | 25.960 | 16.38 | 30.063 |
| 20180502_01 | 7.0 | 26.110 | 26.040 | 26.670 | 26.273 | 16.85 | 31.550 |

Histograms were plotted with the fracture toughness values given in Table 3.1. with four different distribution type (normal, lognormal, weibull, gamma), as shown in Figure 3.8.

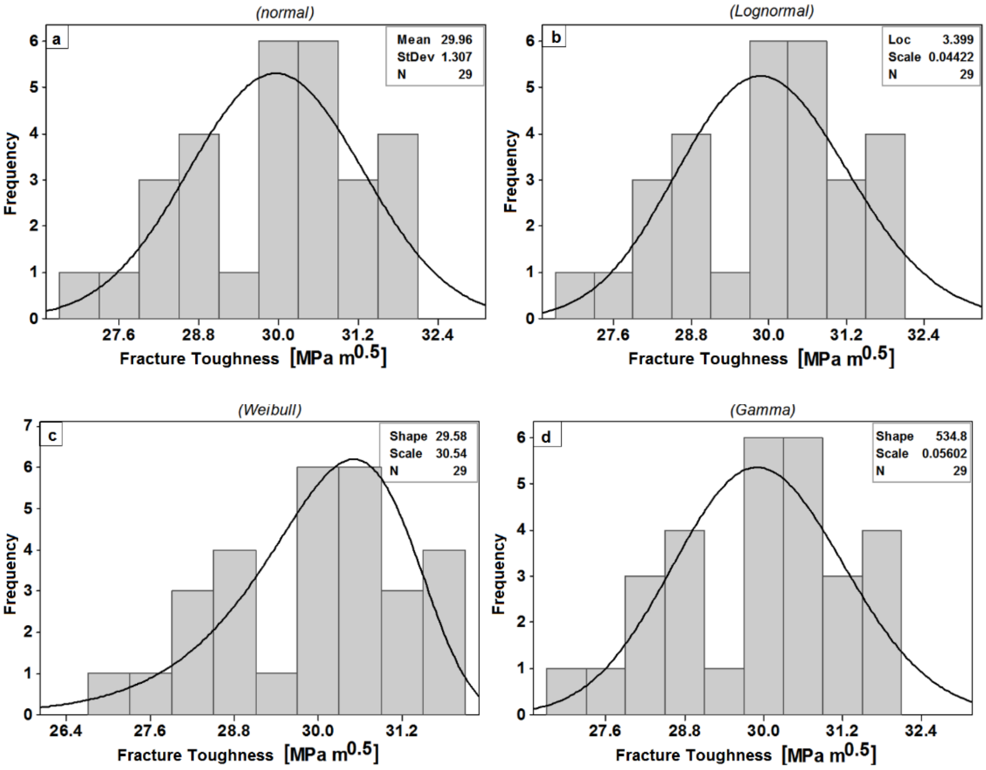

Figure 3.8. Histogram graphs for fracture toughness a) Normal distribution, b) Lognormal distribution, c) Weibull distribution, d) Gamma Distribution

The top view of all specimens after fracture toughness tests are shown in Figure 3.9.

Figure 3.9. Top view of the used specimens for fracture tests

## 3.4. Fatigue Crack Growth Tests Under Constant Amplitude Loading

Fatigue crack growth tests under constant amplitude loading were performed to determine the variability in crack growth properties. CT specimens were machined from 7075-T651 with the dimensions given in Figure 3.3. and the crack was oriented in L-T direction. ASTM E647-15 [38] standard was applied during the tests. Some points regarding the standard are provided below.

- Crack growth direction is expected to be planar under mode-I loading, so the crack growth angle must be less than 10 degrees with the plane.
- The precrack length must be greater than one-tenth of the specimen thickness.
- The applied maximum load to generate the precrack must be smaller than the initial SIF of the fatigue crack growth test.
- Fatigue crack growth length must be measured from both sides of the specimen and the average value must be used in the calculations. The difference between the measurements cannot exceed one-fourth of the specimen thickness.
- 2% sensitivity For maximum fatigue load, should be provided in measurements.
- If “a/w” is smaller than 0.2, Eqn (3.1) cannot be used to calculate the SIF.

The numbers of the fatigue crack growth tests are given in Table 3.2. Constant amplitude tests were planned with four different stress ratios are also shown in Table 3.2. More tests were performed for R = 0.1 and 0.5 than for R = 0.7 and 0.8 stress ratio. For a given ΔK, the crack growth life was shorter in R = 0.7 and 0.8 tests than R = 0.1 and 0.5 tests, therefore the number of tests was not increased in R = 0.7 and 0.8 tests. The crack length was measured by two microscope cameras and crack opening displacement (COD) gage, placed on the specimen.

Table 3.2. Test matrix for FCG under constant amplitude

| Test | Count | Specimen Type |
|---|---|---|
| Fatigue crack growth tests under constant amplitude – R = 0.1 | 21 | CT |
| Fatigue crack growth tests under constant amplitude – R = 0.5 | 20 | CT |
| Fatigue crack growth tests under constant amplitude – R = 0.7 | 10 | CT |
| Fatigue crack growth tests under constant amplitude – R = 0.8 | 10 | CT |

During the tests, the images are taken from two sides of the specimen by two microscope cameras, and the cycle count of the test were monitored from the screen window of the control software of the fatigue machine. The screen was captured periodically by an in-house software. The crack length was measured based on pixel size by using the captured pictures, and crack growth curves were plotted, accordingly. Pixel size was calibrated with a sticker of half-millimeter scale steps. A sample of screen view is seen in Figure 3.10.

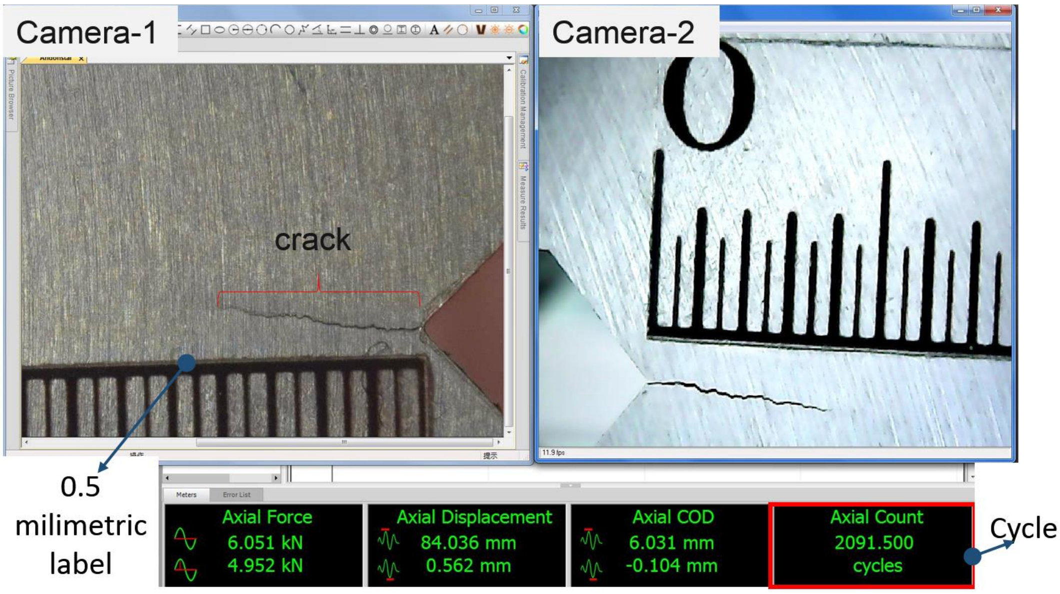

Axial Force 6.051 kN 4.952 kN

Axial Displacement 84.036 mm 0.562 mm

Axial COD 6.031 mm -0.104 mm

Axial Count 2091.500 cycles

Figure 3.10. Camera views and the cycle during the fatigue crack growth test

### 3.4.1. FCG tests under constant amplitude R = 0.1

21 fatigue crack growth tests were performed under constant amplitude loading with stress ratio of 0.1. The linear region was determined from crack growth curves, and C-n crack growth constants in Paris-Erdogan Equation (3.2) were found by using the

trend line tool in Microsoft Excel. One of the graphs of these tests is shown in Figure 3.11. All tests in this category are given in Table 3.3. in detail. In Figure 3.11., da/dN - ΔK measurements on the front and back surfaces are shown with triangle and square markers, respectively. Also, the average values are shown with circle symbols. The trend line and its equation can also be seen in the same graph. Constants in Paris-Erdogan Equation (3.2) are obtained by using the equation of the trend line. The crack length versus cycle graph is also given in Figure 3.11.

$$\frac{da}{dN} = C(\Delta K)^n \tag{3.2}$$

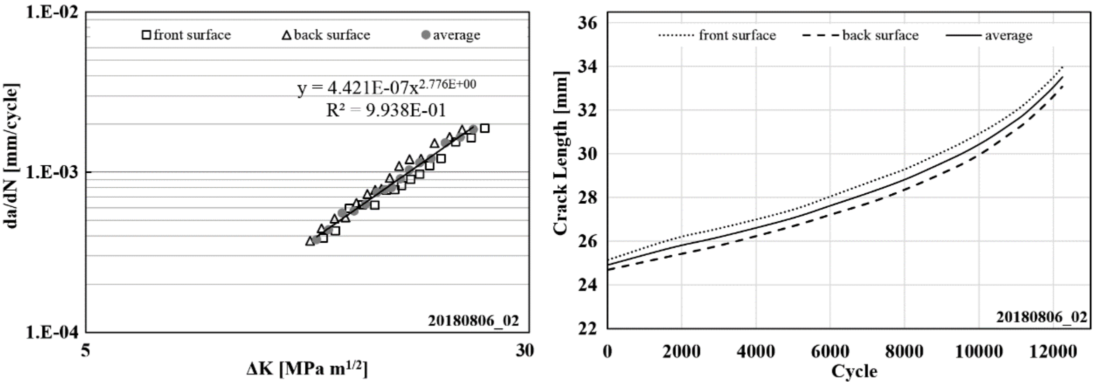

Figure 3.11. Crack growth curves, R = 0.1

Paris-Erdogan constants obtained from all tests under R = 0.1 conditions are also provided in Table 3.3. In the first two tests, a highly scattered crack growth data were observed. Calculated constants using these tests were considered as outliers and were marked in red.

Table 3.3. Details of the R = 0.1 constant amplitude crack growth tests

| | Precrack | | Fatigue crack growth | | | | |
|---|---|---|---|---|---|---|---|
| Specimen Name | Max. Load for Precrack (kN) | $a_{(avg)}$ (mm) | Stress Ratio for FCG R | Max. FCG load (kN) | Cycle | C | n |
| 20171017_01 | 7.0 | 26.445 | 0.1 | 9.0 | 4641 | 5.785E-21 | 13.822 |
| 20171019_01 | 5.0 | 25.670 | 0.1 | 6.5 | 15278 | 1.347E-14 | 2.368 |
| 20171020_01 | 5.0 | 26.350 | 0.1 | 6.5 | 12767 | 9.678E-08 | 3.406 |

Table 3.3. Details of the R = 0.1 constant amplitude crack growth tests (Continued)

| | | | | | | | |
|---|---|---|---|---|---|---|---|
| 20171023_01 | 5.6 | 25.215 | 0.1 | 6.5 | 10925 | 2.150E-07 | 3.177 |
| 20171108_01 | 5.6 | 25.785 | 0.1 | 6.2 | 15787 | 7.421E-07 | 2.569 |
| 20171122_01 | 5.6 | 24.925 | 0.1 | 6.2 | 21429 | 9.993E-07 | 2.432 |
| 20171128_01 | 5.6 | 25.115 | 0.1 | 6.2 | 12900 | 2.061E-07 | 3.202 |
| 20171208_01 | 5.8 | 25.745 | 0.1 | 6.2 | 21264 | 1.227E-07 | 3.161 |
| 20171213_01 | 5.8 | 25.745 | 0.1 | 6.2 | 13515 | 1.340E-06 | 2.349 |
| 20171215_01 | 6.0 | 25.765 | 0.1 | 6.2 | 13325 | 1.120E-06 | 2.511 |
| 20180108_01 | 6.0 | 25.440 | 0.1 | 6.5 | 15022 | 1.633E-07 | 3.159 |
| 20180109_01 | 6.0 | 25.840 | 0.1 | 6.5 | 12615 | 1.859E-06 | 2.279 |
| 20180424_01 | 6.2 | 25.450 | 0.1 | 7.0 | 14576 | 4.039E-07 | 2.805 |
| 20180425_01 | 6.4 | 25.235 | 0.1 | 7.0 | 14545 | 2.141E-06 | 2.192 |
| 20180425_02 | 6.6 | 25.710 | 0.1 | 7.0 | 9217 | 2.611E-08 | 3.948 |
| 20180719_01 | 6.4 | 25.865 | 0.1 | 7.0 | 13028 | 5.041E-07 | 2.728 |
| 20180720_01 | 6.4 | 25.930 | 0.1 | 7.0 | 12239 | 1.828E-07 | 3.103 |
| 20180724_01 | 6.4 | 25.765 | 0.1 | 7.0 | 11749 | 4.353E-07 | 2.815 |
| 20180724_02 | 6.4 | 25.800 | 0.1 | 7.0 | 11416 | 2.211E-07 | 3.082 |
| 20180730_01 | 6.4 | 25.743 | 0.1 | 7.0 | 11274 | 3.841E-07 | 2.869 |
| 20180806_02 | 6.4 | 25.530 | 0.1 | 7.0 | 13079 | 4.421E-07 | 2.776 |

Five different studies [39]–[43] which include crack growth constants for 7075-T6 aluminum alloy under R = 0.1 were used to validate the experimentally determined C-n constants in this study. Crack growth rates were calculated by using Paris-Erdogan Equation (3.2) with different C-n constants between $\Delta K = 10 - 30$ MPa.m$^{0.5}$. Calculated crack growth rates and their comparisons with data in the literature can be seen in Figure 3.12. Calculated crack growth rates are drawn with black dashed lines for the given values of C-n in Table 3.3. and colored lines are used for the literature data. The calculated crack growth rates with obtained C-n values are in line with the literature data as seen in Figure 3.12. In addition, the variability of experimental results in data obtained in this study is close to that of the data from the literature.

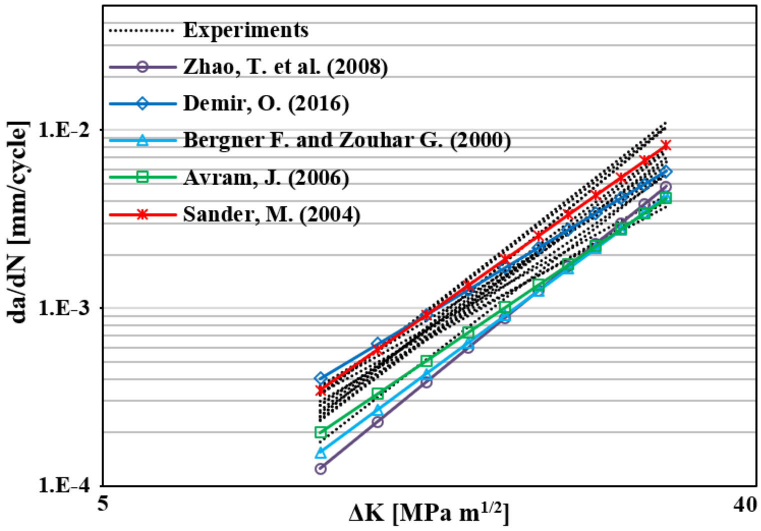

Figure 3.12. Comparison experimentally obtained C-n with data from the literature, R = 0.1

### 3.4.2. FCG tests under constant amplitude R = 0.5

20 fatigue crack growth tests were carried out under constant amplitude loading with the stress ratio of 0.5. The same procedures of R = 0.1 were adopted in these tests. As expected, crack propagation life under R = 0.5 is longer than R = 0.1 for the same maximum fatigue load ($P_{max} = 7$ kN) since the amplitude of the alternating fatigue load is smaller than that of R = 0.1. One of the graphs for these tests is shown in Figure 3.13. Also, detailed information of all tests related to this category can be seen in Table 3.4.

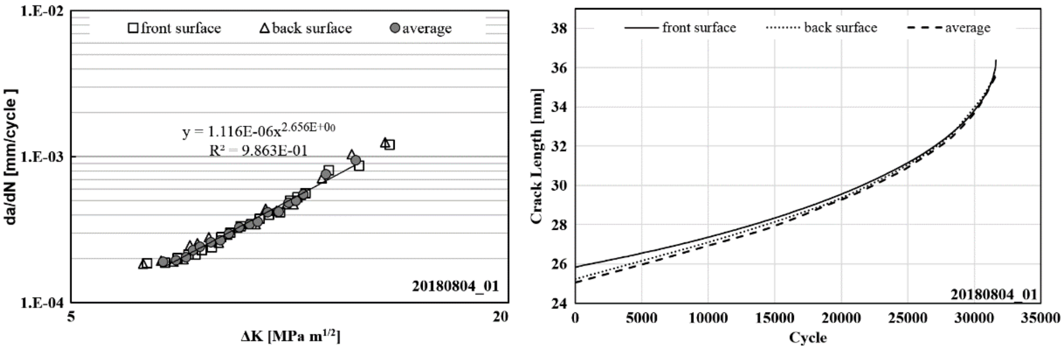

Figure 3.13. Crack growth curves, R = 0.5

Table 3.4. Details of the R = 0.5 constant amplitude crack growth tests

| | Precrack | | Fatigue crack growth | | | | |
|---|---|---|---|---|---|---|---|
| Specimen Name | Max. Load for Precrack (kN) | $a_{(avg)}$ (mm) | Stress Ratio for FCG R | Max. FCG load (kN) | Cycle | C | n |
| 20180430_01 | 6.4 | 25.460 | 0.5 | 7.0 | 28947 | 1.132E-06 | 2.690 |
| 20180503_01 | 6.4 | 25.705 | 0.5 | 7.0 | 29352 | 9.334E-07 | 2.783 |
| 20180511_01 | 6.4 | 25.331 | 0.5 | 7.0 | 29147 | 3.466E-06 | 2.164 |
| 20180507_01 | 6.4 | 25.772 | 0.5 | 7.0 | 26031 | 7.139E-07 | 2.942 |
| 20180514_01 | 6.4 | 25.251 | 0.5 | 7.0 | 37341 | 1.146E-06 | 2.654 |
| 20180515_01 | 6.4 | 25.820 | 0.5 | 7.0 | 32804 | 2.135E-07 | 3.437 |
| 20180515_02 | 6.4 | 25.345 | 0.5 | 7.0 | 33061 | 8.331E-07 | 2.775 |
| 20180516_01 | 6.4 | 25.345 | 0.5 | 7.0 | 32390 | 1.074E-06 | 2.728 |
| 20180517_01 | 6.4 | 25.380 | 0.5 | 7.0 | 29452 | 1.513E-06 | 2.600 |
| 20180521_01 | 6.4 | 25.379 | 0.5 | 7.0 | 29868 | 6.015E-07 | 3.050 |
| 20180731_01 | 6.4 | 25.439 | 0.5 | 7.0 | 30055 | 6.721E-07 | 2.946 |
| 20180731_02 | 6.4 | 26.615 | 0.5 | 7.0 | 24606 | 3.067E-07 | 3.306 |
| 20180801_01 | 6.4 | 25.850 | 0.5 | 7.0 | 27094 | 6.004E-07 | 3.026 |
| 20180804_01 | 6.4 | 25.740 | 0.5 | 7.0 | 31630 | 1.116E-06 | 2.656 |
| 20180804_02 | 6.4 | 25.545 | 0.5 | 7.0 | 23423 | 2.426E-07 | 3.532 |
| 20180805_01 | 6.4 | 25.810 | 0.5 | 7.0 | 33592 | 8.701E-07 | 2.764 |
| 20180805_02 | 6.4 | 25.647 | 0.5 | 7.0 | 33650 | 9.762E-07 | 2.732 |
| 20180806_01 | 6.4 | 26.070 | 0.5 | 7.0 | 30112 | 6.754E-07 | 2.918 |
| 20180806_03 | 6.4 | 26.154 | 0.5 | 7.0 | 26971 | 8.078E-07 | 2.834 |
| 20180806_04 | 6.4 | 26.070 | 0.5 | 7.0 | 28651 | 2.116E-06 | 2.383 |

### 3.4.3. FCG tests under constant amplitude R = 0.7

10 fatigue crack growth tests were performed under constant amplitude loading with the stress ratio of 0.7. The same procedures of R = 0.1 were adopted in these tests. Crack propagation life under R = 0.7 is longer than R = 0.1 and 0.5 for the same maximum fatigue load ($P_{max}$= 7 kN). Thus, the maximum fatigue load was set as 10 kN. One of the graphs for these tests is shown in Figure 3.14. Also, detailed information of all tests related to this category can be seen in Table 3.5.

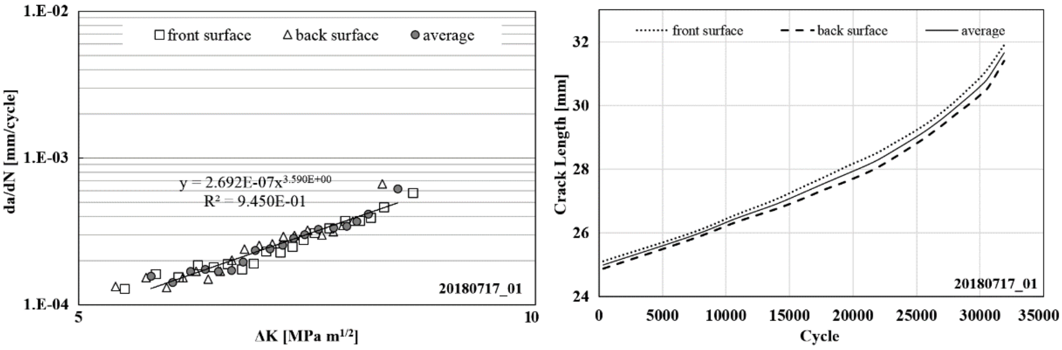

Figure 3.14. Crack growth curves, R = 0.7

Table 3.5. Details of the R = 0.7 constant amplitude crack growth tests

| | Precrack | | Fatigue crack growth | | | | |
|---|---|---|---|---|---|---|---|
| Specimen Name | Max. Load for Precrack (kN) | $a_{(avg)}$ (mm) | Stress Ratio for FCG R | Max. FCG load (kN) | Cycle | C | n |
| 20180604_01 | 6.4 | 25.815 | 0.7 | 7.0 | 111151 | 3.329E-07 | 3.437 |
| 20180605_01 | 6.4 | 26.095 | 0.7 | 7.0 | 91726 | 9.635E-07 | 2.927 |
| 20180607_01 | 6.4 | 25.596 | 0.7 | 7.0 | 119324 | 5.146E-07 | 3.245 |
| 20180613_01 | 6.4 | 25.610 | 0.7 | 10.0 | 31985 | 1.595E-06 | 2.639 |
| 20180710_01 | 6.4 | 25.610 | 0.7 | 10.0 | 26274 | 9.292E-08 | 4.250 |
| 20180716_01 | 6.4 | 26.020 | 0.7 | 10.0 | 24130 | 1.140E-07 | 4.097 |
| 20180717_01 | 6.4 | 25.585 | 0.7 | 10.0 | 31901 | 2.692E-07 | 3.590 |
| 20180718_01 | 6.4 | 25.665 | 0.7 | 10.0 | 29900 | 7.891E-07 | 3.044 |
| 20180719_02 | 6.4 | 25.975 | 0.7 | 10.0 | 31273 | 1.719E-07 | 3.770 |
| 20180903_01 | 6.4 | 26.300 | 0.7 | 10.0 | 21983 | 3.312E-07 | 3.503 |

### 3.4.4. FCG tests under constant amplitude R = 0.8

The last constant amplitude loading test group is generated with the R = 0.8 stress ratio. As the upper and lower levels of the load are very close to each other for R = 0.8, crack growth is the slowest among the constant amplitude loading tests. Initially 10 kN maximum fatigue loading was applied to the specimen, then the load was changed to 11.5 kN incrementally to obtain the desired crack growth life. Crack propagation life under R = 0.8 is longer than R = 0.7 for the same maximum fatigue load ($P_{max}$= 10 kN). One of the graphs for these tests is shown in Figure 3.15. Also, detailed information of all tests related to this category can be seen in Table 3.6.

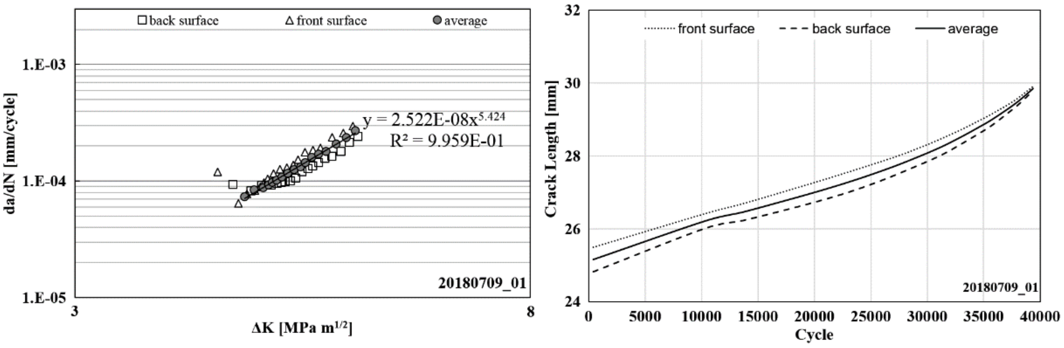

Figure 3.15. Crack growth curves, R = 0.8

Table 3.6. Details of the R = 0.8 constant amplitude crack growth tests

| | Precrack | | Fatigue crack growth | | | | |
|---|---|---|---|---|---|---|---|
| Specimen Name | Max. Load for Precrack (kN) | $a_{(avg)}$ (mm) | Stress Ratio for FCG R | Max. FCG load (kN) | Cycle | C | n |
| 20180619_01 | 6.4 | 25.599 | 0.8 | 10.0 | 68327 | 9.985E-07 | 3.174 |
| 20180620_01 | 6.4 | 26.030 | 0.8 | 12.0 | 24481 | 2.725E-09 | 6.873 |
| 20180622_01 | 6.4 | 25.837 | 0.8 | 11.0 | 51953 | 5.826E-07 | 3.526 |
| 20180626_01 | 7.0 | 26.155 | 0.8 | 11.5 | 31503 | 1.292E-09 | 7.446 |
| 20180628_01 | 6.4 | 26.010 | 0.8 | 11.5 | 28114 | 3.837E-07 | 3.847 |
| 20180629_01 | 7.0 | 26.437 | 0.8 | 11.5 | 33542 | 6.236E-08 | 4.882 |
| 20180702_01 | 6.4 | 25.996 | 0.8 | 11.5 | 41972 | 1.332E-07 | 4.326 |
| 20180704_01 | 6.4 | 25.549 | 0.8 | 11.5 | 32035 | 2.887E-08 | 5.589 |
| 20180709_01 | 6.4 | 25.765 | 0.8 | 11.5 | 39372 | 2.522E-08 | 5.424 |
| 20180709_02 | 6.4 | 25.769 | 0.8 | 11.5 | 40772 | 3.316E-08 | 5.313 |

### 3.4.5. Investigation of variation in crack growth rates under constant amplitude loading

C-n constants of each test were presented in Table 3.3. - Table 3.6. The variability in crack growth rates for different C-n values were calculated by using Equation (3.2). The calculations were performed for the initial, middle and last values of ΔK.

Many types of distributions can represent the scatter obtained in experiments. To select a distribution type and use it through the following steps, the distribution type that best fits the obtained data was analyzed. 12 different distribution types were examined in MINITAB software [44], and the results are given in Table 3.7. The abbreviation "AD" in Table 3.7. refers to the Anderson-Darling value. For a good distribution fit, low values of AD are desired. “P” is another important parameter and if the “P” value is smaller than 0.05, it means that the selected distribution model does not give the correct results. Six distribution types gave appropriate results. For all cases in Table 3.7., the highest “P” value is marked in green and invalid cases of “P” values are marked in red. All cases were examined, and it was concluded that the Lognormal distribution is the most suitable model for the obtained data.

Table 3.7. Results of different distribution models

| R = 0.1 | First Point | | Mid-Point | | End Point | |
|---|---|---|---|---|---|---|
| Distribution | AD | P | AD | P | AD | P |
| Normal | 0.359 | 0.413 | 0.881 | 0.019 | 1.041 | 0.007 |
| Lognormal | 0.343 | 0.452 | 0.523 | 0.16 | 0.417 | 0.298 |
| Exponential | 5.298 | <0.003 | 5.565 | <0.003 | 3.949 | <0.003 |
| 2-Parameter Exponential | 1.84 | <0.010 | 0.286 | >0.250 | 0.227 | >0.250 |
| Weibull | 0.448 | >0.250 | 1.008 | <0.010 | 0.918 | 0.017 |
| Gamma | 0.33 | >0.250 | 0.649 | 0.092 | 0.595 | 0.136 |
| R = 0.5 | First Point | | Mid-Point | | End Point | |
| Distribution | AD | P | AD | P | AD | P |
| Normal | 0.357 | 0.42 | 0.782 | 0.035 | 0.873 | 0.02 |
| Lognormal | 0.365 | 0.403 | 0.477 | 0.211 | 0.414 | 0.305 |
| Exponential | 7.433 | <0.003 | 6.882 | <0.003 | 5.616 | <0.003 |
| 2-Parameter Exponential | 3.379 | <0.010 | 0.462 | >0.250 | 1.233 | 0.03 |
| Weibull | 0.619 | 0.096 | 1.307 | <0.010 | 1.089 | <0.010 |
| Gamma | 0.337 | >0.250 | 0.553 | 0.173 | 0.531 | 0.193 |
| R = 0.7 | First Point | | Mid-Point | | End Point | |
| Distribution | AD | P | AD | P | AD | P |
| Normal | 0.31 | 0.497 | 0.765 | 0.031 | 0.66 | 0.059 |
| Lognormal | 0.327 | 0.45 | 0.616 | 0.078 | 0.431 | 0.243 |
| Exponential | 3.846 | <0.003 | 3.541 | <0.003 | 2.903 | <0.003 |
| 2-Parameter Exponential | 1.33 | 0.012 | 0.497 | >0.250 | 0.597 | 0.185 |
| Weibull | 0.382 | >0.250 | 0.904 | 0.017 | 0.719 | 0.049 |
| Gamma | 0.343 | >0.250 | 0.689 | 0.076 | 0.521 | 0.203 |
| R = 0.8 | First Point | | Mid-Point | | End Point | |
| Distribution | AD | P | AD | P | AD | P |
| Normal | 0.398 | 0.297 | 0.581 | 0.096 | 0.539 | 0.123 |
| Lognormal | 0.33 | 0.443 | 0.433 | 0.24 | 0.337 | 0.426 |
| Exponential | 2.53 | <0.003 | 3.278 | <0.003 | 2.19 | 0.004 |
| 2-Parameter Exponential | 0.501 | >0.250 | 0.617 | 0.169 | 0.185 | >0.250 |
| Weibull | 0.453 | 0.243 | 0.697 | 0.057 | 0.508 | 0.189 |
| Gamma | 0.392 | >0.250 | 0.509 | 0.214 | 0.431 | >0.250 |

Histograms were obtained using MINITAB [44] for specific ΔK values by using da / dN curves calculated for different C-n values in cases of R = 0.1, 0.5, 0.7, 0.8 stress ratios, respectively. The horizontal axis of graphs was labeled as da/dN per 1000 cycles for the initial, middle and final values of ΔK and are shown in Figure 3.16. -Figure 3.19.

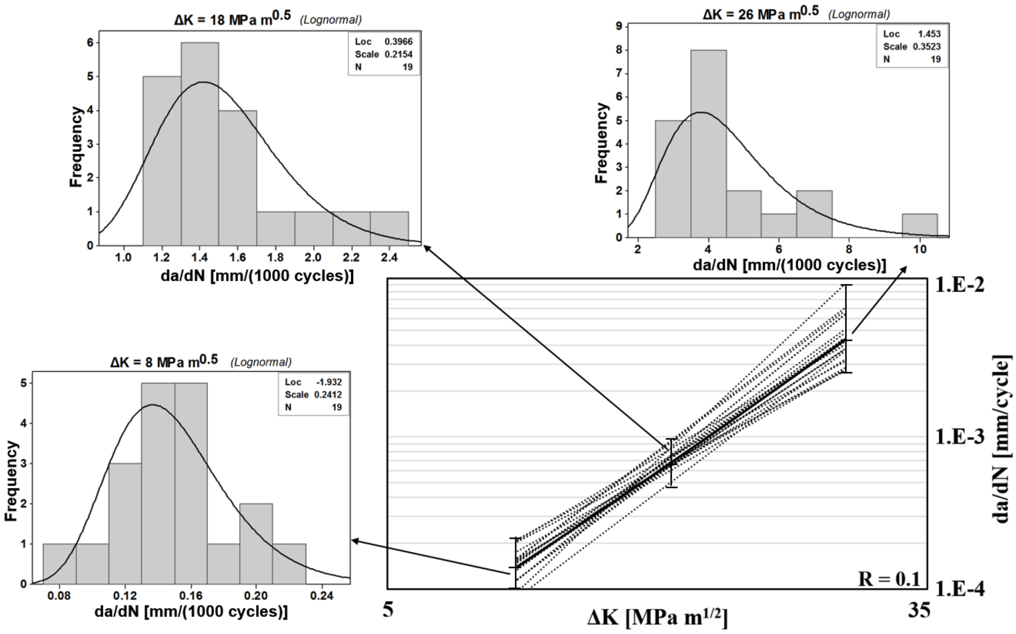

Figure 3.16. da/dN variations under constant amplitude loading, R = 0.1

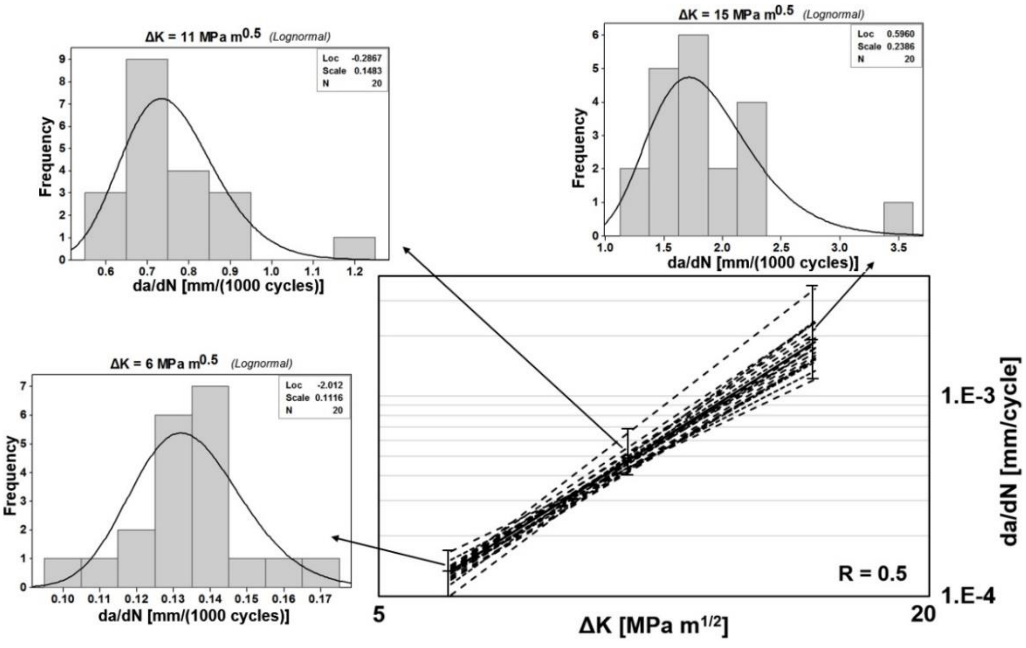

Figure 3.17. da/dN variations under constant amplitude loading, R = 0.5

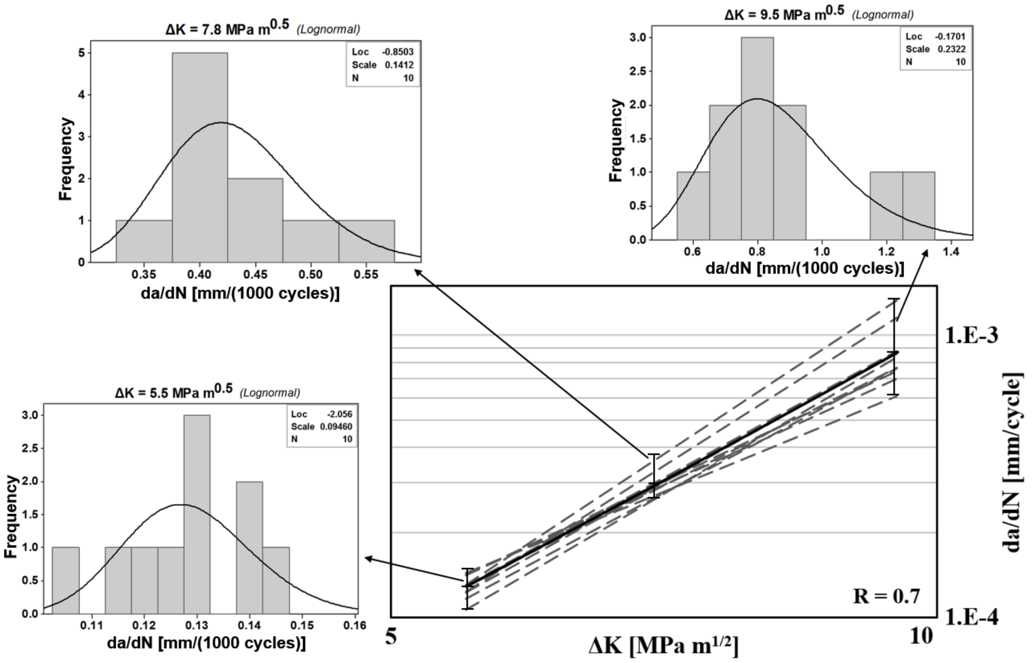

Figure 3.18.da/dN variations under constant amplitude loading, R = 0.7

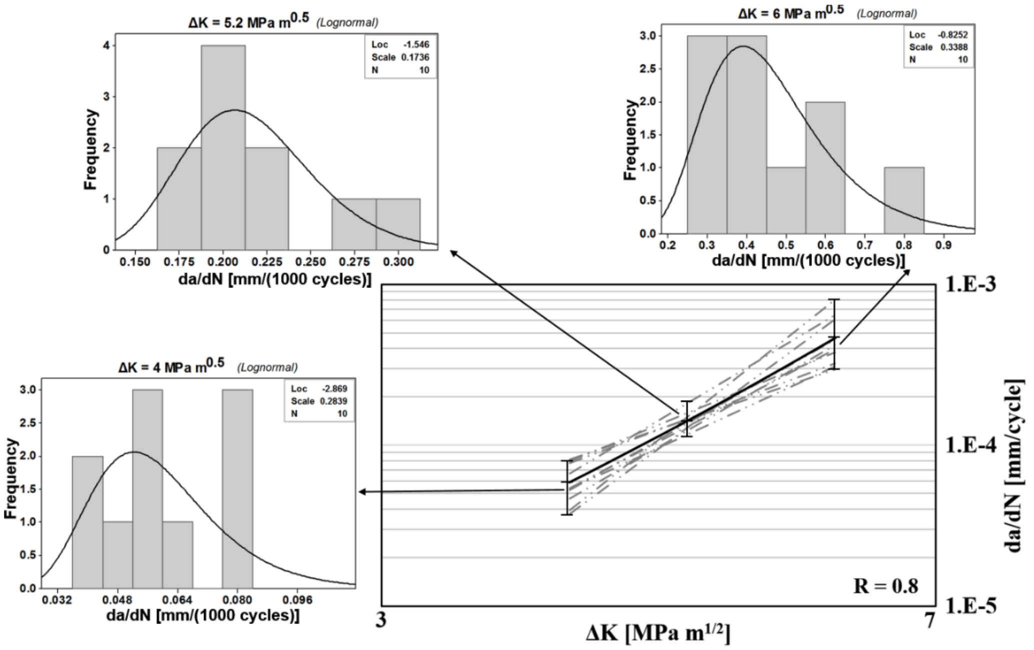

Figure 3.19. da/dN variations under constant amplitude loading, R = 0.8

## 3.5. Fatigue Crack Growth Tests Under Variable Amplitude Loading

Single overload, block loading and random loading tests are discussed in this section. The literature has not provided any standard for the variable amplitude loading tests. CT specimen with the given dimensions in Figure 3.3. is used in the variable amplitude loading tests for two-dimensional crack growth. Performed tests in this category are provided in Table 3.8.

Table 3.8. Test matrix for FCG under variable amplitude

| Test | Performed | Specimen Type |
|---|---|---|
| Single Overload | 9 | CT |
| Single Underload | 5 | CT |
| Block Overload | 14 | CT |
| Block Underload | 3 | CT |
| Random Loading (Artificial spectrum) | 11 | CT |
| Random Loading (Partial FALSTAFF) | 13 | CT |

### 3.5.1. Fatigue crack growth under single overload

Fatigue crack growth was initiated under 7 kN fatigue loading and 0.1 stress ratio by using CT specimen having a precrack. While running the test under constant amplitude, a single overload was applied at the 7000th cycle. The single overload was 9 kN in the early tests, but since the expected retardation effect could not be observed, the magnitude of the single overload was increased for the following tests. During the test, the crack was monitored with two microscope cameras from the back and front surfaces of the specimen. Crack growth curves were plotted by pixel size measurement of pictures. Properties of single overload and the other information about tests are given in Table 3.9.

Table 3.9. Single overload tests

| *Single overload* | Precrack | | | Fatigue crack growth | | | |
|---|---|---|---|---|---|---|---|
| Specimen Name | Stress Ratio for precrack R | Max. Load for Precrack (kN) | $a_{(avg)}$ (mm) | Stress Ratio for FCG R | Max. Load for FCG (kN) | $F_{OL}/F_{da/dN}$ | Cycle |
| 20181031_01 | 0.1 | 6.4 | 24.930 | 0.1 | 7.0 | 2.00 | 28294 |
| 20181101_01 | 0.1 | 6.4 | 25.015 | 0.1 | 7.0 | 1.71 | 15649 |
| 20181005_01 | 0.1 | 6.4 | 24.985 | 0.1 | 7.0 | 1.71 | 13898 |
| 20181007_01 | 0.1 | 6.4 | 24.800 | 0.1 | 7.0 | 1.57 | 13239 |
| 20181012_01 | 0.1 | 6.4 | 24.787 | 0.1 | 7.0 | 1.29 | 11529 |
| 20181013_01 | 0.1 | 6.4 | 24.860 | 0.1 | 7.0 | 1.29 | 12654 |
| 20181013_02 | 0.1 | 6.4 | 24.805 | 0.1 | 7.0 | 1.86 | 18401 |
| 20181014_01 | 0.1 | 6.4 | 24.461 | 0.1 | 7.0 | 1.86 | 17902 |
| 20181014_02 | 0.1 | 6.4 | 24.628 | 0.1 | 7.0 | 1.57 | 16488 |

The effect of using different single overload magnitudes on crack growth life was investigated experimentally. The retardation effect increased in accordance with the application of greater magnitudes of single overload. In addition, it has been observed that the low ratio of single overload (1.29) did not affect crack propagation life significantly.

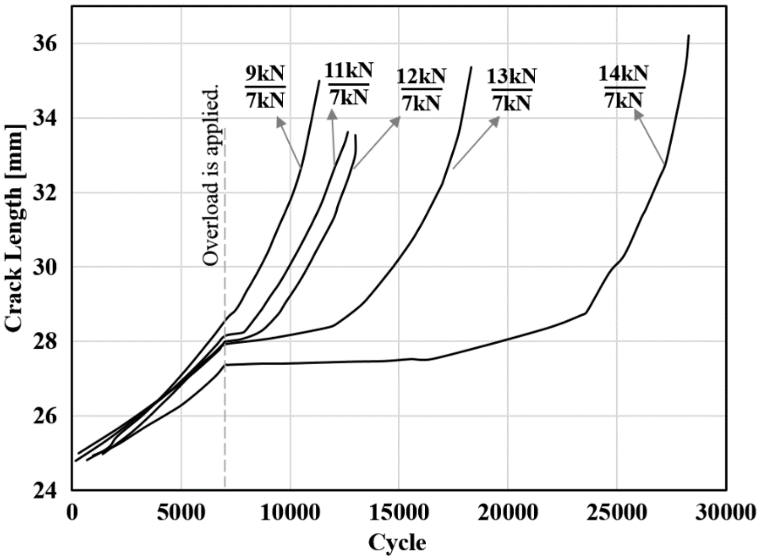

Figure 3.20. Effect of single overload ratio on crack growth life

### 3.5.2. Fatigue crack growth under single underload

The performed experiments indicate that the single underload does not affect the crack propagation life, similar to the literature. Note that, the term underload here means a decrease in load, but the specimen is always in tension and no compression effect is applied to crack surfaces. The compression effect on the crack tip is out of the scope of this dissertation.

Any changes in crack growth behavior are not expected in underload tests since the plastic region generated by underload is smaller than its previous size. Five tests were performed to observe the underload effect on crack growth behavior.

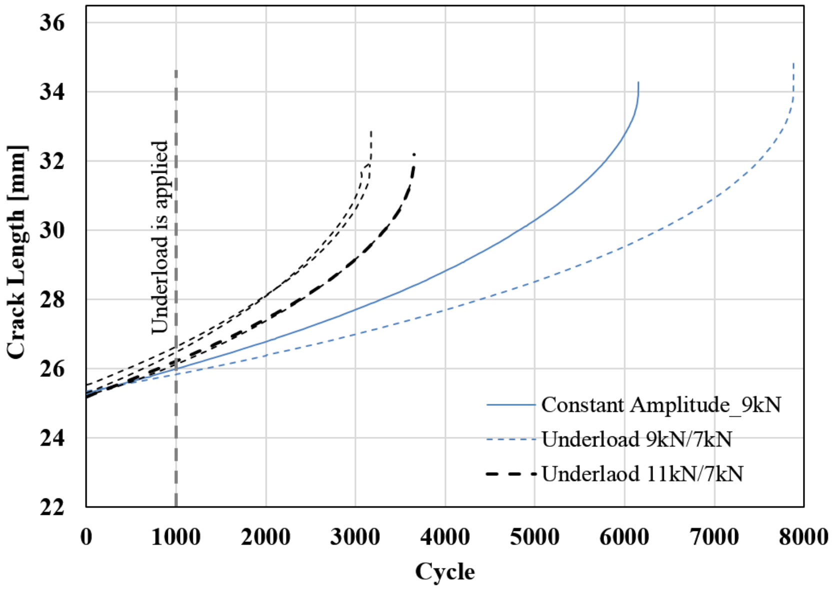

Figure 3.21. Effect of underload on crack growth behavior

In Figure 3.21., the blue colored continuous curve is the result of an experiment at 9 kN constant amplitude fatigue load. Underload tests are indicated with dashed lines. During the 9kN/7kN underload test, 7 kN underload was applied at the 1000th cycle and 9 kN is applied for other cycles. The curves obtained from these two tests are colored blue in Figure 3.21. The difference between blue curves can be interpreted as underload affecting life, but repeated tests were conducted to clarify whether that was caused by material properties, test conditions, or any other effect. The difference between the underload and the FCG load was increased as 11kN/7kN, and the same procedure was applied again. Four tests were performed with this procedure, and it is concluded that the difference in blue curves in Figure 3.21. was not caused by the underload effect. It is clearly seen that there are no changes in the slope of the crack propagation curves immediately after the application of underload. This may show that the single underload has no retarding or accelerating effect on crack propagation. This finding also supports the approach of using positive ΔK values in the crack propagation models under random loading, which will be explained in the next sections.

### 3.5.3. Fatigue crack growth under block overload

Block overload tests were also performed using the CT specimens. Detailed information is given in Table 3.10. for block overload tests with different fatigue load and cycle periods. The first four experiments shown in Table 3.10. can be considered as preliminary tests to determine the cycle periods and magnitude of overload. Then, the magnitude of the fatigue load was determined, and the effect of the block overload period on crack growth life was investigated. 13 kN overload block was applied with "n" cycles between two 7 kN constant amplitude fatigue loading with 1000 cycles, repeatedly. The effect of overload block size on the crack growth rate can be seen in Figure 3.22.

Table 3.10. Block overload tests

| *Block overload* | Precrack | | | Fatigue crack growth | | | | |
|---|---|---|---|---|---|---|---|---|
| Specimen Name | Stress Ratio for precrack R | Max. Load for precrack (kN) | $a_{(avg)}$ (mm) | Stress Ratio for FCG R | Max. Load for FCG (kN) | $\frac{F_{OL}}{F_{da/dN}}$ | Cycle | Block loading behavior |
| 20181206_01 | 0.1 | 6.4 | 24.774 | 0.1 | 7.0 | 1.57 | 28294 | 2000x7kN + 2000x11kN + |
| 20181212_01 | 0.1 | 6.4 | 24.523 | 0.1 | 7.0 | 1.43 | 15649 | 1000x7kN + 1000x10kN + |
| 20181219_02 | 0.1 | 6.4 | 24.880 | 0.1 | 7.0 | 2.00 | 13898 | 100x7kN + 100x14kN + |
| 20181219_03 | 0.1 | 6.4 | 24.765 | 0.1 | 7.0 | 2.00 | 13239 | 200x7kN + 50x14kN +.. |
| 20181225_01 | 0.1 | 6.4 | 24.976 | 0.1 | 7.0 | 1.86 | 11529 | 1000x7kN + 50x13kN +.. |
| 20181225_02 | 0.1 | 6.4 | 25.065 | 0.1 | 7.0 | 1.86 | 12654 | 1000x7kN + 100x13kN+ |
| 20181226_01 | 0.1 | 6.4 | 24.945 | 0.1 | 7.0 | 1.86 | 18401 | 1000x7kN + 50x13kN+ |
| 20181227_01 | 0.1 | 6.4 | 24.829 | 0.1 | 7.0 | 1.86 | 17902 | 1000x7kN + 200x13kN+ |

Table 3.10. Block overload tests (Continued)

| | | | | | | | | |
|---|---|---|---|---|---|---|---|---|
| 20181227_02 | 0.1 | 6.4 | 24.612 | 0.1 | 7.0 | 1.86 | 16488 | 1000x7kN + 500x13kN+ |
| 20181228_01 | 0.1 | 6.4 | 25.320 | 0.1 | 7.0 | 1.86 | 18401 | 1000x7kN + 20x13kN+ |
| 20190103_01 | 0.1 | 6.4 | 24.925 | 0.1 | 7.0 | 1.86 | 17902 | 1000x7kN + 10x13kN+ |

As seen in Figure 3.22., the size of the block overload cycle has an important role in crack growth life. If the block overload is applied for a long time (i.e., n = 500 and 200) new plastic zone is created consequently, and it accelerates the crack growth. In case of a short cycle of block overload, crack propagates slower compared to the case of single overload. The occurring plastic zone size by block overload dominates the crack growth behavior. As a result, crack propagates very slowly under fatigue loading except at the overload block. Thus, a significant increase in crack propagation life is observed. This effect on crack growth life is inversely proportional to the size of the overload cycle. It can be deduced that; although the number of cycles is low, overloads are applied more frequently and each time newly expanded plastic zones are created through which the crack tip slowly passes.

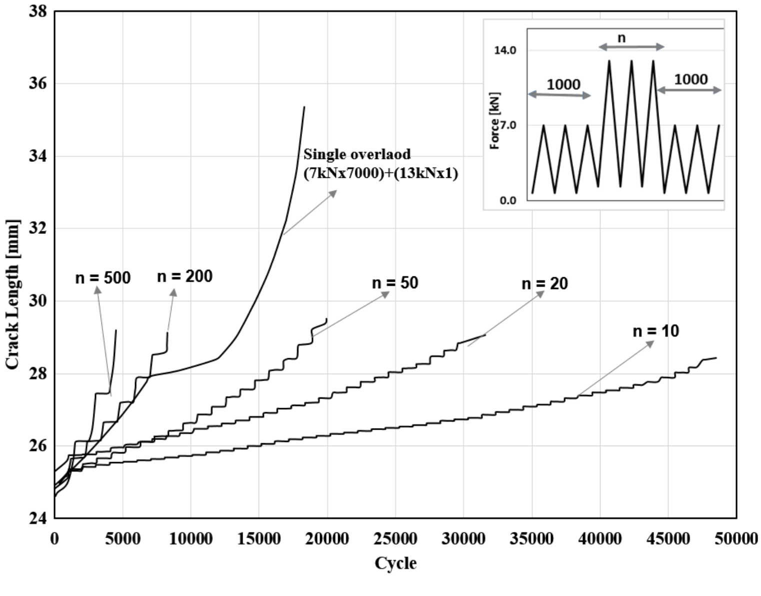

Figure 3.22. Effect of block overload size on crack growth life

### 3.5.4. Fatigue crack growth under block underload

There was no significant change in crack growth life by applying a single underload. It was also seen that the application of underload as blocks did not have an additional significant effect. In other words, the crack propagation behavior in this case is similar to block overload case as explained in Section 3.5.3. The only difference here is the initial order of high and low block loads shifts. Therefore, no additional tests were needed. The underload applied tests can be seen in Figure 3.23.

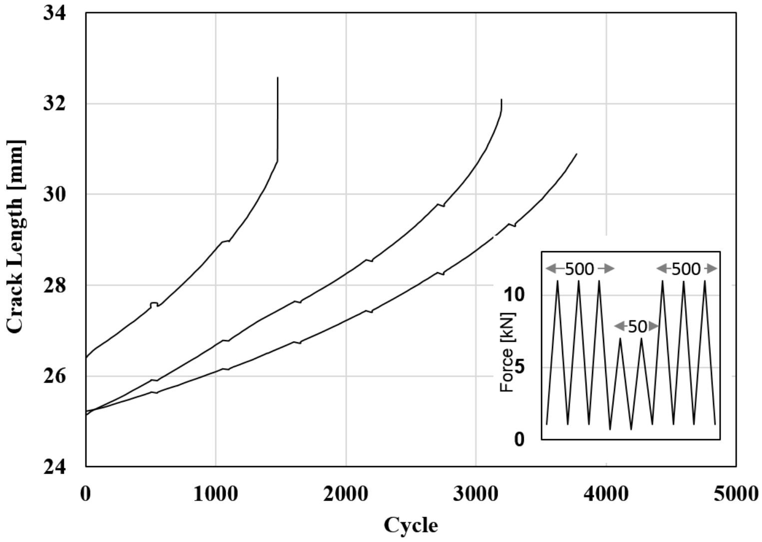

Figure 3.23. Effect of block overload size on crack growth life

### 3.5.5. Fatigue crack growth under random loading

Fatigue crack propagation tests under random loading were performed with CT specimens. Two different load spectrums were used, and each one was repeated continuously until the specimen was fractured. One of these loading spectrums was easier for the investigation of the interaction between load profiles, which will be named as Spectrum-1 (SP-1). The other spectrum is the partial FALSTAFF which was provided by TUSAS (TAI). The FALSTAFF profile is also available in the literature. The partial FALSTAFF spectrum will be named as Spectrum-2 (SP2). The number of the tests in this category of the FCG tests is given in Table 3.8.

The SP1 spectrum was a simple spectrum and self-created to investigate the difficulties of crack propagation under random loading. Firstly, it is aimed to determine the optimum load of SP1 for the tests which will be completed within 3-4 hours at low testing frequency (2-3 Hz). Tests were performed to determine the final load values of the profiles in Spectrum-1, and the modified values of the loading profile are shown in Figure 3.24. The spectrums are given in Figure 3.24. in chronological order, and Figure 3.24-c. is the final version of Spectrum-1.

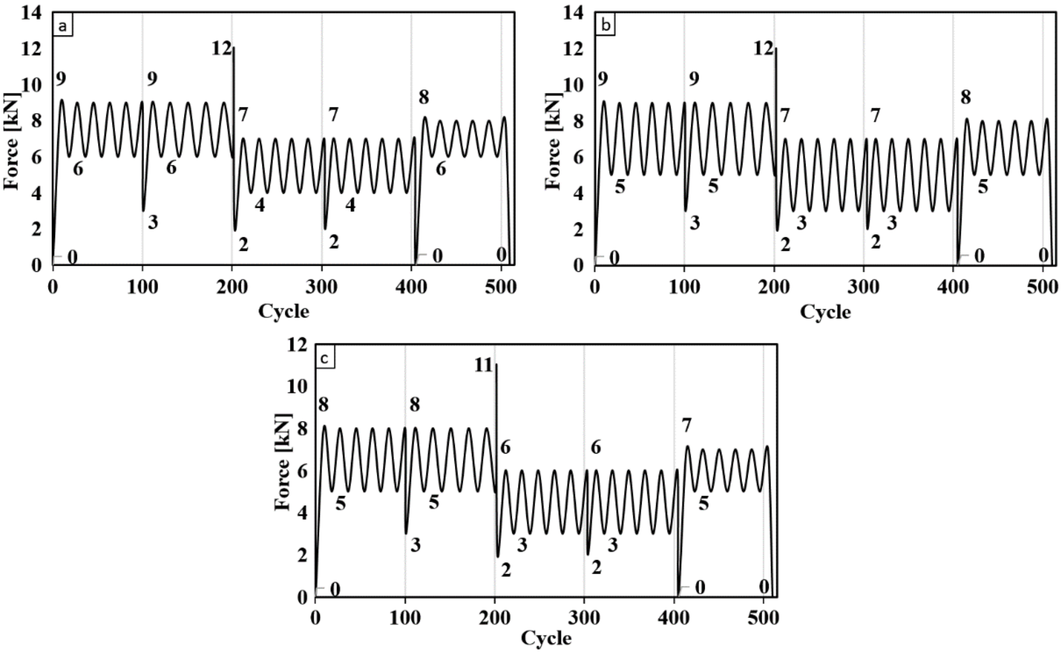

Figure 3.24. Random loading spectrum-1 (SP1)

Table 3.11. Detailed information for Spectrum-1 FCG tests

| *Spectrum -1* | | Precrack | | | Fatigue crack growth | |
|---|---|---|---|---|---|---|
| Specimen Name | Specimen Type | Stress Ratio for precrack R | Max. Load for Precrack (kN) | $a_{(avg)}$ (mm) | Spectrum | Cycle |
| 20190502_01 | CT | 0.1 | 6.4 | 24.780 | Spectrum 1/a+b | 38616 |
| 20190503_01 | CT | 0.1 | 6.4 | 24.260 | Spectrum 1/b | 1195 |
| 20190503_02 | CT | 0.1 | 6.4 | 24.603 | Spectrum 1/b | 6223 |
| 20190506_01 | CT | 0.1 | 6.4 | 24.590 | Spectrum 1/c | 31221 |
| 20190506_02 | CT | 0.1 | 6.4 | 24.459 | Spectrum 1/c | 42706 |
| 20190507_01 | CT | 0.1 | 6.4 | 24.461 | Spectrum 1/c | 28459 |
| 20200330_01 | CT | 0.1 | 6.4 | 24.748 | Spectrum 1/c | 38601 |

Table 3.11. Detailed information for Spectrum-1 FCG tests (Continued)

| | | | | | | |
|---|---|---|---|---|---|---|
| 20200611_01 | CT | 0.1 | 6.4 | 24.377 | Spectrum 1/c | 18381 |
| 20200611_02 | CT | 0.1 | 6.4 | 24.464 | Spectrum 1/c | 29468 |
| 20200612_01 | CT | 0.1 | 6.4 | 24.416 | Spectrum 1/c | 29485 |
| 20200612_02 | CT | 0.1 | 6.4 | 24.470 | Spectrum 1/c | 33654 |

Fatigue crack growth lives are given in Table 3.11. for different versions of Spectrum-1 shown in Figure 3.24.a-b-c. As seen in Table 3.11., the test performed with Spectrum-1a has a higher cycle than Spectrum-1b. Based on these results, it was concluded that the optimal test duration was obtained in Spectrum1-c, and it was applied in the following tests. Crack growth curves obtained with Spectrum-1c are given in Figure 3.25. These curves were drawn by using the microscope camera views.

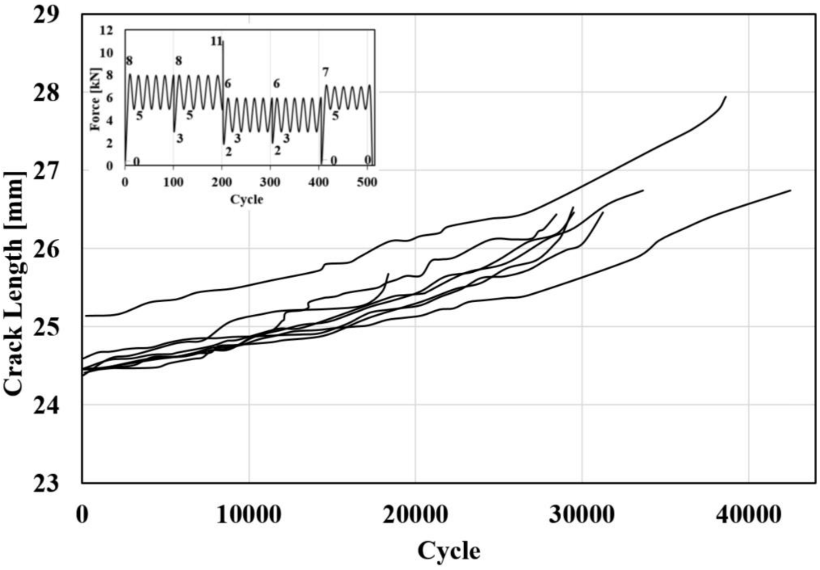

Figure 3.25. Crack growth curves with Spectrum1-c

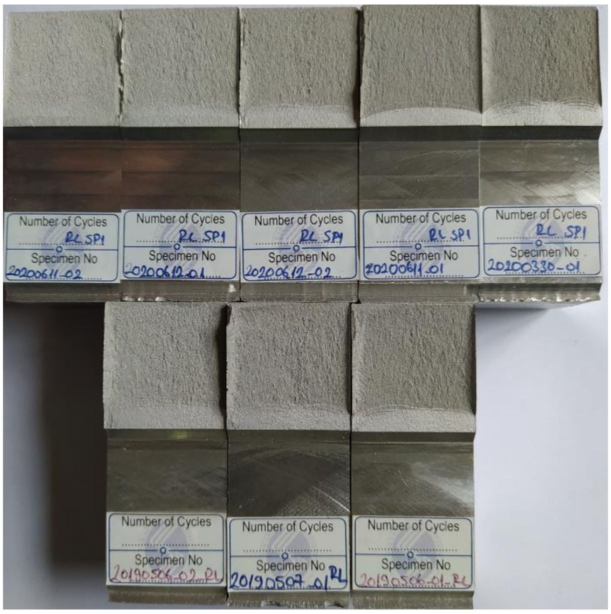

Figure 3.26. Fracture surfaces of the specimen tested under Spectrum-1-c

The second spectrum for random loading crack propagation tests is FALSTAFF (Fighter Aircraft Loading STAndard For Fatigue Evaluation), named Spectrum-2, and it was recorded during a flight of an airplane [45]. The original version of FALSTAFF is 35000 cycles, and some of them have load values. In this study, the most repeated/representative part of the spectrum was selected, and the magnitude of load profiles was scaled for the CT specimen. Compressive loads were made equal to zero to prevent compressive residual stress at the crack tip which causes crack surfaces to contact each other. Adopting from the previous tests, the maximum load in Spectrum-2 was determined as 11 kN. Whole FALSTAFF spectrum and the selected part used in Spectrum-2 are given in Figure 3.27.

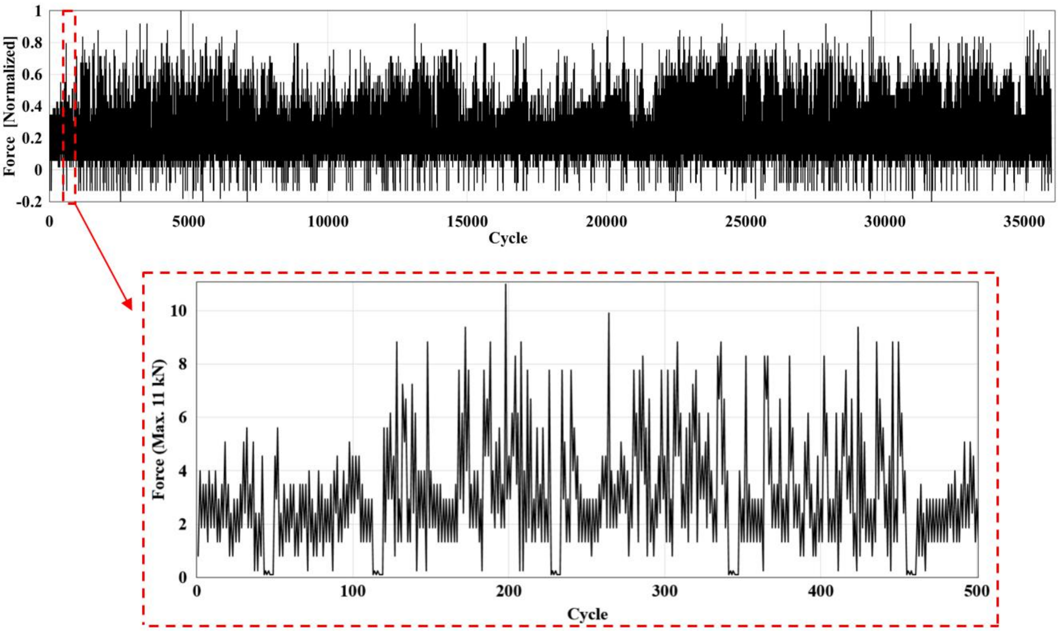

Figure 3.27. FALSTAFF and Partial FALSTAFF (Spectrum-2, SP2) loading profiles for CT Specimen

Table 3.12. Detailed information of Spectrum-2 FCG tests

| *Spectrum -2* | | Precrack | | | Fatigue crack growth | |
|---|---|---|---|---|---|---|
| Specimen Name | Specimen Type | Stress Ratio for precrack R | Max. Load for Precrack (kN) | $a_{(avg)}$ (mm) | Spectrum | Cycle |
| 20190827_01 | CT | 0.1 | 6.4 | 24.863 | Spectum-2 | 17002 |
| 20190828_01 | CT | 0.1 | 6.4 | 24.610 | Spectum-2 | 15964 |
| 20191008_01 | CT | 0.1 | 6.4 | 24.794 | Spectum-2 | 18880 |
| 20191008_02 | CT | 0.1 | 6.4 | 24.985 | Spectum-2 | 7861 |
| 20191009_01 | CT | 0.1 | 6.4 | 24.720 | Spectum-2 | 8889 |
| 20191009_02 | CT | 0.1 | 6.4 | 24.460 | Spectum-2 | 24274 |
| 20191010_01 | CT | 0.1 | 6.4 | 24.430 | Spectum-2 | 19118 |
| 20190826_01 | CT | 0.1 | 6.4 | 24.404 | Spectum-2 | 27885 |
| 20200616_01 | CT | 0.1 | 6.4 | 24.548 | Spectum-2 | 16344 |
| 20200617_01 | CT | 0.1 | 6.4 | 24.668 | Spectum-2 | 21892 |
| 20200617_02 | CT | 0.1 | 6.4 | 25.295 | Spectum-2 | 1594 |
| 20200618_01 | CT | 0.1 | 6.4 | 24.785 | Spectum-2 | 6843 |
| 20200618_02 | CT | 0.1 | 6.4 | 24.473 | Spectum-2 | 23899 |

.

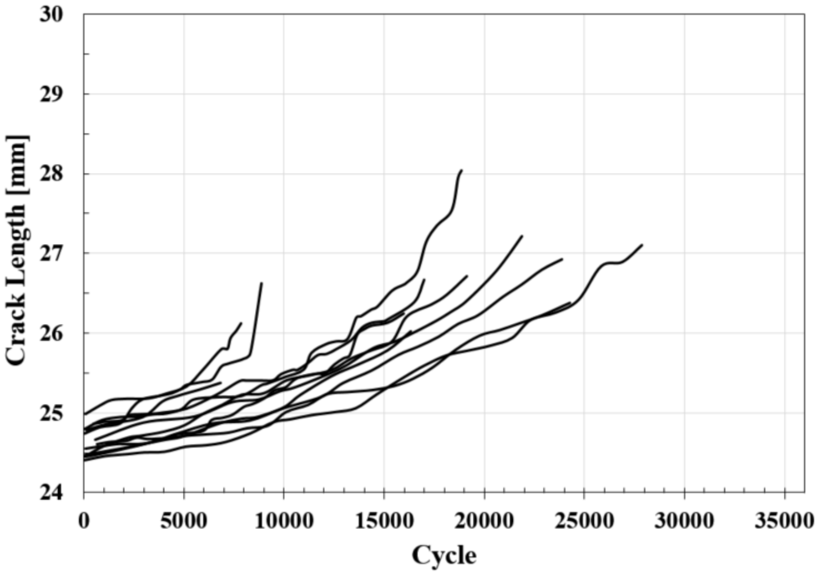

Figure 3.28. Crack growth curves under Spectrum-2

The detailed information is given in Table 3.12. for the tests performed under Spectrum-2. All tests were performed under the same condition, however different crack growth life values were observed in the results, even for the tests with very close initial crack lengths. Fatigue crack growth curves can be seen in Figure 3.28., and fracture surfaces of the used specimen are shown in Figure 3.29

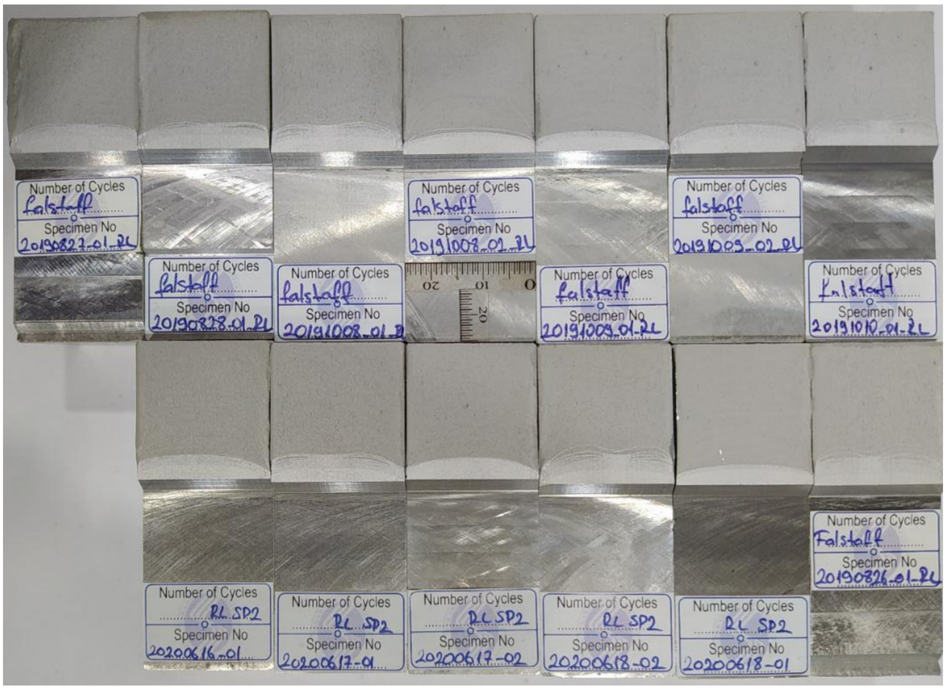

Figure 3.29. Fracture surfaces of the specimen tested under Spectrum-2

## 3.6. Fatigue Crack Growth Models Under Variable Amplitude Loading

In this section, first, constant amplitude loading models are explained, as the fatigue crack growth models for variable amplitude loading are generally based on constant amplitude loading models. Then, the models for variable amplitude loading are discussed that consider the crack growth retardation or acceleration.

### 3.6.1. Fatigue crack growth modeling under constant amplitude loading

#### 3.6.1.1. Paris-Erdogan fatigue crack growth model [7]

This model is commonly used in the literature and it is valid for the second region of the fatigue crack growth curve that exhibits the linear relation between log(da/dN) and log(ΔK). The crack growth rate can be calculated by using Equation (3.3). The stress ratio is not considered in this model as can be noticed from Equation (3.3).

$$\frac{da}{dN} = C(\Delta K)^n \tag{3.3}$$

Calculation of Paris-Erdogan constants ($C$-$n$) was explained in Section 3.4. and the obtained values from the tests were tabulated.

#### 3.6.1.2. Walker's fatigue crack growth model [9]

This model is valid in the second region of the crack growth curve like Paris-Erdogan Model. In addition to Paris-Erdogan model it takes into account the effect of stress ratio as presented in Equation (3.4).

$$\frac{da}{dN} = C\left[\frac{\Delta K}{(1-R)^{1-\gamma_w}}\right]^n \tag{3.4}$$

This model needs an empirical parameter $\gamma_w$ introduced in Equation (3.5). $\Delta K_{Walker}$ is proposed to calculate the empirical parameter $\gamma_w$.

$$\Delta K_{walker} = K_{max}(1-R)^{\gamma_w} \tag{3.5}$$

$$K_{max} = \frac{\Delta K}{(1-R)} \tag{3.6}$$

da/dN vs. $\Delta K_{walker}$ curves from the tests are plotted in the logarithmic scale under different stress ratios. Curves obtained from different stress ratios are gathered as a straight line by changing the $\gamma_w$ exponent. As seen in the literature, finding the appropriate value of this empirical exponent can be difficult, and it might be impossible in some cases.

Crack growth rates of the tests given in Table 3.3. -Table 3.6. were also calculated by using the Walker crack growth model. In this case, $\Delta K_{walker}$ was calculated as explained above, and $\gamma_w$ was determined by using da/dN vs. $\Delta K_{walker}$ curves. Crack growth rates were calculated by using Equation (3.4) under different stress ratios for the same ΔK value by changing the $\gamma_w$. The closest alignment of 4 different $(da/dN)_{walker}$ points were found with $\gamma_w = 0.631$ by using the Microsoft Excel Solver [46]. It is seen in Figure 3.30. that points marked at different stress ratios with the value of $\gamma_w = 0.631$ show a linear trend.

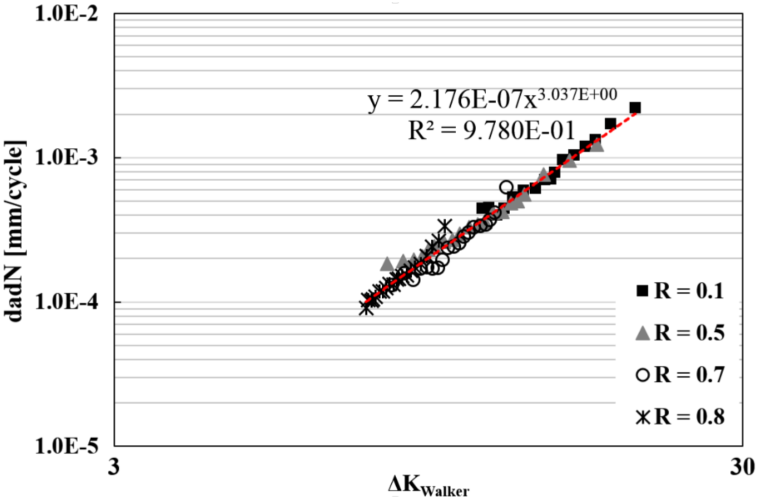

Figure 3.30. Determination of Walker exponent, $\gamma_w$

The function of the trendline gives the *C*-*n* constant for Walker fatigue crack growth model. If the stress ratio equals to zero, the *C*-*n* constants in Walker Equation (3.4) should be equal to the Paris-Erdogan constants in Equation (3.3). As the R value is close to zero (R = 0.1), the obtained coefficients of both models almost match in this study.

### 3.6.1.3. Forman fatigue crack growth model [8]:

This model calculates the crack growth rate in the second and third regions of crack growth curve by using the stress ratio and fracture toughness. The crack growth rate is calculated by using Equation (3.7).

$$\frac{da}{dN} = \frac{C_F(\Delta K)^m}{(1-R)^n K_{IC} - \Delta K} = \frac{C_F(\Delta K)^m}{(1-R)K_{IC} - K_{max}} \tag{3.7}$$

$C_F$ and $m$ are the crack growth constants in Forman model. The $Q$ in Equation (3.8) decides if the Forman model can be used for da/dN calculations.

$$Q = \frac{da}{dN}[(1-R)K_{IC} - \Delta K] = C_F(\Delta K)^m \tag{3.8}$$

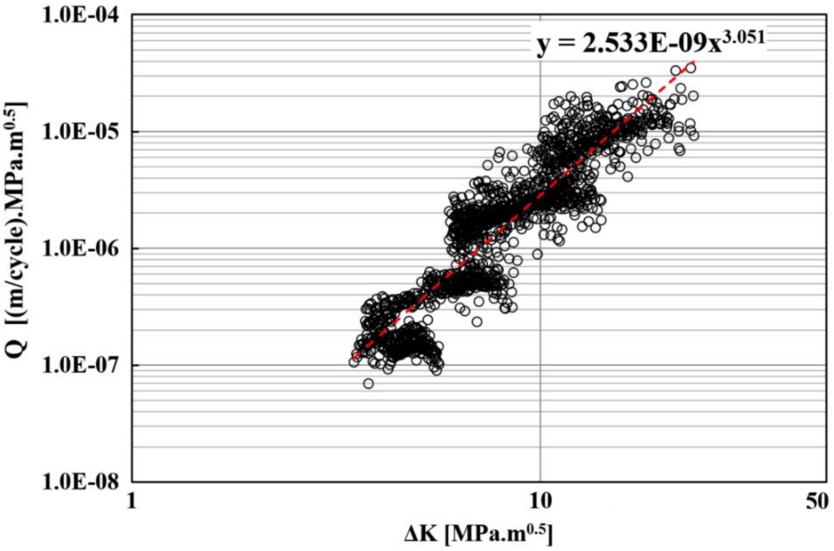

Figure 3.31. Determination of Forman constants depending on Q vs. ΔK

If the calculated $Q$ values points exhibit a linear trend in $Q$ vs ΔK chart in logarithmic axes, then the Forman model can be used. The test results were plotted on a logarithmic scale, and constants were obtained by fitting a linear trendline. The usability of Forman model with the tests were investigated in Figure 3.31. and Forman constants were determined as $C_F$ = 2.533E-9 and m = 3.051. Crack growth rates of different stress ratios were calculated by using these constants and compared with the experimental results for validation. Comparisons can be seen in Figure 3.32.

In addition, a simplified version of the Forman model is also given in Equation (3.9).

$$\frac{da}{dN} = \frac{C(\Delta K)^n}{1 - \frac{\Delta K}{(1-R)K_{IC}}} \tag{3.9}$$

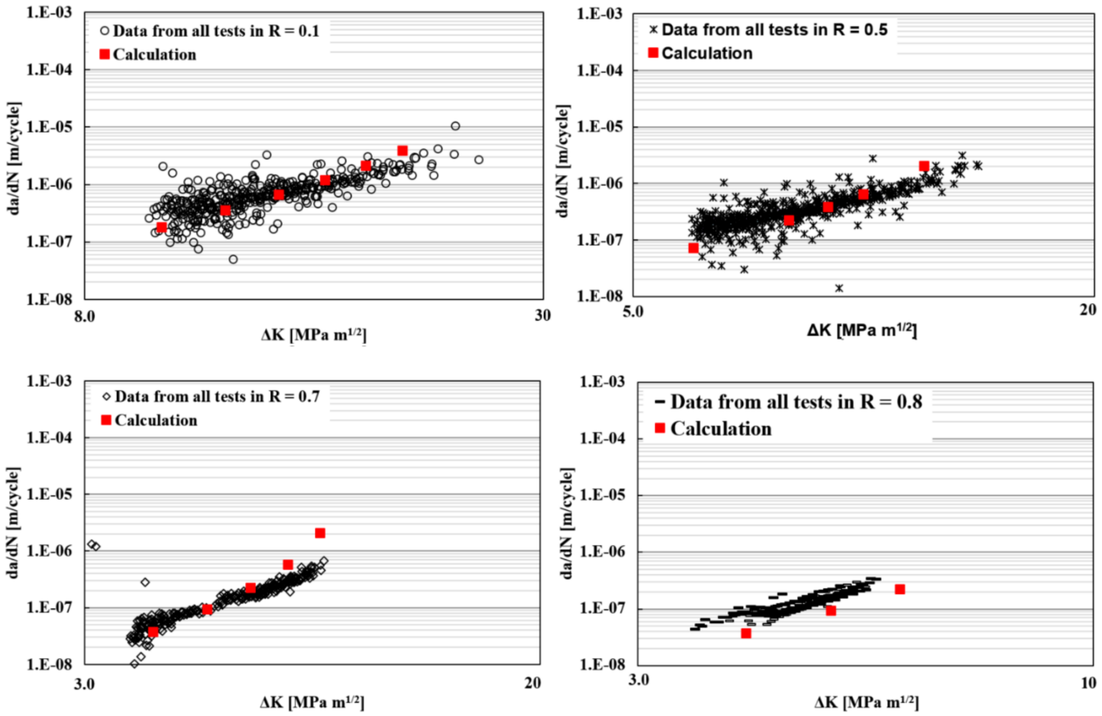

Figure 3.32. Comparison of calculated crack growth rate with experiments under different stress ratios

### 3.6.2. Fatigue crack growth modeling under variable amplitude loading

#### 3.6.2.1. Wheeler Model [12]

Wheeler model can be used to determine the crack growth behavior for single or periodic overload. The model determines the retardation of the crack growth by comparing the largest size of the yield zones from previous cycles with the ongoing plastic zone sizes at the crack tip. Definition of plastic zone sizes at crack tip is seen in Figure 3.33., where the current plastic zone is shown in black for any cycle and its size is compared with the plastic zone size which has been created by the overload at a previous cycle. If the current plastic zone size at the crack tip is smaller than the plastic zone formed under the previously applied overload, the Paris-Erdogan Equation is multiplied by a retardation parameter, otherwise Paris-Erdogan Equation is used as it is.

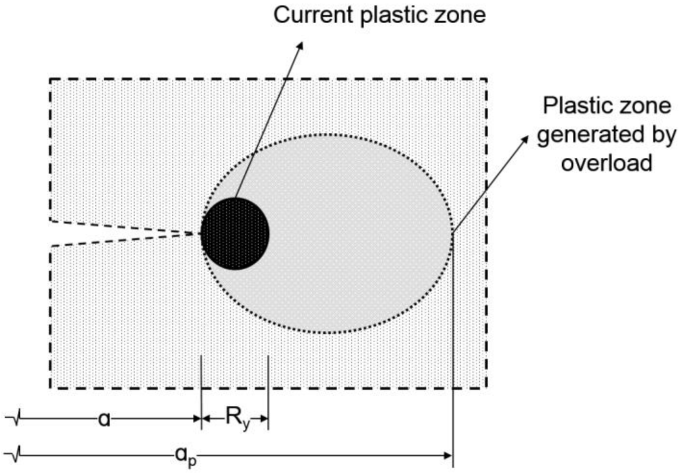

Figure 3.33. Definition of plastic zones at crack tip [12]

$$\frac{da}{dN} = \emptyset_R (C\,\Delta K)^n \tag{3.10}$$

$$\emptyset_R = \begin{cases} \left(\dfrac{R_y}{a_p - a}\right)^y & ; \qquad (a + R_y) < a_p \\ 1 & \qquad\;\; (a + R_y) \geq a_p \end{cases} \tag{3.11}$$

$$R_y = \frac{1}{\pi\, 4\sqrt{2}} \left(\frac{K_I}{\sigma_y}\right)^2 \qquad for\ plain\ strain \tag{3.12}$$

Wheeler exponent in Equation (3.11) depends on the material, overload rate and crack length at the cycle of overload [17]. Determination of the Wheeler exponent "y" is explained below:

- After the overload, the total number of cycles ($N_{test}$) required for the crack growth rate to reach its previous rate before the overload is determined.
- Plastic zone size is calculated for each cycle by Equation (3.12) after the overload.
- Crack growth life is calculated by Equations (3.10) and (3.11) with the estimated values of Wheeler exponent "y" until the retardation parameter $\emptyset_R$ equals to 1.
- The Wheeler exponent "y" is determined by satisfying the condition of that the calculated crack growth life equal to the experimental crack growth life.

### 3.6.2.2. **Sheu Model** [47]

This model is based on the Wheeler model. In the Wheeler model, if the crack tip plastic zone reaches the limits of the plastic region created by the overload, the crack propagation rate turns to its pre-overload value again under the fatigue load. Song P. et al [47] stated that in Sheu model, the crack growth retardation effect lasts longer compared to the Wheeler model. They proposed a modification on the plastic zone to calculate the retardation parameter as "effective plastic zone created by overload". The comparison of the plastic zones at crack tip proposed by Wheeler and this model is given in Figure 3.34.

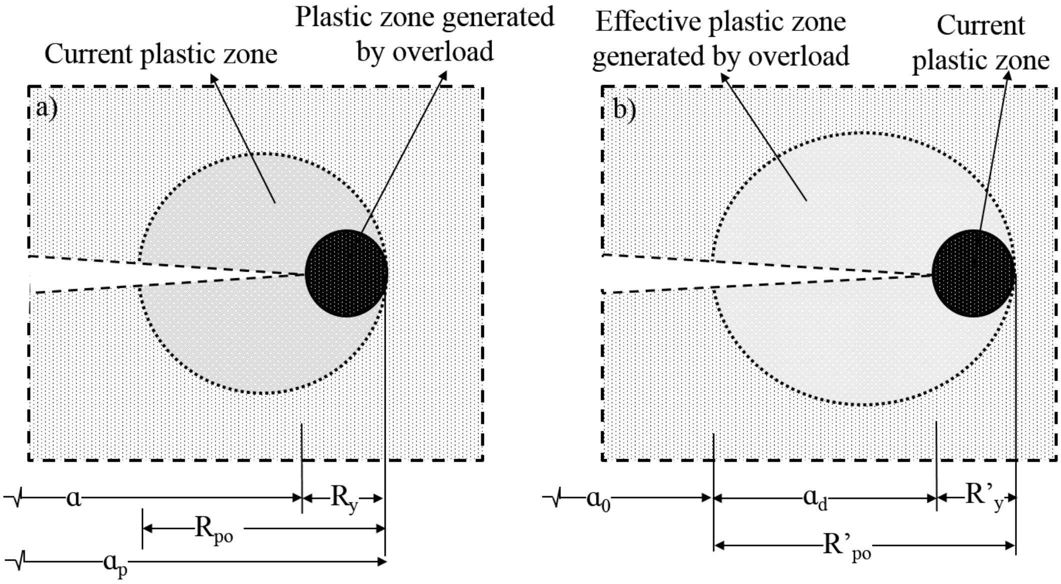

Figure 3.34. Definition of plastic zone at the end of retardation a) Wheeler, b) Sheu [47]

$$\emptyset'_R = \begin{cases} \left(\dfrac{R_y}{a_0 + R'_{po} - a_i}\right)^y & ; \qquad (a_0 + R'_{po}) < a_p \\ 1 & \qquad\;\; (a_0 + R'_{po}) \geq a_p \end{cases} \tag{3.13}$$

In Equation (3.13); $a_0$ represents the crack length at the cycle of overload, $R_{po}$ is the plastic zone radius generated by overload in Wheeler model, $R'_{po}$ is the effective plastic zone radius proposed by Sheu P. et al. and $a_d$ is the crack growth delay under the overload effect.

### **3.6.2.3. Xiaoping Model** [21]

This model proposes some modifications to the Wheeler model by using the equivalent SIF approach to model the crack growth retardation behavior. $\Delta K_{eq0}$ in Equation (3.15) is the SIF for zero stress ratio. Crack growth curves obtained under different stress ratios are converted to R = 0 by using Equations (3.15) and (3.16).

$$\frac{da}{dN} = C\left[(\Delta K_{eq0})^n - (\Delta K_{th0})^n\right] \tag{3.14}$$

$$\Delta K_{eq0} = M_R M_P \Delta K \tag{3.15}$$

$$M_R = \begin{cases} (1-R)^{-\beta_1} & -5 \le R < 0 \\ (1-R)^{-\beta} & 0 \le R < 0.5 \\ (1.05 - 1.4R + 0.6R^2)^{-\beta} & 0.5 \le R < 1 \end{cases} \tag{3.16}$$

$M_R$ is a parameter used to shift all crack growth curves obtained under different stress ratios to R = 0. $M_P$ identifies the interaction effect between load profiles. $\beta$ and $\beta_1$ terms in Equation (3.16) can be found as explained above, in the Walker Model. First, da/dN vs. $M_R\Delta K$ curves are plotted for all tests under different stress ratios with the estimated value of $\beta$. Then, the difference between the curves is approximated to zero by changing $\beta$ parametrically with the help of Microsoft Excel Solver [46].

The value of $\beta$ was obtained as 0.4 by using the tests given in Table 3.3. - Table 3.6., and the combined curves are given in Figure 3.35. $\beta_1$ term was not calculated in this study since the negative stress ratio was not applied in tests.

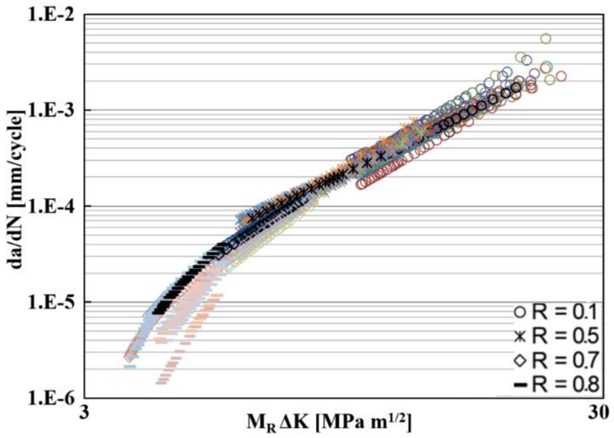

Figure 3.35. Determination of $\beta$ in Xiaoping model

Figure 3.36. is given to better understand the modification proposed by Xiaoping H. et al. to the Wheeler model.

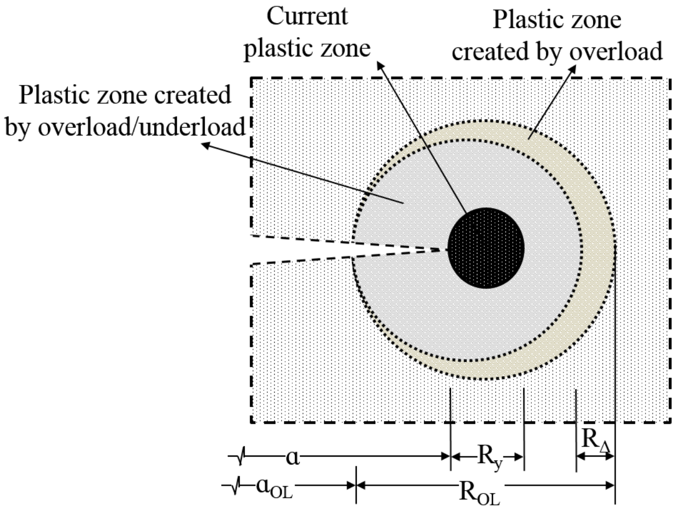

Figure 3.36. Plastic zone size definition in Xiaoping Model [21]

Three different plastic zones are seen in Figure 3.36. One of them is the current plastic zone and the others are created by the overload. This model realizes the determination of the second overload effect where the plastic zone of the first overload is still active. This relation is given in Equation (3.17) - (3.19).

$$M_P = \begin{cases} \left(\dfrac{R_y}{a_{OL} + R_{OL} - a - R_\Delta}\right)^y & ; \qquad a + R_y < a_{OL} + R_{OL} - R_\Delta \\ 1 & \qquad\;\; a + R_y \geq a_{OL} + R_{OL} - R_\Delta \end{cases} \tag{3.17}$$

$$R_\Delta = \alpha \left(\frac{\Delta K_U}{\sigma_Y}\right)^2 \tag{3.18}$$

$$\Delta K_U = F\sqrt{\pi a}\,(\sigma_{min}^{i-1} - \sigma_{min}^{i}) \tag{3.19}$$

#### 3.6.2.4. Yuen and Taheri Model [48]

This model can be used in the crack propagation experiments where single or multiple overloads are applied together. As a modification to the Wheeler model, the acceleration of the crack growth rate right after the overload, the retardation, the interaction between the loading profiles and the yielding in the critical cross-section were taken into account. Thus, four parameters are used in this model. One of them is the same with retardation parameter $Ø_R$ in the Wheeler Model. $Ø_D$ is the delay parameter for crack growth and $Ø_I$ is the interaction parameter related to the loading profiles. The crack growth calculation of the proposed model is provided in Equation (3.20).

$$\frac{da}{dN} = \emptyset_R\, \emptyset_D\, \emptyset_I\, [C(\Delta K_{ac})^n] \tag{3.20}$$

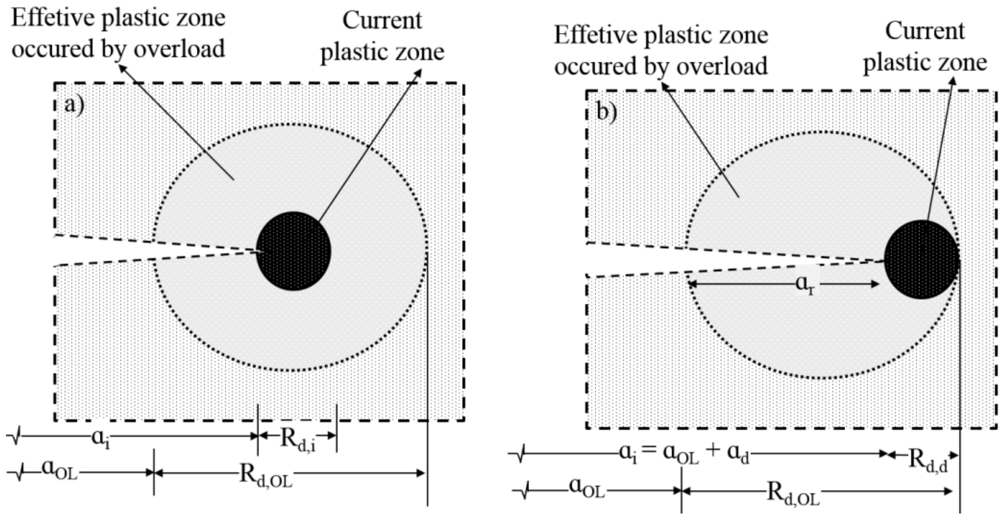

Figure 3.37. Definition of plastic zones in Yuen and Taheri Model [48]

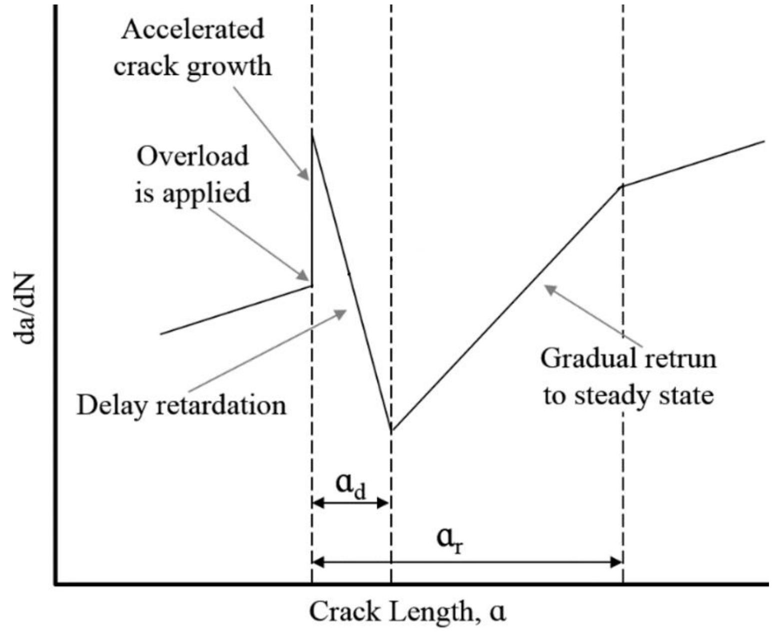

Figure 3.38. Crack growth behavior after an overload [48]

In Figure 3.37a. plastic zones are presented for the cycle after overload and in Figure 3.37b. crack length is demonstrated at the position just before the end of the retardation effect caused by overload. The schematic view is given in Figure 3.38. for the crack growth retardation behavior and the length of the crack in delay retardation is indicated as $a_d$.

$$\emptyset_D = \begin{cases} \left(\dfrac{a_{OL} + R_{d,OL} - a_i}{R_{D,i}}\right)^{y_{mod}} & ; \qquad \left(a_i + R_{d,i}\right) < \left(a_{OL} + R_{d,OL}\right) \\ 1 & \qquad \left(a_{OL} + R_{d,OL}\right) \leq \left(a_i + R_{d,i}\right) \end{cases} \tag{3.21}$$

$$a_d = r_{d,OL} - r_{d,d} = \beta\left[\left(\frac{K_{OL}}{\sigma_y}\right)^2 - \left(\frac{K_d}{\sigma_y}\right)^2\right] \tag{3.22}$$

$\emptyset_D$ is used for modeling the delay retardation given in Figure 3.38. $\beta$ is the effective plastic zone parameter in Equation (3.22).

$$\Delta K_{ac} = \begin{cases} \Delta K_i + (\Delta K_{OL} - \Delta K_i).\left(1 - \dfrac{R_{d,i}}{a_{OL} + R_{d,OL} - a_i}\right)^{y_{mod}} & ; \ (a_i + R_{d,i}) < (a_{OL} + R_{d,OL}) \\ \Delta K_i & (a_{OL} + R_{d,OL}) \leq (a_i + R_{d,i}) \end{cases} \tag{3.23}$$

$\Delta K_{ac}$ is a main parameter of Equation (3.20) and it is calculated by Equation (3.23) which is a piecewise function of plastic zone size. $K_{OL}$ is the SIF at the overload cycle and $K_i$ is the SIF at the current cycle.

In order to calculate the effects of consecutive overloads, the $\emptyset_i$ term is added to the Wheeler model. The relationship between the two overloads can be in three different types as presented in Equation (3.24). For this, a piecewise function representing three different situations is given in Equation (3.24).

$$\emptyset_i = \begin{cases} 1 - (1 - \emptyset_{min,i}).\left(1 - \dfrac{R_{p,i}}{a_{OL} + R_{p,OL} - a_i} \dfrac{a_{OL} + R_{p,OL} - a_i}{R_{d,i}}\right)^{y_{mod}} & a_i + R_{d,i} < a_{OL} + R_{d,OL} \\ 1 - (1 - \emptyset_{min,i}).\left(1 - \dfrac{R_{p,i}}{a_{OL} + R_{p,OL} - a_i} \dfrac{a_{OL} + R_{p,OL} - a_i}{R_{d,i}}\right)^{y_{mod}} & \begin{array}{l} a_{OL} + R_{d,OL} \leq a_i + R_{d,i} \\ a_i + R_{d,i} < a_{OL} + R_{p,OL} \end{array} \\ 1 & (a_{OL} + R_{p,OL}) \leq (a_i + R_{p,i}) \end{cases} \tag{3.24}$$

### 3.6.2.5. **Willenborg Model** [13]

In this model, the retardation of the crack growth rate is defined as a function of the SIF. Therefore, empirical parameters like Wheeler exponent are not required. In the Willenborg model, Forman fatigue crack growth model is used along with the effective SIF. By using the Forman model, the crack propagation rate becomes dependent on the stress ratio.

$$\frac{da}{dN} = \frac{C_F(\Delta K_{eff})^m}{(1 - R_{eff})K_C - \Delta K_{eff}} \tag{3.25}$$

$$R_{eff} = \frac{K_{\min eff}}{K_{\max eff}} \tag{3.26}$$

$$K_{\min eff} = K_{min} - K_r \qquad ; \qquad K_{\max eff} = K_{max} - K_r \tag{3.27}$$

$$K_r = (K_{max})_{OL}\left\{1 - \frac{\Delta a}{Z_{OL}}\right\}^{0.5} - K_{max} \tag{3.28}$$

$$Z_{OL} = \frac{1}{\beta\pi}\left[\frac{(K_{max})_{OL}}{\sigma_y}\right]^2 \tag{3.29}$$

$$\Delta K_{eff,i} = \begin{cases} \Delta K_i & ; \qquad K_{max,eff,i} \text{ and } K_{min,eff,i} > 0 \\ K_{max,eff,i} & \qquad K_{min,eff,i} \leq 0 \\ 0 & \qquad K_{max,eff,i} \leq 0 \end{cases} \tag{3.30}$$

The crack growth rate can be calculated by using Equation (3.25)-(3.30). $C_F$ and $m$ are crack growth constants in Forman Equation. $R_{eff}$ is effective stress ratio, $K_{max,eff}$ and $K_{min,eff}$ are effective stress intensity factors obtained from Equation (3.27). If the result of Equation (3.27) is negative, these parameters become zero. $K_r$ is the residual SIF and if the plastic zone size at the current cycle is smaller than the plastic zone size at the overload cycles, then $K_r$ is calculated. Otherwise, it is equal to zero. $(K_{max})_{OL}$ is the SIF at the overload cycle. $\Delta a$ is the crack growth distance under the retardation effect. In this model, if the overload ratio is greater than or equals to 2, the crack growth rate cannot be calculated because of the math error in Equation (3.27).

### **3.6.2.6. Generalized Willenborg Model** [18]

This model includes a modification of the Willenborg model. The equations in the Willenborg model are valid, except that the residual SIF, *Kr*, suggested in Equation (3.28) is multiplied with a *Ø* parameter. Adding the parameter *Ø* makes it possible to crack growth modelling in the case of the overload ratio is greater than or equals to 2. Parameter *Ø* is calculated by Equation (3.31).

$$\emptyset = \frac{1 - \frac{\Delta K_{th}}{\Delta K}}{(R_{So} - 1)} \tag{3.31}$$

$R_{SO}$ is the shut-off ratio and it is obtained as 3.0 for 7075-T651 aluminum alloy from the literature [49]. In the same reference, it is stated that the change of this value between 2.5 and 3.5 has an effect of only 3% on results.

The generalized Willenborg model also calculates the crack growth rate for the underload effect. This capability of the model has been added thanks to the updates by NASGRO [50]. After this update, the model is named as Modified Generalized Willenborg Model. Equation (3.32) was proposed to calculate the effects of underload [50]. The $\emptyset_0$ term is equal to the $\emptyset$ obtained for $R_{UL}= 0$. $K_{UL}$ is the SIF for the cycle where the underload is applied.

$$\emptyset = \begin{cases} \dfrac{2.523\emptyset_0}{[1 + 3.5(0.25 - R_{UL})^{0.6}]} & ; \qquad R_{UL} = {}^{K_{UL}}/_{K_{OL}} < 0.25 \\ 1 & \qquad\;\; R_{UL} = {}^{K_{UL}}/_{K_{OL}} > 0.25 \end{cases} \tag{3.32}$$

### 3.6.2.7. Root Mean Square Approach for Crack Growth Life Calculation [16]

This method is quite different from the methods that determine the crack propagation behavior according to the crack tip plastic zone size. It proposes a simple approach for random loading. Root mean square (RMS) is determined along the loading spectrum and crack growth life is calculated like constant amplitude loading. K* SIF is calculated by using Equation (3.33) as the driving force in crack growth, and $\Delta K^+$ symbolizes the positive changes in SIF. α is taken 0.5 for aluminum alloy [16].

$$K^* = [(\Delta K^+)^\alpha (K_{max})^{1-\alpha}] \tag{3.33}$$

$$\sigma_{min}^{rms} = \left[\frac{1}{N}\sum_{i=1}^{N_r}(\sigma_{min})^2\right]^{0.5} \quad , \quad \sigma_{max}^{rms} = \left[\frac{1}{N}\sum_{i=1}^{N_r}(\sigma_{max})^2\right]^{0.5} \tag{3.34}$$

$$\frac{da}{dN} = C_1(\Delta K^*)^{C_2}\frac{[1 - (\Delta K_{th}^*/\Delta K^*)^2]}{[1 - (\Delta K^*/C_3)^2]} \tag{3.35}$$

The crack growth rate is calculated by using Equation (3.35). This equation includes four different parameters ($C_1$, $C_2$, $C_3$, $K_{th}$) which must be obtained experimentally. After substituting the values of $K_{th}$ and $C_3 = K_{Ic}$ in Equation (3.35), $C_1$ and $C_2$ are determined by fitting a sinusoidal spline to experimental results.

### 3.6.3. Validation of the fatigue crack growth models for variable amplitude loading with experimental results

Crack growth life was calculated with different FCG models under single overload, block overload and random loading. The comparisons of these models with experimental results are discussed in this section.

#### 3.6.3.1. Modeling of single overload tests

Fatigue crack propagation models were applied for single overload tests after the 7000th load cycle under 7 kN (R = 0.1) constant amplitude and the results are plotted in Figure 3.20.

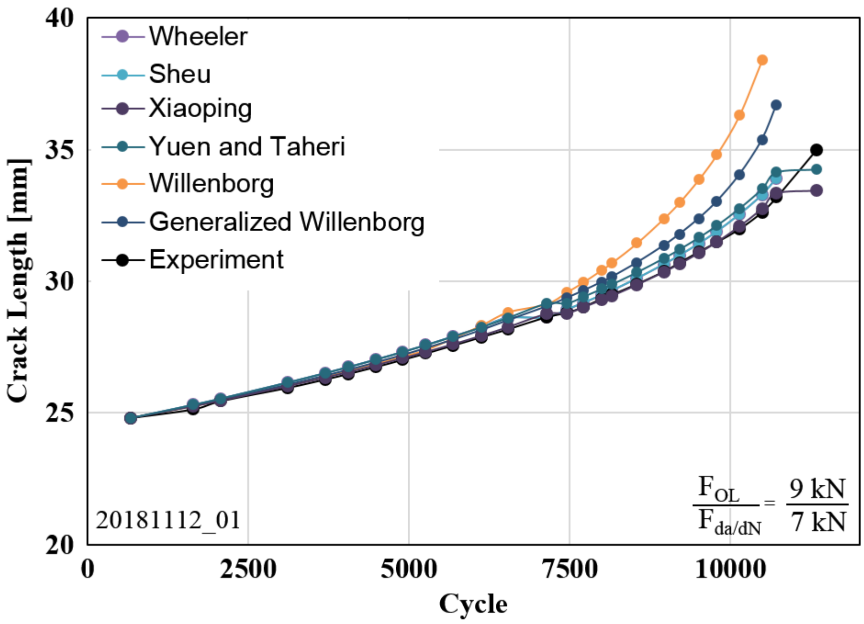

Figure 3.39. Comparison of variable amplitude loading models for $F_{OL}/F_{da/dN} = 1.29$ overload ratio

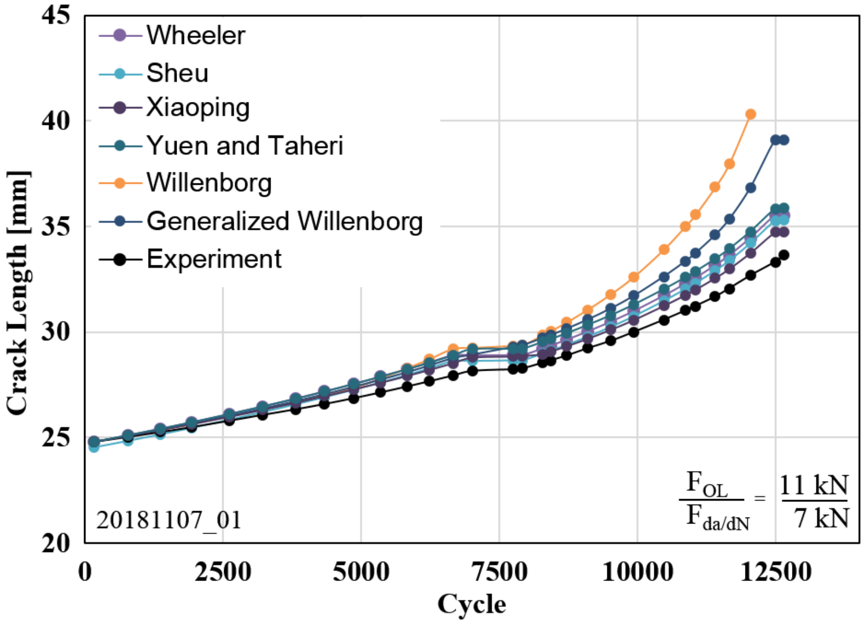

Figure 3.40. Comparison of variable amplitude loading models for $F_{OL}/F_{da/dN}$ = 1.57 overload ratio

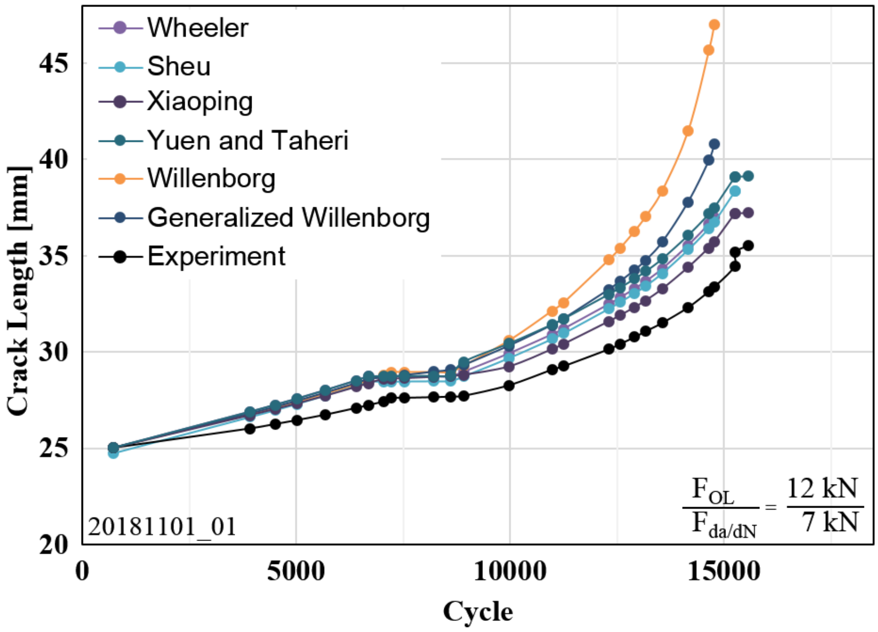

Figure 3.41. Comparison of variable amplitude loading models for $F_{OL}/F_{da/dN}$ = 1.71 overload ratio

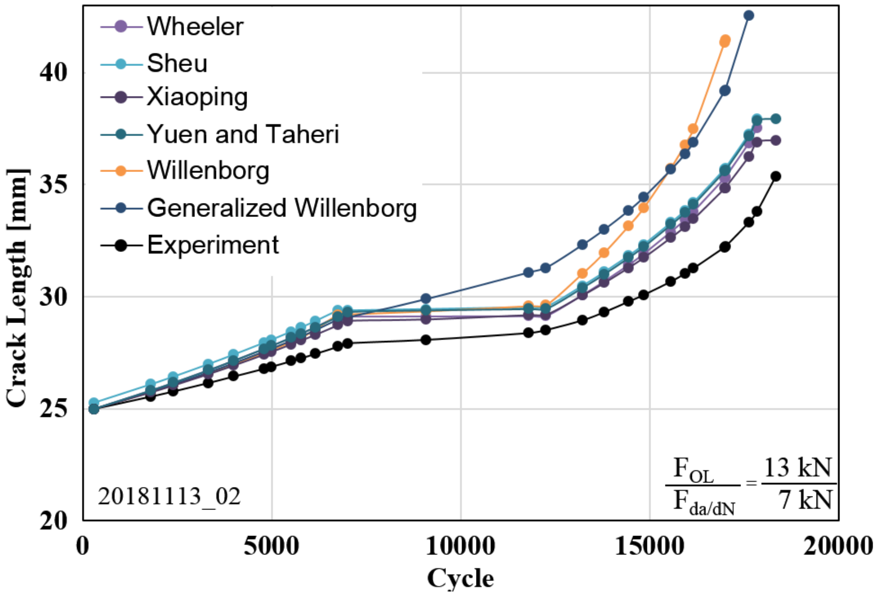

Figure 3.42. Comparison of variable amplitude loading models for $F_{OL}/F_{da/dN}$ = 1.85 overload ratio

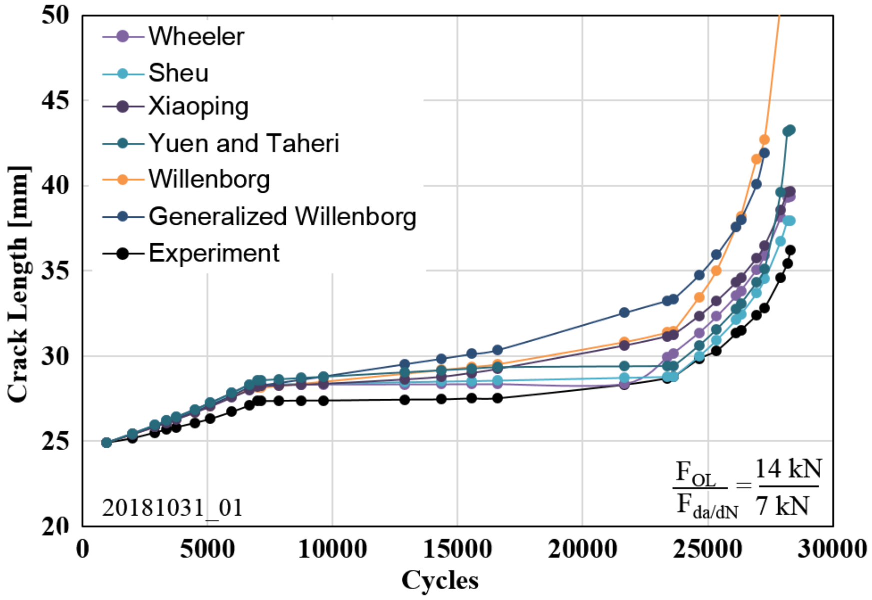

Figure 3.43. Comparison of variable amplitude loading models for $F_{OL}/F_{da/dN}$ = 2.0 overload ratio

The crack growth rates for different levels of overloads were calculated using the previously defined models and the results are presented in Figure 3.39. - Figure 3.43. Strong agreements between test results and predictions are observed using Wheeler model and its modified versions as seen in the figures. The Willenborg model and the other two modifications do not show a good agreement with experiments. It is stated in the literature that if the overload ratio is equal to or greater than two, reasonable results cannot be obtained by the Willenborg model [13]. Also, the Generalized Willenborg model, proposed to solve the overload ratio problem, does not show a good agreement with experimental results.

#### 3.6.3.2. Modeling of block overload tests

The block overload tests were discussed in Section 3.5.3. Different overload cycle sizes and their effects on crack growth behavior were demonstrated experimentally. Crack growth life was calculated with different models from the literature, and the calculated results were presented comparatively in graphs.

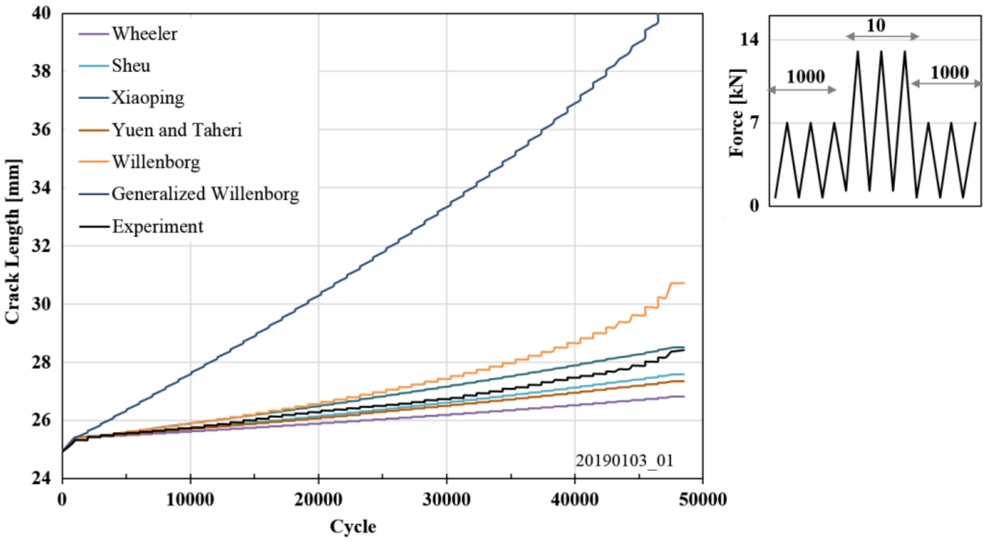

Figure 3.44. Comparison of variable amplitude loading models for block overload, n = 10

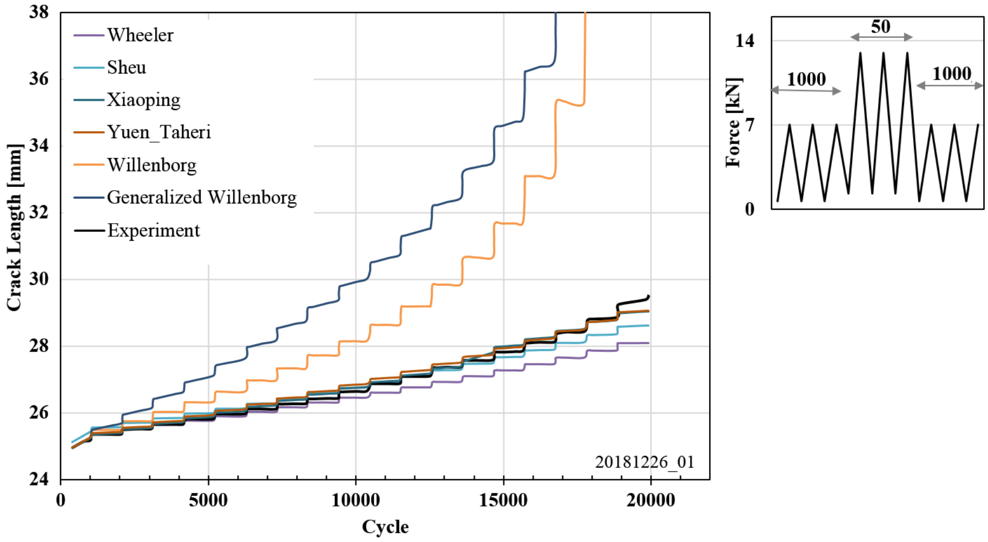

Figure 3.45. Comparison of variable amplitude loading models for block overload, n = 50

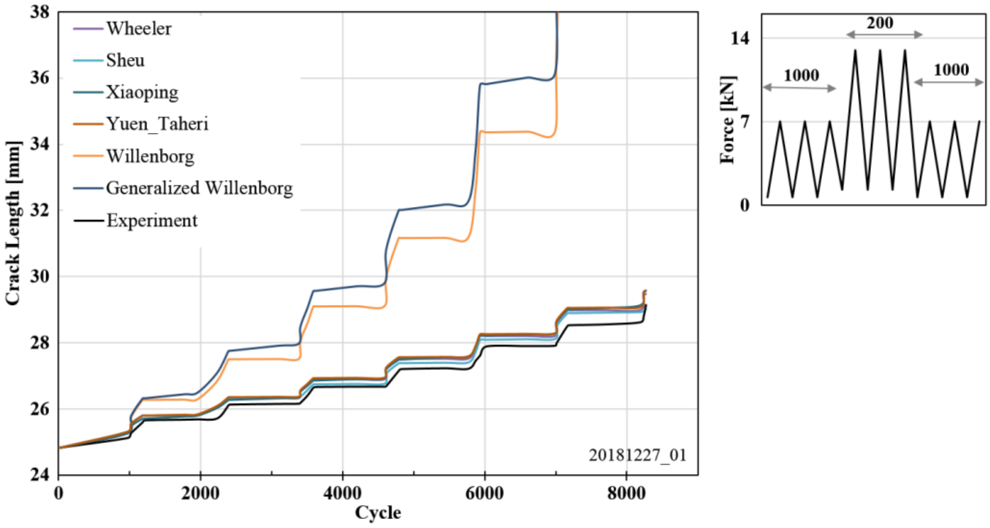

Figure 3.46. Comparison of variable amplitude loading models for block overload, n = 200

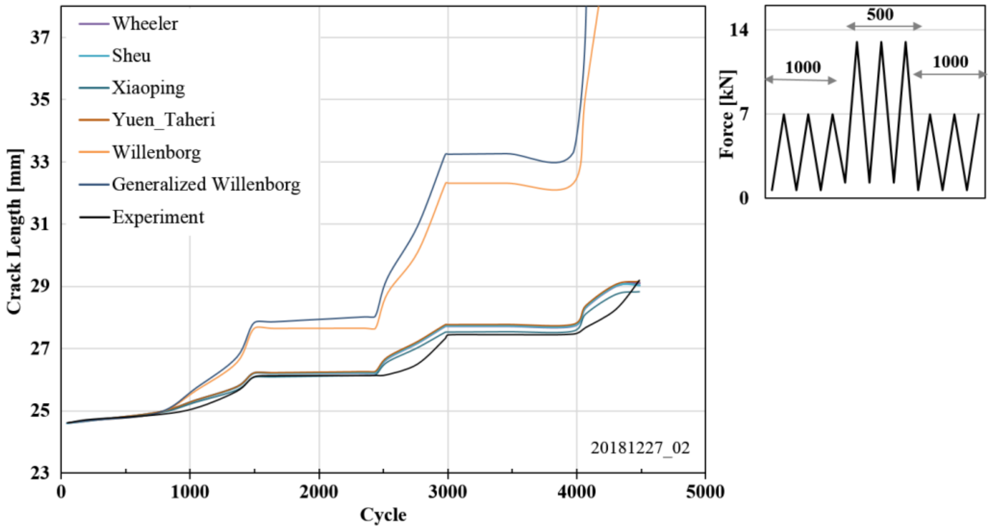

Figure 3.47. Comparison of variable amplitude loading models for block overload, n = 500

As can be seen in Figure 3.44. - Figure 3.47., the experimental results are closely predicted when the Wheeler Model and its modifications are used. Life calculations using the Willenborg model and its modifications don’t match with the experimental results.

### 3.6.3.3. Modeling of random loading tests

Cycle by cycle analyses were performed for modeling of crack growth under random loading tests. Modeling crack growth under random loading is challenging since the changes in stress ratio depend on the loading profiles. In practice, increases in SIF propagate the crack. Crack growth rate was calculated for the positive part of ΔK in the loading spectrum, and the negative part (load release) was not used in crack growth. The stress ratio was also calculated in the positive part. In Figure 3.48., one cycle is determined with three different points (ex: 1-2-3) called as Spectrum Profile Position Index (SPPI).

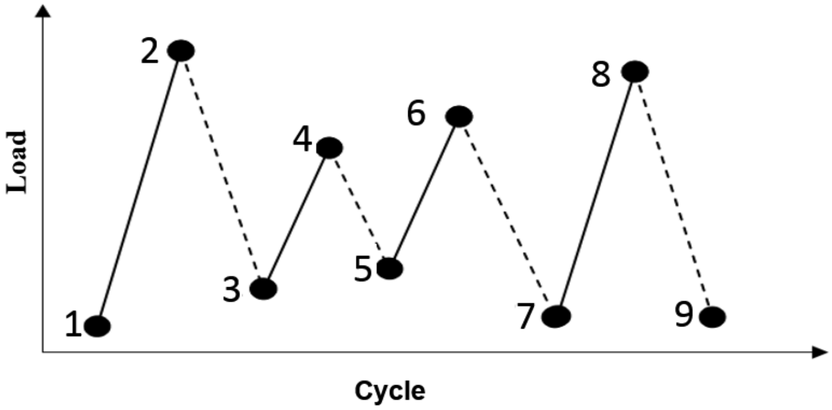

Figure 3.48. Definition of spectrum profile positions

Crack growth life calculation for random loading will be explained by using a random loading spectrum, including four-cycles in different amplitudes, given in Figure 3.48. The continuous lines show the increment of load and the dashed lines show the decrease of load. The first cycle in Figure 3.48. consists of points 1,2 and 3, identifying the profile position. All numbers (1,2,3,4…) are named as Profile Position Index. Increments in load, in other words, continuous lines are used to calculate the stress ratio. For example, the ratio of point 1 over point 2 gives the stress ratio for the first cycle, consisting of profile positions, 1, 2 and 3. The same calculation process is used for stress ratio along the whole spectrum.

As explained in Section 3.6.2., the fatigue crack growth rate is calculated by using Paris-Erdogan Equation in the Wheeler model. This approach was sufficient since the Wheeler model was intentionally proposed to determine crack growth behavior under single overloads. The stress ratio always varies in the random loading. Even if the maximum stresses of fatigue load profiles of different amplitudes are the same, the difference between the maximum and the minimum stresses should not be equal. It is known that this difference directly affects the crack growth rate. Therefore, using a crack growth model, considering the stress ratio, is a reasonable approach for random loading. Wheeler model was used with Forman and Walker crack propagation equations to calculate crack growth rate under random loading in this study.

In order to propose a different approach, the Paris-Erdogan Equation was used in the original Wheeler model with the coefficients obtained from Walker or Forman Equations. Thus, a simpler model was also studied by expressing the experimental data of different amplitudes in a composite manner. Modeling studies have also been carried out with the Generalized Willenborg, Xiaoping and root mean square (RMS) approach are explained in Section 3.6.2.

Table 3.13. Comparison of variable amplitude fatigue crack growth model results

| | | | CT SP1 | | | | CT SP2 | | | |
|---|---|---|---|---|---|---|---|---|---|---|
| | | | Cycle | | Edge crack length | | Cycle | | Edge crack length | |
| Model | FCG model | FCG equation | Test | Sim. | Test | Sim. | Test | Sim. | Test | Sim. |
| Composite C-n | Wheeler | Forman Const wth Paris-Erdogan | ≈ 31590 | 57200 | ≈ 26.8 mm | 27.8 mm | ≈ 21892 | 30996 | ≈ 27.2 mm | 27.5 mm |
| Composite C-n | Wheeler | Walker Const. wth Paris-Erdogan | | 175000 | | 25.6 mm | | 56677 | | 26.4 mm |
| Walker | Wheeler | Walker | | 63500 | | 27.5 mm | | 38868 | | 27.6 mm |
| Forman | Wheeler | Forman | | 82200 | | 27.2 mm | | 41574 | | 27.4 mm |
| Xiaoping | Wheeler | Paris-Erdogan | | 189000 | | 39.6 mm | | 52890 | | 27.3 mm |
| G.Willenborg | GWillenborg | Forman | | 95700 | | 30.5 mm | | 52156 | | 29.9 mm |
| RMS (Manjunatha) | RMS | Similar to Newman | | 26700 | | 31.1 mm | | 28556 | | 31.0 mm |

Measurement of crack length was done on the surface of the specimen since it was not possible to measure it from inside the crack front, which is close to being straight for the CT specimen. From the broken specimens' fracture surfaces after the random loading tests, it was observed that the crack lengths were different in the middle and the edge of the specimen. This difference, named as crack tunneling in the literature, had not been observed in constant amplitude loading tests. Crack tip plastic zone sizes change between the surface and middle of the specimen since the plane stress condition is dominating on the free-surfaces of the specimen, while the middle is under the plane strain condition. Therefore, crack propagation at the edge of the specimen is slower than that of the middle point on the crack front. Therefore, the measured distance from the surface of the specimen during the test is shorter than the measured one from the inner part of the specimen. It was deduced from the comparison between simulations and experiments, there is no need to calculate crack growth retardation in the middle of the specimen in the models since the plastic zone size is much smaller in the interior point of the crack front than that of the free-surface points (Figure 3.49).

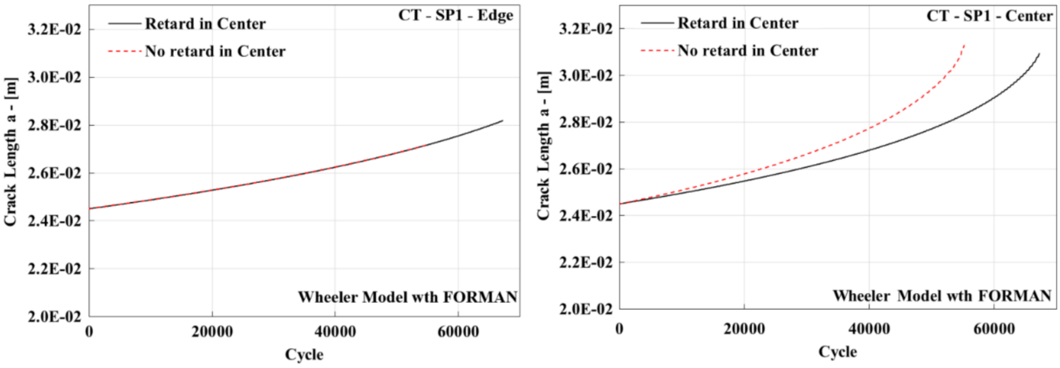

Figure 3.49. Consideration of the retardation in the center of the specimen

As seen in Table 3.13. the crack growth life predictions obtained by the simulations are significantly higher than the experiments. Thus, improvements on the model are necessary.

### 3.6.3.4. Improvements on 2-D crack growth models under random loading

To improve the FCG models in the literature the loading spectrum was used to develop a multiplier independent from the experimental results. For this, a cycle-by-cycle analysis was performed on the loading spectrum to obtain an index, named Spectrum Overload Index. The determination of "Spectrum Overload Index" is explained below.

- The average of the peaks along the spectrum is calculated.
- The percent deviation of each peak from the average is calculated.
- The percent deviation of each peak from average is compared to the ratio of the number of peaks that are equal to or greater than the specified peak for all peaks above the average. After operating the process for all peaks, the closest value of comparison (ideally equal) is selected, and it is added to 1. The obtained value is called the Spectrum Overload Index (SOL Index). For example, in a spectrum loading profile, if 25% of all peaks are at least 25% above the average, the SOL Index equals to 1.25.

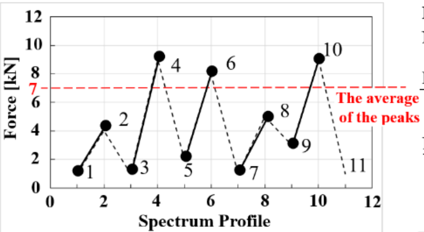

Number of the peaks : 5
Average of the peaks : 7 kN
Number of peaks that greater than the average : 3

Difference between the magnitude of profile 4 and the average : 9 - 7 kN = 2 kN
Number of profiles equal to or greater than the magnitude of profile 4 : 2

$$\frac{\text{Difference between the magnitude of profile 4 and the average}}{\text{Average of the peaks}} = \frac{2}{7} = \boxed{0.285}$$

$$\frac{\text{Number of profiles equal to or greater than the magnitude of profile 4}}{\text{Number of peaks that greater than the average}} = \frac{2}{3} = 0.666$$

Difference between the magnitude of profile 6 and the average : 8 - 7 kN = 1 kN
Number of profiles equal to or greater than the magnitude of profile 6 : 3

$$\frac{\text{Difference between the magnitude of profile 6 and the average}}{\text{Average of the peaks}} = \frac{1}{7} = 0.143$$

$$\frac{\text{Number of profiles equal to or greater than the magnitude of profile 6}}{\text{Number of peaks that greater than the average}} = \frac{3}{3} = 1.0$$

Figure 3.50. Calculation of Spectrum Overload Index

For the spectrum profile given in Figure 3.50., the ratio of the difference between the average and point 4 to the average of the peaks above the average is 0.285. For point 4, the ratio of the cumulative number of peaks above average to the total number of peaks above the average in the spectrum is 0.666. For point 6, these two values were calculated as 0.143 and 1.0, respectively. Since the values of 0.285 and 0.666 are closer to each other than the values obtained for point 6, the Spectrum Overload Index is determined as 1 + 0.285 = 1.285. Similar calculations can be done for other points above the average such as point 10 and it can be seen that the results are similar as the one for point 4.

In this study, as an improvement for predictions of crack propagation lives under spectrum loading conditions, the SOL Index is used as a multiplier of the ΔK term in the fatigue crack propagation equations. In Equations (3.36) - (3.39), the use of SOL Index with different models is demonstrated.

Wheeler model with Forman or Walker constants

$$\frac{da}{dN} = \emptyset_R (C \, . \, SOL\_index \, . \Delta K)^n \tag{3.36}$$

Wheeler with Forman Eqn.

$$\frac{da}{dN} = \emptyset_R \left[ \frac{C_F (SOL\_index \, . \Delta K)^m}{(1-R)^n K_{IC} - \Delta K} \right] \tag{3.37}$$

Wheeler with Walker Eqn.

$$\frac{da}{dN} = \emptyset_R C \left[ \frac{SOL\_index \, . \Delta K}{(1-R)^{1-\gamma_w}} \right]^n \tag{3.38}$$

Willenborg model

$$\frac{da}{dN} = \frac{C_F (SOL\_index \, . \Delta K_{eff})^m}{\left(1 - R_{eff}\right) K_C - \Delta K_{eff}} \tag{3.39}$$

In Table 3.14., analyses performed with or without SOL Index in different models, and comparisons with experimental results obtained by CT specimen are presented. As can be seen from the table, when the SOL Index is used, the simulation results become closer to the experimental results. The SOL Index values are found to be 0.14 + 1 = 1.14 and 0.24 + 1 = 1.24 for the Spectrum-1 (Figure 3.24.) and Spectrum-2 (Figure 3.27.), respectively. The crack growth curves for each model are plotted for Spectrum-1 in Figure 3.52. - Figure 3.58. and for Spectrum-2 in Figure 3.59. -Figure 3.65.

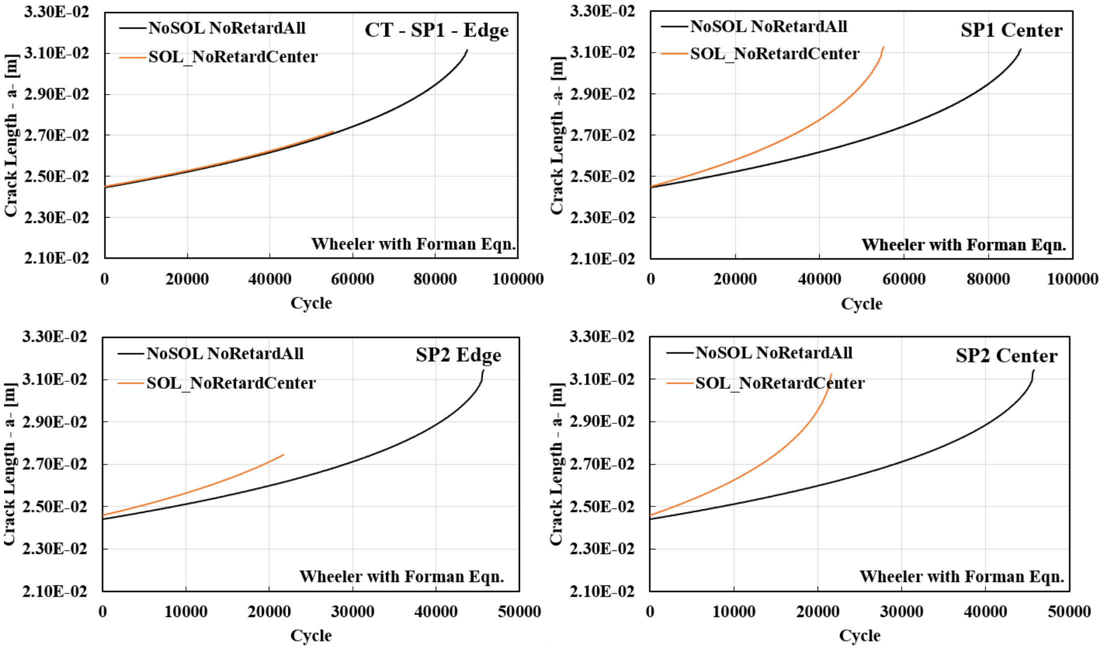

Figure 3.51. The effect of SOL index with retardation

Wheeler with Forman Eqn. is used to investigate the effect of SOL_index in Figure 3.51. for SP1 and SP2 spectrums. In the figure, considering the retardation_ALL case, the effect of SOL_index on the results is observed. As can be seen, especially in SP2 spectrum, SOL_index affects the results regardless of the retardation effect. Since the SOL_index value is low in SP1, this effect cannot be clearly seen in the figure. Figure 3.49. also can be seen for the comparison of the case of retardation applied to the edge and center of the specimen or only the edge.

Table 3.14. Comparison of variable amplitude fatigue crack growth model with the use of SOL index or not

| | | | | CT SP1 | | | | CT SP2 | | | |
|---|---|---|---|---|---|---|---|---|---|---|---|
| | | | | **Cycle** | | **Edge crack length** | | **Cycle** | | **Edge crack length** | |
| **Model** | **FCG model** | **FCG equation** | **SOL index** | **Test** | **Sim.** | **Test** | **Sim.** | **Test** | **Sim.** | **Test** | **Sim.** |
| Composite C-n | Wheeler | Forman Const wth Paris-Erdogan | ✓ | ≈ 31590 | 44200 | ≈ 26.8 mm | 27.8mm | ≈ 21892 | 20418 | ≈ 27.2 mm | 27.6 mm |
| Composite C-n | Wheeler | Forman Const wth Paris-Erdogan | ✗ | | 57200 | | 27.8 mm | | 30996 | | 27.5 mm |
| Composite C-n | Wheeler | Walker Const. wth Paris-Erdogan | ✓ | | 111200 | | 25.6 mm | | 23124 | | 26.0 mm |
| Composite C-n | Wheeler | Walker Const. wth Paris-Erdogan | ✗ | | 175000 | | 25.6 mm | | 56677 | | 26.4 mm |
| Walker | Wheeler | Walker | ✓ | | 43200 | | 27.6 mm | | 20172 | | 27.7 mm |
| Walker | Wheeler | Walker | ✗ | | 63500 | | 27.5 mm | | 38868 | | 27.6 mm |
| Forman | Wheeler | Forman | ✓ | | 55200 | | 27.2 mm | | 21648 | | 27.5 mm |
| Forman | Wheeler | Forman | ✗ | | 82200 | | 27.2 mm | | 41574 | | 27.4 mm |
| Xiaoping | Wheeler | Paris-Erdogan | ✗ | | 189000 | | 39.6 mm | | 52890 | | 27.3 mm |
| GWillenborg | GWillenborg | Forman | ✓ | | 63200 | | 27.2 mm | | 29593 | | 26.4 mm |
| G.Willenborg | GWillenborg | Forman | ✗ | | 95700 | | 30.5 mm | | 52156 | | 29.9 mm |
| RMS (Manjunatha) | RMS | Similar to Newman | ✗ | | 26700 | | 31.1 mm | | 28556 | | 31.0 mm |

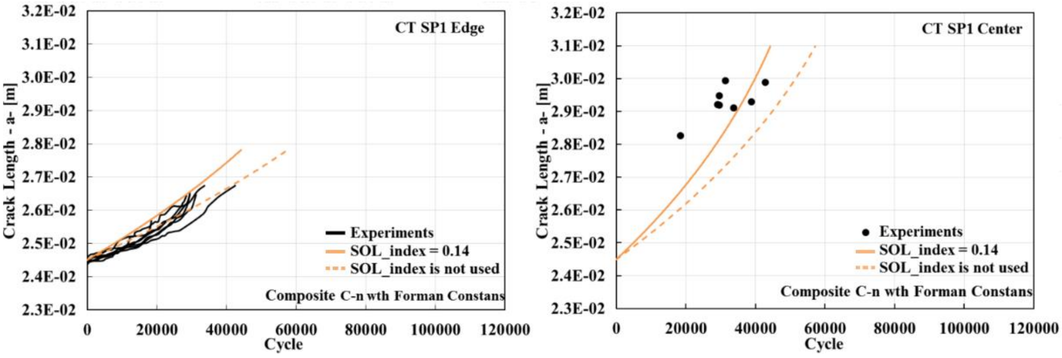

Figure 3.52. Crack growth curve by using the Wheeler model with Forman FCG constants (SP1)

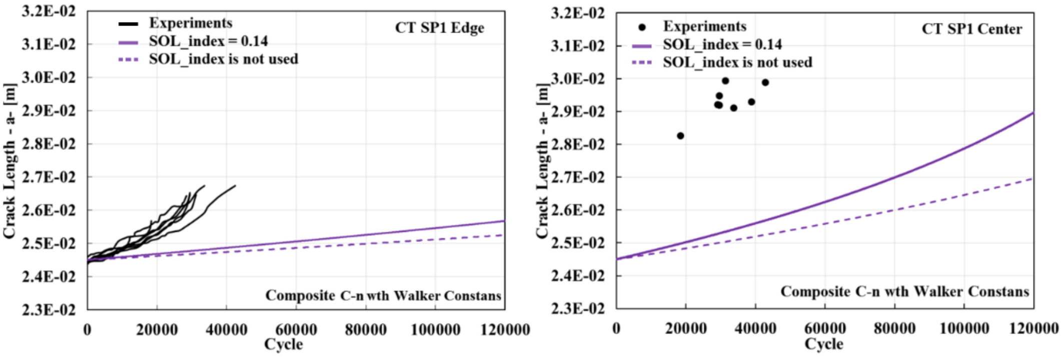

Figure 3.53. Crack growth curve by using the Wheeler model with Walker FCG constants (SP1)

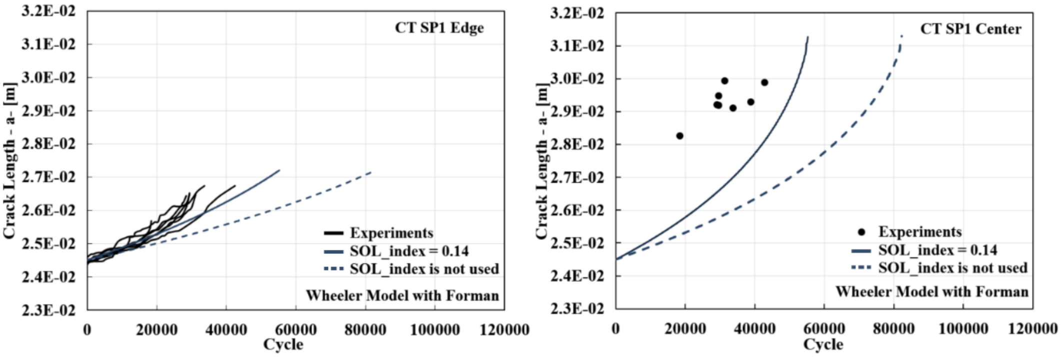

Figure 3.54. Crack growth curve by using the Forman FCG Eqn in the Wheeler model (SP1)

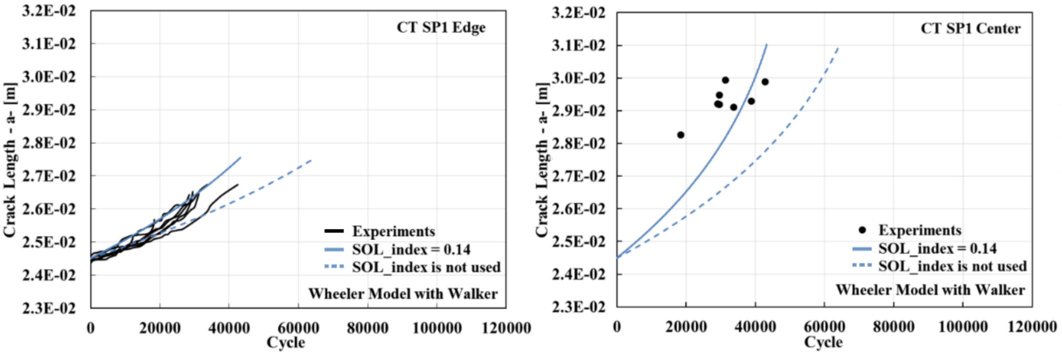

Figure 3.55. Crack growth curve by using the Walker FCG Eqn in the Wheeler model (SP1)

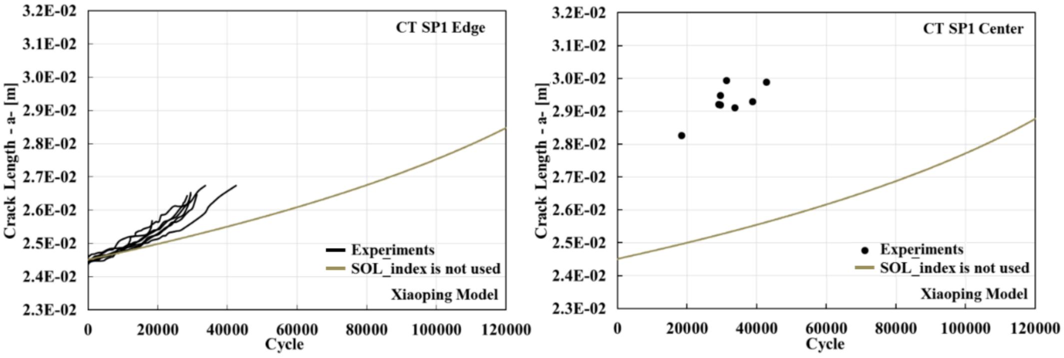

Figure 3.56. Crack growth curve by using Xiaoping model (SP1)

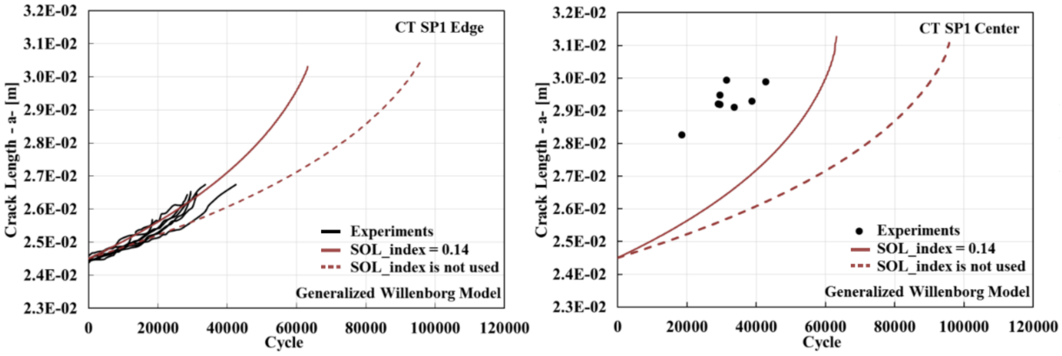

Figure 3.57. Crack growth curve by using Generalized Willenborg Model (SP1)

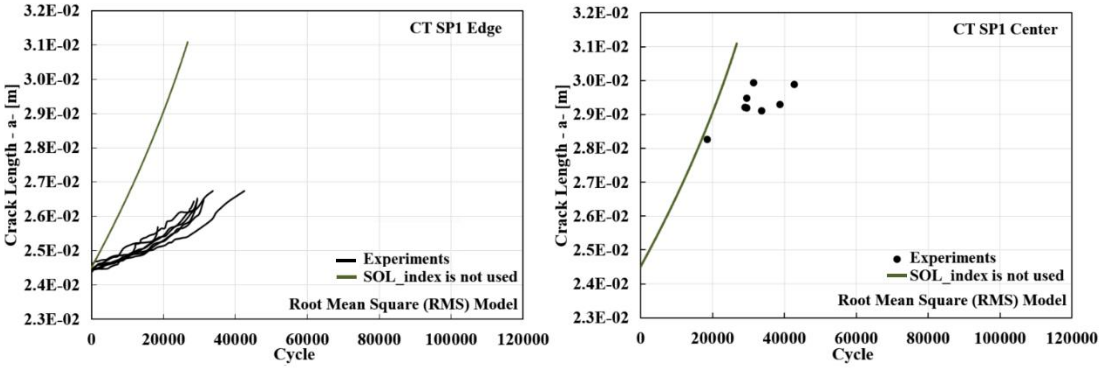

Figure 3.58. Crack growth curve by the Root Mean Square (RMS) approach (SP1)

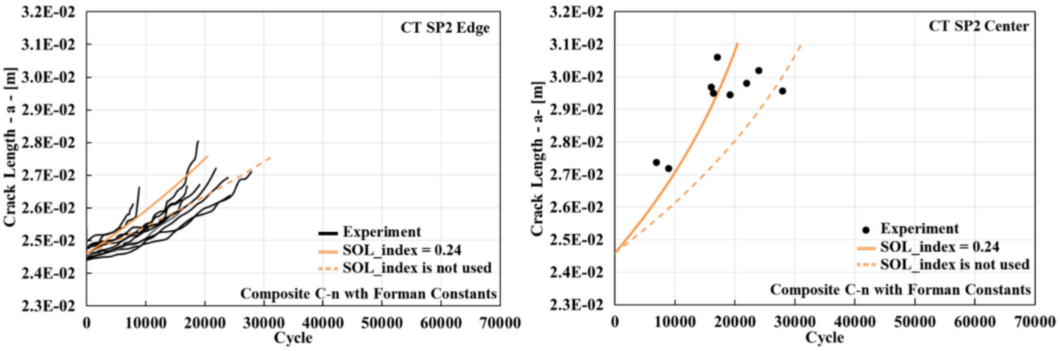

Figure 3.59. Crack growth curve by using the Wheeler model with Forman FCG constants (SP2)

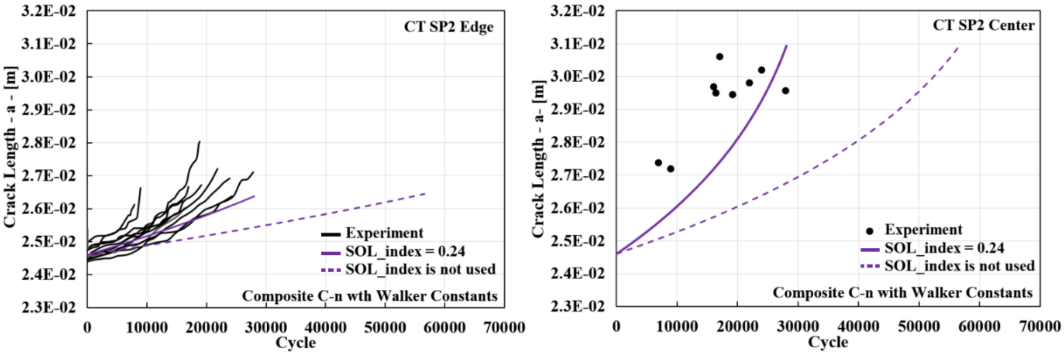

Figure 3.60. Crack growth curve by using the Wheeler model with Walker FCG constants (SP2)

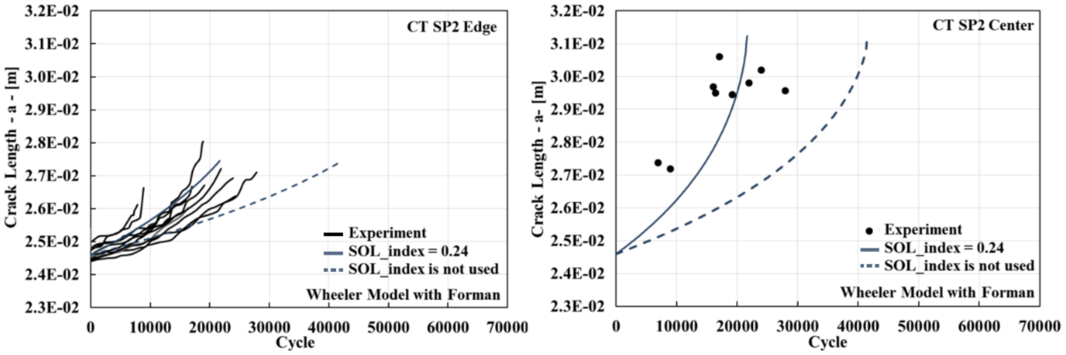

Figure 3.61. Crack growth curve by using the Forman FCG Eqn in the Wheeler model (SP2)

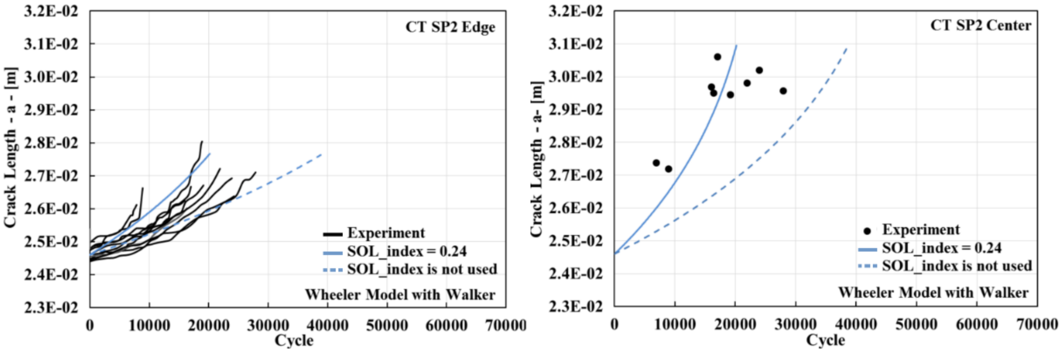

Figure 3.62. Crack growth curve by using the Walker FCG Eqn in the Wheeler model (SP2)

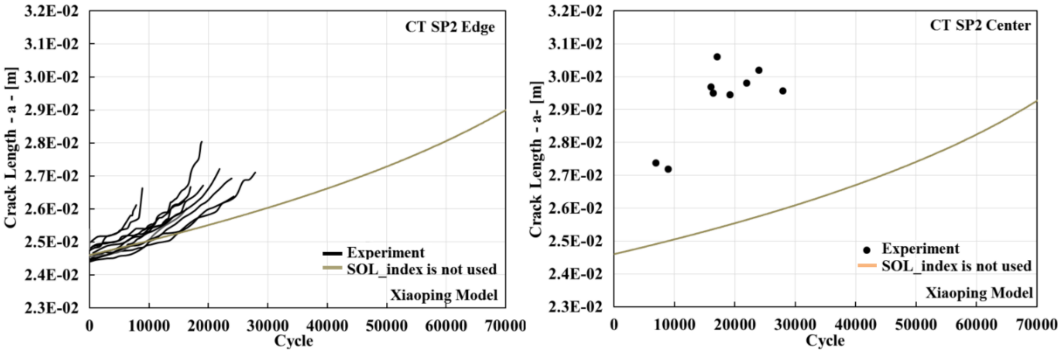

Figure 3.63. Crack growth curve by using Xiaoping model (SP2)

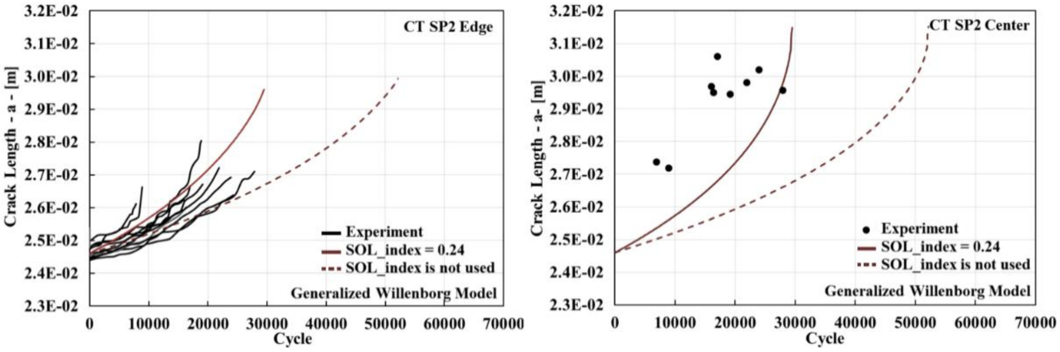

Figure 3.64. Crack growth curve by using Generalized Willenborg Model (SP2)

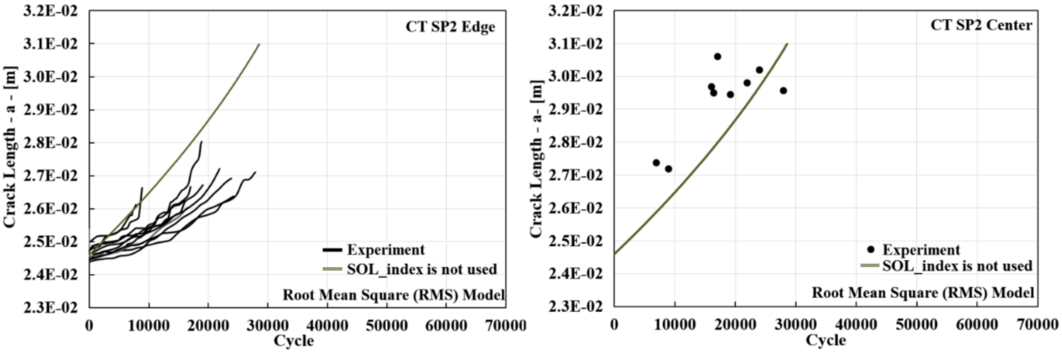

Figure 3.65. Crack growth curve by the Root Mean Square (RMS) approach (SP2)

Simulations performed using the SP1 and SP2 loading profiles show that the use of SOL Index is appropriate for 2-D, i.e., straight or through-thickness crack front, fatigue crack propagation. Among the different models applied with SOL Index, the closest results to experiments are obtained by using the Walker or Forman crack growth equation with the Wheeler model (Figure 3.54. - Figure 3.55., Figure 3.61. - Figure 3.62.).

The proposed SOL Index approach is also validated with the experimental results in the literature by using the in-house FORTRAN code [51], [52]. In the referred papers, two-dimensional crack propagation in a plate under random loading was studied. The SIF formula was updated according to the references, and simulations were performed with the spectrum and crack size given by R. Porter [34]. Since the material coefficients C-n were not given in this study, the coefficients for the same material were taken from the literature [53] and presented below.

$C_{walker} = 1.42\ 10^{-8}$ [mm/cycle & MPa.m$^{0.5}$] and n = 3.59 m = 6.80

$C_{Forman} = 2.31\ 10^{-6}$ [mm/cycle & MPa.m$^{0.5}$] and n = 3.38

As can be seen from Figure 3.66., the experimental crack growth curve was excellently predicted by using the SOL Index. Calculated SOL Index was 0.14 + 1 = 1.14 for the loading profile, presented in the study. Therefore, the proposed crack growth model with SOL Index under variable amplitude load has been validated with an independent study from the literature.

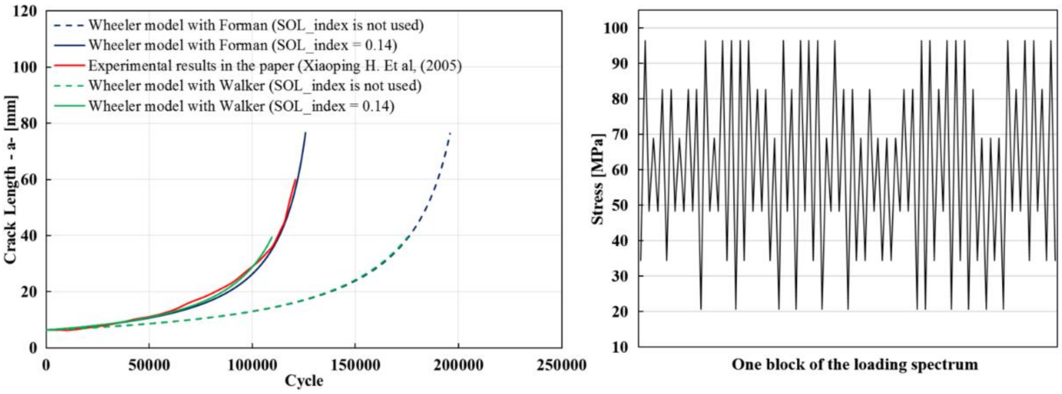

Figure 3.66. Comparison of the results with literature

# CHAPTER 4. PROBABILISTIC FRACTURE MECHANICS STUDIES FOR THREE-DIMENSIONAL FATIGUE CRACK GROWTH

In this chapter, three-dimensional crack propagation on a specimen containing surface cracks was investigated. Experimental and computational analyses were performed after determining the specimen type and geometric dimensions. Tolerances were determined in the specimen geometry and the effect of these tolerances on the SIF was investigated by the Design of Experiment (DOE) analyses. Transfer functions were obtained to calculate the SIFs for different points along the crack front, namely the free-surface points and the depth point, by evaluating the results of the DOE. A chart showing the workflow in Chapter-4 is given in Figure 4.1.

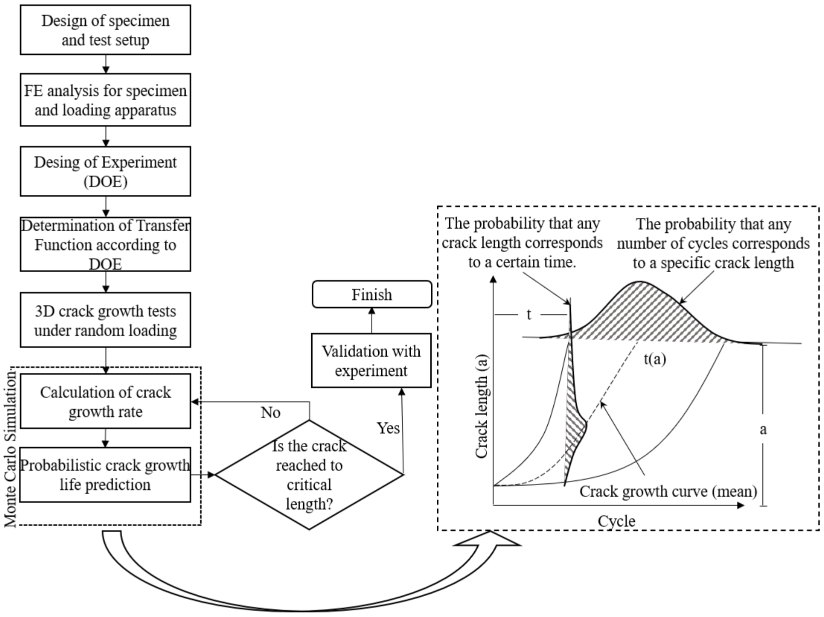

Figure 4.1. Flow chart in Chapter-4

## 4.1. Design of the Specimen and the Test Setup

CT specimen in ASTM standard is used for two-dimensional crack propagation (two-dimensional finite element model is required in modeling), and there is no standardized testing specimens with three-dimensional surface crack. Therefore, firstly, specimen geometries were determined in order to study the three-dimensional surface cracking both experimentally and computationally. Studies were conducted on two different specimen types.

First, it was planned to apply a tensile load on a plate with a countersunk hole as seen in Figure 4.2. A countersunk hole was drilled on a 10 mm thick plate and the tensile load required for fracture point in the experiment was calculated using the finite element method.

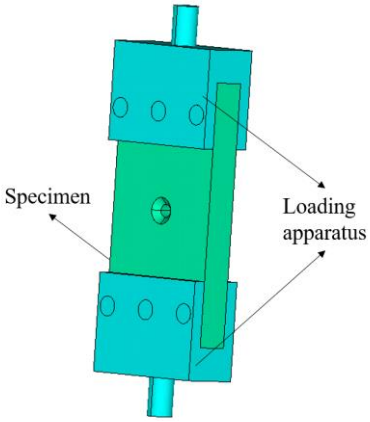

Figure 4.2. A countersunk plate for 3-D fatigue crack growth tests

Finite element analysis was performed with crack being modeled along the countersunk hole in the thickness direction and the SIF results are as shown in Figure 4.3. The SIFs at the crack front are quite low under the 10 kN tensile force applied in the model. Also, since the plate with a thickness of 10 mm may lead the plane stress condition in the tests, increasing the specimen thickness would also be required. Both the low SIFs and increasing the specimen thickness will require even higher loads for fracturing the specimen.

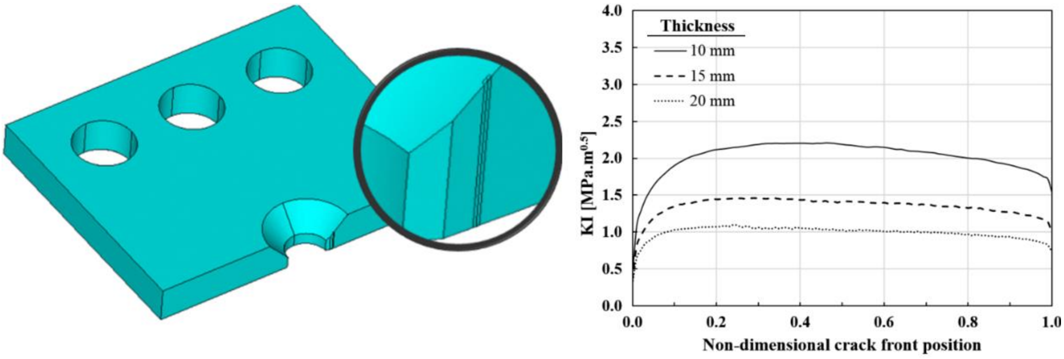

Figure 4.3.SIFs along the countersunk at different plate thickness

Since the SIFs obtained in the countersunk plate are quite low, another specimen from the literature was analyzed, named Lee James Specimen [54], [55]. This specimen is similar to CT specimen, except its height is longer and contains a semi-elliptical surface crack. Thus, this makes it possible to view the crack in the specimen from the front.

Lee James (LJ) specimen with its original dimensions and the ellipsoid notch on it can be seen in Figure 4.4. An initial crack was generated as ($ɑ/2c = 1$, $ɑ = 2.75$ mm) and crack growth simulation was performed under 10 kN mode-I load. Propagating crack profiles and the corresponding KI stress intensity factors are also given in Figure 4.4.

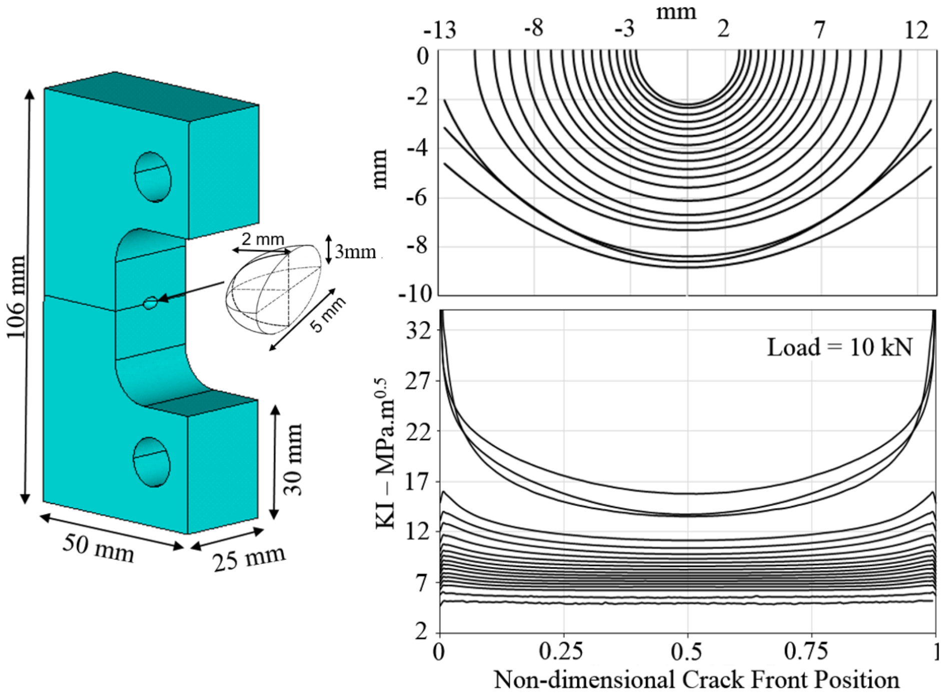

Figure 4.4.KI SIFs and crack profiles for Lee James Specimen with the original dimensions

As can be seen from the figure, the SIFs are much higher compared to the plate with countersunk hole. It was decided to make modifications in Lee James specimen in order to increase crack growth rate under the same load. The specimen width was increased from 50 mm to 62.5 mm to enlarge the cross-section for crack propagation, and the specimen height was reduced incrementally from 106 mm to 90 mm and to 80 mm to save material in manufacturing of specimens. The final geometry of the specimen is given in Figure 4.5.

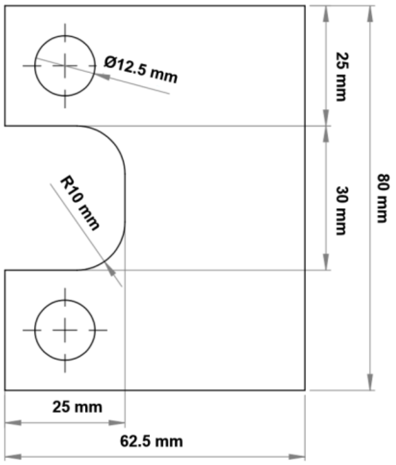

Figure 4.5. Final dimensions of Lee James specimen

Elasto-plastic analysis was also performed with the final geometry (62.5 mm width & 80 mm height) using the 7075-T6 aluminum alloy material properties. In the FEA model, a surface crack (a/c = 1, a = 6 mm) was generated around an spherical notch (r =5 mm), and contact mechanics between the specimen, pins and loading apparatus were defined. In elasto-plastic analysis, it was controlled whether the applied load to generate the desired SIFs causes a yielding in some points of the specimen. In addition, the linearity of the load-displacement curve in the vicinity of the crack tips was checked. It was seen that the yield stress was not exceeded in any point except at the crack tip of the designed specimen. In addition, it was observed that the crack tip opening displacements were directly proportional to the force according to changes in distance between points A and B in Figure 4.8. Thus, there was no additional non-linear deformation on the specimen that would affect the SIFs at the crack tip. Details of the elasto-plastic analysis are given in Figure 4.6. - Figure 4.8.

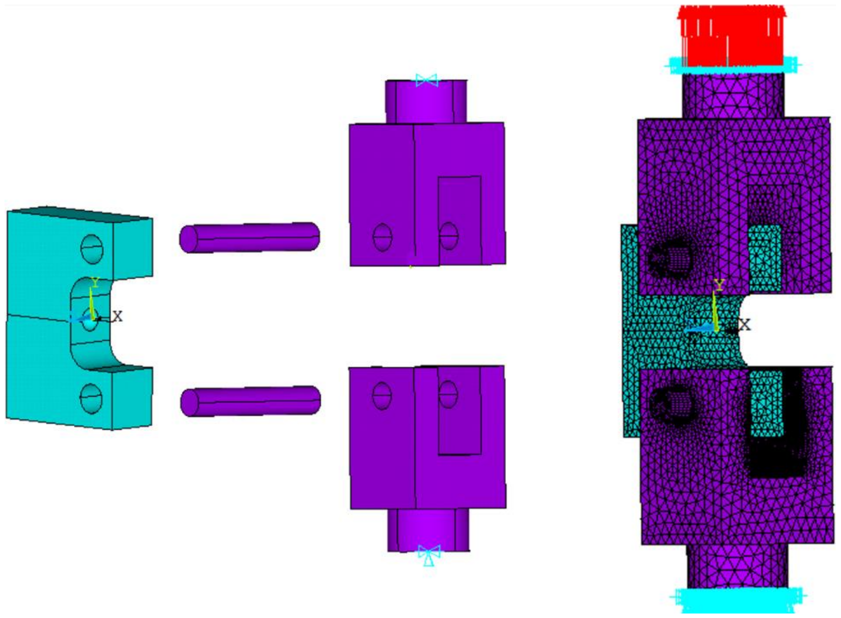

Figure 4.6. Lee James specimen, loading apparatus and applied boundary conditions for elasto-plastic analysis

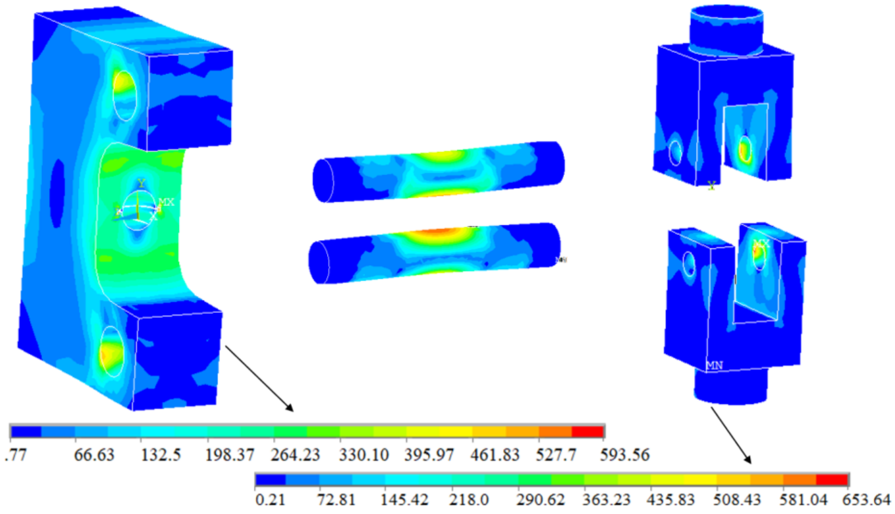

Figure 4.7. Von-Mises stress results from elasto-plastic analysis with a spherical notch under 35 kN

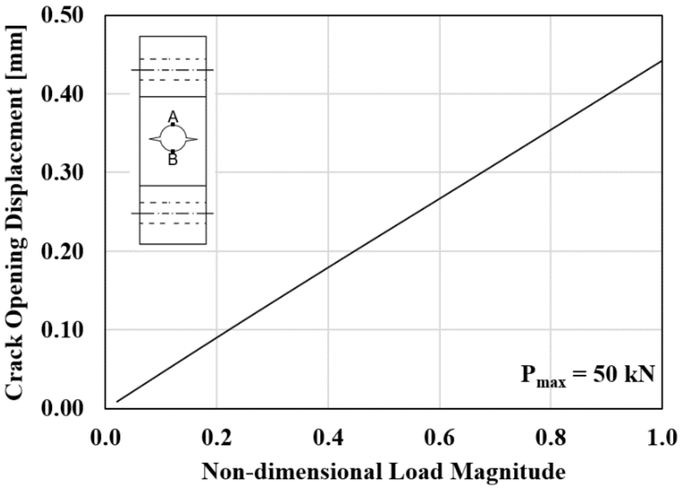

Figure 4.8. The relation between the crack opening displacement and non-dimensional load magnitude

After determining the external dimensions of the specimen, fracture analyses were performed. First, a surface crack with 6 mm crack width (c) and aspect ratio ($a / 2c = 0.5$) was placed in front of the specimen and analyzed. As expected, the SIFs were very low in this case. Thereupon, a notch was generated that creates stress concentration, and fracture analyses were re-performed to optimize the notch geometry. After many analyses, two alternatives were selected, and their results are presented in Figure 4.9. in terms of notch dimensions (width, depth, height) and the corresponding SIFs. Similar SIFs were obtained in both alternatives and the ellipsoid (10 mm total width, 2 mm total height and 4 mm depth) was chosen.

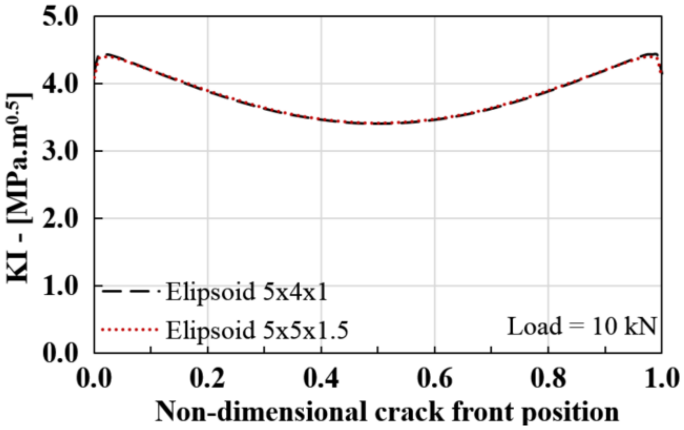

Figure 4.9. Notch geometry and its effect on stress intensity factor

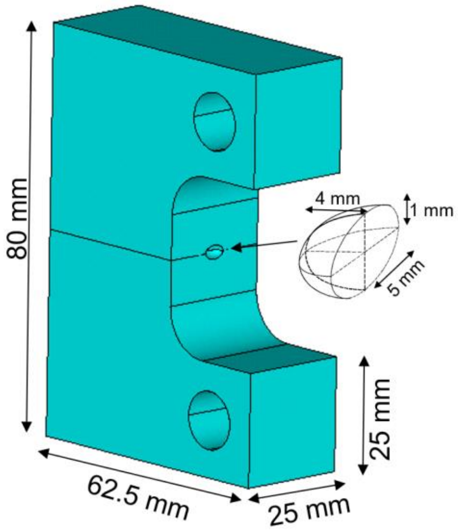

Figure 4.10. The final dimensions of the LJ specimen

## 4.2. Design of Experiment (DOE) Analyses

In fatigue crack propagation experiments, material properties were investigated as the main effect that cause scattering in life values in Section 3.1. Another factor that causes scattering is the geometric tolerances in the specimen. A large number of experiments with combinations of tolerances in specimen geometry are required to determine the effect of scattering on the results. Considering the time, difficulty and cost of hundreds of tests, it is more reasonable to use FEM, representing the experiments.

### 4.2.1. Strain gauge measurements for verification of Finite Element Analysis

In order to verify that the results obtained by FEA fully represent the experiments, strain gauge measurements were compared with the strains obtained from the analyses. A total of five strain gauges were pasted to the left and right of the notch placed on the front side, to the back, and left and right surfaces of the specimen.

The locations and directions of strain gauges were determined by FEA, using the maximum principal stresses and their directions at the corresponding node, presented in Figure 4.11.

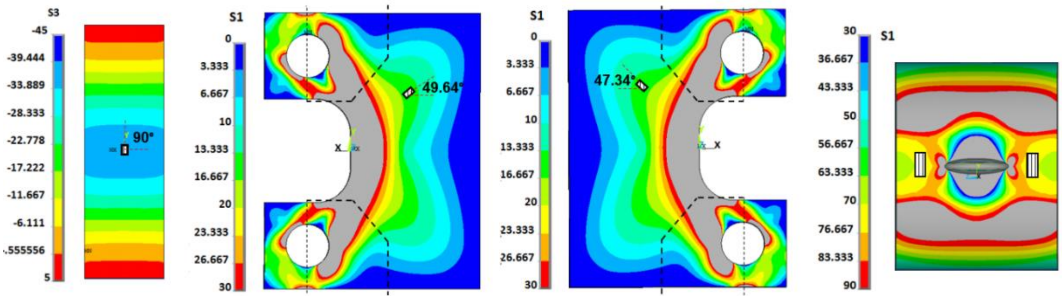

Figure 4.11. Location and direction of the strain gauges on different surfaces of the specimen

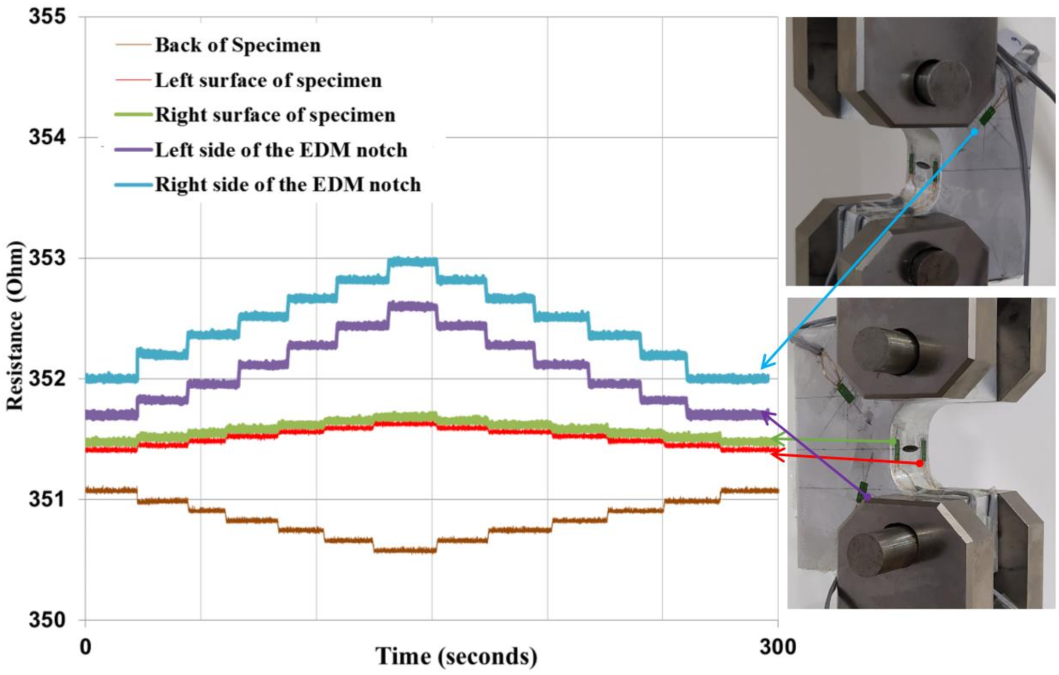

Figure 4.12. Measured resistance by using strain gauges

The strain gauge-assembled specimen was loaded at 0-2-4-6-8-10-12 kN incrementally and then unloaded gradually. Resistance changes were measured, and the results are plotted in Figure 4.12., and the data is given in Table 4.1. In the bottom row of the table, strain values calculated by the finite element method are given on a gray background. The minimum difference of the strain between the measurements and computational results was 0.67% and the maximum difference was 12.47%, which are obtained at the left and right sides of the notch, respectively. These two strain gauges were in similar positions and directions at the right and left of the notch. According to the results of FEA, the strain values of these two points are very close to each other. Different results from the two strain gauges might be caused by the factors such as adhesion or measurement error. As can be seen from the table, since the strain values obtained from the finite element model and experiments are very close, it was proved that the load and related boundary conditions in the experiments are correctly represented in the finite element model.

Table 4.1. Strain gauge measurement data

| | Left of the notch | % error | Right of the notch | % error | Back of Specimen | % error | Left side of Specimen | % error | Right side of Specimen | % error |
|---|---|---|---|---|---|---|---|---|---|---|
| ε for 0-2 kN | 0.00086 | -13 | 0.00135 | 37.6 | -0.00059 | 15.0 | 0.00026 | 14.6 | 0.00024 | 5.8 |
| ε for 0-4 kN | 0.00123 | -12 | 0.00123 | 25.0 | -0.00056 | 9.2 | 0.00025 | 10.2 | 0.00024 | 7.7 |
| ε for 0-6kN | 0.00117 | -5.6 | 0.00117 | 18.6 | -0.00056 | 8.1 | 0.00026 | 13.7 | 0.00024 | 5.6 |
| ε for 0-8kN | 0.00113 | -1.5 | 0.00113 | 14.5 | -0.00055 | 7.1 | 0.00025 | 10.7 | 0.00024 | 4.5 |
| ε for 0-10kN | 0.00111 | 0.7 | 0.00111 | 12.5 | -0.00056 | 8.1 | 0.00025 | 8.2 | 0.00023 | 3.1 |
| | Left of the notch | % error | Right of the notch | % error | Back of Specimen | % error | Left side of Specimen | % error | Right side of Specimen | % error |
| ε for 10 kN (ANSYS) | 0.00100 | 0.67 | 0.00098 | 12.4 | -0.00052 | 8.14 | 0.00023 | 8.17 | 0.00023 | 3.09 |

### 4.2.2. Determining the effect of geometric variables on the SIF

Geometric tolerances in specimen dimensions were observed due to machining process. In order to consider these geometric tolerances, some dimensions on the specimen were determined as variables. The variables are summarized in Table 4.2. Six different variables were defined, and in total, 405 different cases were analyzed as the combination of variables. Three of the geometric parameters, x-y-z positions of the ellipsoid as shown in Figure 4.13., can affect the SIFs. The machining tolerance was selected as ± 0.2 mm for x-y-z positions of the ellipsoid considering the machining process performed by the Electro Discharge Machining (EDM). The length and depth of the initial crack and the thickness of the specimen machined by CNC milling was also determined as variables.

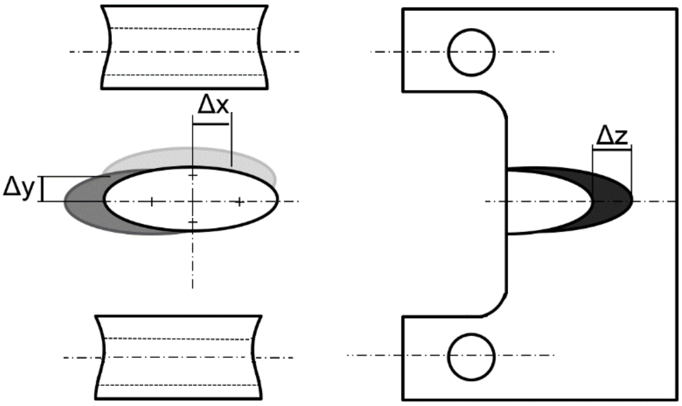

Figure 4.13. Offsets of the ellipsoid notch

Table 4.2. Tolerances of Lee James Specimen

| **Variables** | **Min. Value** | **Max. Value** | **Increment** | **Factor** |
|---|---|---|---|---|
| **Precrack Length** | 6.6 mm | 7.4 mm | 0.2 mm | 5 |
| **Precrack Depth** | Function of Precrack Length | | | |
| **Ellipsoid DX** | -0.2 mm | 0.2 mm | 0.2 mm | 3 |
| **Ellipsoid DY** | -0.2 mm | 0.2 mm | 0.2 mm | 3 |
| **Ellipsoid DZ** | -0.2 mm | 0.2 mm | 0.2 mm | 3 |
| **Thickness** | 24.9 mm | 25.1 mm | 0.1 mm | 3 |

Before starting the DOE Analysis, a mesh sensitivity analysis on crack front mesh was performed. In the sensitivity analysis, a full model with loading apparatus including contacts between the specimen, pins, and loading apparatus was considered. The element size at the crack front was defined as one 50th - 100th - 200th - 300th - 400th of the crack depth, and other conditions in the analysis were kept constant. As can be seen from Figure 4.14., the results are very close to each other. 2.2% difference was calculated between the coarsest and finest cases. Thus, crack tip element size was defined as one percent of the crack depth.

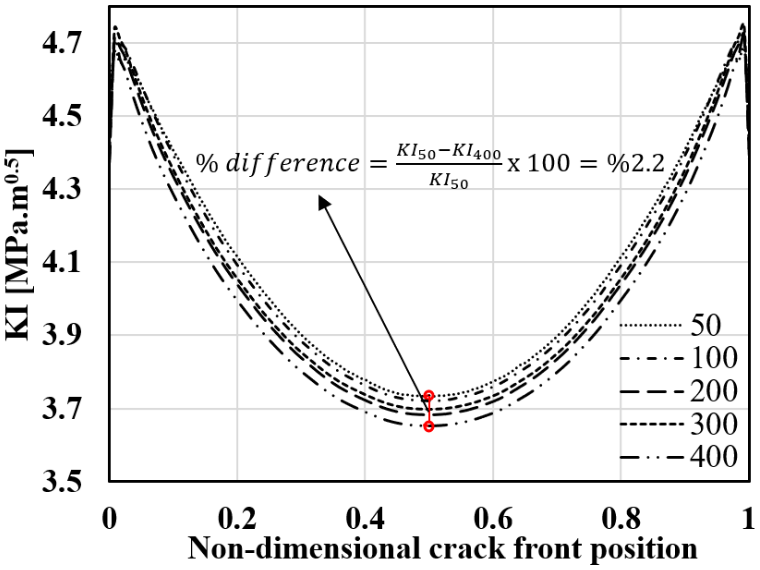

Figure 4.14. Effect of element size on SIF in Lee James Specimen

A macro in ANSYS APDL was prepared that can parametrically place the ellipsoid notch and the surface crack in the Lee James specimen. In the macro, the specimen, the pins and the loading apparatus were modeled according to the test conditions, and the contact mechanics were used between the parts. ANSYS v12.1 [56] was used in the stress analysis of the assembled model. Displacements of nodes, belonging to the loading holes, were read from the ANSYS solution file, and written as the displacement boundary condition in the fracture analysis. SIFs were calculated along the crack front by sub-modeling, using FCPAS.

### 4.2.3. Determining the transfer function for calculating KI SIF

405 DOE Analyses were conducted in order to observe the effect of each geometric variable on the SIF. The SIF results from these 405 cases were analyzed independently by using MINITAB software [44]. A sample view of the DOE table is presented in Figure 4.15.

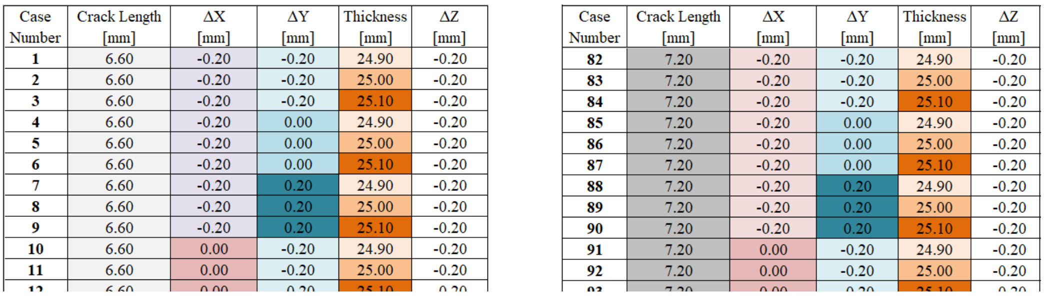

| Case Number | Crack Length [mm] | ΔX [mm] | ΔY [mm] | Thickness [mm] | ΔZ [mm] |
|---|---|---|---|---|---|
| **1** | 6.60 | -0.20 | -0.20 | 24.90 | -0.20 |
| **2** | 6.60 | -0.20 | -0.20 | 25.00 | -0.20 |
| **3** | 6.60 | -0.20 | -0.20 | 25.10 | -0.20 |
| **4** | 6.60 | -0.20 | 0.00 | 24.90 | -0.20 |
| **5** | 6.60 | -0.20 | 0.00 | 25.00 | -0.20 |
| **6** | 6.60 | -0.20 | 0.00 | 25.10 | -0.20 |
| **7** | 6.60 | -0.20 | 0.20 | 24.90 | -0.20 |
| **8** | 6.60 | -0.20 | 0.20 | 25.00 | -0.20 |
| **9** | 6.60 | -0.20 | 0.20 | 25.10 | -0.20 |
| **10** | 6.60 | 0.00 | -0.20 | 24.90 | -0.20 |
| **11** | 6.60 | 0.00 | -0.20 | 25.00 | -0.20 |

| Case Number | Crack Length [mm] | ΔX [mm] | ΔY [mm] | Thickness [mm] | ΔZ [mm] |
|---|---|---|---|---|---|
| **82** | 7.20 | -0.20 | -0.20 | 24.90 | -0.20 |
| **83** | 7.20 | -0.20 | -0.20 | 25.00 | -0.20 |
| **84** | 7.20 | -0.20 | -0.20 | 25.10 | -0.20 |
| **85** | 7.20 | -0.20 | 0.00 | 24.90 | -0.20 |
| **86** | 7.20 | -0.20 | 0.00 | 25.00 | -0.20 |
| **87** | 7.20 | -0.20 | 0.00 | 25.10 | -0.20 |
| **88** | 7.20 | -0.20 | 0.20 | 24.90 | -0.20 |
| **89** | 7.20 | -0.20 | 0.20 | 25.00 | -0.20 |
| **90** | 7.20 | -0.20 | 0.20 | 25.10 | -0.20 |
| **91** | 7.20 | 0.00 | -0.20 | 24.90 | -0.20 |
| **92** | 7.20 | 0.00 | -0.20 | 25.00 | -0.20 |

Figure 4.15. A sample view of the DOE table

The results of the main effect analysis for different points at the crack front are given in Figure 4.16. - Figure 4.18. In the main effect analysis performed in MINITAB [44]. it is seen that the thickness has a linear effect and the Δx and Δy (right/left - down/up offset of the ellipsoid notch) have no significant effect on the SIF. The depth of the EDM notch, denoted by Δz, has a nearly linear effect on the results. It has also been observed that the crack size and the specimen thickness affect the results linearly.

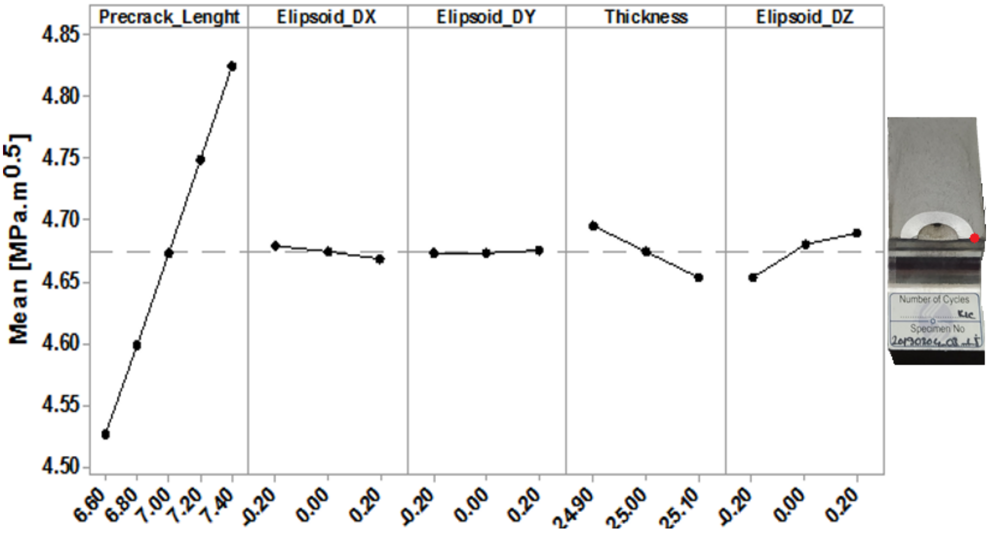

Figure 4.16. Effect of geometric variables on KI SIF (Right end)

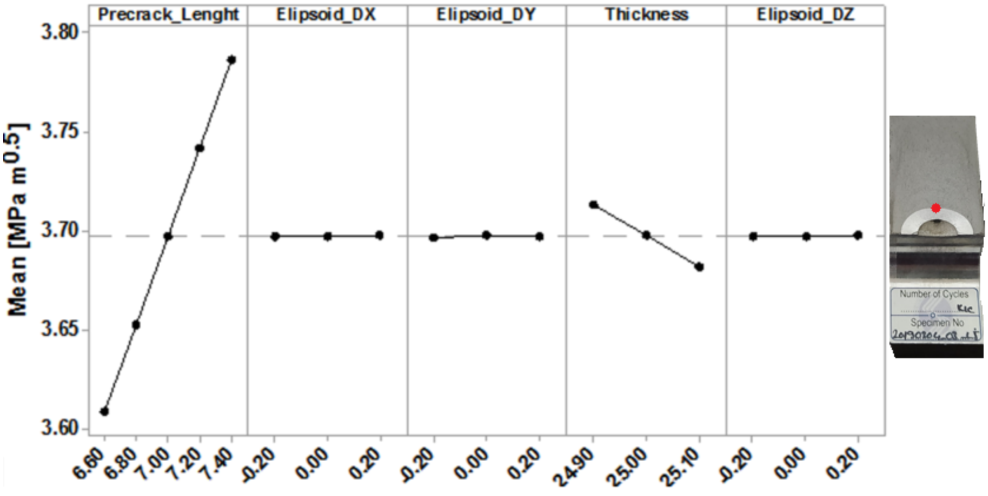

Figure 4.17. Effect of geometric variables on KI SIF (center)

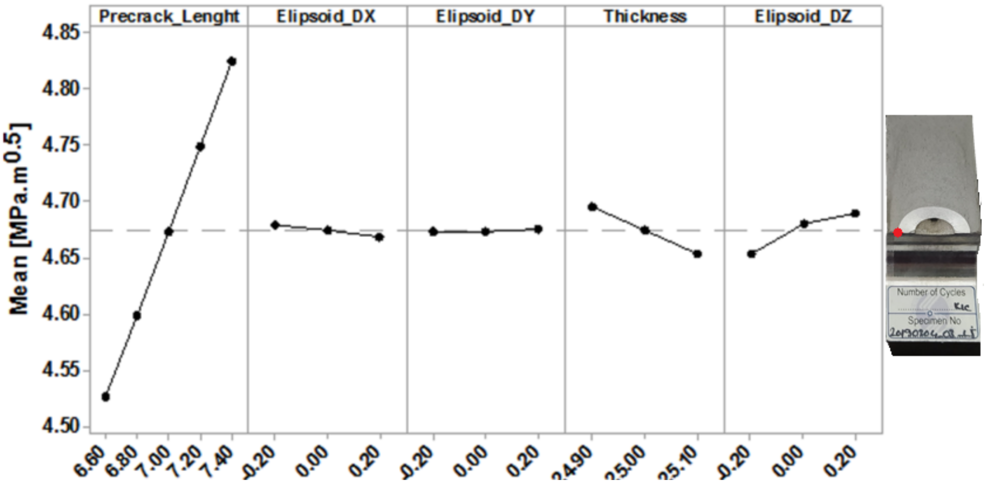

Figure 4.18. Effect of geometric variables on KI SIF (Left end)

The interaction effects of the variables are seen in Figure 4.19. Since the graphics at the right, left and midpoints on the crack front are very similar, the interaction effect is given only for the center point. According to Figure 4.19., the crack length and the thickness affect the results together. However, any interaction was not observed between Δx, Δy and Δz of the ellipsoid and the crack length.

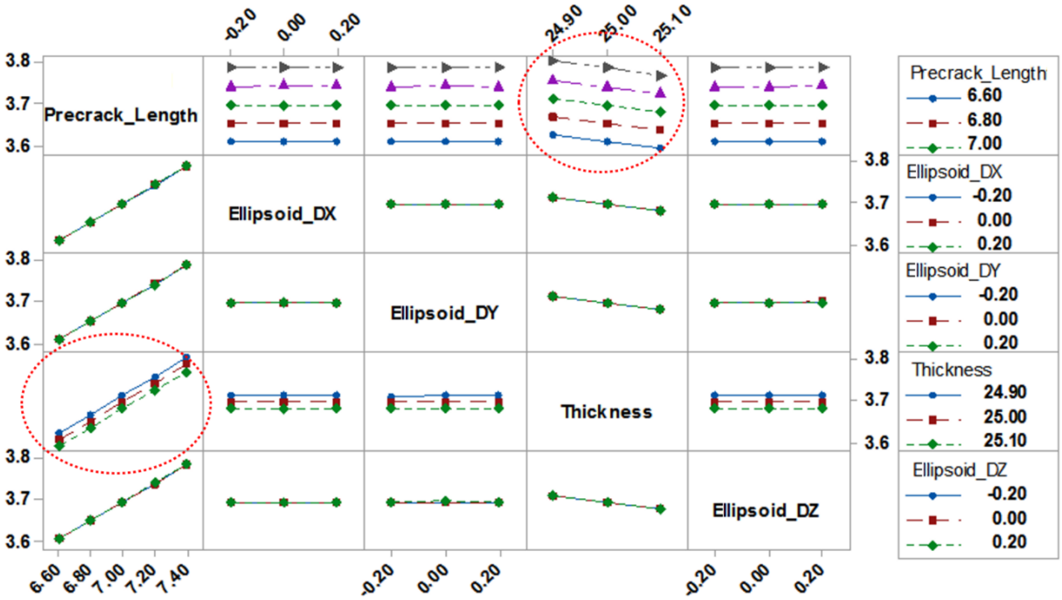

Figure 4.19. The interaction effect between the geometric variables on SIF (center of crack front)

The ineffective variables were removed and then the DOE table was updated with the crack dimensions given in Figure 4.20. Since the variable Δx, representing the horizontal eccentricity of the ellipsoid EDM notch, was removed from the equation, a separate transfer function for the right and left ends in the KI calculation is not needed, since the problem becomes symmetric with respect to the centerline of the specimen.

The values in the box indicated with different colors in Figure 4.20. show the cross combinations and include a total of 76 different cases after excluding the repeated cases. The boxes were created with reasonable crack lengths and depths by taking into account possible crack growth patterns and shapes obtained from the previous simulations. Considering three different factors of the Δz parameter for the ellipsoid notch, the DOE Analysis Matrix, therefore, contains a total of 228 analyses.

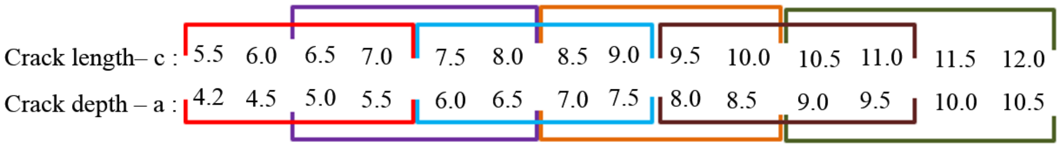

Figure 4.20. Combinations of the crack dimensions for DOE

From the results of the fracture analyses performed for 228 different cases, a multi-parameter regression analysis was conducted by using the values of crack depth and free surface points. The obtained transfer functions are given below.

$$KI_{edge} = 1.1458 - 248.3\,A + 69.66\,B - 94.7\,C + 17710\,A^2 - 264201\,C^2 \tag{4.1}$$

$$KI_{center} = 0.33277 + 52.214\,A - 20.119\,B + 7.86\,C + 36443\,C^2 \tag{4.2}$$

In the equations above, crack length, crack depth and ellipsoid ΔZ are expressed as A, B and C, respectively. Normal probability plots and histograms are given in Figure 4.21. for the transfer functions.

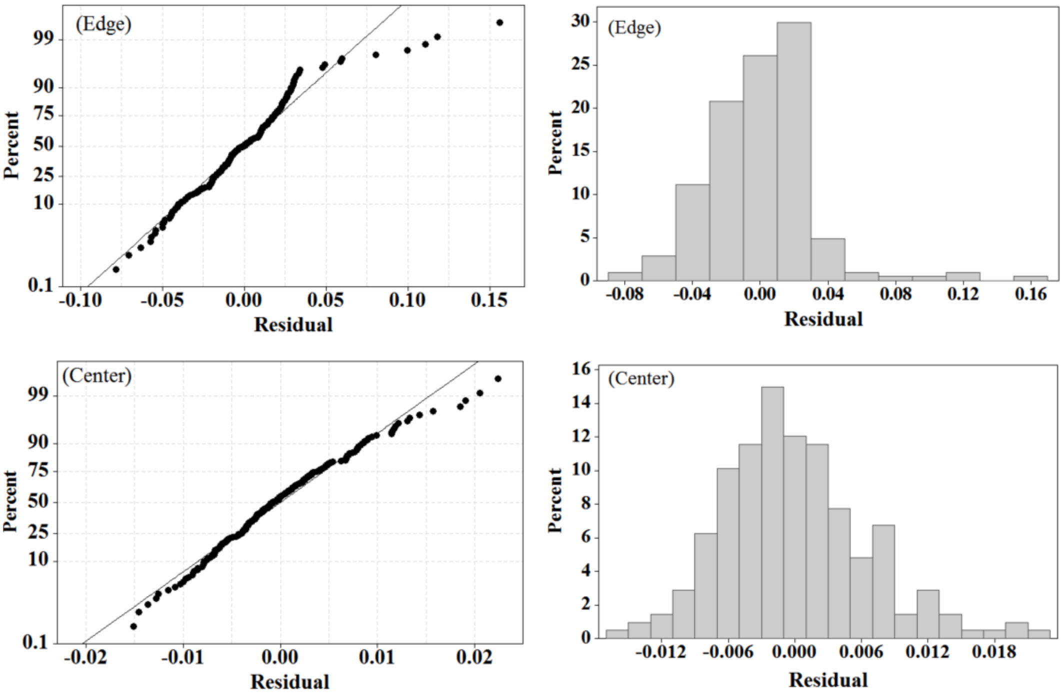

Figure 4.21. Residual plots for transfer functions

In order to verify the accuracy of the transfer functions given in Equations (4.1) and (4.2), independent crack propagation analyses were performed on the LJ specimen. The results are presented in Figure 4.22., and the crack growth curve obtained with the transfer function is plotted in blue. The red line shows the test result which was performed under constant amplitude loading (R = 0.1) with LJ specimen. Besides, another crack propagation simulation was performed explicitly using FCPAS, which calculates the SIFs in the crack front by using enriched element formulation.

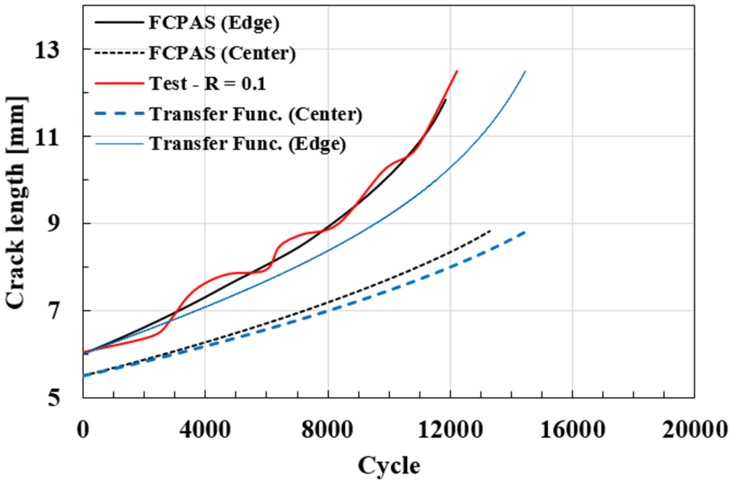

Figure 4.22. Crack propagation analysis by using transfer function and comparison with the test

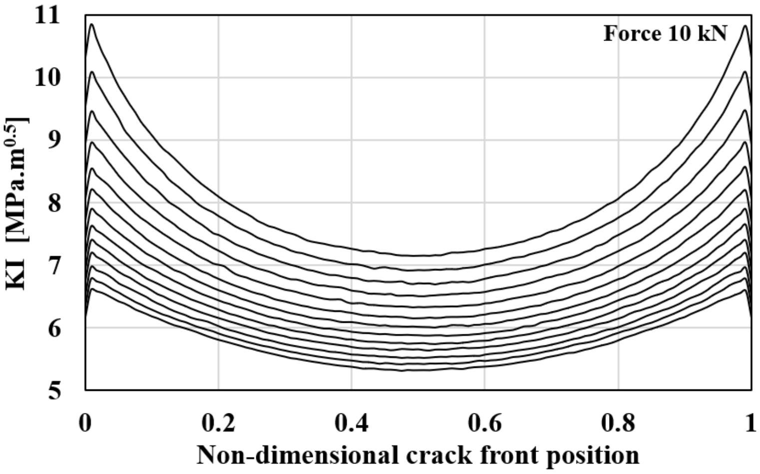

Figure 4.23. KI SIFs for LJ specimen calculated by FCPAS

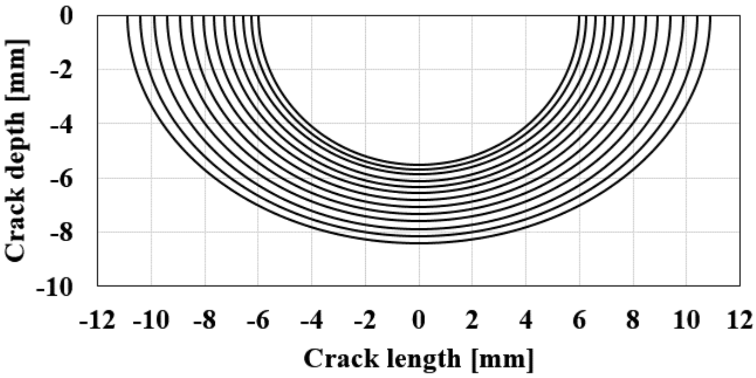

Figure 4.24. Crack profiles for LJ specimen obtained by FCPAS

SIFs and crack growth profiles can be seen in Figure 4.23. and Figure 4.24., respectively. As expected, SIFs are lower at the depth point of the crack than the edges. Based on the depth point, 5.5 MPa.m$^{0.5}$ SIF is generated under 10 kN for the initial crack. This means that crack propagates slowly under 10 kN. Considering this finding, higher load will be applied in the tests in 3D crack propagation tests.

### 4.2.4. 3-D crack growth tests under variable amplitude loading

#### 4.2.4.1. Fracture tests by using Lee James Specimen

Lee James Specimens were machined from 7075-T651 aluminum alloy with CNC milling in the dimensions mentioned in Section 4.1. Then, the notch was created by using the electro-discharge machining (EDM). Details of the notching process with EDM are given in Figure 4.25. EDM process can cause the change in the microstructure of the material which affects crack growth behavior but the boundaries of this change in microstructure do not reach precrack length. Therefore, this change does not affect fracture or crack growth in the test results.

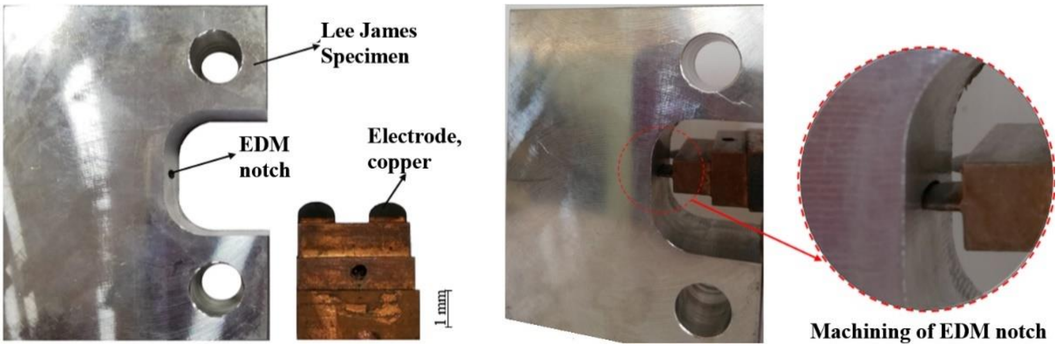

Figure 4.25. Creating ellipsoid notch on Lee James Specimen by using EDM

15 kN fatigue load was applied to generate the precrack around the ellipsoid notch. The precrack fatigue load was terminated as the crack length on the free surface monitored by the camera reaches around 1.5 mm. Then, the fracture toughness test was done under the static tensile load of 0.65 kN/s. The dimensions of the notch created by EDM were checked on fracture surfaces. Details of the fracture toughness tests are given in Table 4.3. Fracture toughness results could not be obtained from the last two

tests indicated in gray background in Table 4.3. Since the crack size is very small, the required load for fracture was quite high in the 20190304_05 test. For this reason, fracture load was not applied to avoid any damage to the test machine and apparatus.

Table 4.3. Fracture toughness tests with Lee James Specimen

| Specimen Name | Stress Ratio for precrack R | Max. Load for Precrack (kN) | Crack depth (mm) | Crack length (mm) | Force rate (kN/s) | Fracture Load (kN) |
|---|---|---|---|---|---|---|
| 20190220_01 | 0.1 | 15 | 28.44 | 5.79 | 0.65 | 56.461 |
| 20190222_01 | 0.1 | 15 | 30.8 | 8.59 | 0.65 | 35.332 |
| 20190226_01 | 0.1 | 15 | 29.82 | 6.865 | 0.65 | 41.023 |
| 20190304_01 | 0.1 | 15 | 28.66 | 6.63 | 0.65 | 48.374 |
| 20190304_02 | 0.1 | 15 | 31.35 | 9.845 | 0.65 | 30.538 |
| 20190304_03 | 0.1 | 15 | 29.94 | 6.615 | 0.65 | 41.152 |
| 20190304_04 | 0.1 | 15 | 31 | 9.26 | 0.65 | 31.979 |
| 20190304_05 | 0.1 | 15 | 27.81 | 4.36 | 0.65 | NaN |
| 20190304_06 | 0.1 | 15 | 33 | 9.91 | 0.65 | NaN |

Another finding was also noticed other than fracture load from the tests given in Table 4.3. Since there is three-dimensional crack propagation in Lee James specimen, it is not possible to monitor the crack propagation along with the depth point during the test. To monitor this, the depths and surface lengths of the cracks were measured by using pixel sizes from the fracture surface pictures and the data were shown in Figure 4.26. after the tests. It was observed that the dimensions in the surface and depth directions of the crack were related. A linear equation with a high $R^2$ between the crack depth and the crack length is given in Figure 4.26.

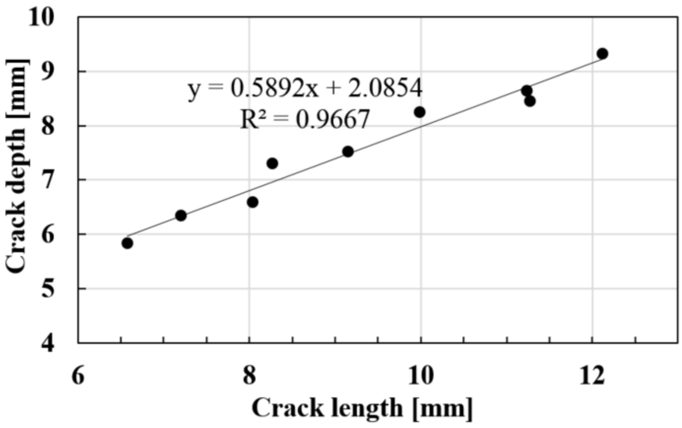

Figure 4.26. The relation between crack depth and length

Since there is no test standard for three-dimensional crack propagation and an empirical formula similar to that used for the CT specimen was used in calculating the SIFs, it was investigated if the fracture load obtained in the experiments for LJ specimen can be calculated computationally. Fracture analyses were performed by employing FCPAS and using the crack dimensions from the experiments given in Table 4.3. The SIFs distributions obtained from analyses are given in Figure 4.27.

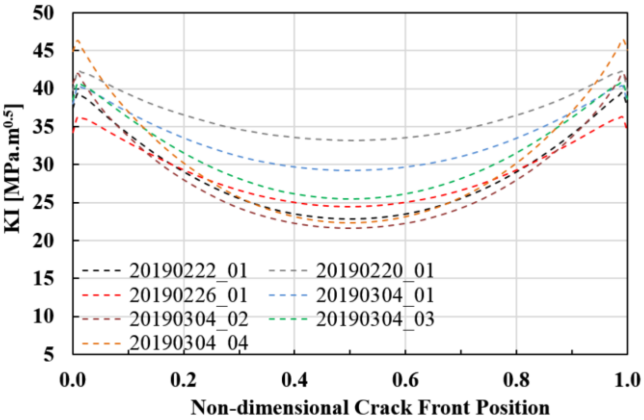

Figure 4.27. KI SIF distribution for different surface crack size

As can be seen from Figure 4.27., in the analyses under the fracture loads obtained from the experiments, the SIFs were calculated around 35-40 MPa.m$^{0.5}$ at the free surface points. The difference in SIF between the midpoint and the edge was greater in smaller cracks. This means that there is a constraint effect on fracture in the depth direction of the crack. As the crack size increases, constraint effect decreases, and the variability of the SIFs along the crack front decreases. The specimens used in the tests are shown in Figure 4.28.

Figure 4.28. Lee James specimen used in fracture toughness tests

In Figure 4.28., the LJ specimens used in fracture tests are shown in an increasing order of fatigue pre-crack sizes from left to right. In the three specimens on the right, fast fracture surfaces are perpendicular to the loading direction as expected but if the first three specimens on the left are carefully examined, unexpected fracture surfaces forming under mode-I loading can be seen. To investigate the underlying mechanics- and materials-related mechanisms for the fast fracture surface deflection seen in the Figure 4.28., a stress-based approach is performed. The findings can be explained with the material properties for differently oriented cracks in the same material. To carry out this, principal stresses around the free-surface crack tips for the different crack sizes in the tested specimens are analyzed by finite element method. In Figure 4.29., the principal stress distributions around the crack tip obtained from finite element analysis are given for surface crack size 2c = 14.42 mm. In this case, the distance of one-sided pre-crack length from the edge of the ellipsoid notch is 2.21 mm, which is a small to mid-level FCG increment. Since the fatigue precrack is quite small in these specimens, the magnitude of the second principal stress in the crack tip is close to its primary principal stress. Although no external loading is applied in the thickness direction of the specimen, a constraint effect is generated by the Poisson’s ratio and deformation kinematics of the solid material surrounding the ellipsoid notch. The crack surfaces through the thickness and the constraint effect cause the high-magnitude second principal stress for short surface cracks. According to the scheme given in Figure 4.29., a crack surface propagating in the described direction is the S-L direction. As can be found from İriç and Ayhan's study, fracture toughness in L-T direction is around 29 MPa-m$^{0.5}$, and in S-L direction is around 25 MPa-m$^{0.5}$ [57]. Also, same findings has been reported by Campell F.C as 32 MPa-m$^{0.5}$ in L-T direction and 21 MPa-m$^{0.5}$ in S-L direction [58]. Therefore, the crack is oriented perpendicular to the initial pre-crack (S-L direction) by the second principal stress. This explains that if the required tensile component of the stress for an S-L-direction crack is present, the crack can propagate in the S-L direction.

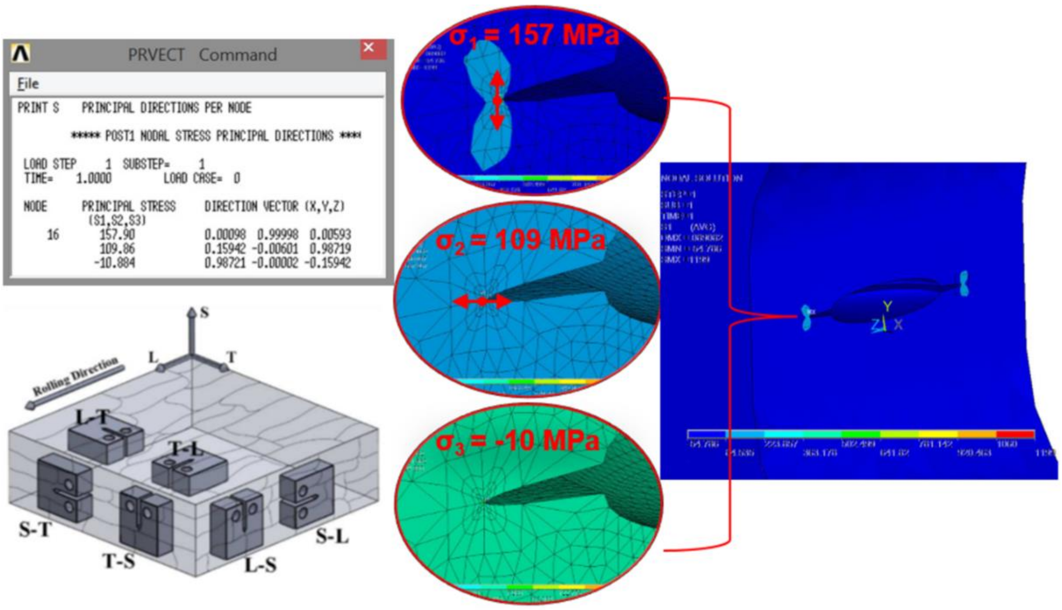

```
PRINT S    PRINCIPAL DIRECTIONS PER NODE

        ***** POST1 NODAL STRESS PRINCIPAL DIRECTIONS ****

 LOAD STEP     1  SUBSTEP=     1
 TIME=    1.0000         LOAD CASE=  0

 NODE       PRINCIPAL STRESS     DIRECTION VECTOR (X,Y,Z)
              (S1,S2,S3)
    16         157.90            0.00098  0.99998  0.00593
               109.86            0.15942 -0.00601  0.98719
              -10.884            0.98721 -0.00002 -0.15942
```

(a) (b)

Figure 4.29. a) Crack growth according to the rolling direction, b) principal stress distributions

The finite element analysis given in Figure 4.29. was repeated for all crack lengths in the experiments and the principal stress values were obtained. For all specimens and their fatigue pre-crack lengths tested under monotonically increasing loads, the ratio of the first and the second principal stress is plotted in Figure 4.30. If the ratio of the first and the second principal stress is around 1.2 or less, fast fracture surfaces are formed in the parallel direction to the mode-I loading.  As the crack length increases, the first principal stress dominates, and fracture surfaces are formed in the mode-I opening direction, i.e., L-T direction.

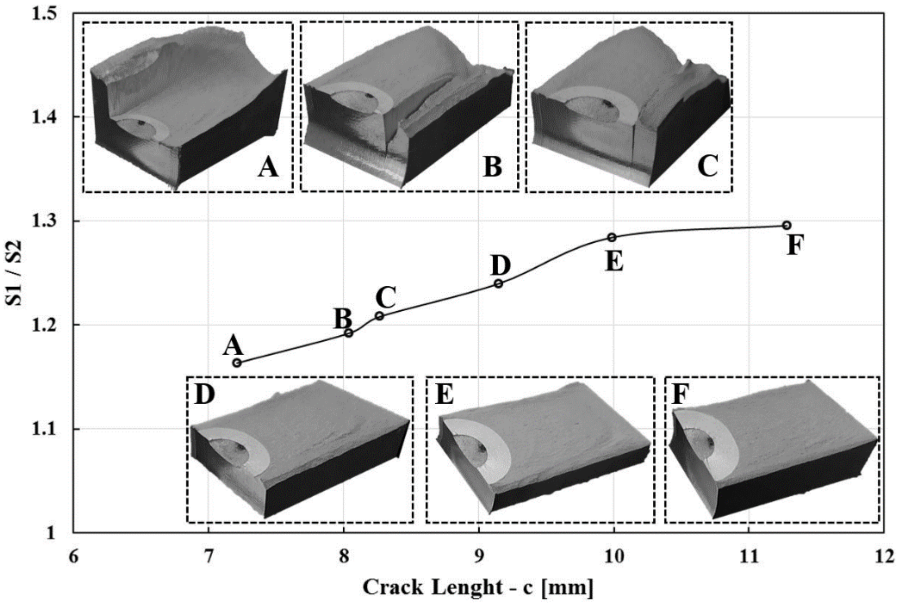

Figure 4.30. Change of the ratio of principal stresses (S1/S2) depending on crack sizes

### 4.2.4.2. Fatigue crack growth tests under constant amplitude loading by using Lee James Specimen

A total of 49 tests were performed with Lee James specimen under constant amplitude (R = 0.1, 0.5, 0.8) and random (spectrum) loading (SP1-SP2-SP3). A similar test setup to that given in Section 3 was used for three-dimensional crack growth tests. The numbers of tests are given in Table 4.4. During these tests, two crack tips on the specimen were monitored with a single camera. In Figure 4.31., the experimental setup and screenshots of the computer screen taken during the tests are presented. Screenshots were recorded periodically in order to plot the cycle vs. crack length curves.

Table 4.4. Numbers of 3-D fatigue crack growth tests

| Test | Count | Specimen Type |
|---|---|---|
| Fatigue crack growth tests under constant amplitude – R = 0.1 | 5 | LJ |
| Fatigue crack growth tests under constant amplitude – R = 0.5 | 5 | LJ |
| Fatigue crack growth tests under constant amplitude – R = 0.8 | 9 | LJ |
| Fatigue crack growth under random loading - LJ-SP1 | 10 | LJ |
| Fatigue crack growth under random loading - LJ-SP2 | 10 | LJ |
| Fatigue crack growth under random loading -LJ-SP3 | 10 | LJ |

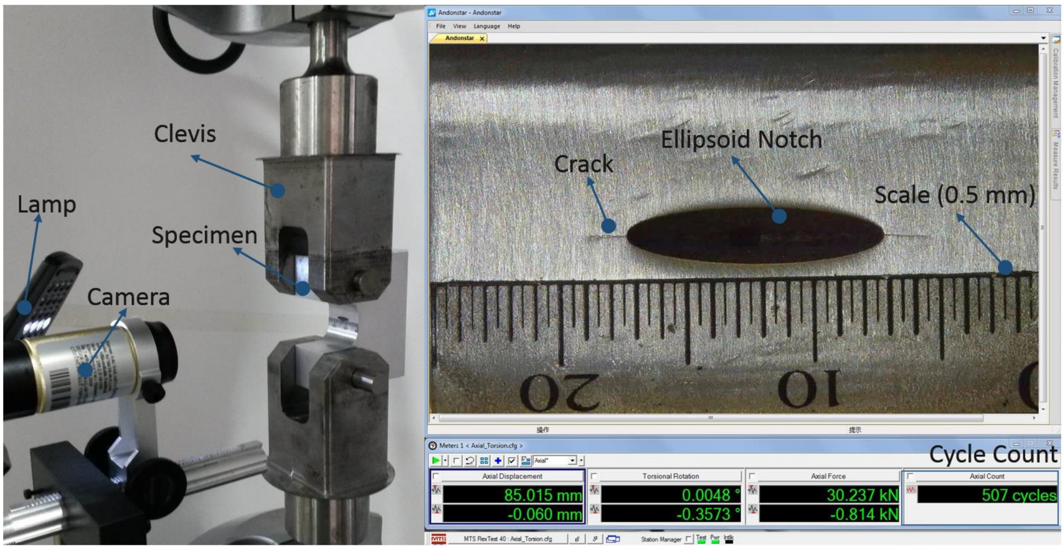

Figure 4.31. Test setup for 3-D fatigue crack growth and the screenshot [59]

Table 4.5. 3-D fatigue crack growth tests under constant amplitude

| | | Precrack | | | Fatigue crack growth | | |
|---|---|---|---|---|---|---|---|
| Specimen Name | Specimen Type | Stress Ratio for precrack R | Max. Load for Precrack (kN) | $a_{(avg)}$ (mm) | Stress Ratio for FCG R | Max. Load for FCG (kN) | Cycle |
| 20191011_01 | LJ | 0.1 | 12.4 | 5.805 | 0.1 | 15.5 | 12224 |
| 20191011_02 | LJ | 0.1 | 12.4 | 6.530 | 0.1 | 15.5 | 10978 |
| 20191014_01 | LJ | 0.1 | 12.4 | 6.125 | 0.1 | 15.5 | 12487 |
| 20191014_02 | LJ | 0.1 | 12.4 | 6.006 | 0.1 | 15.5 | 14698 |
| 20191015_01 | LJ | 0.1 | 12.4 | 6.079 | 0.1 | 15.5 | 14176 |
| 20191015_02 | LJ | 0.1 | 13 | 5.883 | 0.5 | 17 | 34296 |
| 20191016_01 | LJ | 0.1 | 13 | 6.305 | 0.5 | 20 | 20218 |
| 20191016_02 | LJ | 0.1 | 13 | 5.963 | 0.5 | 20 | 23200 |
| 20191017_02 | LJ | 0.1 | 13 | 6.110 | 0.5 | 20 | 18321 |
| 20191025_01 | LJ | 0.1 | 13 | 6.255 | 0.5 | 20 | 18298 |
| 20191018_01 | LJ | 0.1 | 17 | 7.440 | 0.8 | 30 | 33246 |
| 20191022_01 | LJ | 0.1 | 17 | 6.310 | 0.8 | 32 | 51679 |
| 20191023_01 | LJ | 0.1 | 17 | 6.215 | 0.8 | 32 | 44590 |
| 20191024_02 | LJ | 0.1 | 17 | 6.243 | 0.8 | 32 | 56501 |
| 20191101_02 | LJ | 0.1 | 17 | 7.920 | 0.8 | 32 | 22930 |
| 20191111_01 | LJ | 0.1 | 17 | 6.243 | 0.8 | 32 | 54388 |
| 20191113_01 | LJ | 0.1 | 17 | 7.920 | 0.8 | 32 | 53222 |
| 20191113_02 | LJ | 0.1 | 17 | 7.920 | 0.8 | 32 | 55623 |
| 20191203_01 | LJ | 0.1 | 17 | 7.920 | 0.8 | 32 | 64835 |
| 20191204_01 | LJ | 0.1 | 17 | 6.405 | 0.8 | 32 | 74322 |

The fatigue crack growth curves of the performed tests are given in Figure 4.32. Also, fracture surfaces formed under R = 0.1, 0.5 and 0.8 are given in Figure 4.33. -Figure 4.35., respectively. The crack surface did not occur symmetrically in some of the tests, especially under R = 0.8. The specimens exhibiting high anti-symmetry at the crack front were not used and these experiments were repeated. Details about the problem of anti-symmetry on the crack front will be explained in Section 4.2.4.4.

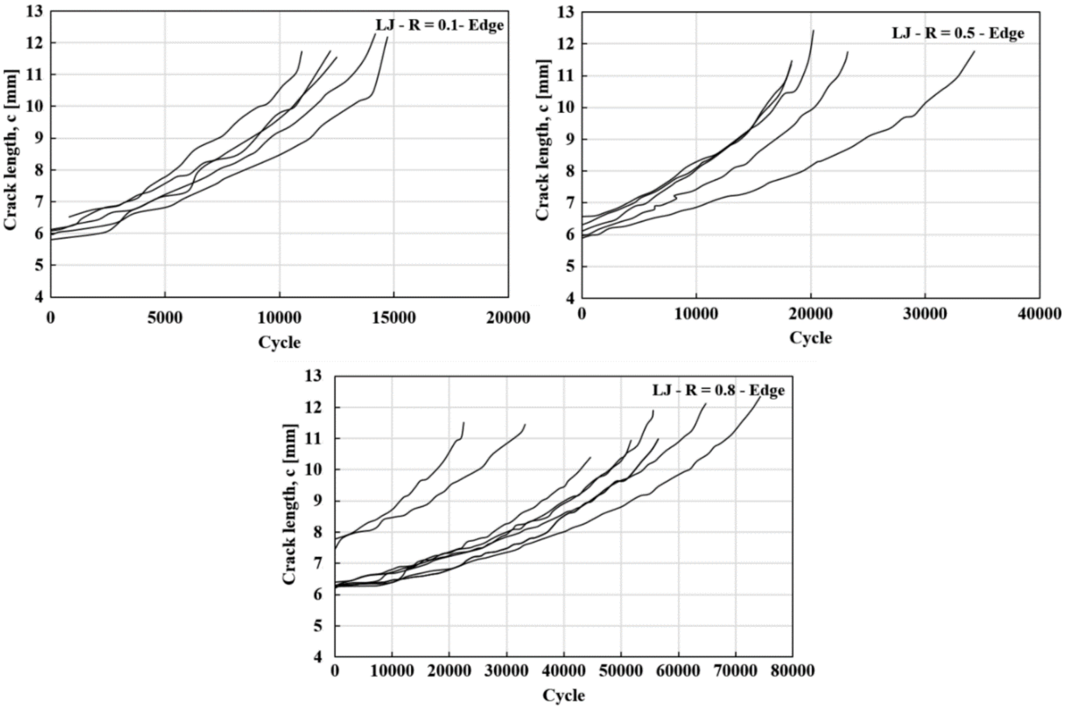

Figure 4.32. Curves obtained from constant amplitude 3-D fatigue crack growth tests

Figure 4.33. Fracture surfaces from 3-D fatigue crack growth tests under R= 0.1 constant amplitude

Figure 4.34. Fracture surfaces from 3-D fatigue crack growth tests under R= 0.5 constant amplitude

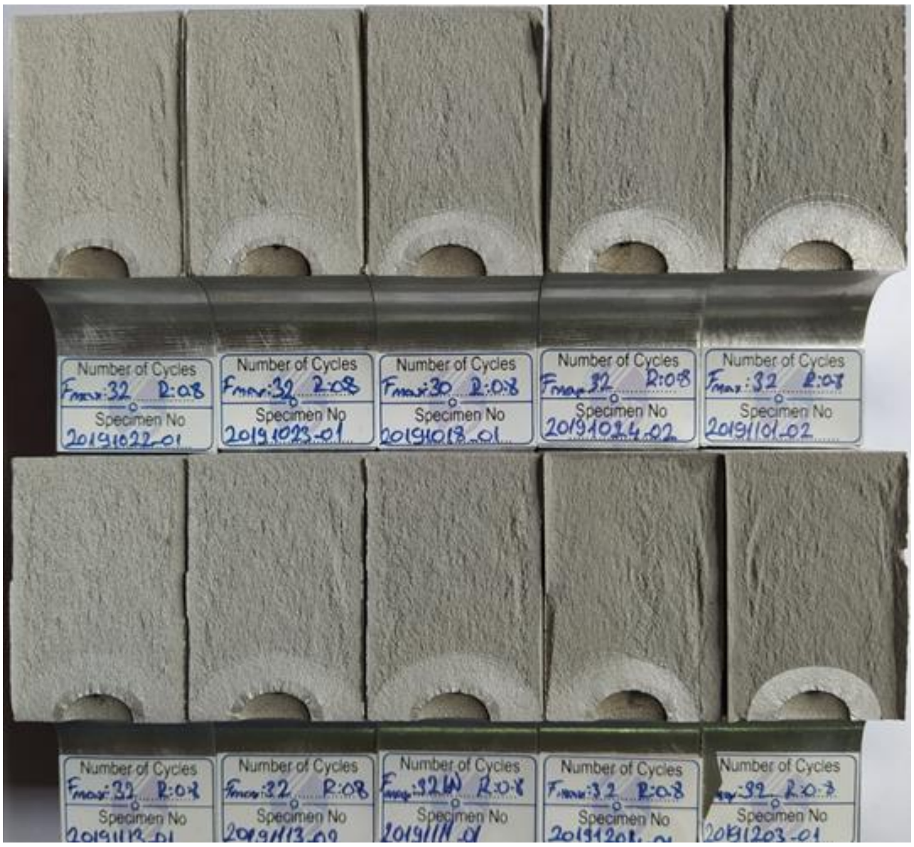

Figure 4.35. Fracture surfaces from 3-D fatigue crack growth tests under R= 0.8 constant amplitude

The scatter of the experimental results are compared with a study in the literature that experimentally investigated the crack propagation under constant amplitude loading by using aluminum 7075 alloy. [60]. Crack growth curves of the repeated tests conducted by the reference are given in Figure 4.36a. Figure 4.36b. was the experimental results of the tests with LJ specimens under R = 0.1 conducted in this dissertation as described in the previous sections. There is no similarity between Figure 4.36a-b. in terms of loading conditions and specimen type. The two graphs are given together only to show that the scatters are within reasonable boundaries. In the reference study [60], the ratio of the minimum number of cycles to the maximum is 0.72. This value is 0.89 in the experimental study presented in this dissertation. In other words, the scattering in this study is slightly less than the scattering obtained in the compared study.

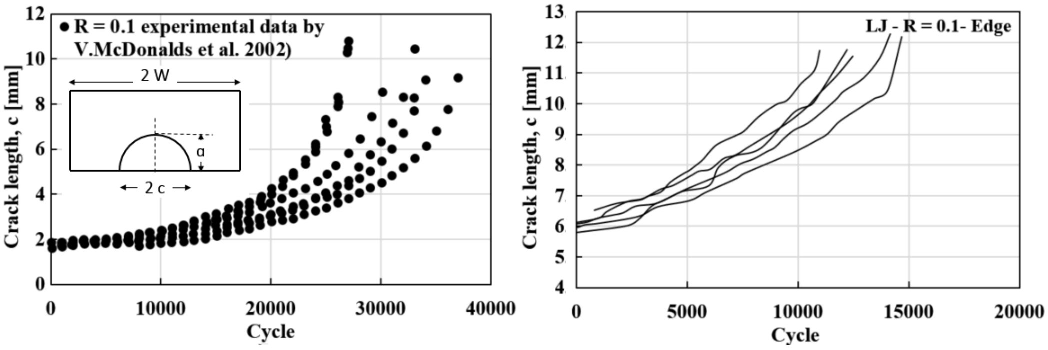

(a) (b)

Figure 4.36. Comparison of the scatters from the tests under R = 0.1 with the reference study [60]

#### 4.2.4.3. 3-D Fatigue crack growth tests under random loading

After constant amplitude loading tests, random loading conditions were applied on the LJ specimen. As in the two-dimensional crack propagation tests using the CT specimen, two spectrums (SP1 and SP2) were used for random loading experiments, and another spectrum (SP3) was applied for validation. First, SP1, given in Section 3.5, was scaled by a factor of 3.18 for the LJ specimen, yielding a maximum load of 35 kN. The spectrum (SP1) is presented in Figure 4.37. Details of tests performed with this spectrum are also given in Table 4.6.

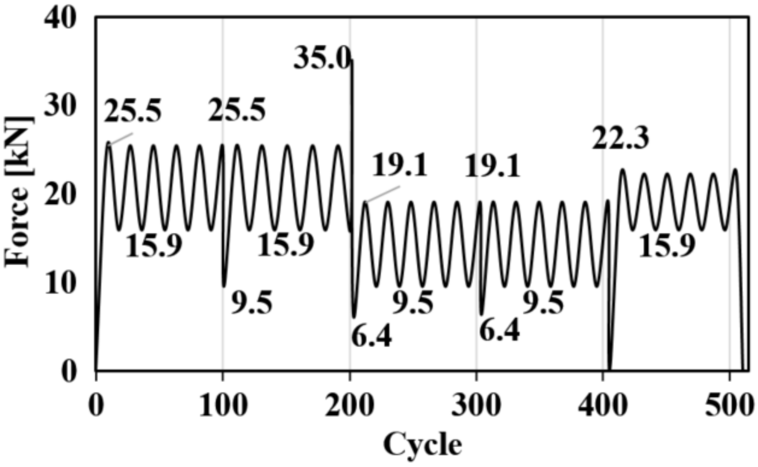

Figure 4.37. Spectrum-1 for 3-D fatigue crack growth

Table 4.6. Details of the 3-D FCG tests performed under Spectrum-1

| | | Precrack | | | Fatigure crack growth | | |
|---|---|---|---|---|---|---|---|
| Specimen Name | Specimen Type | Stress Ratio for precrack R | Max. Load for Precrack (kN) | $a_{(avg)}$ (mm) | Spectrum | Max. Load for FCG (kN) | Cycle |
| 20191030_01 | LJ | 0.1 | 17 | 6.305 | Spectrum-1 | 35 | 40128 |
| 20191030_02 | LJ | 0.1 | 17 | 6.090 | Spectrum-1 | 35 | 42650 |
| 20191031_01 | LJ | 0.1 | 17 | 6.665 | Spectrum-1 | 35 | 37044 |
| 20191031_02 | LJ | 0.1 | 17 | 6.920 | Spectrum-1 | 35 | 32024 |
| 20191101_01 | LJ | 0.1 | 17 | 6.670 | Spectrum-1 | 35 | 35022 |
| 20200619_01 | LJ | 0.1 | 17 | 6.160 | Spectrum-1 | 35 | 44638 |
| 20200622_01 | LJ | 0.1 | 17 | 6.285 | Spectrum-1 | 35 | 47104 |
| 20200622_02 | LJ | 0.1 | 17 | 6.390 | Spectrum-1 | 35 | 43608 |
| 20200623_01 | LJ | 0.1 | 17 | 6.318 | Spectrum-1 | 35 | 43192 |
| 20200623_02 | LJ | 0.1 | 17 | 5.953 | Spectrum-1 | 35 | 53266 |

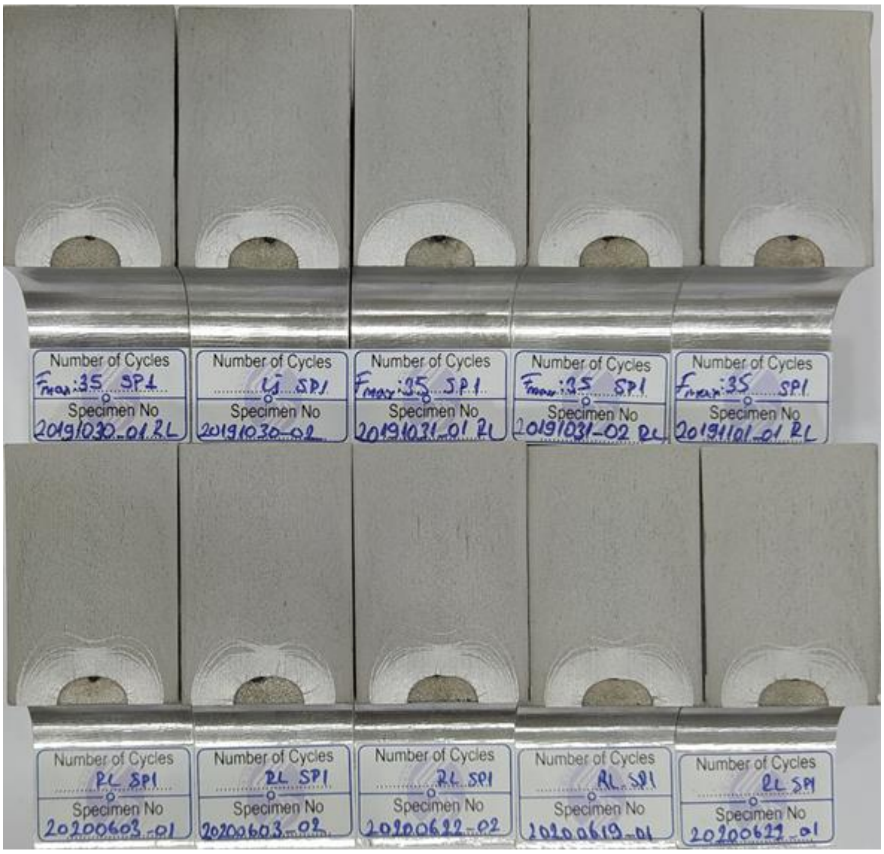

Figure 4.38. Fracture surfaces occurred under Spectrum-1 loading for 3-D FCG

The fracture surfaces generated by Spectrum-1 are shown in Figure 4.38. Crack propagation curves obtained from the tests under Spectrum-1 are given in Figure 4.39., in which results from specimens with different initial crack lengths are given as separate curves. Since it was not possible to monitor the crack depths during the test, they were measured from the fracture surface after the tests and are presented in a separate graph. The size of the crack depth is only given for the last step since overload striation markings could not be seen clearly around the precrack.

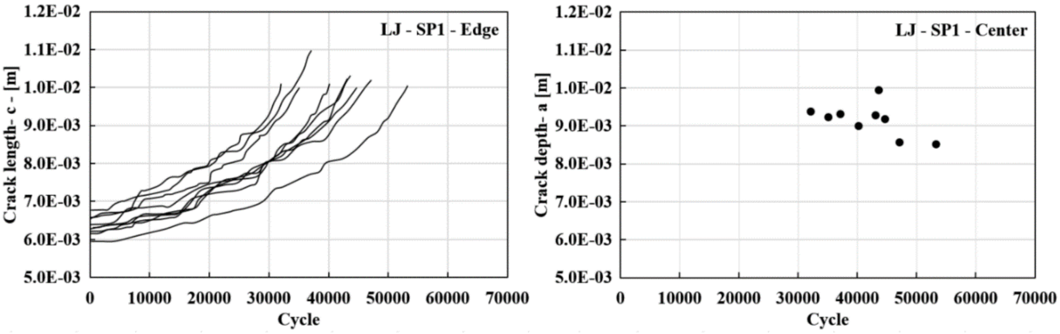

Figure 4.39. Crack growth curves obtained from 3-D FCG tests under Spectrum-1

In Section 3.5, a partial FALSTAFF (Spectrum-2) spectrum was explained for CT specimen. This spectrum was used repeatedly in the tests and simulations until the end of the crack growth life. It was decided to scale this spectrum and use it in three-dimensional crack propagation tests. Since the critical load for LJ specimen is higher than CT specimen, the maximum load value of 11 kN for CT specimen in the Spectrum-2 was scaled to 35 kN for LJ specimen. Thus, reasonable crack growth life cycles were obtained for 3-D crack growth tests. The applied Spectrum-2 load profile to LJ specimen is shown in Figure 4.40.

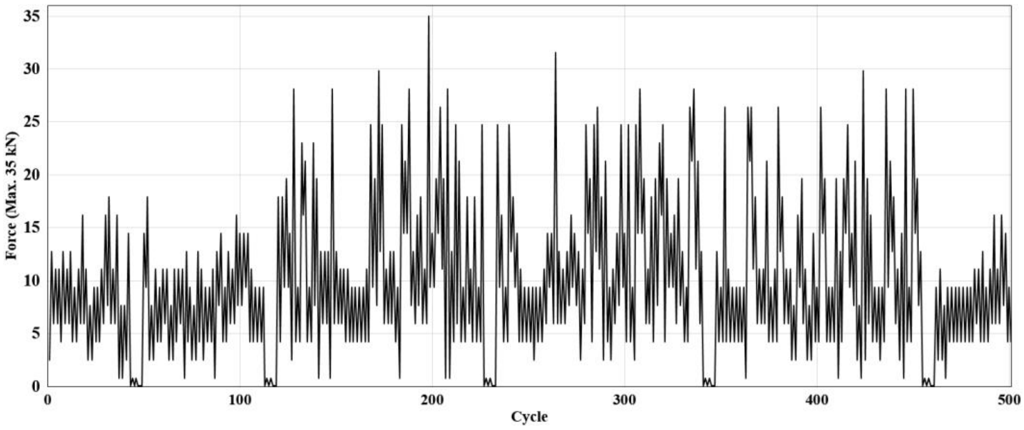

Figure 4.40. Partial FALSTAFF (Spectrum-2) loading profiles for LJ Specimen

Table 4.7. Details of the 3-D FCG tests performed under Spectrum-2

| | | Precrack | | | Fatigure crack growth | | |
|---|---|---|---|---|---|---|---|
| Specimen Name | Specimen Type | Stress Ratio for precrack R | Max. Load for Precrack (kN) | $a_{(avg)}$ (mm) | Spectrum | Max. Load for FCG (kN) | Cycle |
| 20200624_02 | LJ | 0.1 | 17 | 6.205 | Spectrum-2 | 35 | 37968 |
| 20200625_01 | LJ | 0.1 | 17 | 6.163 | Spectrum-2 | 35 | 35626 |
| 20200625_02 | LJ | 0.1 | 17 | 6.720 | Spectrum-2 | 35 | 28657 |
| 20200626_01 | LJ | 0.1 | 17 | 6.100 | Spectrum-2 | 35 | 33826 |
| 20200626_02 | LJ | 0.1 | 17 | 5.886 | Spectrum-2 | 35 | 37436 |
| 20200627_01 | LJ | 0.1 | 17 | 5.916 | Spectrum-2 | 35 | 38536 |
| 20200629_01 | LJ | 0.1 | 17 | 6.003 | Spectrum-2 | 35 | 35169 |
| 20200630_01 | LJ | 0.1 | 17 | 5.694 | Spectrum-2 | 35 | 42209 |
| 20200630_02 | LJ | 0.1 | 17 | 5.948 | Spectrum-2 | 35 | 37508 |
| 20200701_01 | LJ | 0.1 | 17 | 5.823 | Spectrum-2 | 35 | 39718 |

The details of the tests performed under Spectrum-2 are given in Table 4.7. The numbers of life cycles and initial crack lengths show that the tests are repeatable.

The fracture surfaces obtained under fatigue crack growth tests using Spectrum-2 loading are shown in Figure 4.41. Crack propagation curves obtained from the tests under Spectrum-2 are presented in Figure 4.42., in terms of crack surface lengths and crack depths in separate plots.

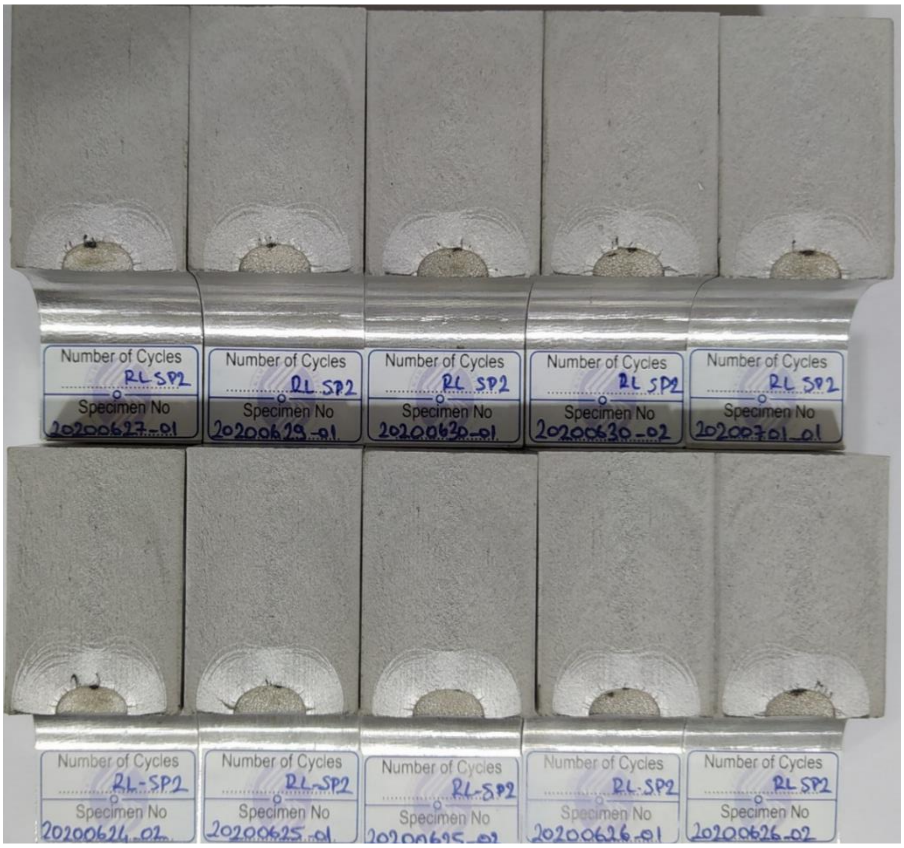

Figure 4.41. Fracture surfaces occurred under Spectrum-2 loading for 3-D FCG

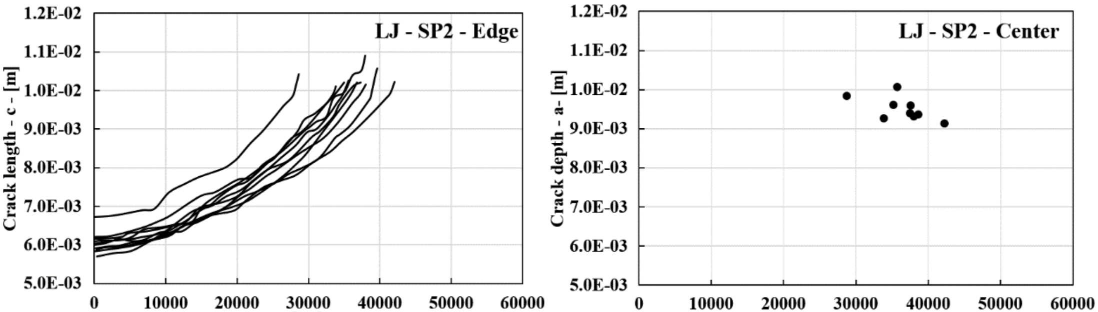

Figure 4.42. Crack growth curves obtained from 3-D FCG tests under Spectrum-2

#### 4.2.4.4. Investigation of the non-symmetry in crack front

In many tests performed with Lee James specimen, it was observed that the crack size on both edges of the notch was not symmetrical in the front view. Thereupon, the angular/axial adjustment of the test device, the geometry of the specimen and the loading apparatus were checked, and it was realized that the problem was not caused by these factors. A similar problem had also been observed in CT specimens before. This problem was investigated in detail in our study titled *"Effects of microstructural through-thickness non-uniformity and crack size on fatigue crack propagation and fracture of rolled Al-7075 alloy"* which has been published in Fatigue & Fracture of Engineering Materials & Structures, and the explanations are presented below [59].

In two or three-dimensional crack propagation tests, it was observed that both crack tips in a specimen were not symmetrical and that the striation is discontinuous along the crack front. In some regions near the center of the specimen, the crack did not propagate as much as the side regions, and thus the symmetry of the crack tips on both surfaces is disrupted. In addition, there was a difference in the color of the fast fracture surface at the point where the crack propagation lagged. A non-symmetry crack front obtained in 3-D FCG tests and a close view of the lagging is given in Figure 4.43. Furthermore, the difference in the color of the fast fracture surface at the lagging region, which has a darker appearance, is shown in Figure 4.44.

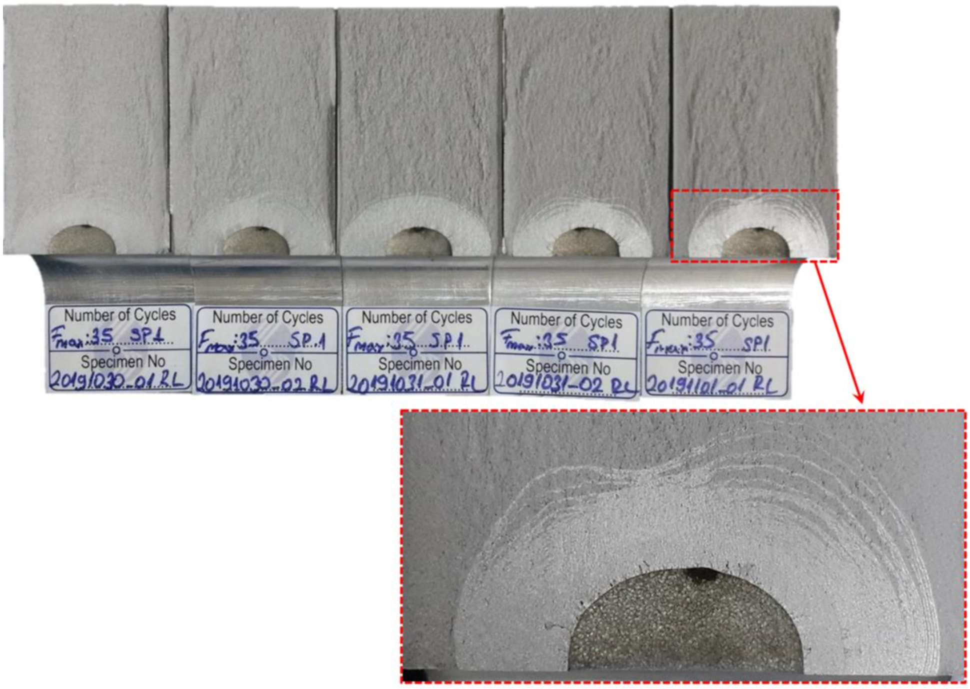

Figure 4.43. Tops views of 3-D crack fronts and a close-up view of FCG region

The material Al 7075-T651 is supplied as a plate with a thickness of 30 mm. The thickness was decreased to 25 mm by milling from both sides. If the plate was machined in equal amounts from both surfaces (2.5 mm from each), it was seen that the dark color on the fast fracture surface was at the center of the specimen, and if it was machined 5 mm from one side or unequally from both sides, the dark color was seen closer to the machined side. The effect of machining is observed in three LJ specimens in Figure 4.44. One of them (in the middle) was machined from both surfaces equally and the others were machined only from one side. As can be seen from the specimen in the middle, when thickness-reduction machining is performed equally from both sides, the surface crack grows symmetrically.

Figure 4.44. Fracture surfaces of CT and LJ specimens with FCG lagging

In the regions of darker color, higher surface roughness is expected. Roughness measurement on fast fracture surfaces in specimen thickness direction confirms that the darker color band is not just a visual effect. Roughness measurements were taken along the thickness of the specimen CT-4 in Figure 4.44. According to roughness measurement, the average surface roughness downstream of the lagged crack front region is 3-5 times higher than the other regions, presented in Figure 4.45.

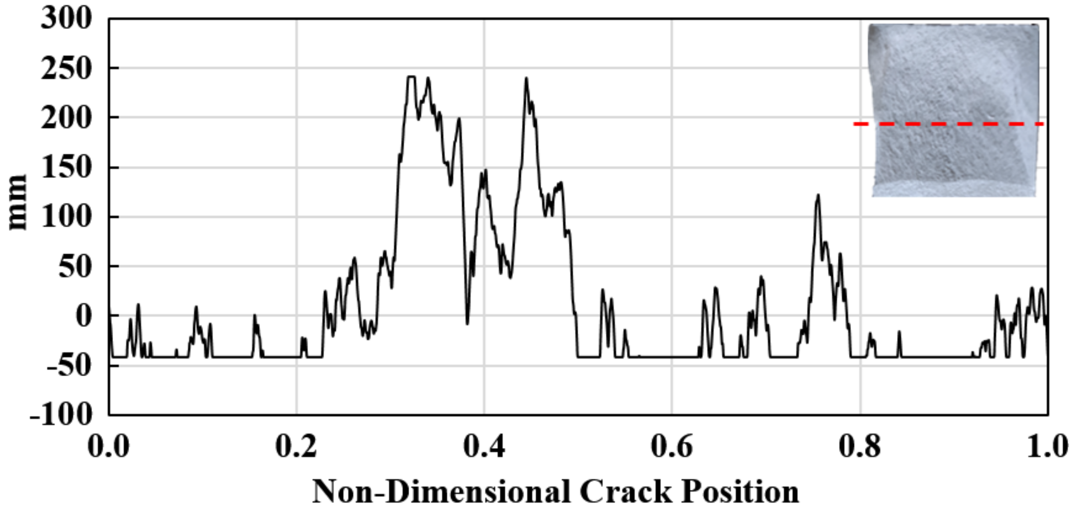

Figure 4.45. Surface roughness measurements along the thickness of CT specimen (CT-4)

Based on all these findings that the non-symmetry might be caused by the non-uniformity of the material grains in the thickness direction. Optical microscope and scanning electron microscope (SEM) images were also taken to investigate the material. The surface was polished then etched about 20 seconds by using Keller solution (5% HF 10% $H_2SO_4$ 85% $H_2O$). The optical microscope images in Figure 4.46. and Figure 4.47. and the SEM image in Figure 4.48. show that the grains in the lagged region did not flatten as much as it was in the side regions of the specimen. It is seen that the grains flattened at the surfaces were parallel to the rolling direction, but the desired orientation cannot be achieved as much in the center. This makes crack propagation difficult in the center part of the specimen compared to side regions along with the thickness of the specimen.

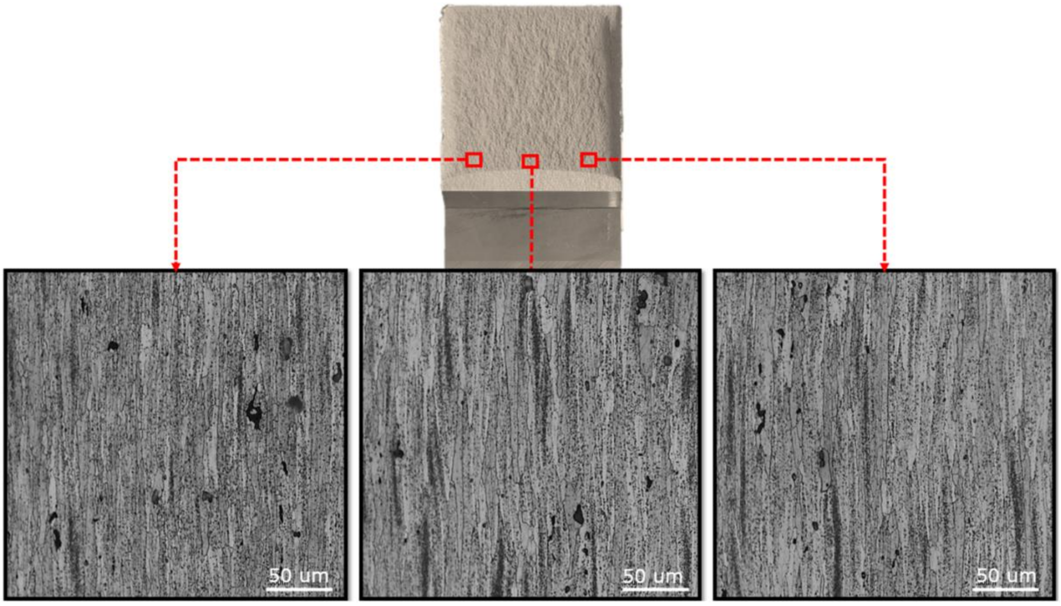

Figure 4.46. Optical microscopy images of marked regions of the 1st CT specimen in Figure 4.44

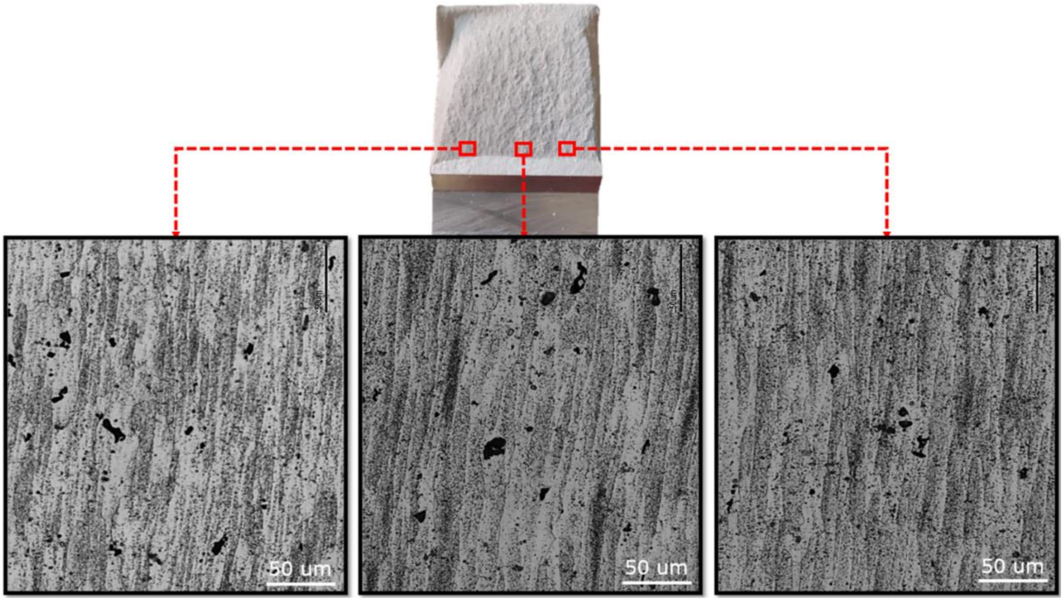

Figure 4.47. Optical microscopy images of marked regions of the 3rd CT specimen in Figure 4.44

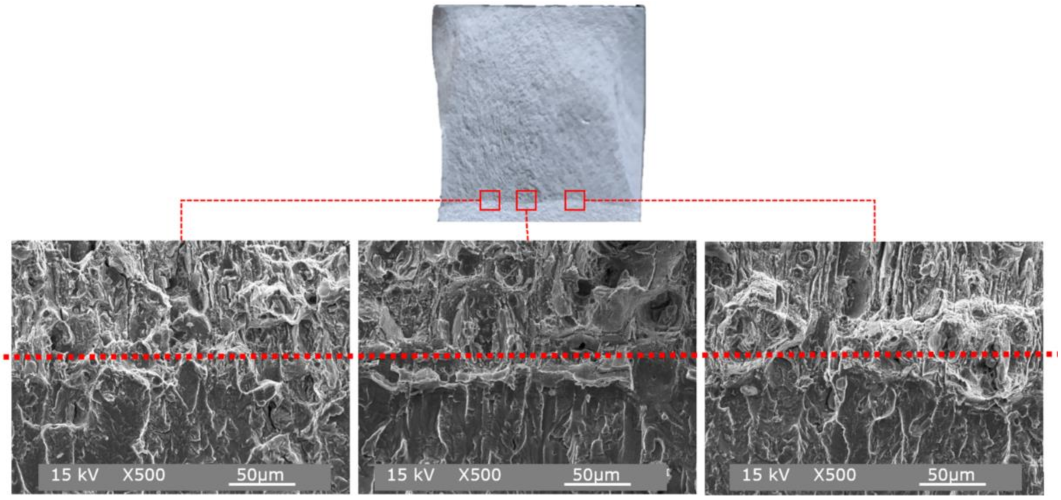

Figure 4.48. SEM images of different zones of the crack front of CT specimen (CT-4).

Based on the optical investigations and additional elasto-plastic analyses performed to simulate the rolling process of the bulk plate material, it was concluded that the difference in grain orientation between center and surfaces causes more ductile crack growth in the center and lagging regions. Therefore, crack growth rate in the ductile region becomes slower than side regions. In addition, when the specimen is not machined equally from both surfaces, the more ductile region generates eccentricity relative to the center of the specimen. So, crack growth rate becomes slower for a specific point and leading to an anti-symmetric crack front.

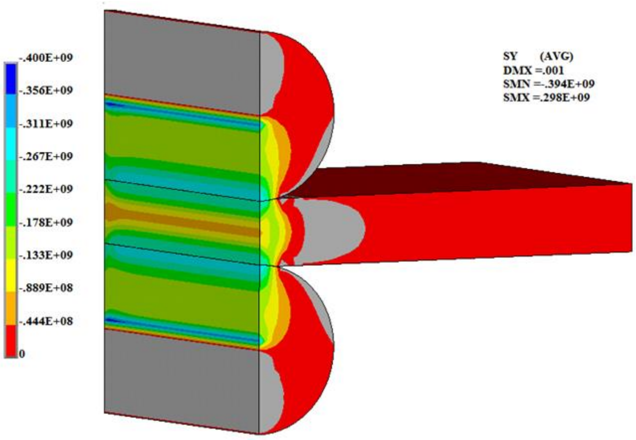

Figure 4.49. Thickness-direction stress contours for an initially 32-mm thick plate (MPa)

An elasto-plastic analysis is performed in ANSYS for rolling process to investigate the changes in stress contours through the thickness. Al-7075-T651 at 260$^{o}$C material property is identified using data from the reference [61]. Initially, 32-mm thick plate is pressed by cylindrical rollers down to 30-mm thickness. Standard frictional contact mechanics is applied between the rollers and the plate. ¼ symmetric boundary conditions are identified. The stress contours can be seen in Figure 4.49., where minimum value is obtained in the middle of the plate. Thus, it shows that if the pressuring displacement of the rollers is not high enough material’s grains near the middle of the plate will not flatten and thin as much as its side regions, resulting in thicker-grain microstructure. In addition, other factors such as the speed of the production line, and changes in temperature will also affect the results.

# CHAPTER 5. CRACK GROWTH SIMULATION USING THE MONTE CARLO METHOD

Distributions representing the variables such as material properties, load and geometric tolerances were obtained from the experiments described in previous sections. The variabilities of these parameters generate scattered crack propagation curves. Monte-Carlo simulations were performed to estimate the variabilities and distributions of crack propagation lives. Material properties, geometric dimensions and variations in load were considered as input variables within their specified limits for Monte Carlo simulations.

First, random input values of geometric tolerances on specimen and material properties, determined in previous sections, were picked from the distributions. Using these picked values, crack propagation life analysis was performed cycle by cycle for the corresponding loading spectrum, and the calculated life was written in a file. In this process, the load cell sensitivity of the test device was considered (class 0.5) for the given loading profile. By picking new random values from the distributions of parameters, the next case analysis was performed with the same procedure. This process was repeated until the desired number of Monte Carlo simulations is reached. During the simulation, picking random values by using a probability distribution, covering the range of input values, is important. In this way, the effects of the variabilities of input parameters on the results can be estimated realistically.

Although many software packages perform Monte-Carlo analyses, it was thought that these packages may not provide sufficient flexibility and the necessary adaptations for crack propagation simulations. Therefore, an in-house Monte-Carlo Simulation code was created.

The algorithm of the prepared simulation code is given in Figure 5.1. As seen in the algorithm, a nested loop is the basis of the algorithm. The outer loop is used to determine the distributions of the variables and to pick them randomly for each Monte-Carlo simulation case. The inner loop of the algorithm is designed to perform cycle by cycle crack propagation analysis for a given loading profile. Load profiles are read from the "Loadspec.txt" file placed in the same directory of the program.

"Pick variable values from distributions" box is the first process of the algorithm given in Figure 5.1. Random number generation in accordance with the distribution of the variable considered is necessary for this process. An open-source random number generation code in FORTRAN was found from the open sources [62] and it was verified using MINITAB. Using the statistical data given in Section 3.4.5, the open-source code was run, and the results were plotted in a histogram graph by MINITAB. In addition, MINITAB and Fortran Code was used to generate random data with the same Loc-Scale values, and plotted as a histogram. The histogram plotted by using the data from two different programs came out very close to each other.

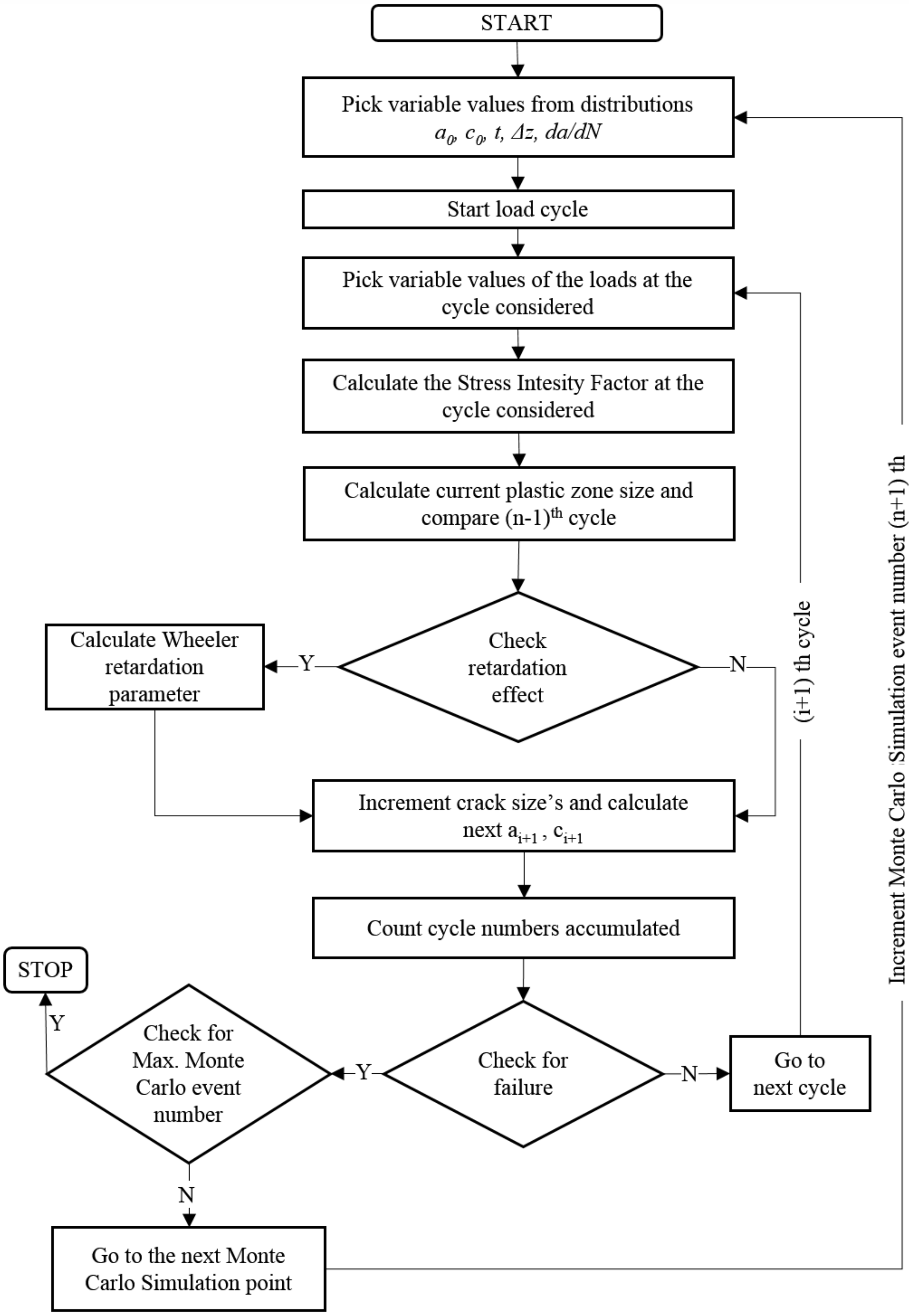

Figure 5.1. Algorithm of crack growth life estimation code with Monte Carlo Simulation

Initial crack length - depth, specimen thickness, and the variations on load, conforming to the normal distribution, and the normal distribution function was defined for picking random values. Since the load cell sensitivity of the test device was Class 0.5, the average value was taken as 0 and the standard deviation was assumed 0.005 to define the load distribution.

In order to determine the crack propagation rate of each cycle, first the average crack propagation rate was calculated. Afterwards, the standard deviation value (0.001) was calibrated according to the scattering of the crack propagation curves obtained from the random loading tests performed with CT specimen is added to the calculated average crack propagation rate by scaling with a randomly picked number from the probability distribution. The decision of the Standard deviation value (0.001) will be explained below in Figure 5.2. - Figure 5.4. A value called "da/dN multiplier" was used to scale the standard deviation in the histogram plots. The mean of da/dN multiplier and its standard deviation (σ) is 0 and 1, respectively, and it is picked randomly from the normal distribution in ± 3σ range. In order to perform mathematical operations with the da/dN multiplier picked randomly from a normal distribution, the other elements in the calculation must also show a normal distribution. For this reason, the mean of crack growth rate and standard deviation was converted to the normal distribution by taking their logarithm. After summation of the scaled standard deviation value and the crack propagation rate, the value was transformed back into a lognormal distribution with the inverse logarithm. Equation (5.1) shows the calculation of da/dN crack propagation rate used in Monte Carlo analysis.

$$\log_{10}\left({}^{da}/_{dN}\right) = \log_{10}\left({}^{da}/_{dN}\right)_{mean} + (dadN\ Multiplier).\log_{10}\left({}^{da}/_{dN}\right)_{std.dev} \quad (5.1)$$

SIFs were calculated using the equation in ASTM E399 standard for two-dimensional crack propagation of CT specimen, and the transfer function given in Section 4 was used to calculate the SIF for three-dimensional cracks in LJ specimen.

The term of ($\log_{10}\left({da}/{dN}\right)_{std.dev}$) in Equation (5.1) was obtained around 0.1 from the experiments performed by using CT specimen. However, it was noticed that the calculated crack growth life values obtained from the MC simulations are in a wide range if the standard deviation value was taken 0.1. First, the cause of this scattering was investigated and then calibration studies were carried out to determine a closer range to experiments.

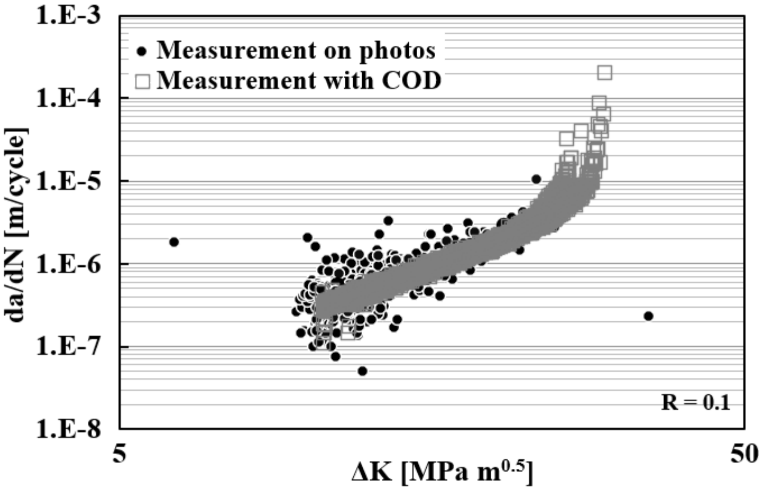

Figure 5.2. Comparison of two different crack length measurement methods

In the previous sections, it was noted that the crack length was measured by two different methods in constant amplitude tests with CT specimens. One of them is the measurement of images by pixel sizing and the other is the measurement with COD, and the latter was used only for validation of the first measurement method. Since the data from COD was not recorded in variable amplitude loading tests and in the tests with the nonstandard specimen (LJ), COD was not preferred as a primary measurement method in this study. A comparison of two different measurement methods is given in Figure 5.2. The COD measurements are more sensitive as expected. More scattered data observed in pixel sizing affect the calculated crack growth life and eventually the MC simulations.

When a small number of Monte Carlo simulations are performed with the 0.1 standard deviation value of experiments, the obtained range was matching with experiments. However, an increased number of Monte Carlo simulations result in an increase in the range of the scatters consisting of the life curves due to the picking of random numbers from extreme points of the distribution. In Figure 5.3. and Figure 5.4., the lower and upper bands of the MC simulations are given for the event number of 10 and 100, respectively.

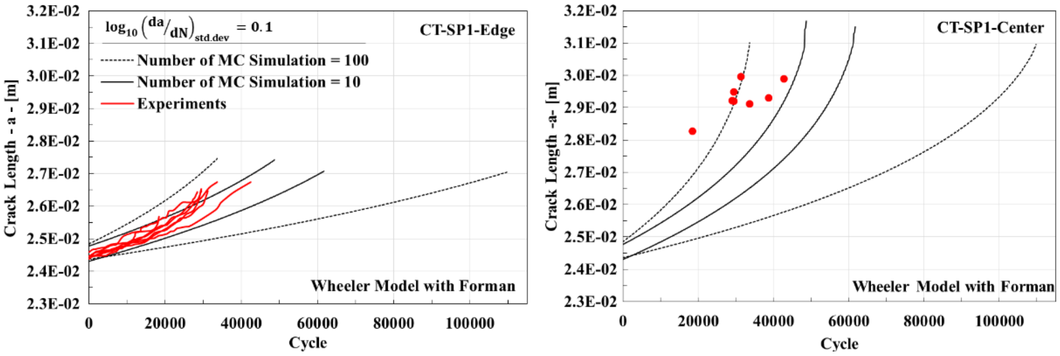

Figure 5.3. The relation between the number of MC simulations and scattering of life curves

When a large number of Monte Carlo simulations were performed, the logarithm of the calibrated standard deviation value was used to obtain a similar range with the experiments. As can be seen in Figure 5.4., closer results to the experiments were obtained by reducing the value of the logarithm of standard deviation. Figure 5.4. shows the experimental and simulation results performed with CT specimen under Spectrum-1 loading. Similar graphs were also observed in other specimen and loading spectrums.

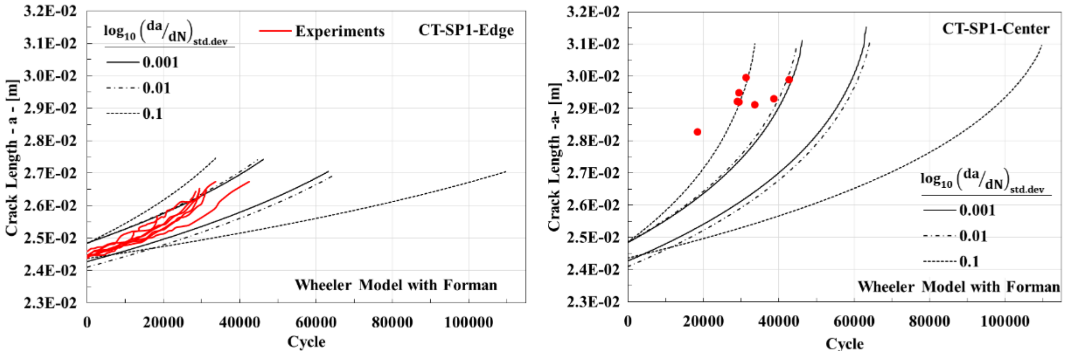

Figure 5.4. Calibration of the logarithm of standard deviation

## 5.1. Probabilistic Crack Growth Life Prediction

After verification studies of the open-source FORTRAN sub-program for random data generation, the main code for crack propagation based on Monte Carlo method was generated by using the algorithm given in Figure 5.1. The total number of simulated events in the Monte Carlo Simulation is an input value and sets the number of values randomly picked from distributions for each variable. If a distribution is scanned with a larger number of random data within the range defined by mean and standard deviation, the sensitivity increases. Therefore, the maximum number of Monte Carlo Simulation must not be too small. In order to ensure that the number of Monte Carlo Simulation was sufficient, two different simulations were carried out for two-dimensional crack propagation with a maximum number of 250 and 100. Histogram plots of randomly picked variables are given in Figure 5.5. As can be seen in the figure, there was no significant difference between the simulations in histogram plots. Since it is easier to analyze and plot results from a smaller number of events, the maximum event simulation number was defined as 100, in this study.

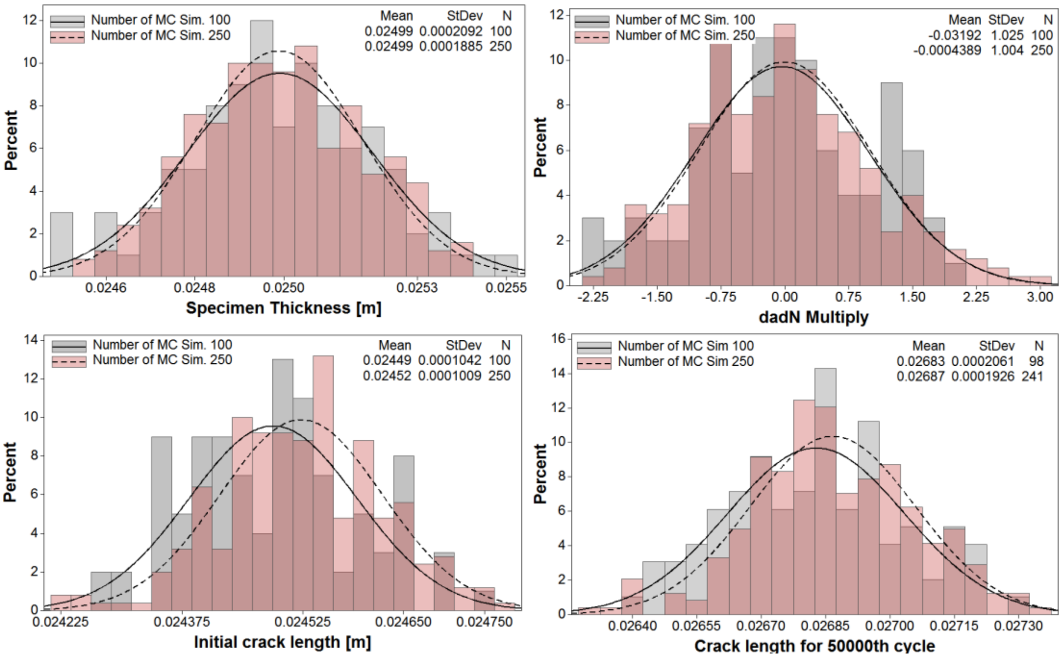

Figure 5.5. Effect of the number of Monte Carlo Simulation on the distribution of variables

The load spectrum was written into an external text file for Monte Carlo Simulation. Then, the mean and standard deviation values of the specimen thickness, initial crack length, sensitivity of the load cell, and da/dN multiplier were defined as inputs in the code. Two different codes were prepared for CT and LJ specimen due to the difference in variables and calculation of SIFs. If LJ specimen is used in the simulation, the width and depth of the initial crack and the ΔZ tolerance in the EDM notch should also be defined as separate variables. After these variables are entered, the code calculates the crack growth rate for each load cycle and computes the crack growth lives for all cases of events defined by the randomly picked values of variables from their individual distributions. At the end of the Monte Carlo simulation, three separate output text files are generated. One of these files is named as "***.txt" containing the crack propagation rate and the other results calculated for each cycle of the load spectrum. Other files are named as "***. Plot_txt" and "***. Edge_plot_txt", where results are written at the specified cycle intervals for the center and edge points of the crack front, respectively. Considering that calculations are made for thousands of points of the spectrum profile for each simulation, it is easier to plot the "***.Plot_txt" files written only at specific cycles. As an example of the created files, a screenshot is given in Figure 5.6.

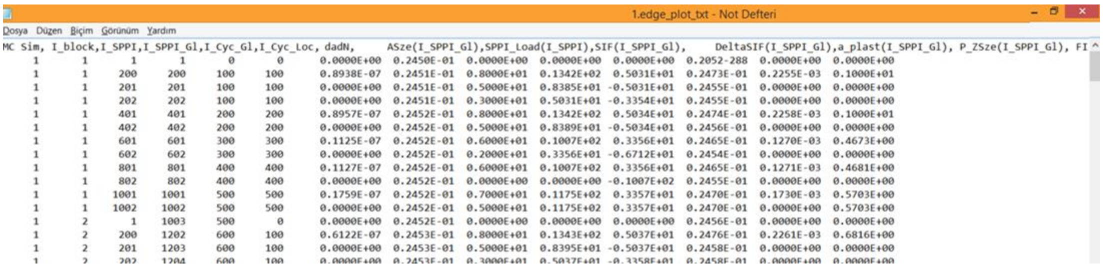

```
MC Sim, I_block,I_SPPI,I_SPPI_Gl,I_Cyc_Gl,I_Cyc_Loc, dadN,     ASze(I_SPPI_Gl),SPPI_Load(I_SPPI),SIF(I_SPPI_Gl),     DeltaSIF(I_SPPI_Gl),a_plast(I_SPPI_Gl), P_ZSze(I_SPPI_Gl), FI
      1       1       1       1       0       0      0.0000E+00  0.2450E-01  0.0000E+00  0.0000E+00  0.0000E+00  0.2052-288  0.0000E+00  0.0000E+00
      1       1     200     200     100     100      0.8938E-07  0.2451E-01  0.8000E+01  0.1342E+02  0.5031E+01  0.2473E-01  0.2255E-03  0.1000E+01
      1       1     201     201     100     100      0.0000E+00  0.2451E-01  0.5000E+01  0.8385E+01 -0.5031E+01  0.2455E-01  0.0000E+00  0.0000E+00
      1       1     202     202     100     100      0.0000E+00  0.2451E-01  0.3000E+01  0.5031E+01 -0.3354E+01  0.2455E-01  0.0000E+00  0.0000E+00
      1       1     401     401     200     200      0.8957E-07  0.2452E-01  0.8000E+01  0.1342E+02  0.5034E+01  0.2474E-01  0.2258E-03  0.1000E+01
      1       1     402     402     200     200      0.0000E+00  0.2452E-01  0.5000E+01  0.8389E+01 -0.5034E+01  0.2456E-01  0.0000E+00  0.0000E+00
      1       1     601     601     300     300      0.1125E-07  0.2452E-01  0.6000E+01  0.1007E+02  0.3356E+01  0.2465E-01  0.1270E-03  0.4673E+00
      1       1     602     602     300     300      0.0000E+00  0.2452E-01  0.2000E+01  0.3356E+01 -0.6712E+01  0.2454E-01  0.0000E+00  0.0000E+00
      1       1     801     801     400     400      0.1127E-07  0.2452E-01  0.6000E+01  0.1007E+02  0.3356E+01  0.2465E-01  0.1271E-03  0.4681E+00
      1       1     802     802     400     400      0.0000E+00  0.2452E-01  0.0000E+00  0.0000E+00 -0.1007E+02  0.2455E-01  0.0000E+00  0.0000E+00
      1       1    1001    1001     500     500      0.1759E-07  0.2452E-01  0.7000E+01  0.1175E+02  0.3357E+01  0.2470E-01  0.1730E-03  0.5703E+00
      1       1    1002    1002     500     500      0.0000E+00  0.2452E-01  0.5000E+01  0.1175E+02  0.3357E+01  0.2470E-01  0.0000E+00  0.5703E+00
      1       2       1    1003     500       0      0.0000E+00  0.2452E-01  0.0000E+00  0.0000E+00  0.0000E+00  0.2456E-01  0.0000E+00  0.0000E+00
      1       2     200    1202     600     100      0.6122E-07  0.2453E-01  0.8000E+01  0.1343E+02  0.5037E+01  0.2476E-01  0.2261E-03  0.6816E+00
      1       2     201    1203     600     100      0.0000E+00  0.2453E-01  0.5000E+01  0.8395E+01 -0.5037E+01  0.2458E-01  0.0000E+00  0.0000E+00
      1       2     202    1204     600     100      0.0000E+00  0.2453E-01  0.3000E+01  0.5037E+01 -0.3358E+01  0.2458E-01  0.0000E+00  0.0000E+00
```

Figure 5.6. A screenshot from ***.plot.txt file

After the MC Simulations, the cycle number (I_Cyc_Gl) and crack length (ASze (I_SPPI_Gl)) values from each file are copied into Microsoft Excel [46] and plotted. Since this process is tedious with many files, a VBA macro has been prepared in the Excel Developer. The macro automatically copies the values from the txt files to Excel. The Excel and ***. txt files must be in the same directory and the last number of MC Simulation must be entered in the first sheet of the Excel workbook. The code of the macro can be seen in Figure 5.7. After the values are copied as individual columns for each MC simulation in Excel, MINITAB [44] is used to obtain probability distributions.

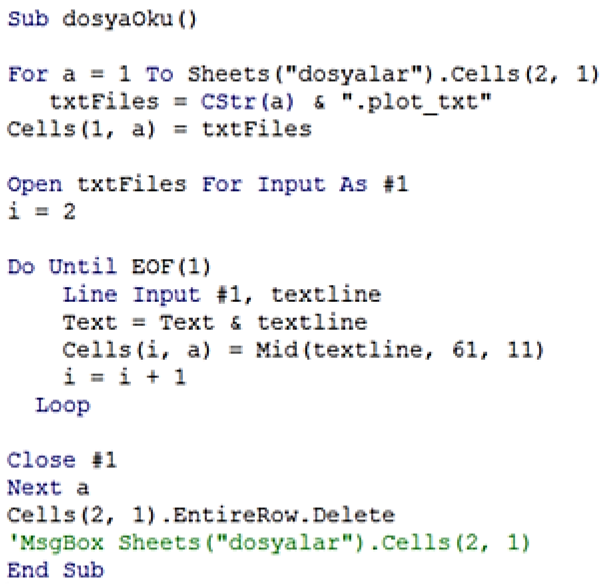

```
Sub dosyaOku()

For a = 1 To Sheets("dosyalar").Cells(2, 1)
   txtFiles = CStr(a) & ".plot_txt"
Cells(1, a) = txtFiles

Open txtFiles For Input As #1
i = 2

Do Until EOF(1)
    Line Input #1, textline
    Text = Text & textline
    Cells(i, a) = Mid(textline, 61, 11)
    i = i + 1
  Loop

Close #1
Next a
Cells(2, 1).EntireRow.Delete
'MsgBox Sheets("dosyalar").Cells(2, 1)
End Sub
```

Figure 5.7. The Excel VBA macro copying the values from txt files to Excel

## 5.2. Comparison with Experiments and Model Improvement

In Section 3.6.3, deterministically calculated lives for two-dimensional crack propagation with CT specimens and comparisons with experiments were explained. In this section, the results of crack propagation simulations considering the mean and standard deviation of variables using the Monte Carlo method will be explained. The Spectrum Overload Index (SOL index), explained in Section 3.6.3., was used to calculate the two-dimensional crack growth rate. Further details were given in Section 3.6.3. In Figure 5.8. -Figure 5.64., plots of crack propagation lives and input-output distributions obtained by MC Simulations performed under SP1 and SP2 loading spectrums for CT specimen are given for each model employed in the simulation. Distributions of outputs obtained by MC Simulations can be displayed in two different versions, as the crack length probability distribution corresponding to any number of cycles or as the probability distribution of the load cycles corresponding to any crack length. The histograms were plotted as normal distributions. Also, survival plots (inverse of cumulative distribution curve) were prepared by using these distributions. The results in Figure 5.8. are given for both the crack front free surface (edge) and the center points of the CT specimen. MC Simulation results obtained for different models under different spectrums are given separately. In the first two models, namely "Forman C-n values with Wheeler" and "Walker C-n values with Wheeler", presented for each specimen and loading spectrum, the stress ratio was not directly used for each load cycle. Instead, crack growth rate was calculated with C-n values of combined da/dN curves generated with different R-ratios, using Forman or Walker models. In other words, a mean stress effect approach was used with composite da/dN curves obtained by Forman or Walker model, and crack growth retardation was determined for each load cycle according to the Wheeler model. In all other models, crack growth retardation and/or R-ratio calculations were made on a cycle-by-cycle basis.

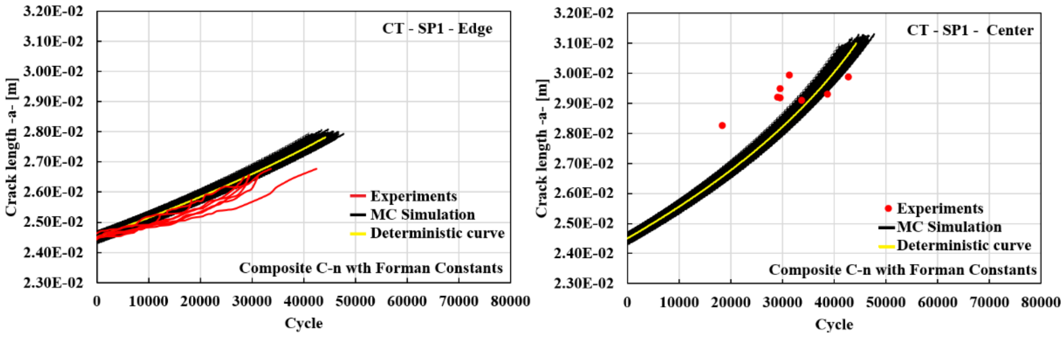

Figure 5.8. Probabilistic crack growth life curves and their comparison with the experiments (CT specimen, SP1 loading spectrum, Composite C-n with Forman Constants)

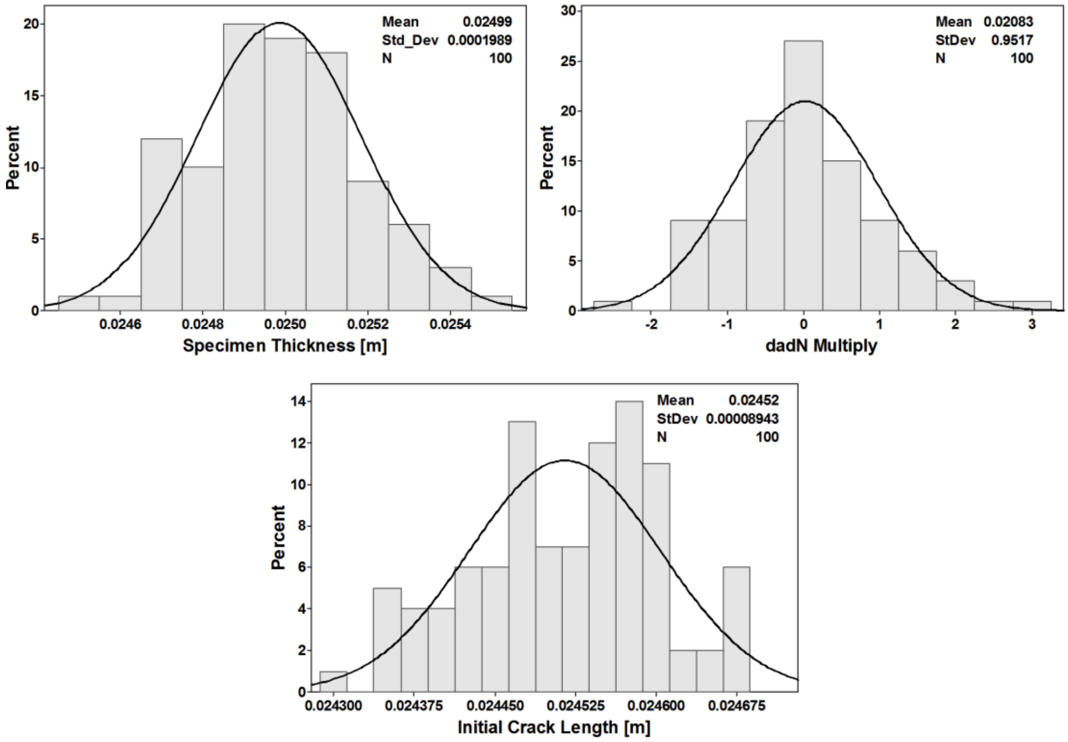

Figure 5.9. Distributions of the inputs used in crack growth life analysis (CT specimen, SP1 loading spectrum, Composite C-n with Forman Constants)

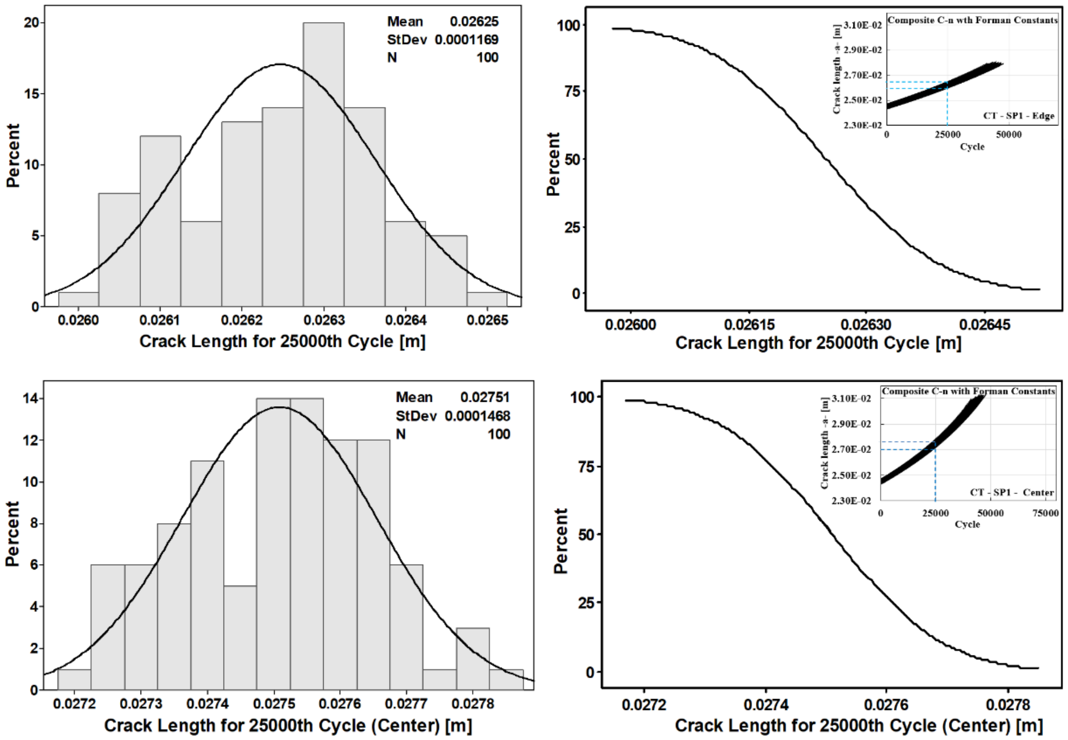

Figure 5.10. Histogram and CDF for crack length under 25000th cycle load conditions (CT specimen, SP1 loading spectrum, Composite C-n with Forman Constants)

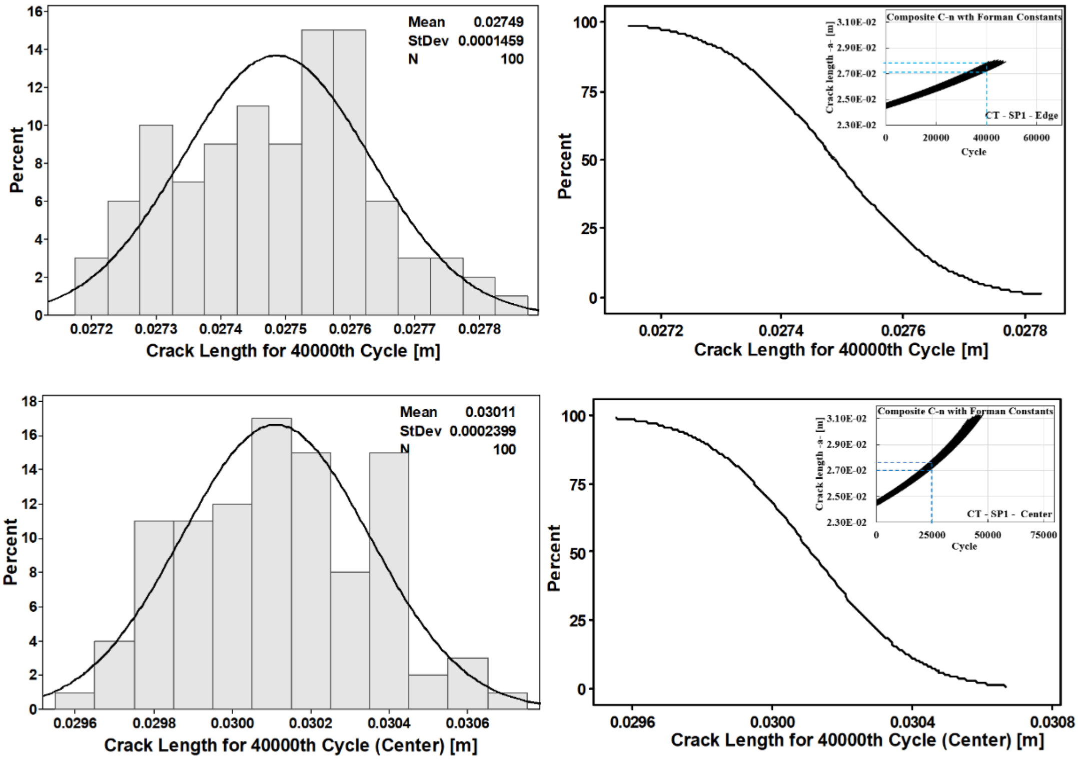

Figure 5.11. Histogram and CDF for crack length under 40000th cycle load conditions (CT specimen, SP1 loading spectrum, Composite C-n with Forman Constants)

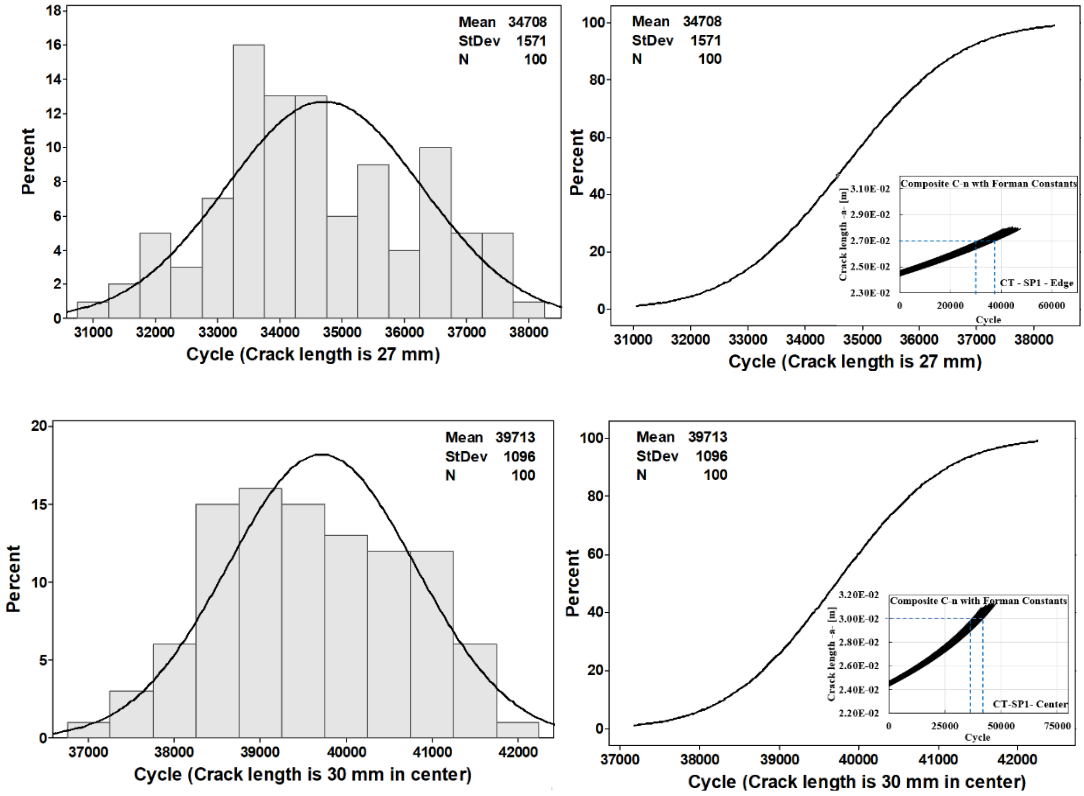

Figure 5.12. Histogram and CDF for crack length under constant crack length conditions (CT specimen, SP1 loading spectrum, Composite C-n with Forman Constants)

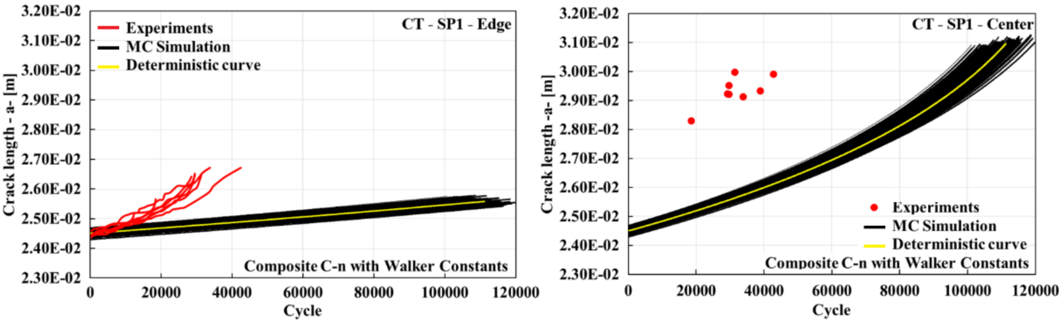

Figure 5.13. Probabilistic crack growth life curves and their comparison with the experiments (CT specimen, SP1 loading spectrum, Composite C-n with Walker Constants)

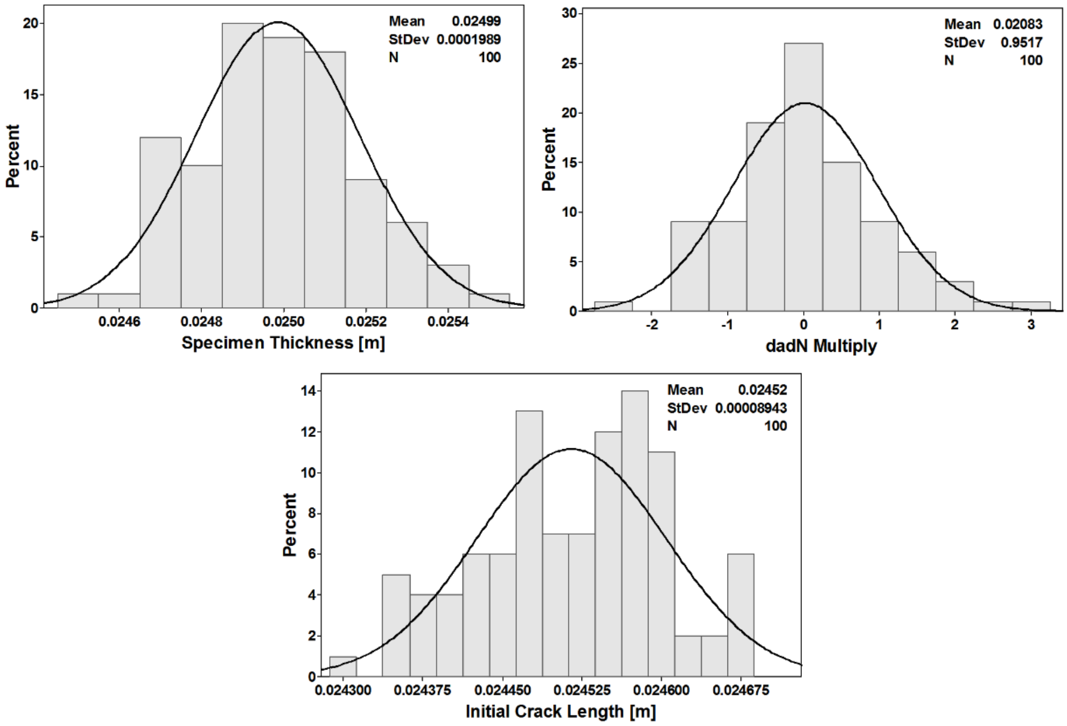

Figure 5.14. Distributions of the inputs used in crack growth life analysis (CT specimen, SP1 loading spectrum, Composite C-n with Walker Constants)

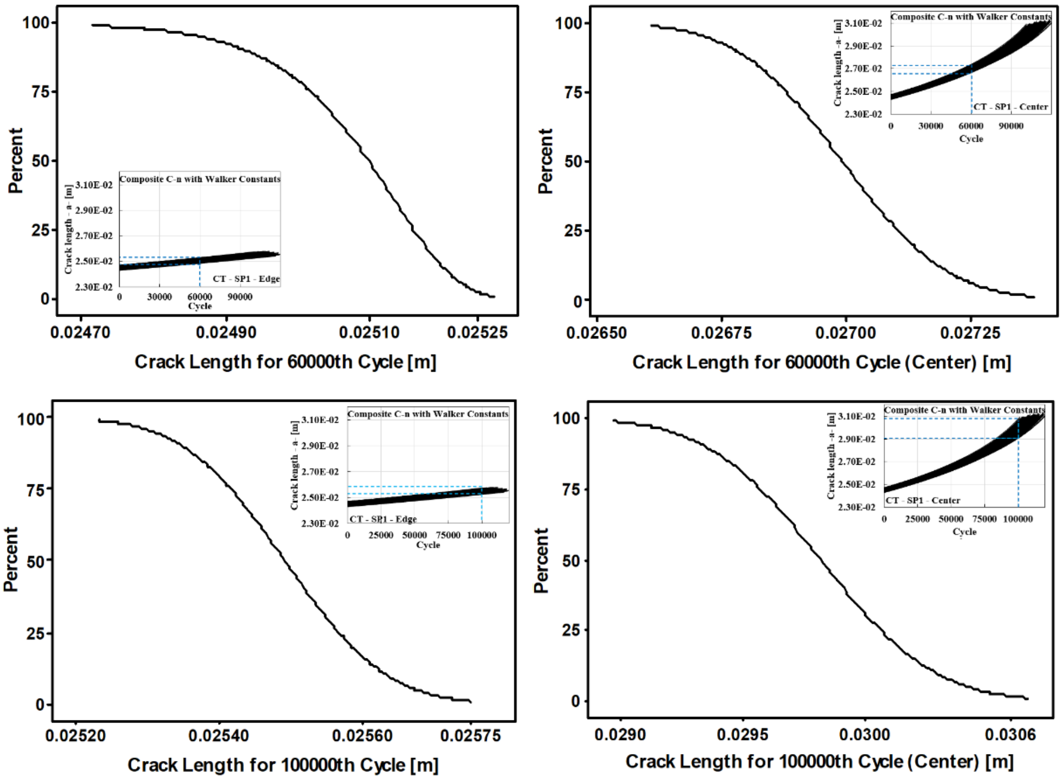

Figure 5.15. CDF for crack lengths under constant cycle load conditions (CT specimen, SP1 loading spectrum, Composite C-n with Walker Constants)

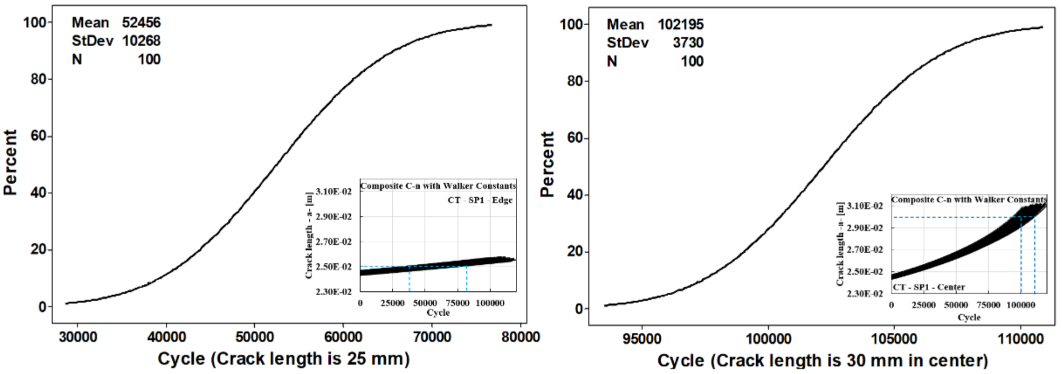

Figure 5.16. CDF for load cycles under constant crack length conditions (CT specimen, SP1 loading spectrum, Composite C-n with Walker Constants)

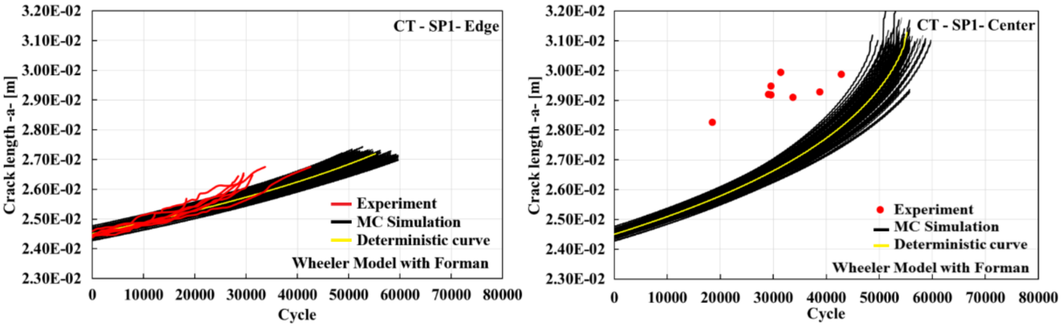

Figure 5.17. Probabilistic crack growth life curves and their comparison with the experiments (CT specimen, SP1 loading spectrum, Wheeler model with Forman)

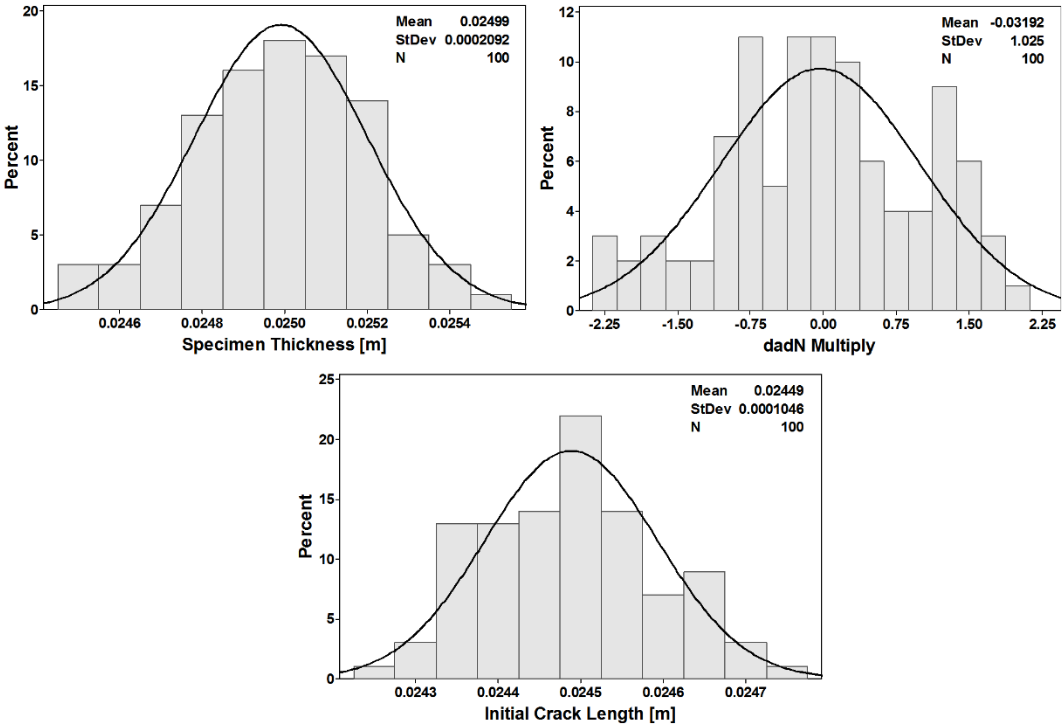

Figure 5.18. Distributions of the inputs used in crack growth life analysis (CT specimen, SP1 loading spectrum, Wheeler model with Forman)

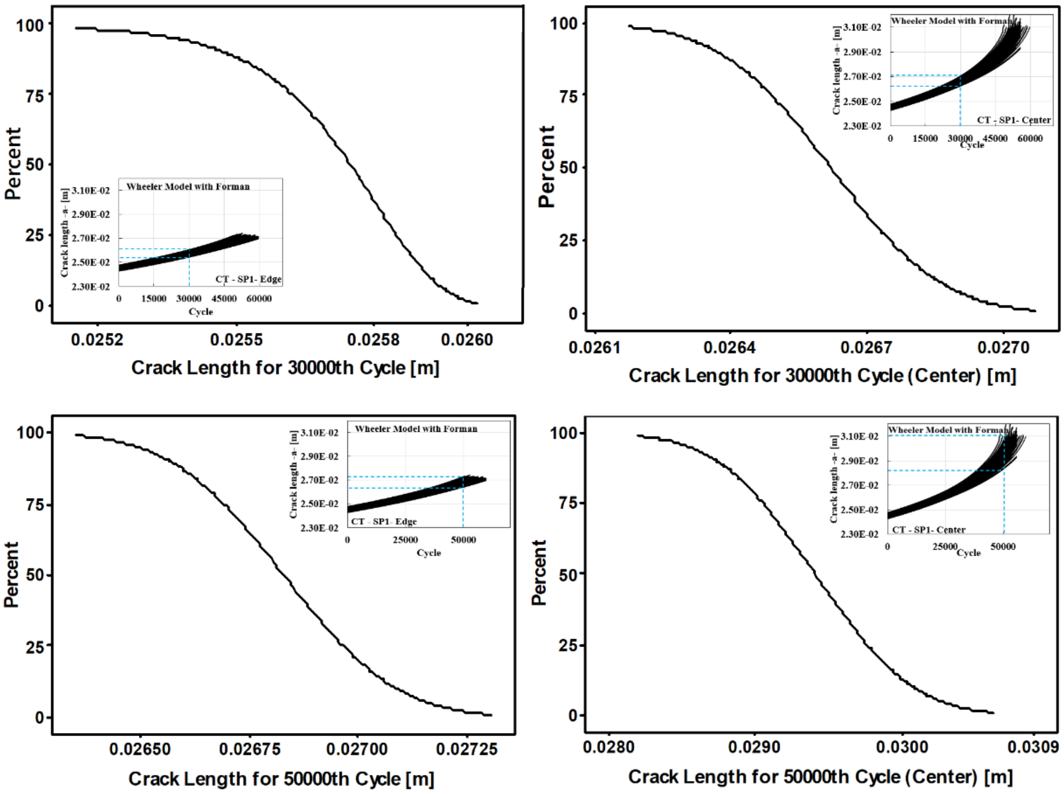

Figure 5.19. CDF for crack lengths under constant cycle load conditions (CT specimen, SP1 loading spectrum, Wheeler model with Forman)

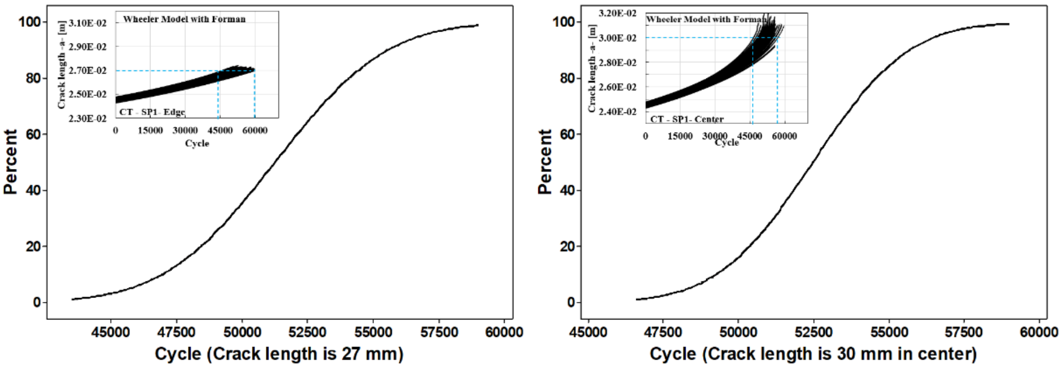

Figure 5.20. CDF for load cycles under constant crack length conditions (CT specimen, SP1 loading spectrum, Wheeler model with Forman)

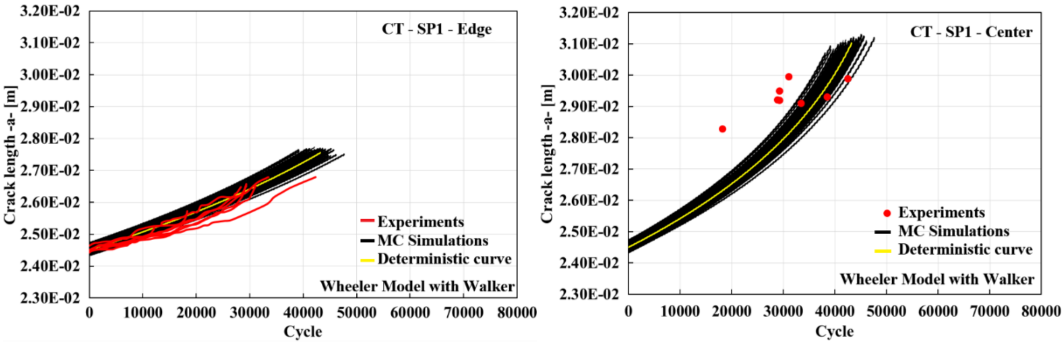

Figure 5.21. Probabilistic crack growth life curves and their comparison with the experiments (CT specimen, SP1 loading spectrum, Wheeler model with Walker)

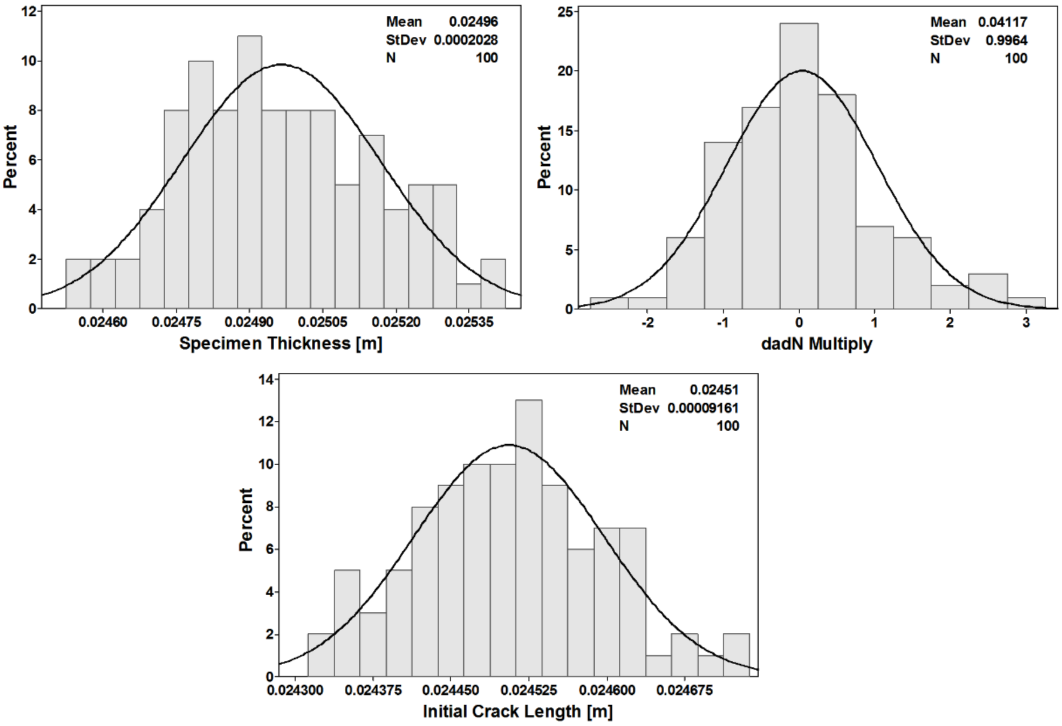

Figure 5.22. Distributions of the inputs used in crack growth life analysis (CT specimen, SP1 loading spectrum, Wheeler model with Walker)

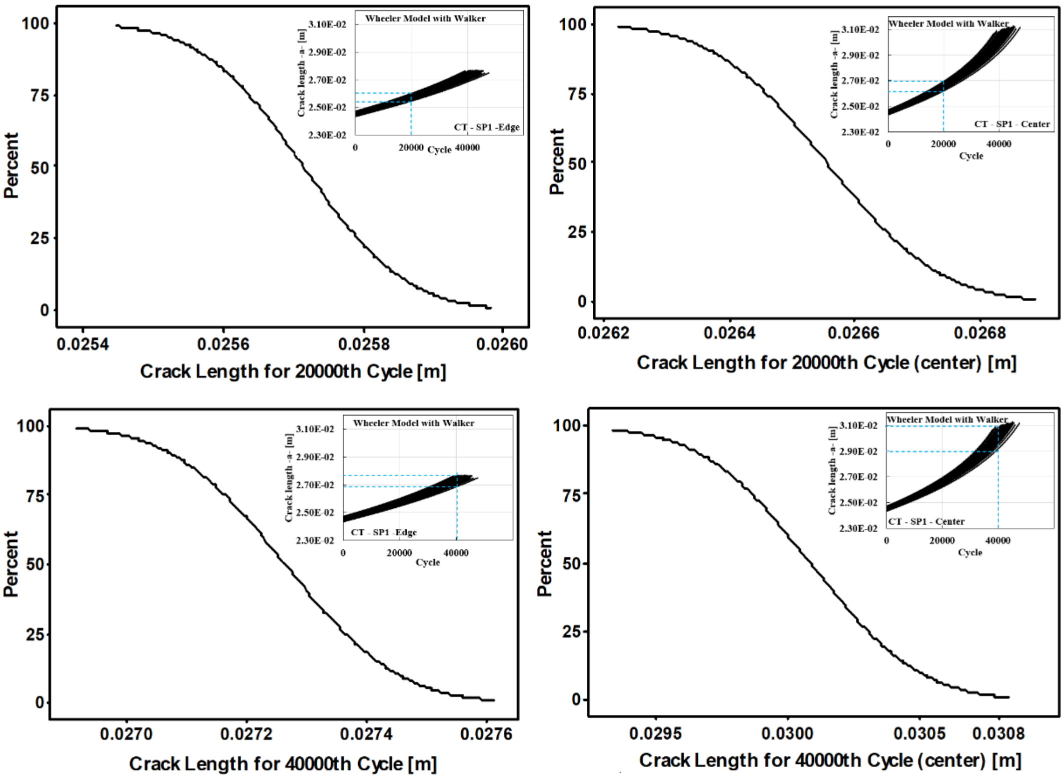

Figure 5.23. CDF for crack lengths under constant cycle load conditions (CT specimen, SP1 loading spectrum, Wheeler model with Walker)

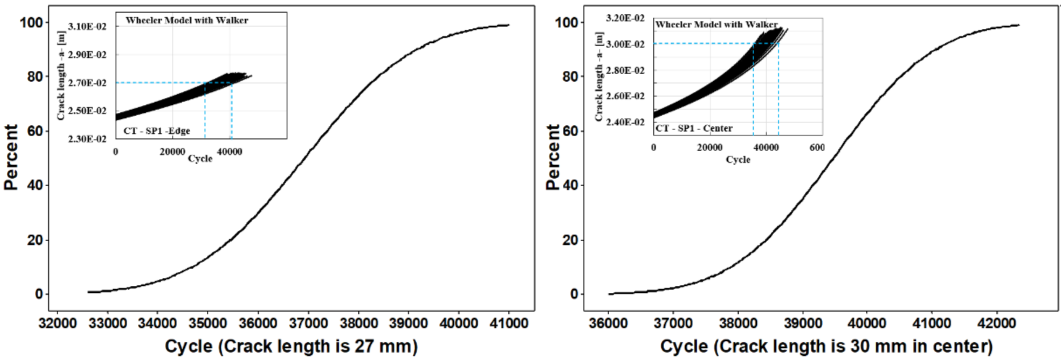

Figure 5.24. CDF for load cycles under constant crack length conditions (CT specimen, SP1 loading spectrum, Wheeler model with Walker)

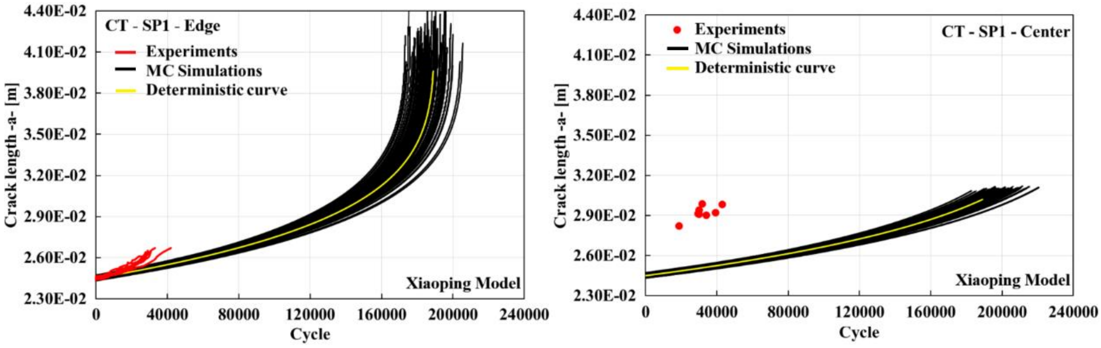

Figure 5.25. Probabilistic crack growth life curves and their comparison with the experiments (CT specimen, SP1 loading spectrum, Xiaoping model)

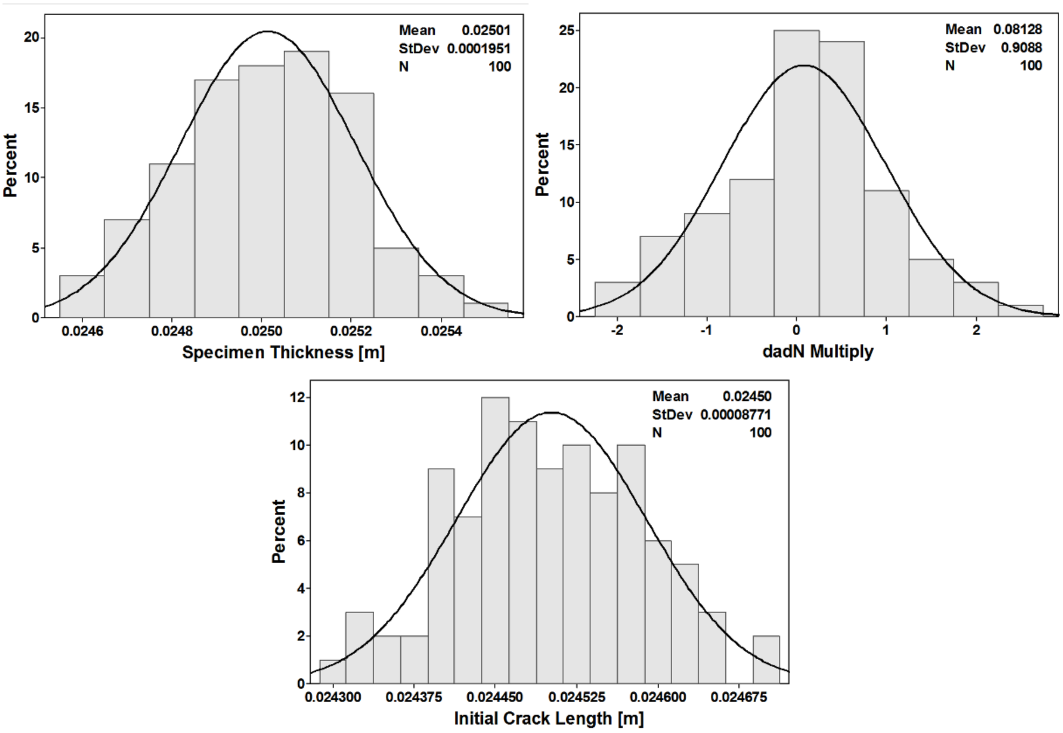

Figure 5.26. Distributions of the inputs used in crack growth life analysis (CT specimen, SP1 loading spectrum, Xiaoping model)

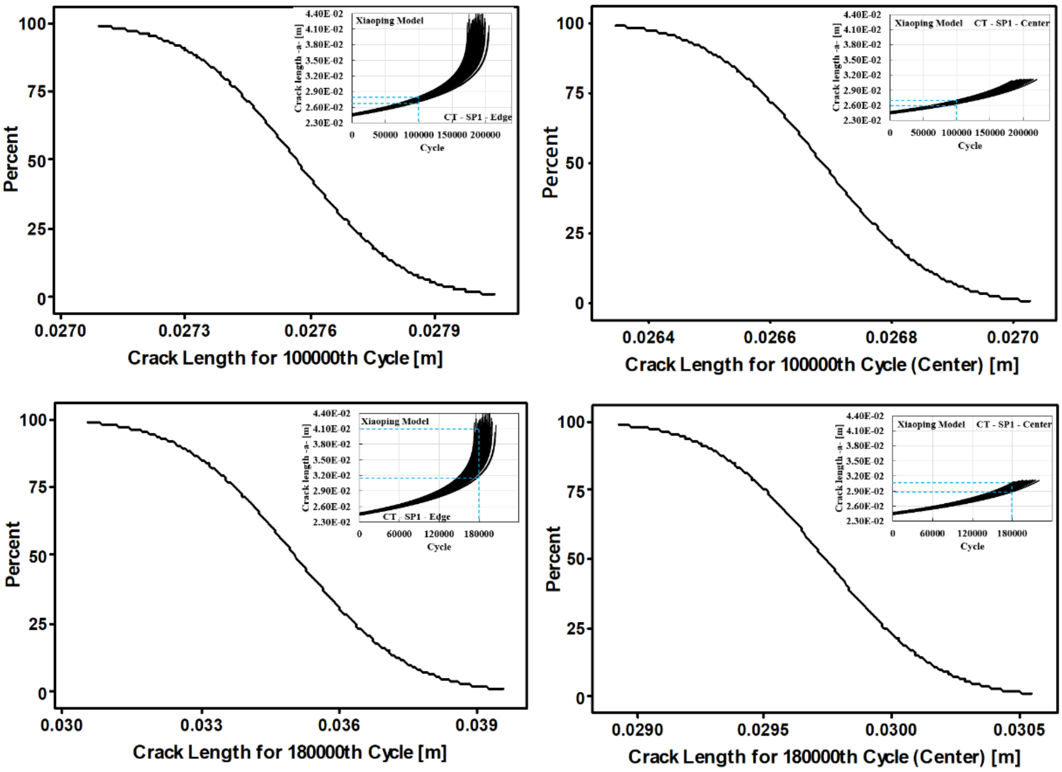

Figure 5.27. CDF for crack lengths under constant cycle load conditions (CT specimen, SP1 loading spectrum, Xiaoping model)

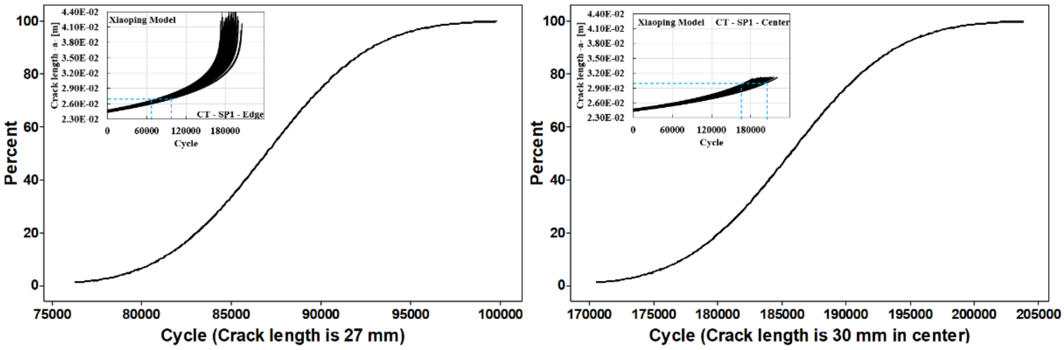

Figure 5.28. CDF for load cycles under constant crack length conditions (CT specimen, SP1 loading spectrum, Xiaoping model)

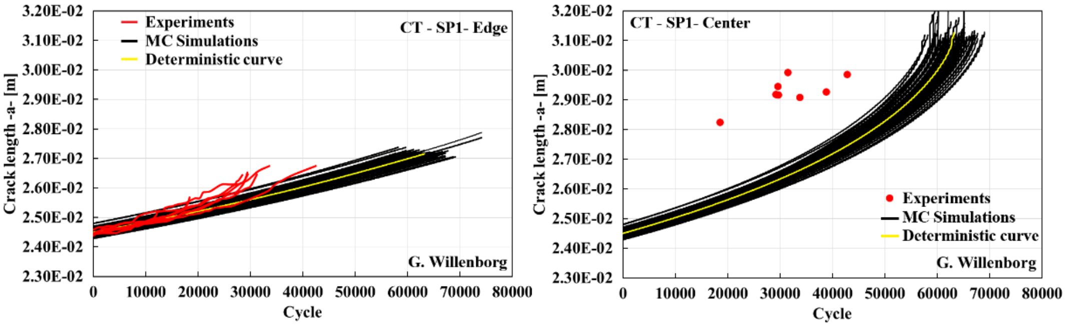

Figure 5.29. Probabilistic crack growth life curves and their comparison with the experiments (CT specimen, SP1 loading spectrum, Generalized Willenborg model)

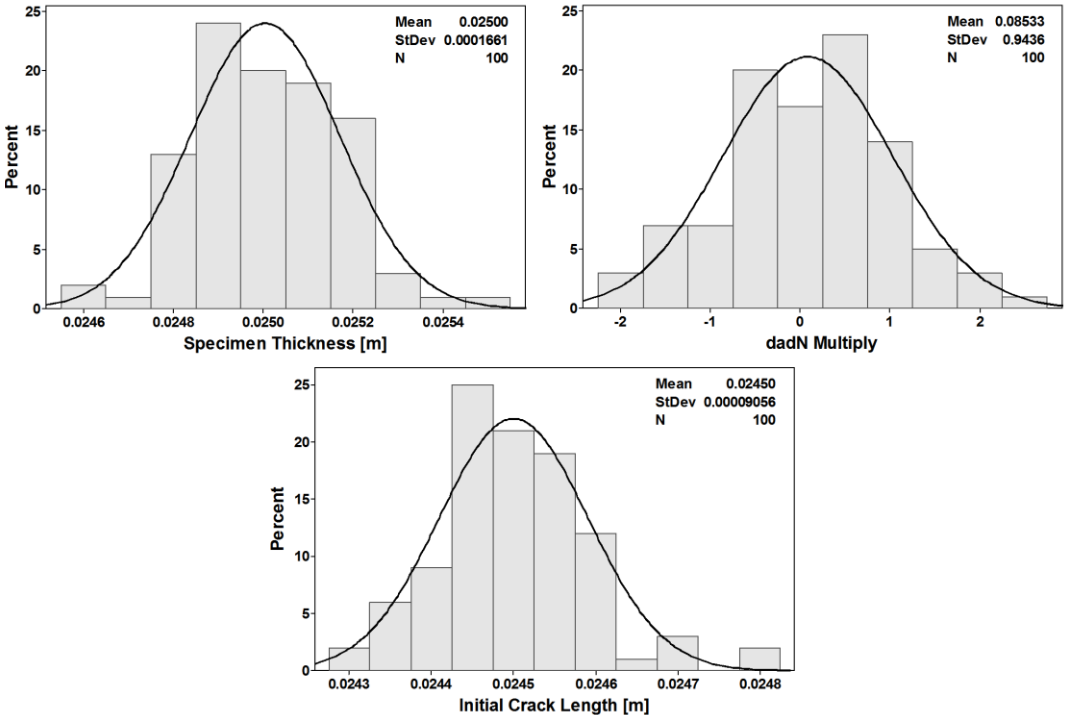

Figure 5.30. Distributions of the inputs used in crack growth life analysis (CT specimen, SP1 loading spectrum, Generalized Willenborg model)

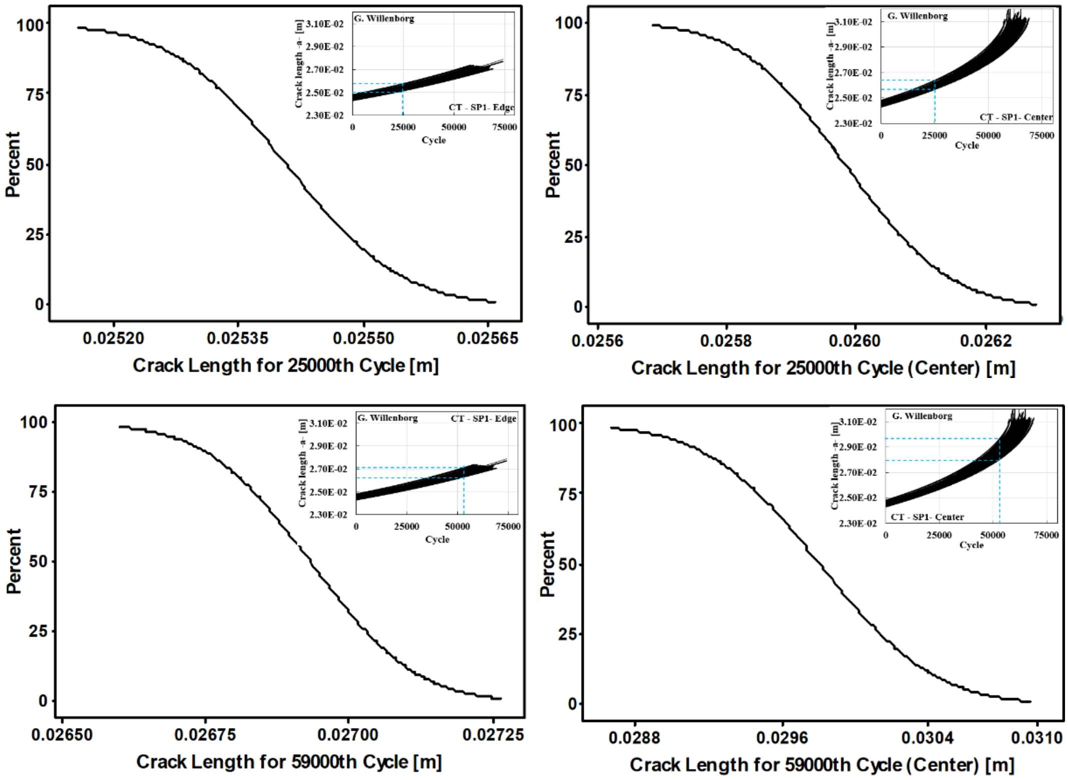

Figure 5.31. CDF for crack lengths under constant cycle load conditions (CT specimen, SP1 loading spectrum, Generalized Willenborg model)

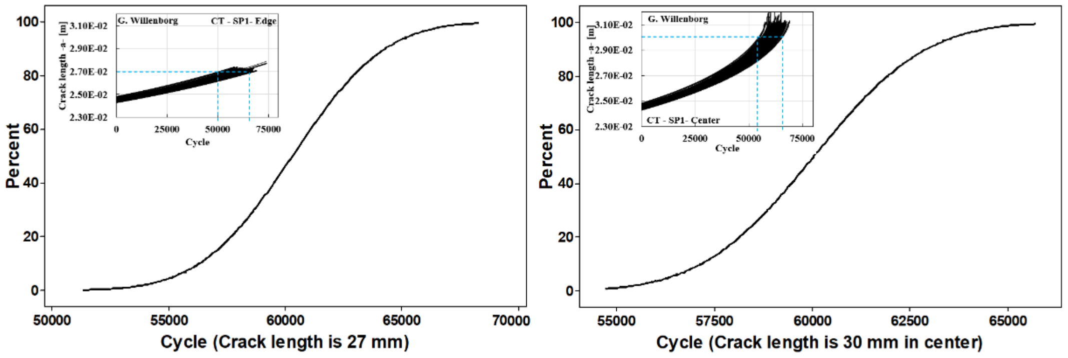

Figure 5.32. CDF for load cycles under constant crack length conditions (CT specimen, SP1 loading spectrum, Generalized Willenborg model)

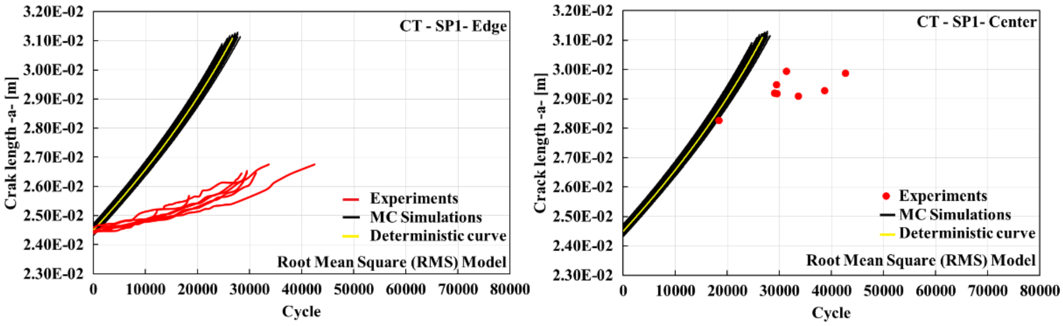

Figure 5.33. Probabilistic crack growth life curves and their comparison with the experiments (CT specimen, SP1 loading spectrum, Root mean square model)

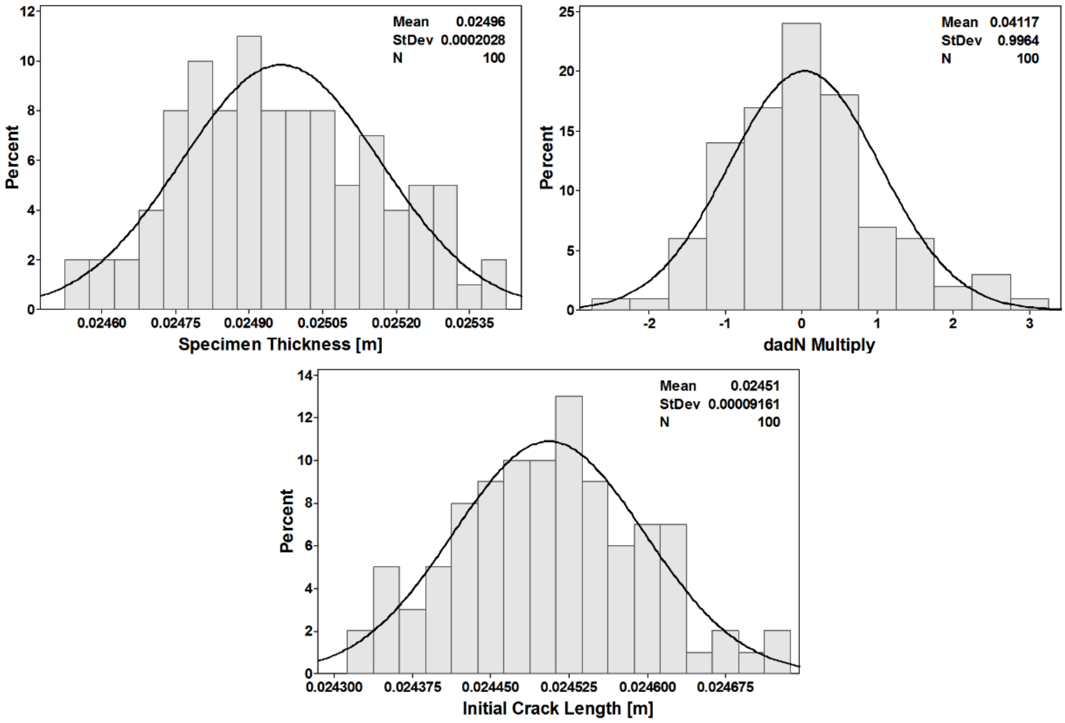

Figure 5.34. Distributions of the inputs used in crack growth life analysis (CT specimen, SP1 loading spectrum, Root mean square model)

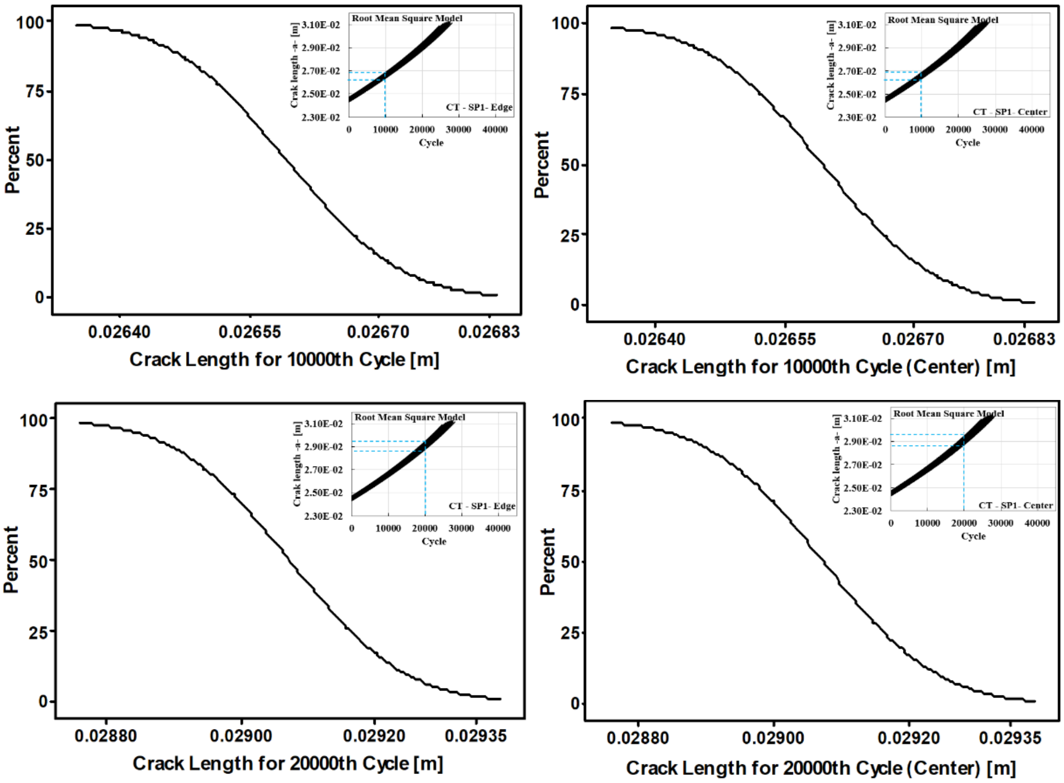

Figure 5.35. CDF for crack lengths under constant cycle load conditions (CT specimen, SP1 loading spectrum, Root mean square model)

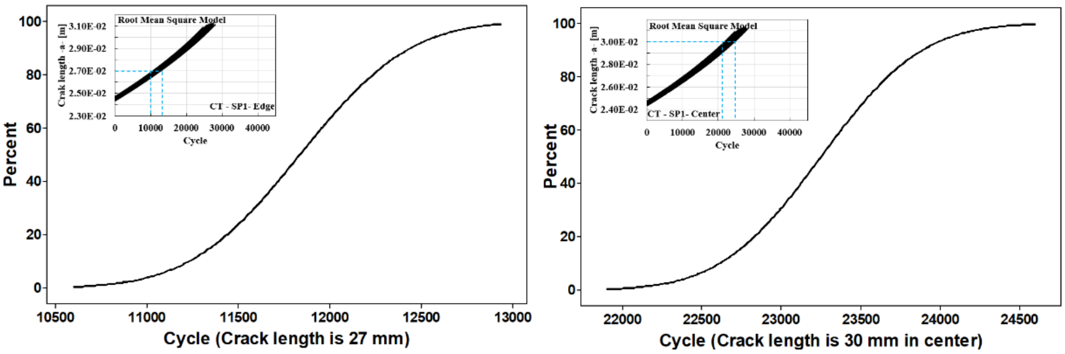

Figure 5.36. CDF for load cycles under constant crack length conditions (CT specimen, SP1 loading spectrum, Root mean square model)

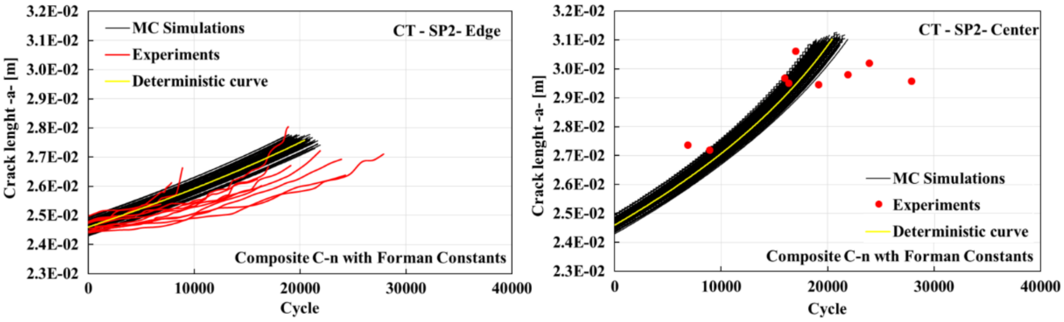

Figure 5.37. Probabilistic crack growth life curves and their comparison with the experiments (CT specimen, SP2 loading spectrum, Composite C-n with Forman Constants)

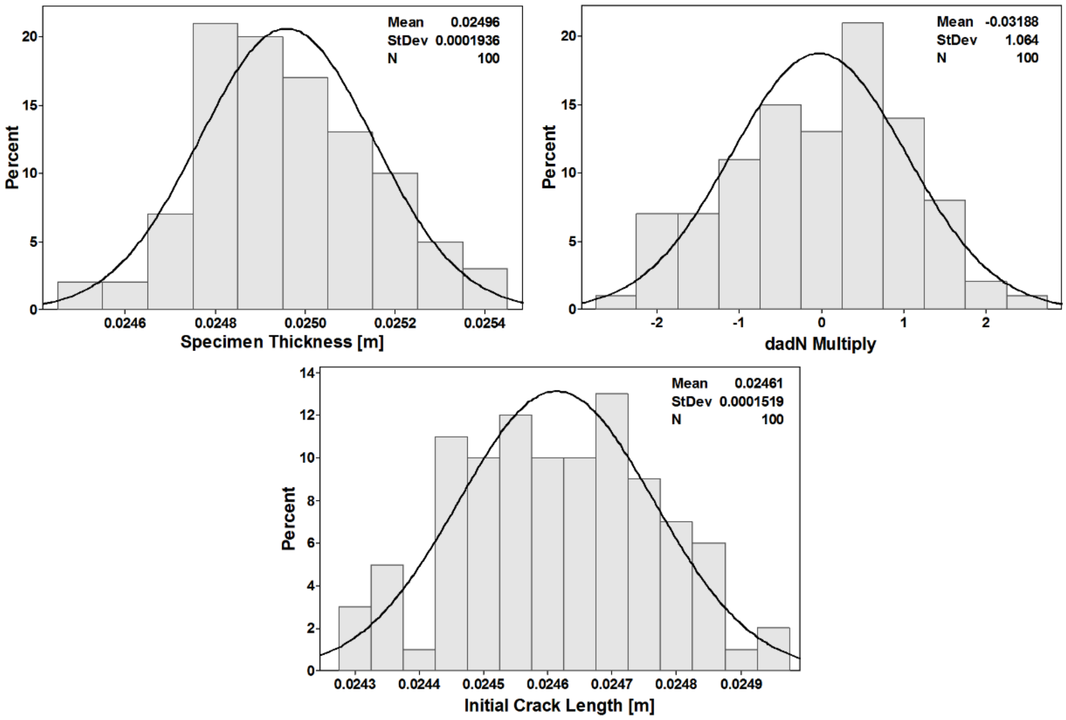

Figure 5.38. Distributions of the inputs used in crack growth life analysis (CT specimen, SP2 loading spectrum, Composite C-n with Forman Constants)

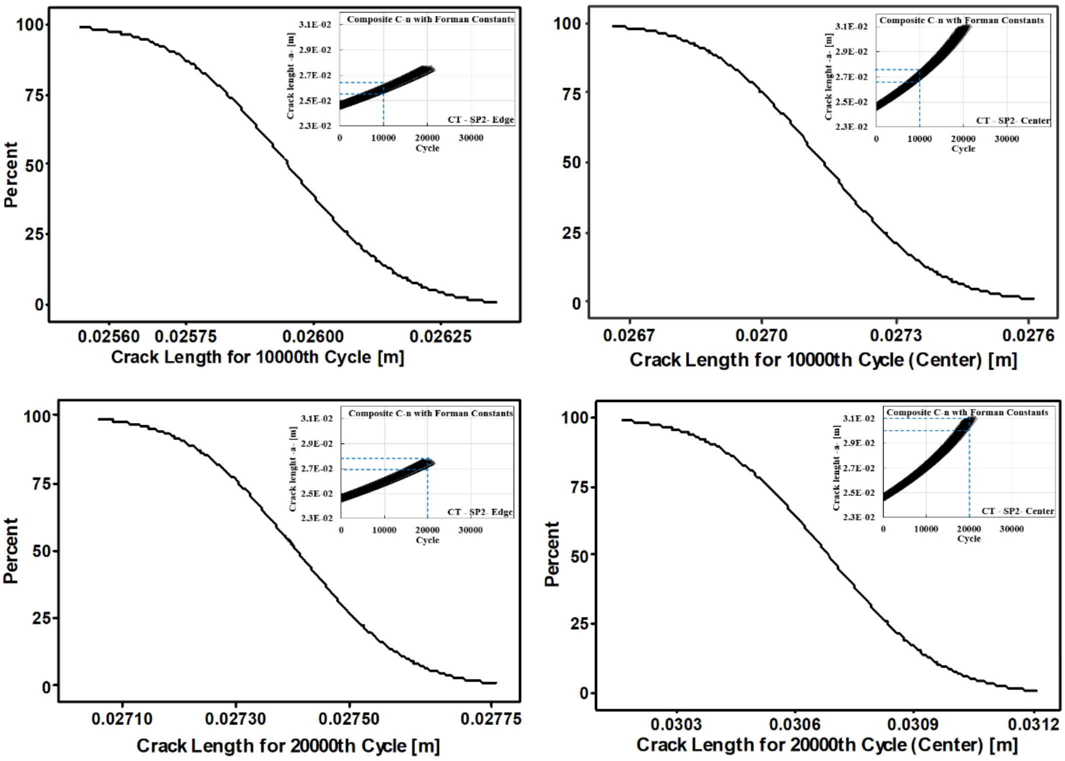

Figure 5.39. CDF for crack lengths under constant cycle load conditions (CT specimen, SP2 loading spectrum, Composite C-n with Forman Constants)

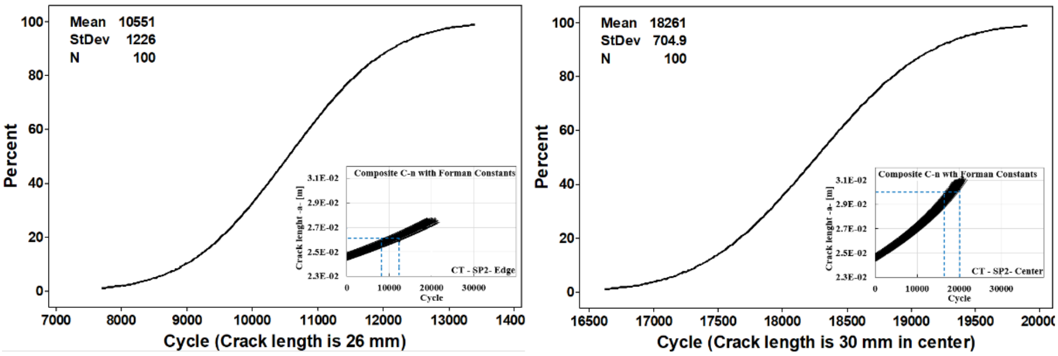

Figure 5.40. CDF for load cycles under constant crack length conditions (CT specimen, SP2 loading spectrum, Composite C-n with Forman Constants)

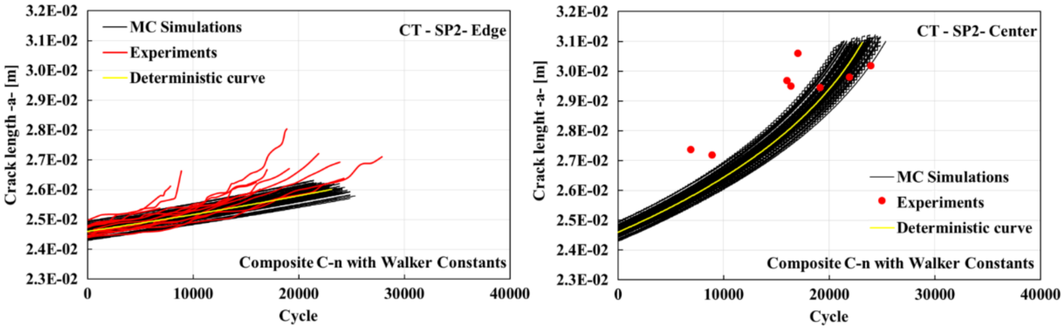

Figure 5.41. Probabilistic crack growth life curves and their comparison with the experiments (CT specimen, SP2 loading spectrum, Composite C-n with Walker Constants)

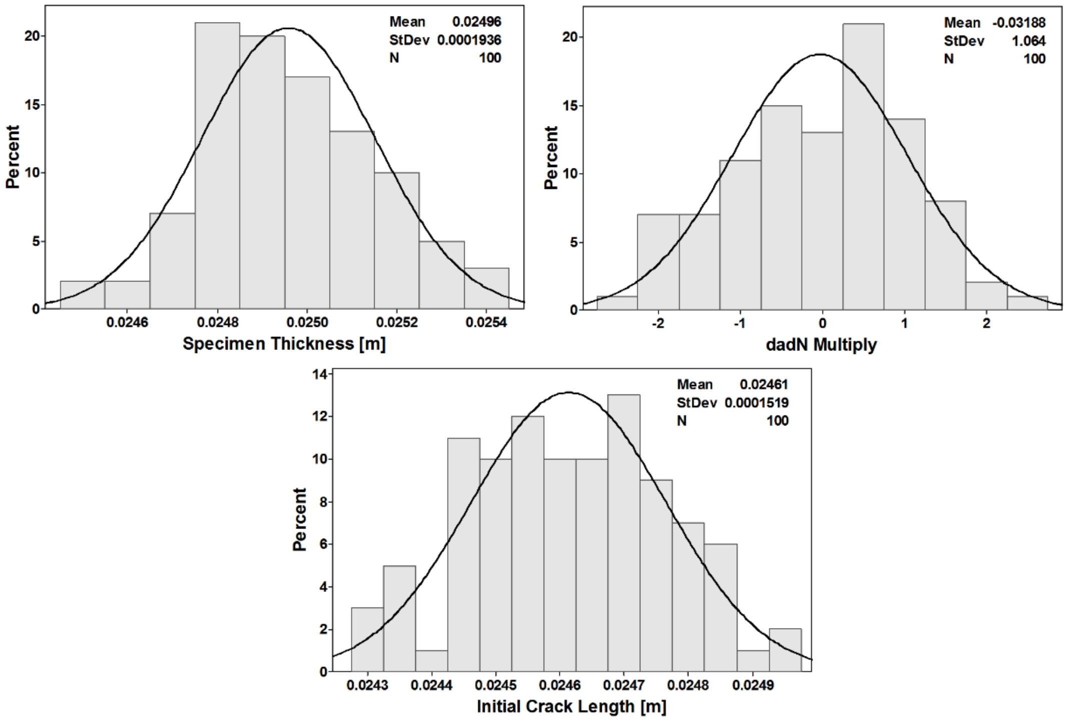

Figure 5.42. Distributions of the inputs used in crack growth life analysis (CT specimen, SP2 loading spectrum, Composite C-n with Walker Constants)

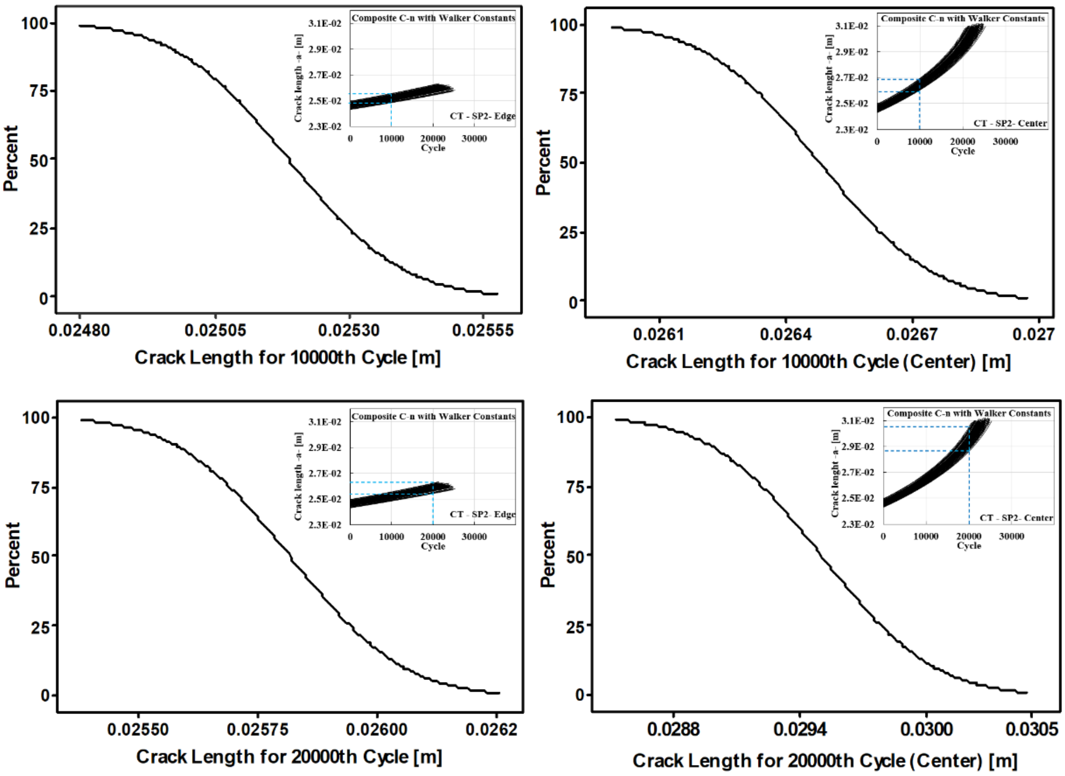

Figure 5.43. CDF for crack lengths under constant cycle load conditions (CT specimen, SP2 loading spectrum, Composite C-n with Walker Constants)

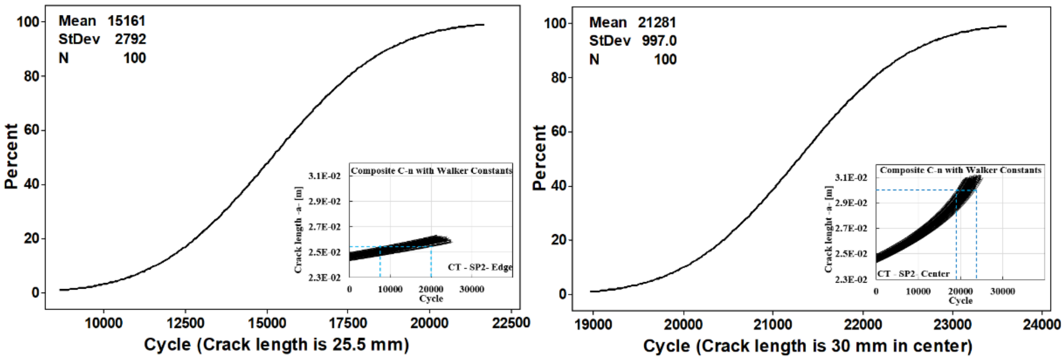

Figure 5.44. CDF for load cycles under constant crack length conditions (CT specimen, SP2 loading spectrum, Composite C-n with Walker Constants)

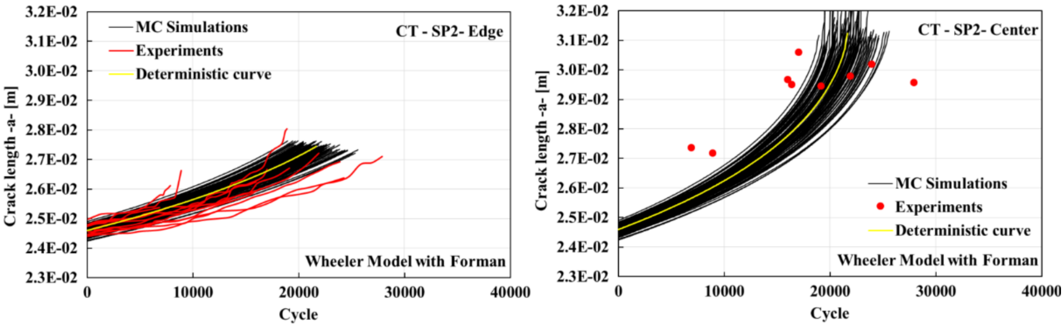

Figure 5.45. Probabilistic crack growth life curves and their comparison with the experiments (CT specimen, SP2 loading spectrum, Wheeler model with Forman)

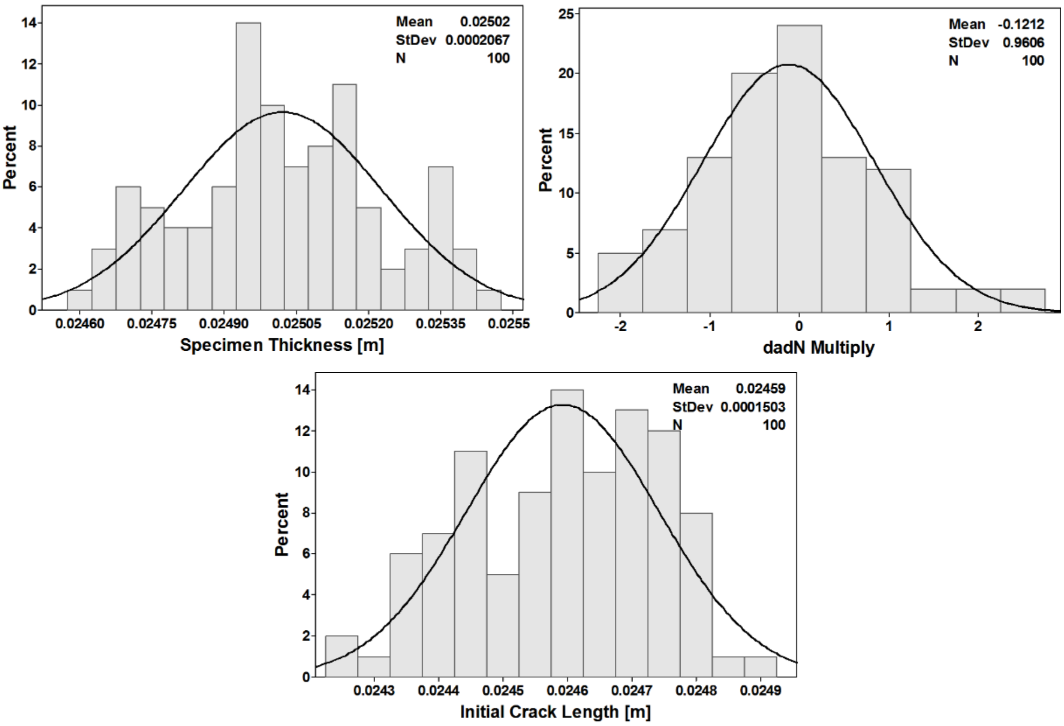

Figure 5.46. Distributions of the inputs used in crack growth life analysis (CT specimen, SP2 loading spectrum, Wheeler model with Forman)

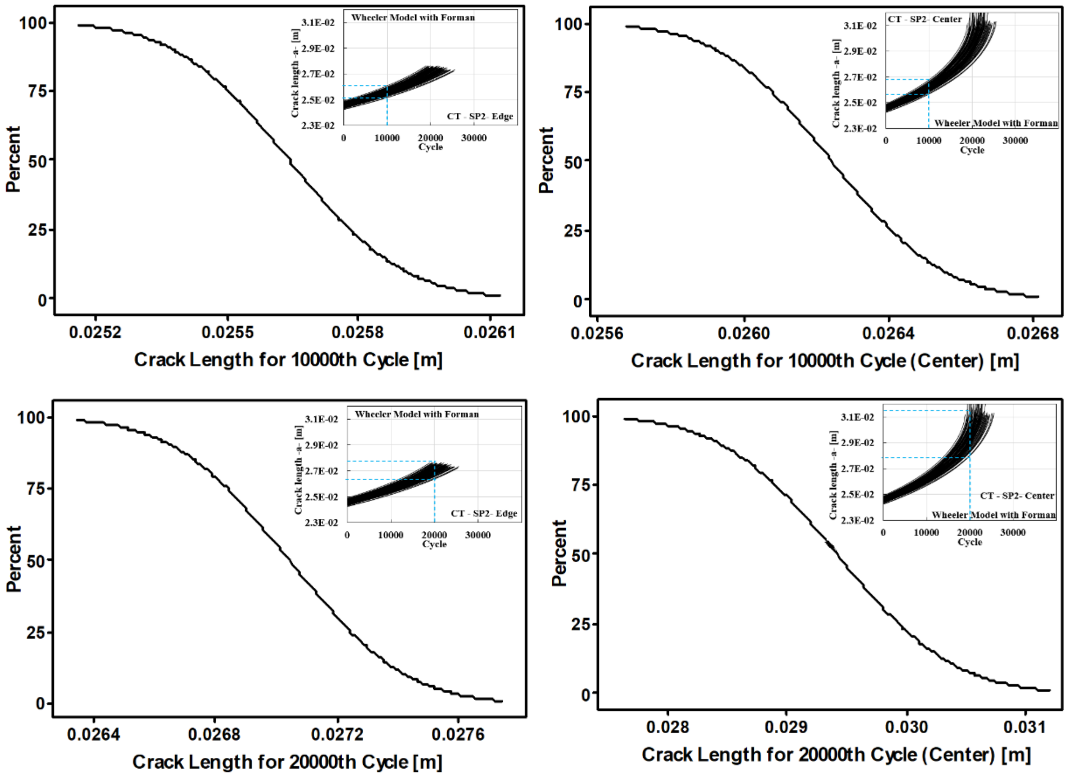

Figure 5.47. CDF for crack lengths under constant cycle load conditions (CT specimen, SP2 loading spectrum, Wheeler model with Forman)

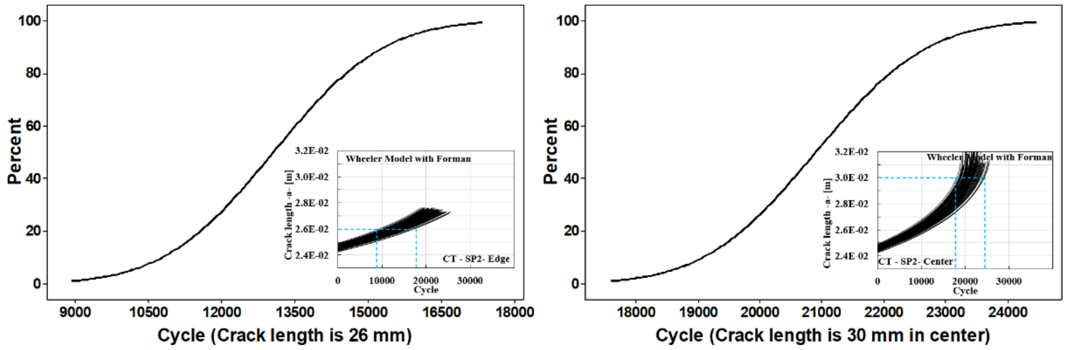

Figure 5.48. CDF for load cycles under constant crack length conditions (CT specimen, SP2 loading spectrum, Wheeler model with Forman)

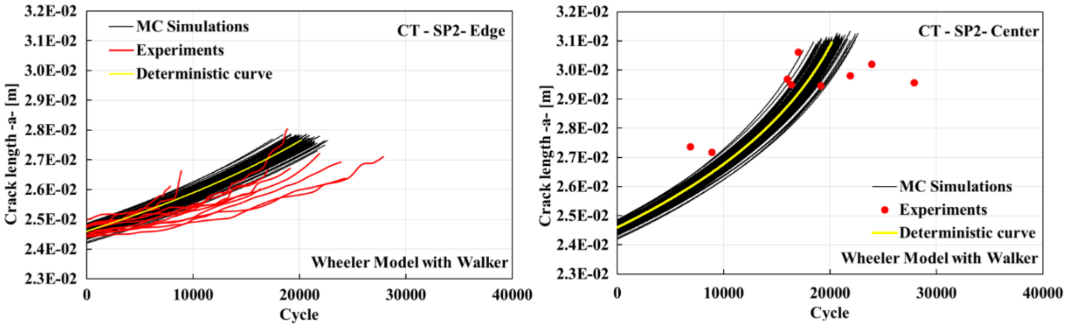

Figure 5.49. Probabilistic crack growth life curves and their comparison with the experiments (CT specimen, SP2 loading spectrum, Wheeler model with Walker)

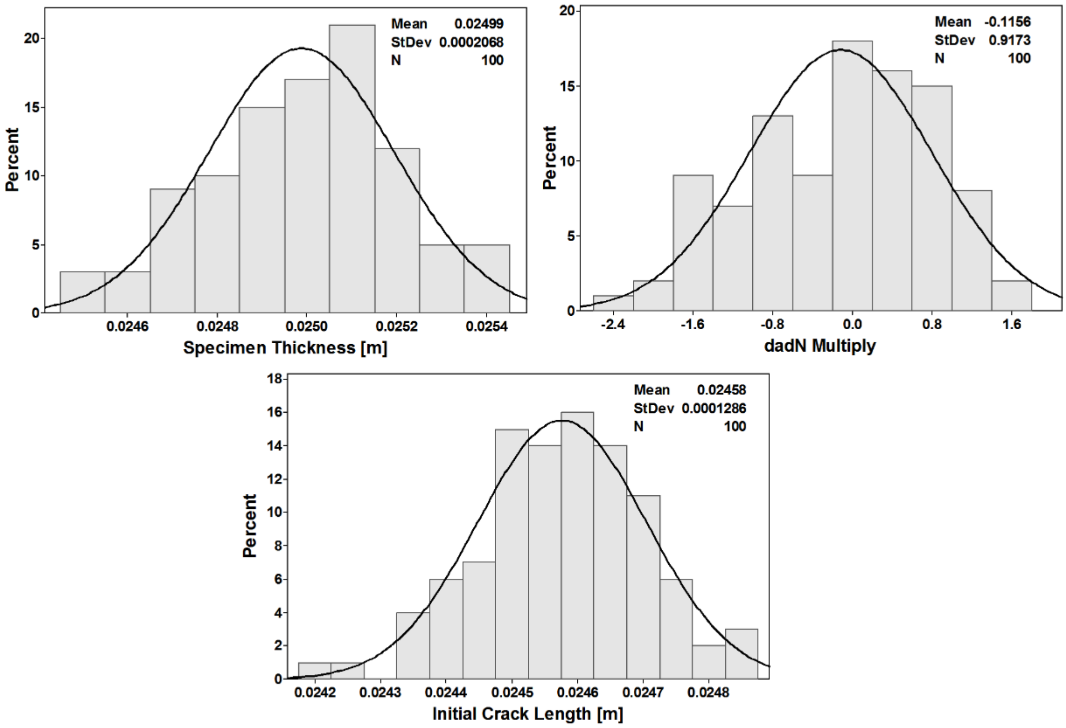

Figure 5.50. Distributions of the inputs used in crack growth life analysis (CT specimen, SP2 loading spectrum, Wheeler model with Walker)

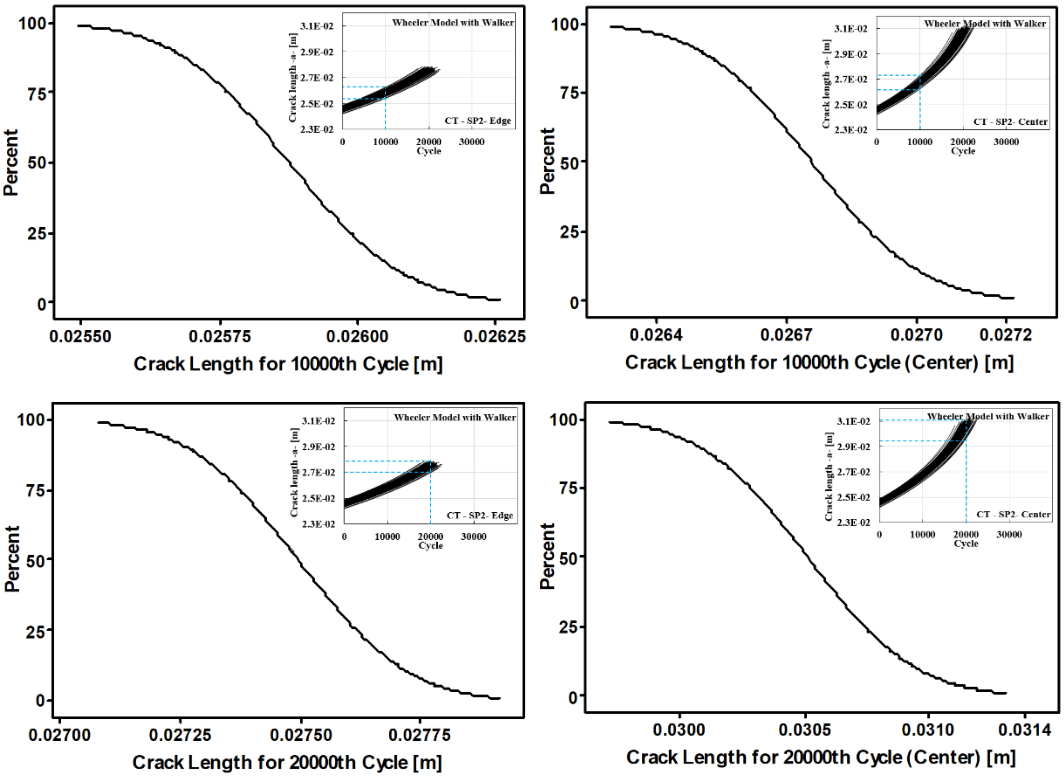

Figure 5.51. CDF for crack lengths under constant cycle load conditions (CT specimen, SP2 loading spectrum, Wheeler model with Walker)

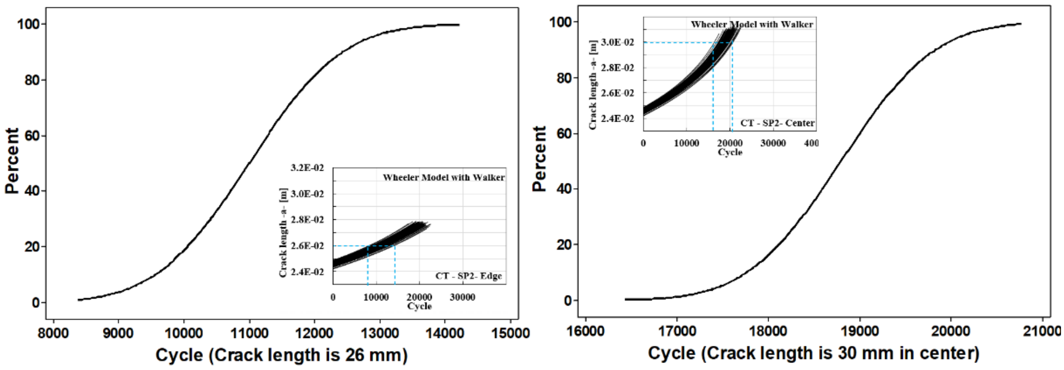

Figure 5.52. CDF for load cycles under constant crack length conditions (CT specimen, SP2 loading spectrum, Wheeler model with Walker)

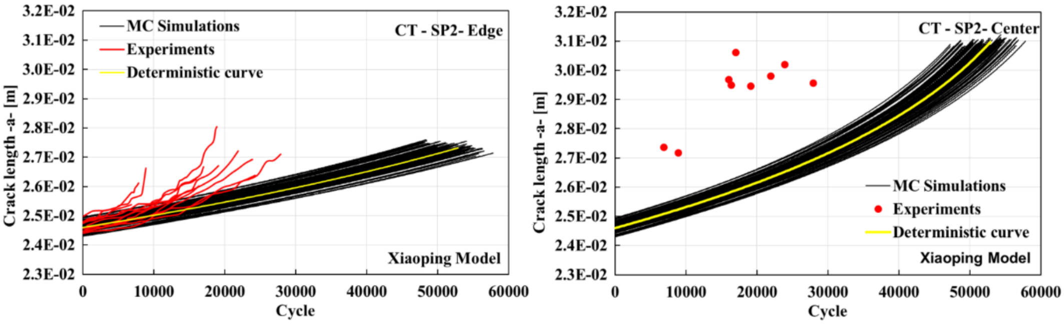

Figure 5.53. Probabilistic crack growth life curves and their comparison with the experiments (CT specimen, SP2 loading spectrum, Xiaoping model)

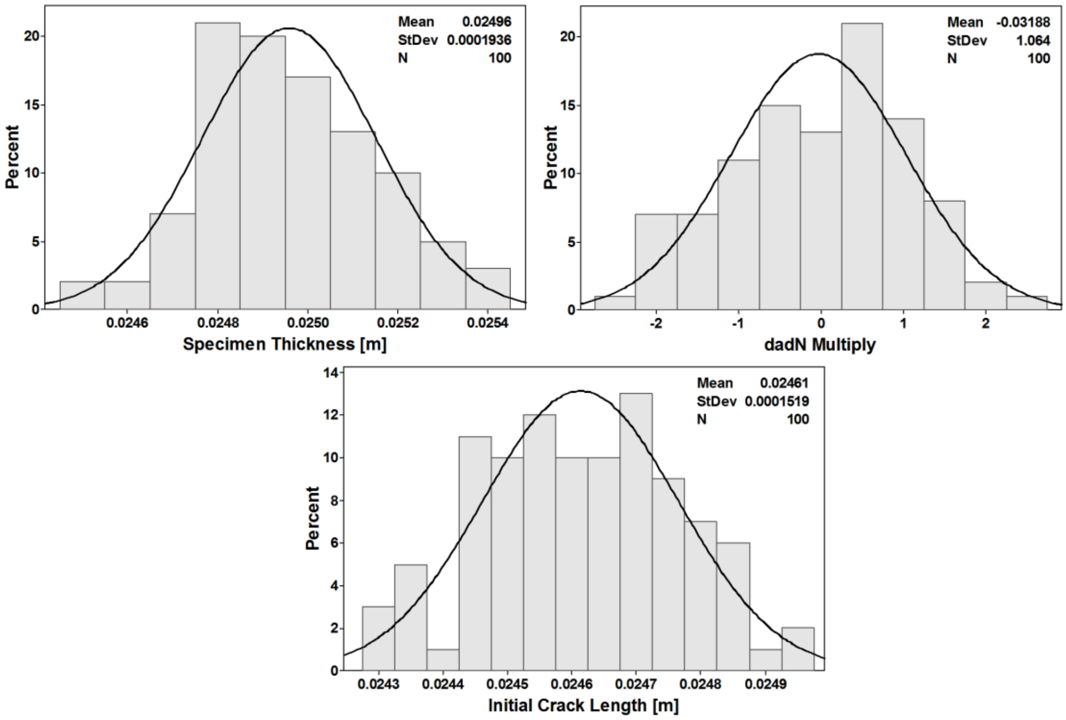

Figure 5.54. Distributions of the inputs used in crack growth life analysis (CT specimen, SP2 loading spectrum, Xiaoping model)

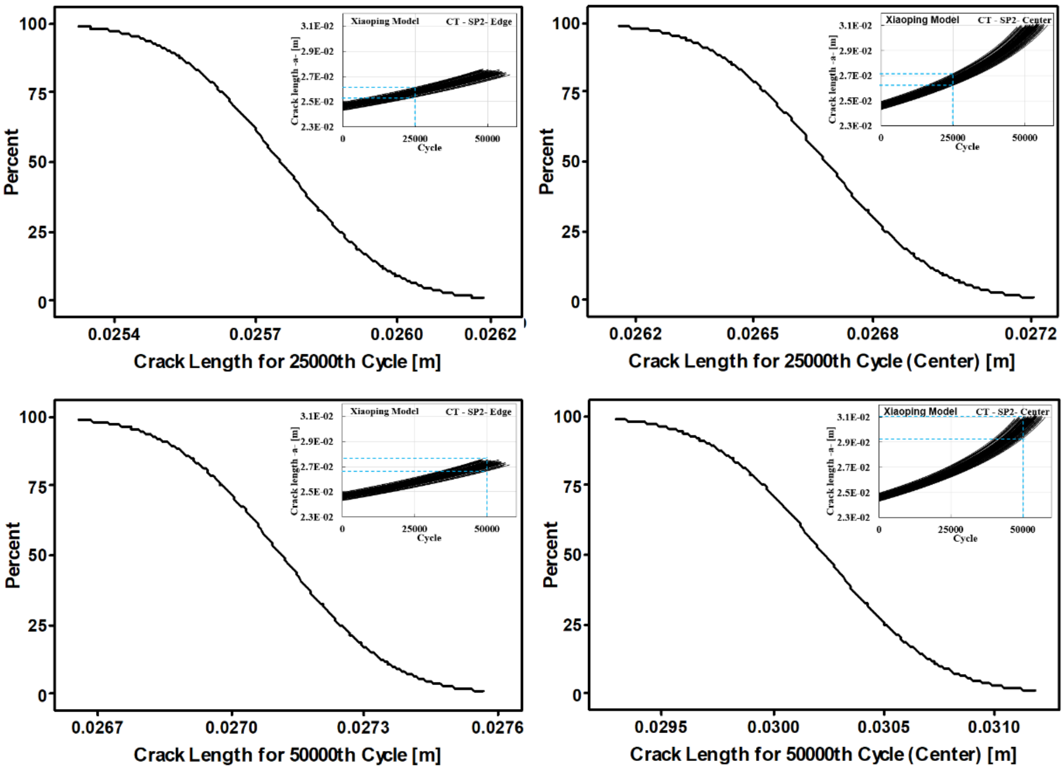

Figure 5.55. CDF for crack lengths under constant cycle load conditions (CT specimen, SP2 loading spectrum, Xiaoping model)

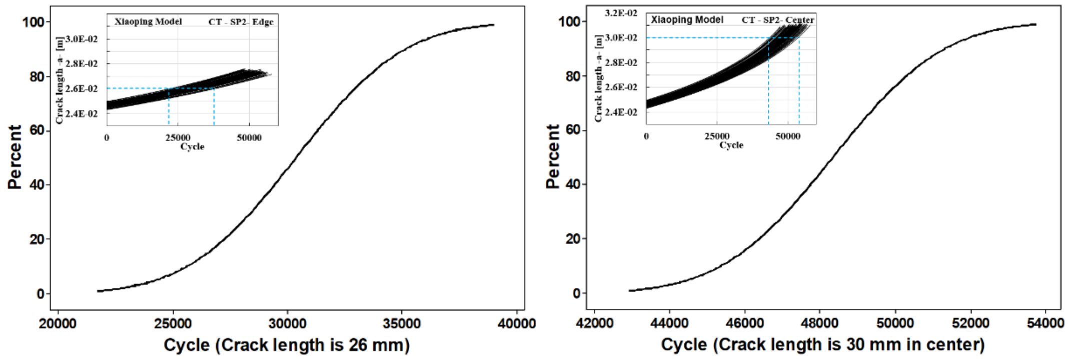

Figure 5.56. CDF for load cycles under constant crack length conditions (CT specimen, SP2 loading spectrum, Xiaoping model)

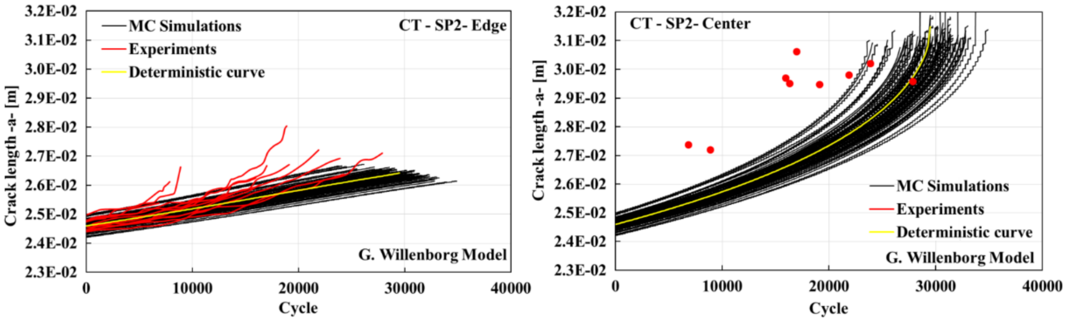

Figure 5.57. Probabilistic crack growth life curves and their comparison with the experiments (CT specimen, SP2 loading spectrum, Generalized Willenborg model)

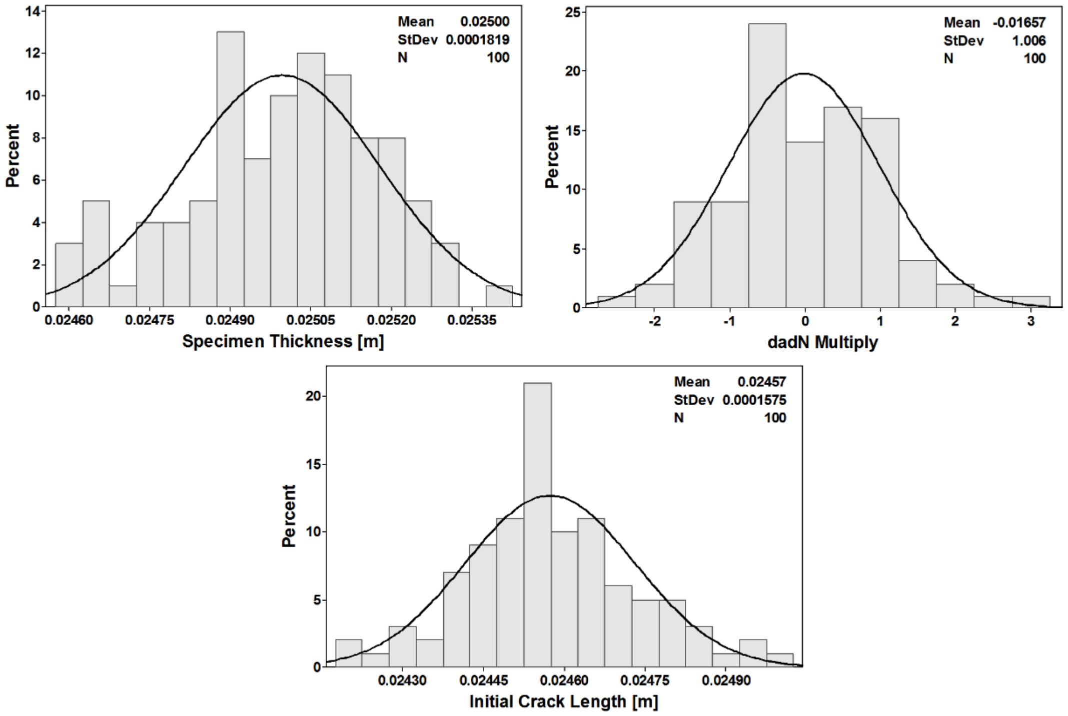

Figure 5.58. Distributions of the inputs used in crack growth life analysis (CT specimen, SP2 loading spectrum, Generalized Willenborg model)

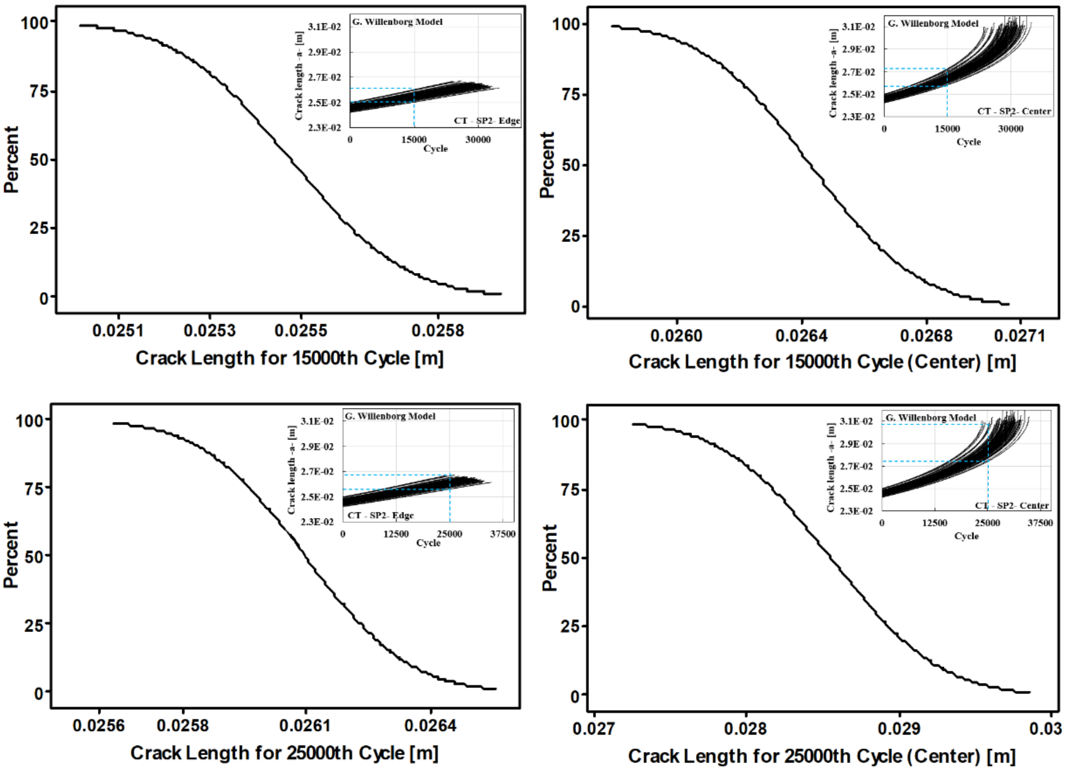

Figure 5.59. CDF for crack lengths under constant cycle load conditions (CT specimen, SP2 loading spectrum, Generalized Willenborg model)

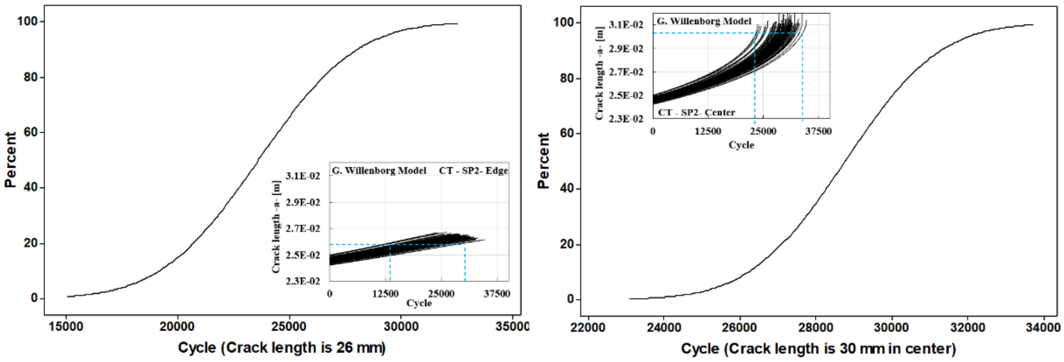

Figure 5.60. CDF for load cycles under constant crack length conditions (CT specimen, SP2 loading spectrum, Generalized Willenborg model)

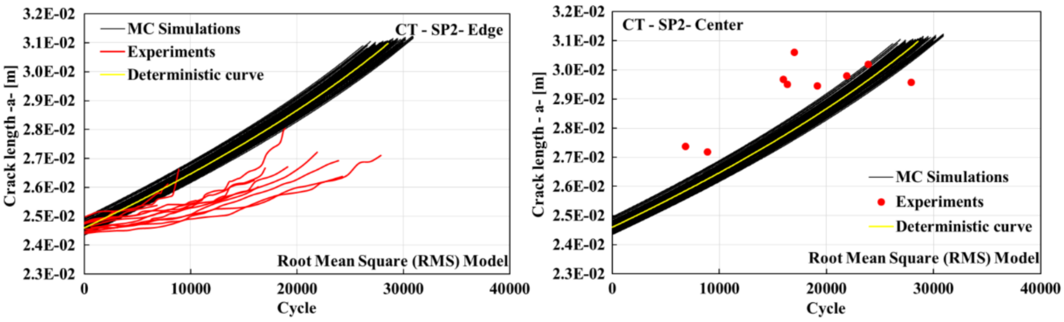

Figure 5.61. Probabilistic crack growth life curves and their comparison with the experiments (CT specimen, SP2 loading spectrum, Root mean square model)

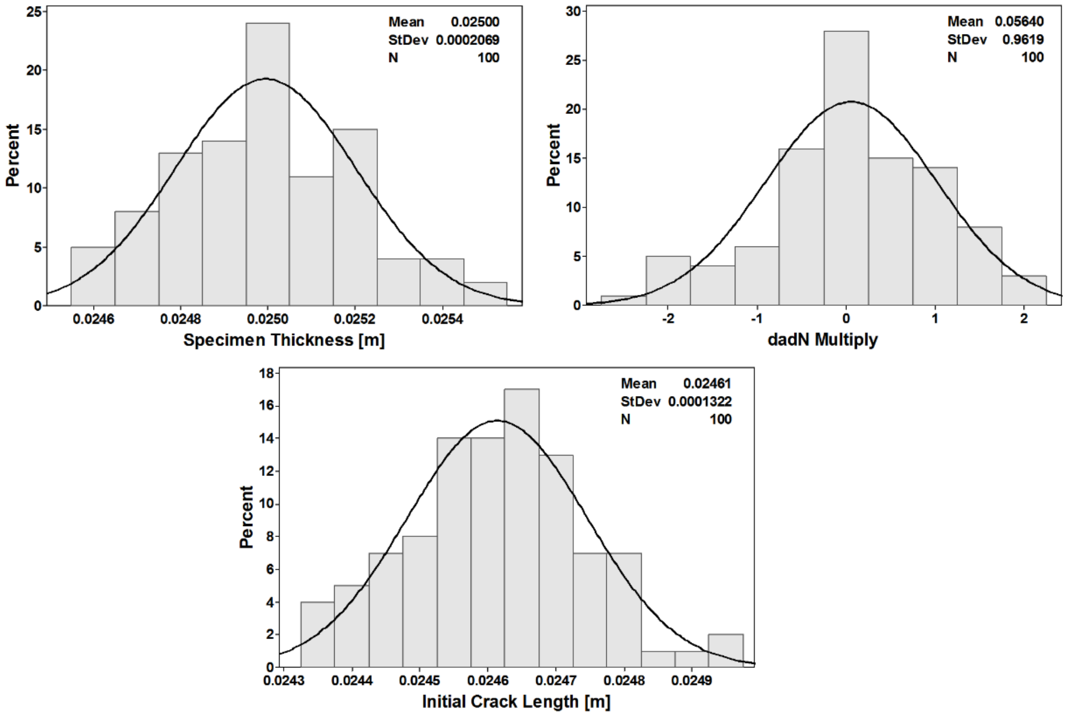

Figure 5.62. Distributions of the inputs used in crack growth life analysis (CT specimen, SP2 loading spectrum, Root mean square model)

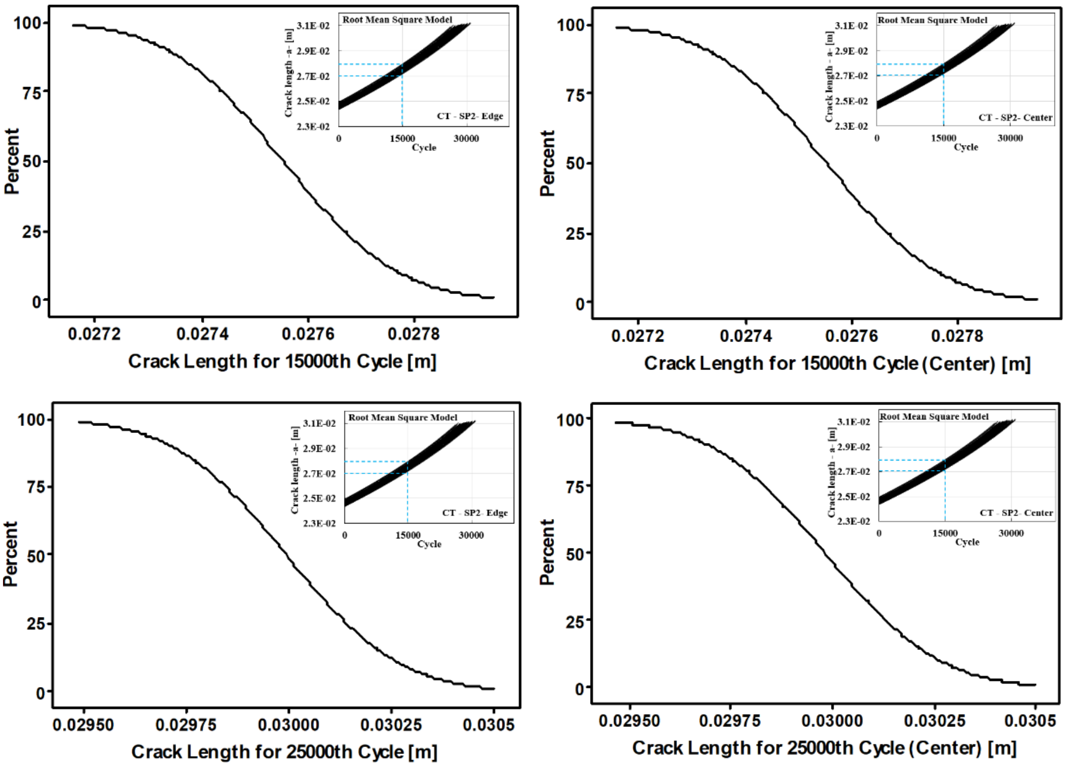

Figure 5.63. CDF for crack lengths under constant cycle load conditions (CT specimen, SP2 loading spectrum, Root mean square model)

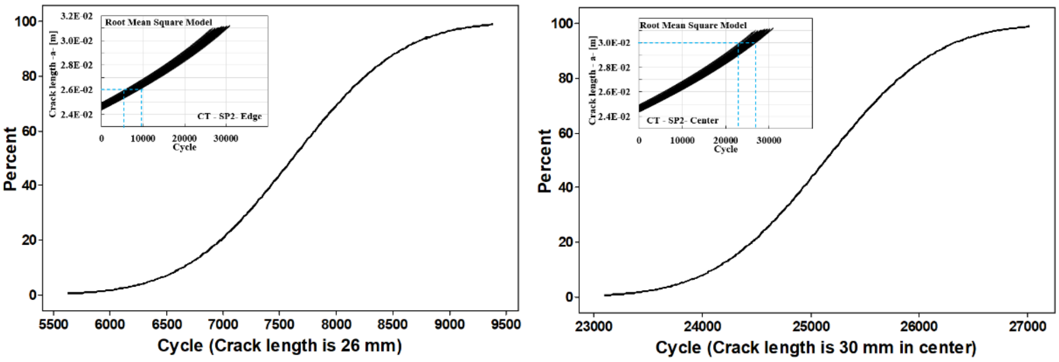

Figure 5.64. CDF for load cycles under constant crack length conditions (CT specimen, SP2 loading spectrum, Root mean square model)

As in the two-dimensional crack propagation explained above, different crack propagation models were used for three-dimensional mode-I crack propagation in LJ specimen, and the comparison of the models is given in Table 5.1. SOL index, which was previously described, was also applied and not applied for three-dimensional crack propagation simulations. As can be seen from Table 5.1., simulations without SOL index are closer to experimental results. Since propagation of a semi-elliptical surface crack is subjected to geometrical constraint due to elliptical shape, it is considered that after the overload, the three-dimensional crack propagation rate is not as fast as the two-dimensional crack. As a result, as can be seen from the simulation results with LJ specimen, the SOL index was not used in the three-dimensional mode-I crack propagation analysis.

Probabilistic crack propagation curves obtained from Monte Carlo simulations with different crack propagation models for LJ specimen are presented in Figure 5.65. - Figure 5.120. Input and output distributions are also given for each model. The distributions in MC Simulation outputs are expressed in two different ways as the crack length probability distribution corresponding to any number of cycles or as the probability distribution of the load cycles corresponding to any crack length. The normal probability distributions and cumulative distribution graphs can also be obtained by using output distributions. In the graphs, the results are given for both the free surface (edge) and the center of crack tip (center) points of the LJ specimen.

Table 5.1. Comparison of variable amplitude fatigue crack growth model results (LJ Specimen)

| | | | | LJ SP1 | | | | LJ SP2 | | | | LJ SP3 | | | |
|---|---|---|---|---|---|---|---|---|---|---|---|---|---|---|---|
| | | | | **Cycle** | | **Edge crack length** | | **Cycle** | | **Edge crack length** | | **Cycle** | | **Edge crack length** | |
| **Model** | **FCG model** | **FCG equation** | **SOL index** | **Test** | **Sim.** | **Test** | **Sim.** | **Test** | **Sim.** | **Test** | **Sim.** | **Test** | **Sim.** | **Test** | **Sim.** |
| Composite C-n | Wheeler | Forman Const wth Paris-Erdogan | ✓ | 42650 | 26200 | ≈ 10.2 mm | 10.7 mm | 35169 | 16164 | ≈ 10.2 mm | 10.7 mm | 31586 | 20029 | ≈ 10.3 mm | 10.7 mm |
| Composite C-n | Wheeler | Forman Const wth Paris-Erdogan | ✗ | | 34200 | | 10.7 mm | | 25200 | | 10.8 mm | | 27057 | | 10.8 mm |
| Composite C-n | Wheeler | Walker | ✓ | | 55700 | | 10.1 mm | | 14514 | | 11.1 mm | | 20369 | | 10.9 mm |
| Composite C-n | Wheeler | Walker | ✗ | | 83700 | | 10.1 mm | | 24140 | | 11.1 mm | | 32072 | | 10.9 mm |
| Walker | Wheeler | Walker | ✓ | | 20200 | | 11.0 mm | | 12980 | | 10.8 mm | | 16100 | | 10.7 mm |
| Walker | Wheeler | Walker | ✗ | | 29700 | | 10.7 mm | | 22183 | | 10.8 mm | | 25647 | | 10.7 mm |
| Forman | Wheeler | Forman | ✓ | | 37200 | | 11.4 mm | | 21240 | | 11.1 mm | | 25598 | | 10.8 mm |
| Forman | Wheeler | Forman | ✗ | | 55200 | | 10.9 mm | | 36108 | | 10.9 mm | | 40438 | | 11.1 mm |
| Xiaoping | Wheeler | Paris-Erdogan | ✗ | | 55700 | | 10.9 mm | | 40356 | | 11.0 mm | | 45301 | | 11.0 mm |
| GWillenborg | GWillenborg | Forman | ✓ | | 50200 | | 11.9 mm | | 20532 | | 11.7 mm | | 24553 | | 11.2 mm |
| RMS (Manujatha) | RMS | Similar to Newman | ✗ | | 19900 | | 12.5 mm | | 24036 | | 12.5 mm | | 24800 | | 12.5 mm |

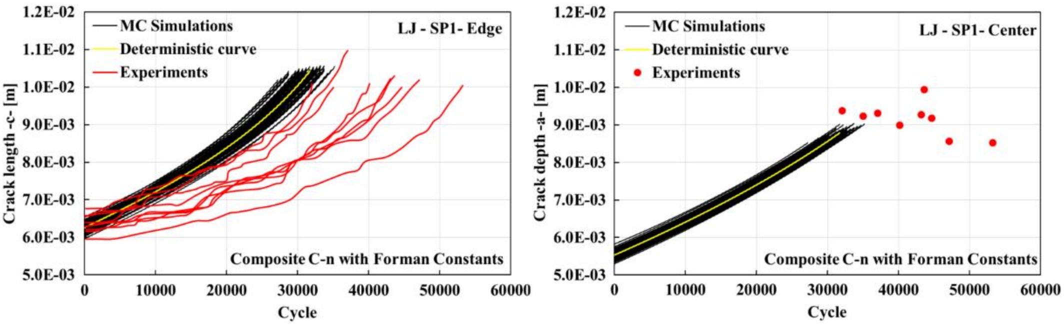

Figure 5.65. Probabilistic crack growth life curves and their comparison with the experiments (LJ specimen, SP1 loading spectrum, Composite C-n with Forman Constants)

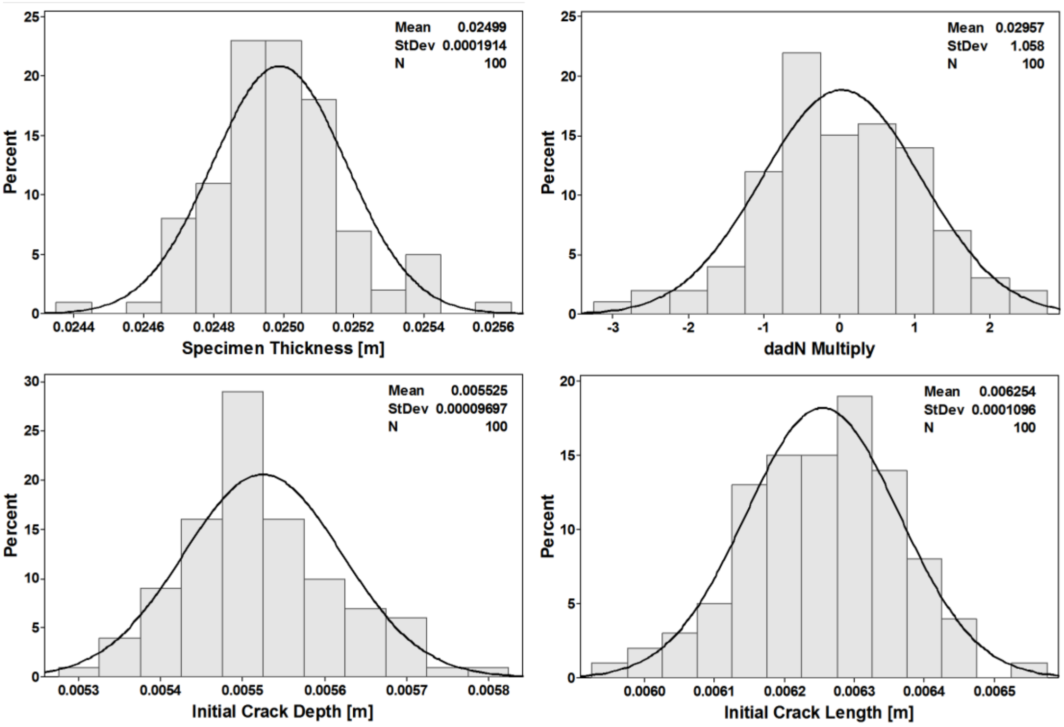

Figure 5.66. Distributions of the inputs used in crack growth life analysis (LJ specimen, SP1 loading spectrum, Composite C-n with Forman Constants)

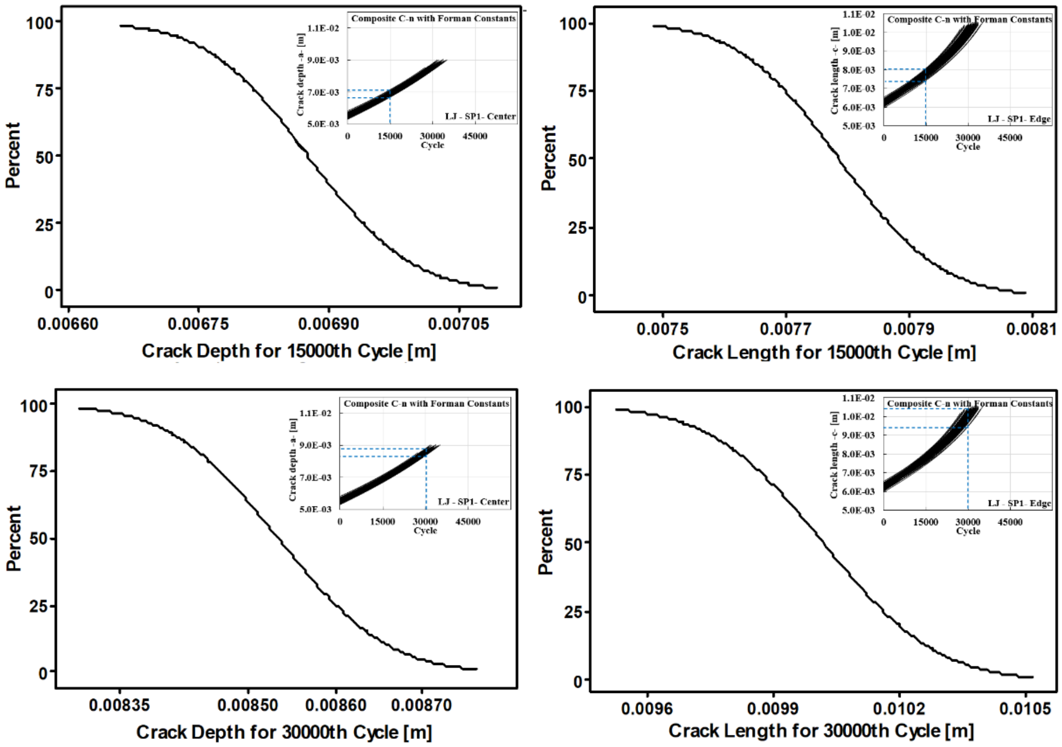

Figure 5.67. CDF for crack lengths under constant cycle load conditions (LJ specimen, SP1 loading spectrum, Composite C-n with Forman Constants)

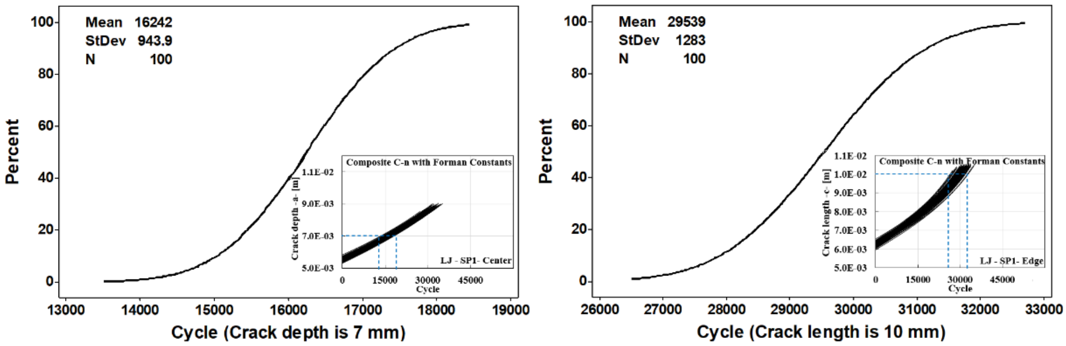

Figure 5.68. CDF for load cycles under constant crack length conditions (LJ specimen, SP1 loading spectrum, Composite C-n with Forman Constants)

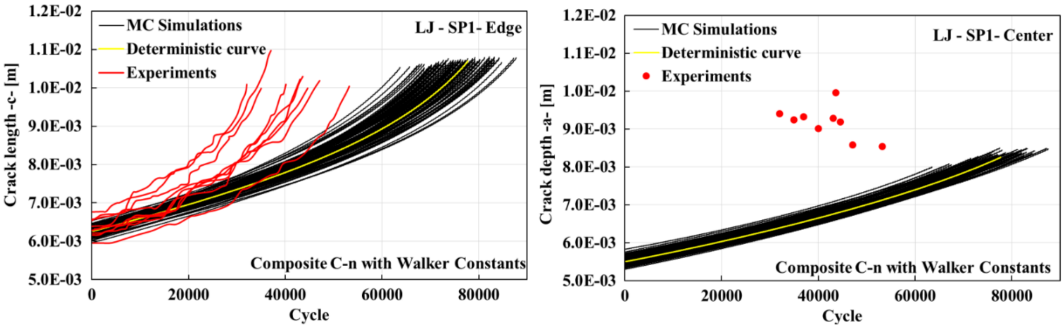

Figure 5.69. Probabilistic crack growth life curves and their comparison with the experiments (LJ specimen, SP1 loading spectrum, Composite C-n with Walker Constants)

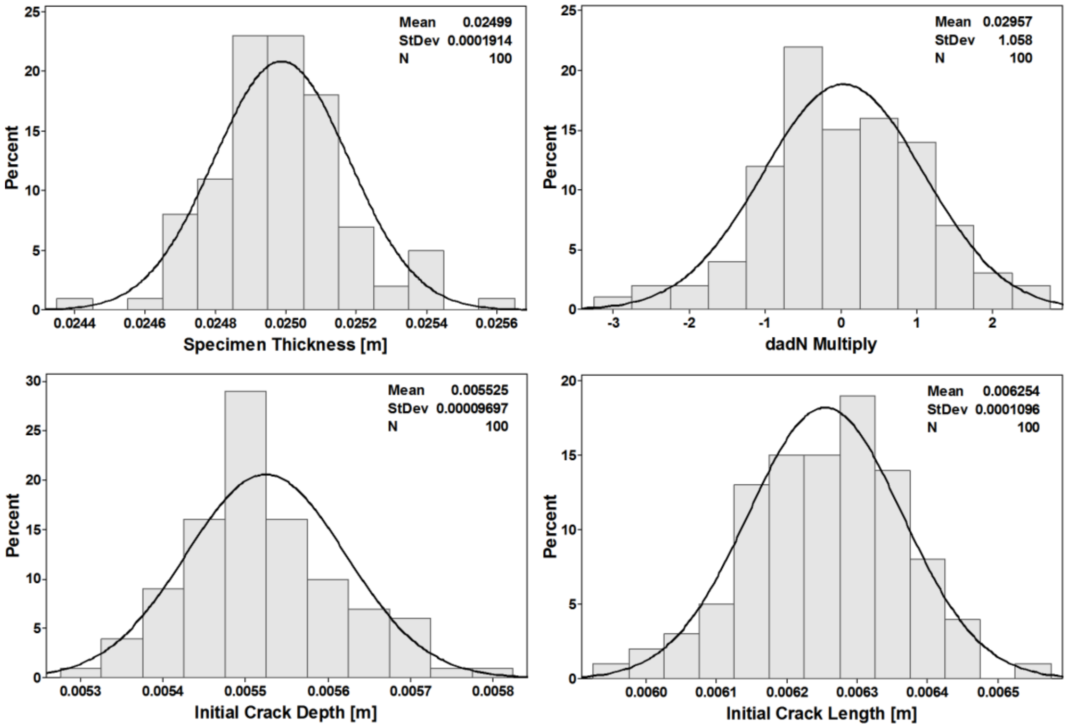

Figure 5.70. Distributions of the inputs used in crack growth life analysis (LJ specimen, SP1 loading spectrum, Composite C-n with Walker Constants)

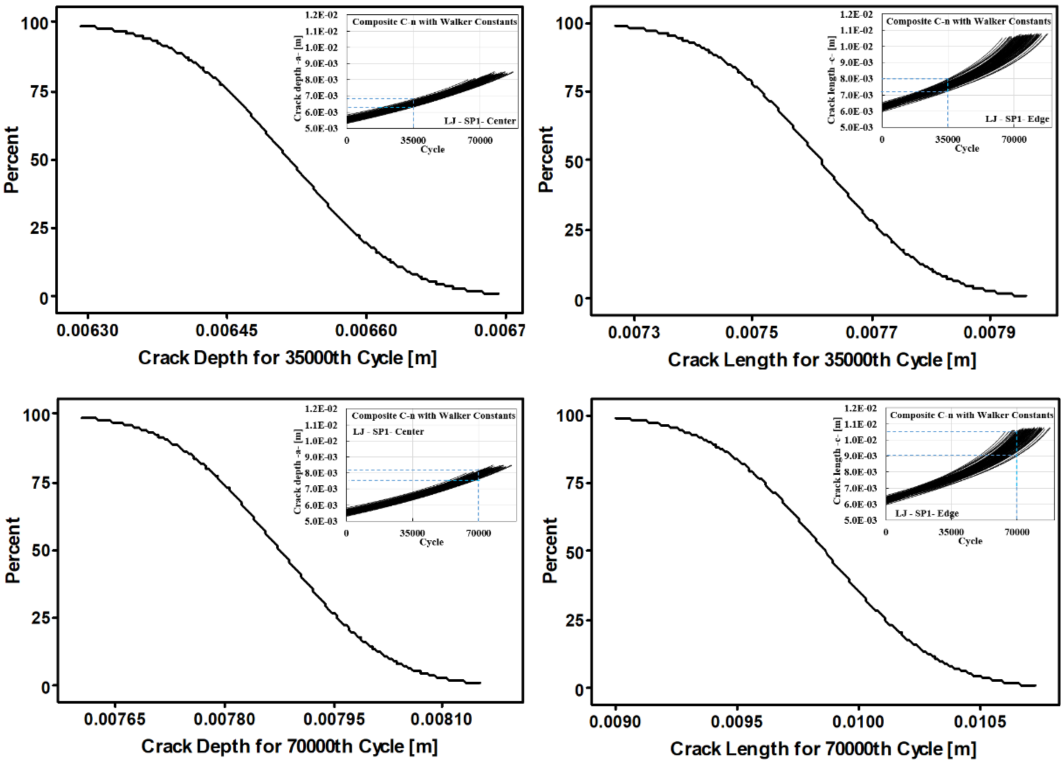

Figure 5.71. CDF for crack lengths under constant cycle load conditions (LJ specimen, SP1 loading spectrum, Composite C-n with Walker Constants)

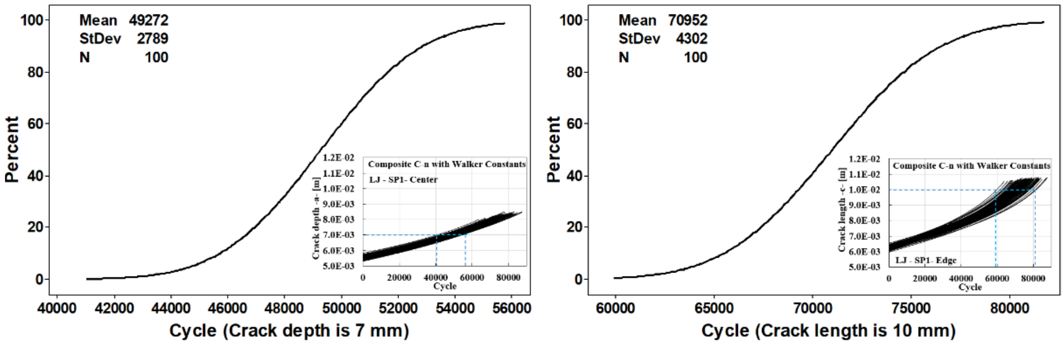

Figure 5.72. CDF for load cycles under constant crack length conditions (LJ specimen, SP1 loading spectrum, Composite C-n with Walker Constants)

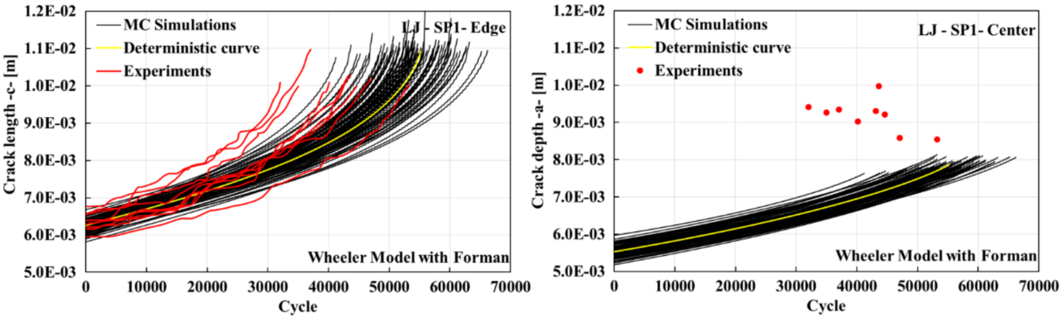

Figure 5.73. Probabilistic crack growth life curves and their comparison with the experiments (LJ specimen, SP1 loading spectrum, Wheeler model with Forman)

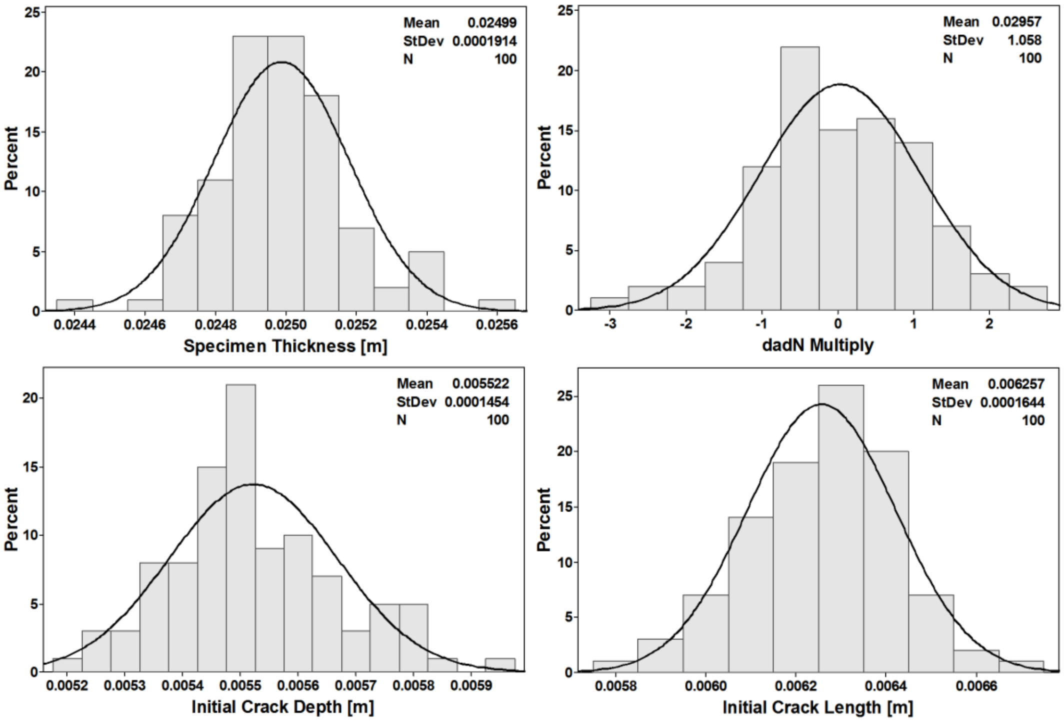

Figure 5.74. Distributions of the inputs used in crack growth life analysis (LJ specimen, SP1 loading spectrum, Wheeler model with Forman)

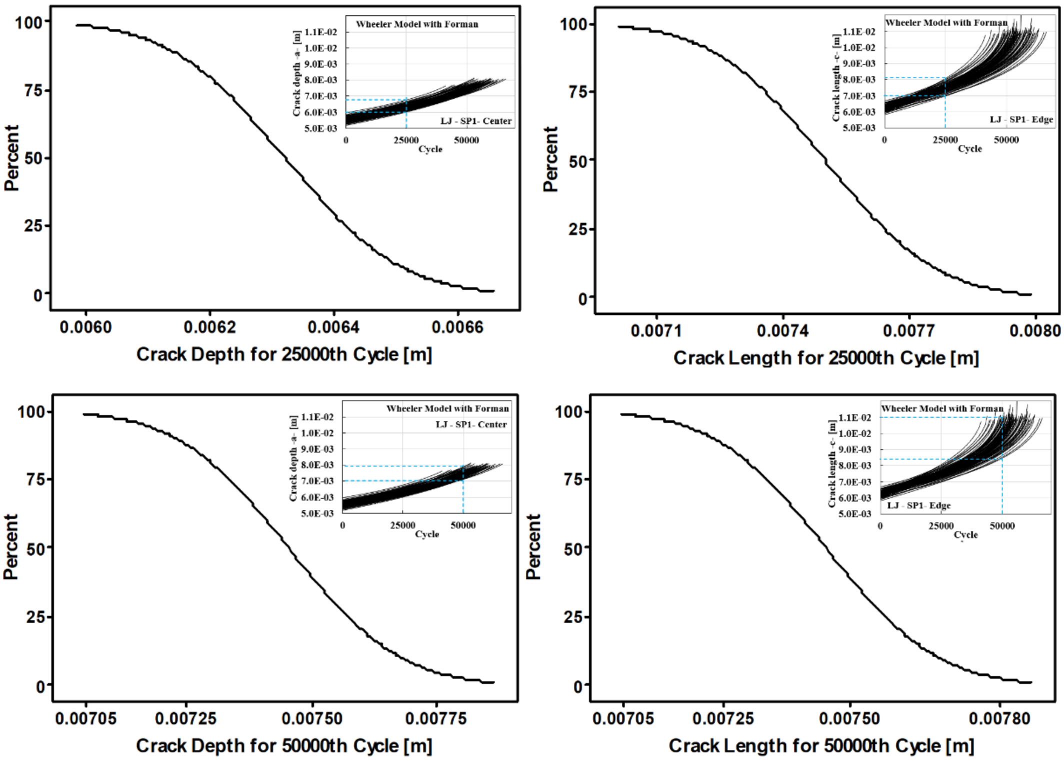

Figure 5.75. CDF for crack lengths under constant cycle load conditions (LJ specimen, SP1 loading spectrum, Wheeler model with Forman)

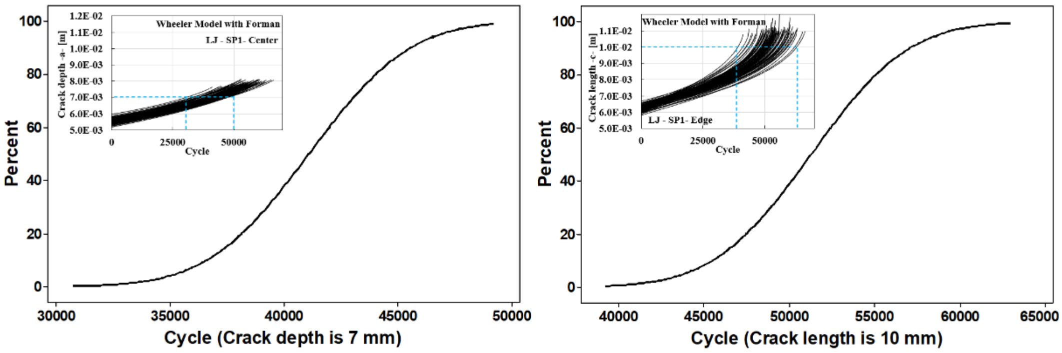

Figure 5.76. CDF for load cycles under constant crack length conditions (LJ specimen, SP1 loading spectrum, Wheeler model with Forman)

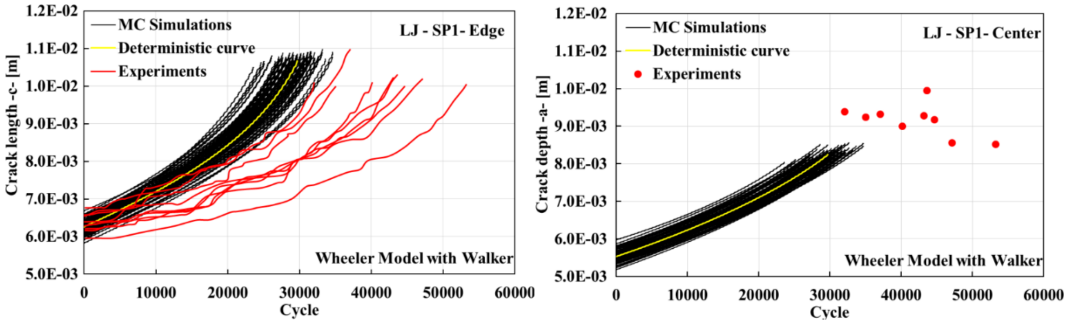

Figure 5.77. Probabilistic crack growth life curves and their comparison with the experiments (LJ specimen, SP1 loading spectrum, Wheeler model with Walker)

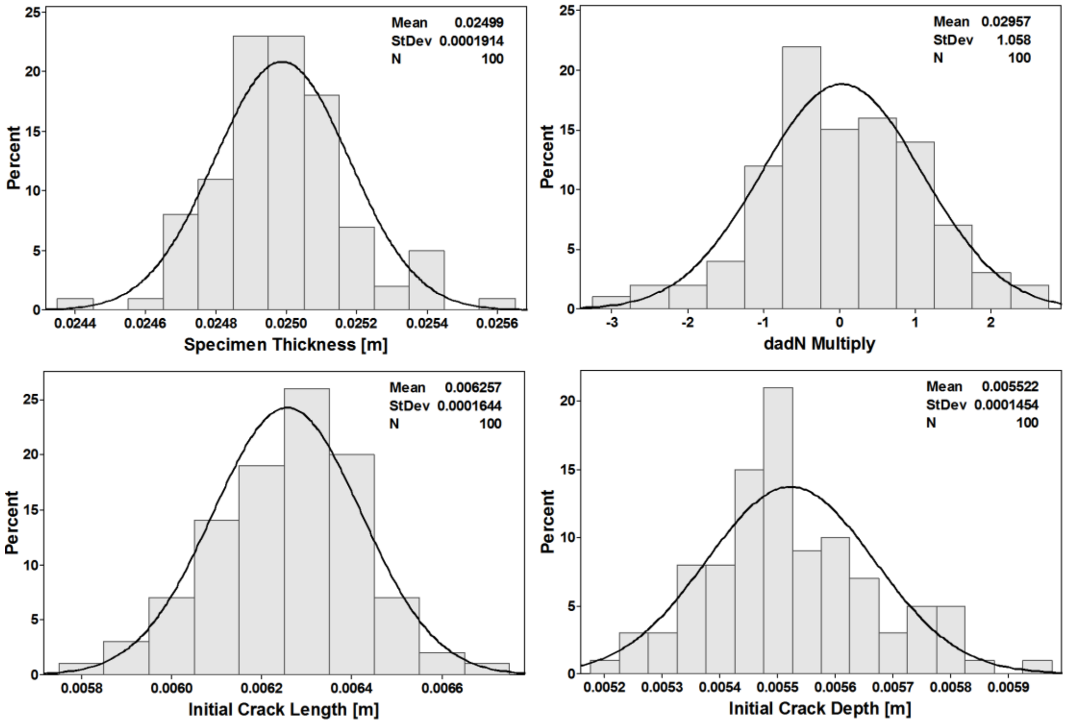

Figure 5.78. Distributions of the inputs used in crack growth life analysis (LJ specimen, SP1 loading spectrum, Wheeler model with Walker)

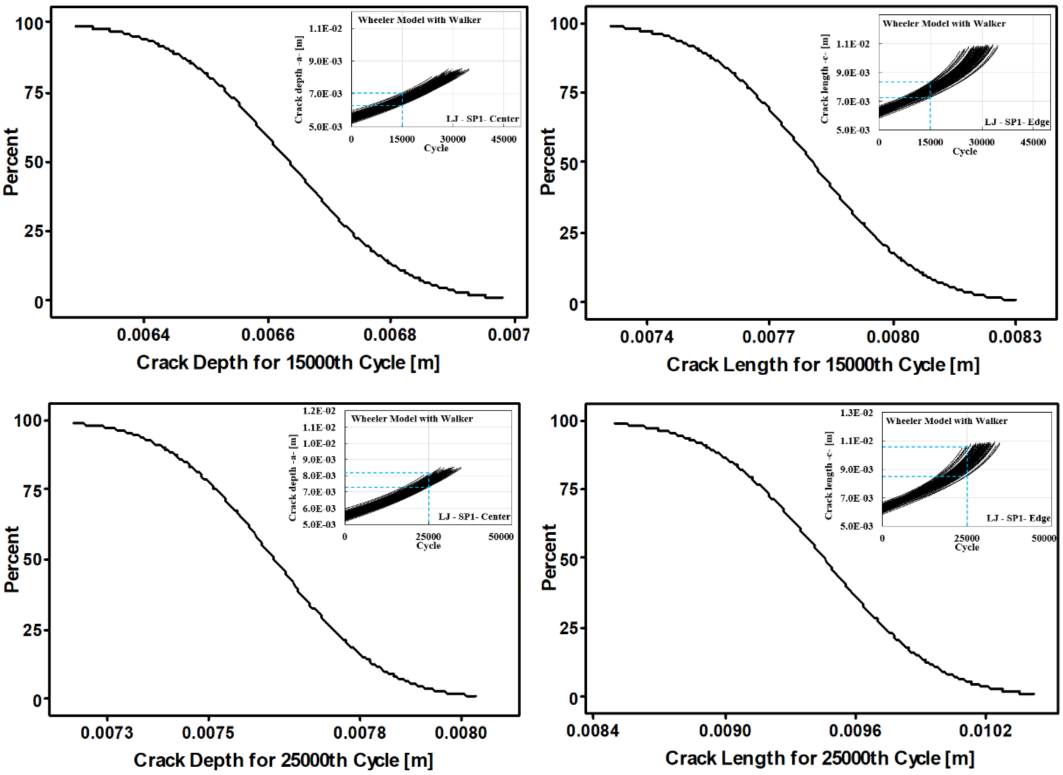

Figure 5.79. CDF for crack lengths under constant cycle load conditions (LJ specimen, SP1 loading spectrum, Wheeler model with Walker)

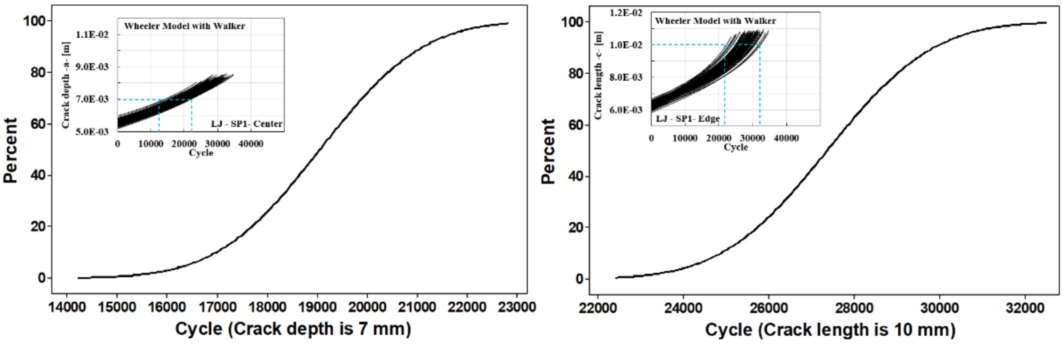

Figure 5.80. CDF for load cycles under constant crack length conditions (LJ specimen, SP1 loading spectrum, Wheeler model with Walker)

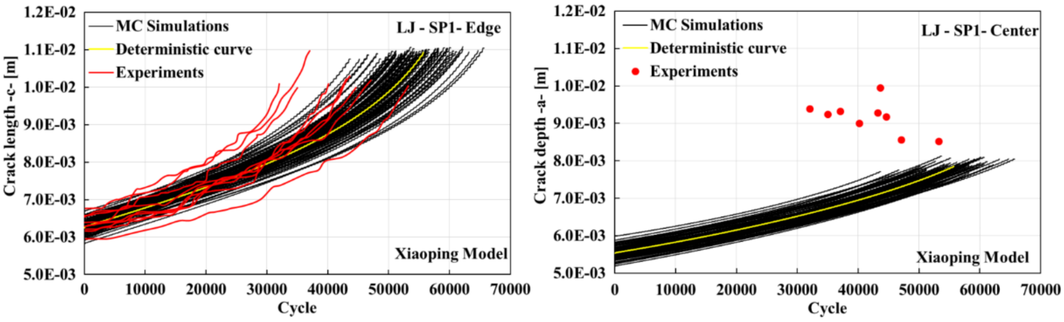

Figure 5.81. Probabilistic crack growth life curves and their comparison with the experiments (LJ specimen, SP1 loading spectrum, Xiaoping model)

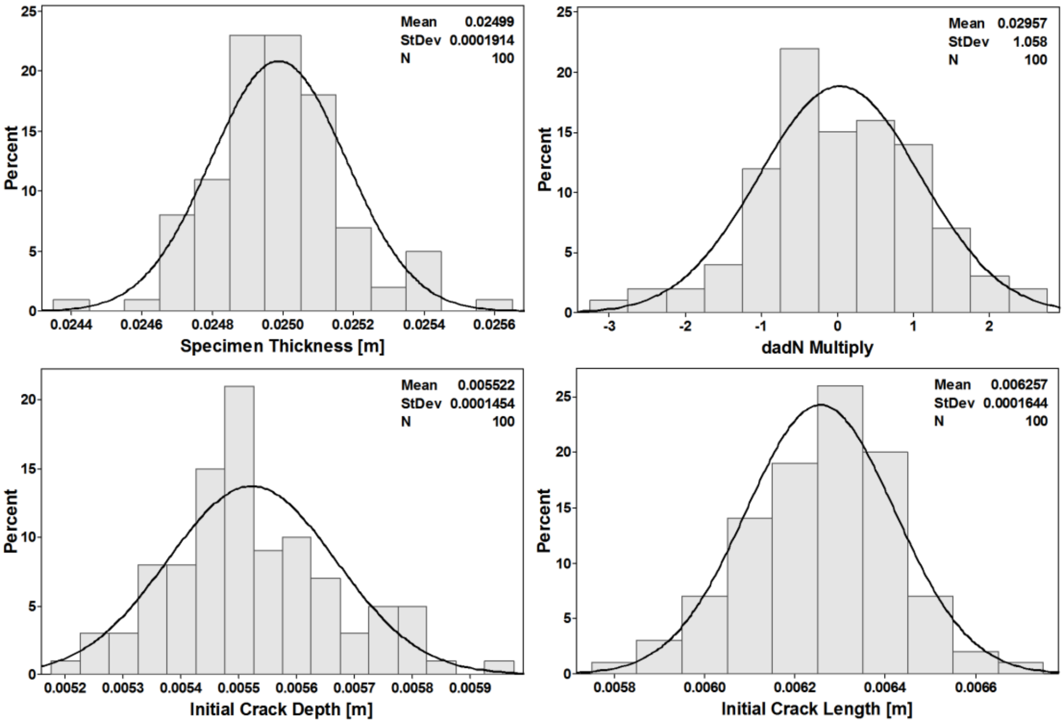

Figure 5.82. Distributions of the inputs used in crack growth life analysis (LJspecimen, SP1 loading spectrum, Xiaoping model)

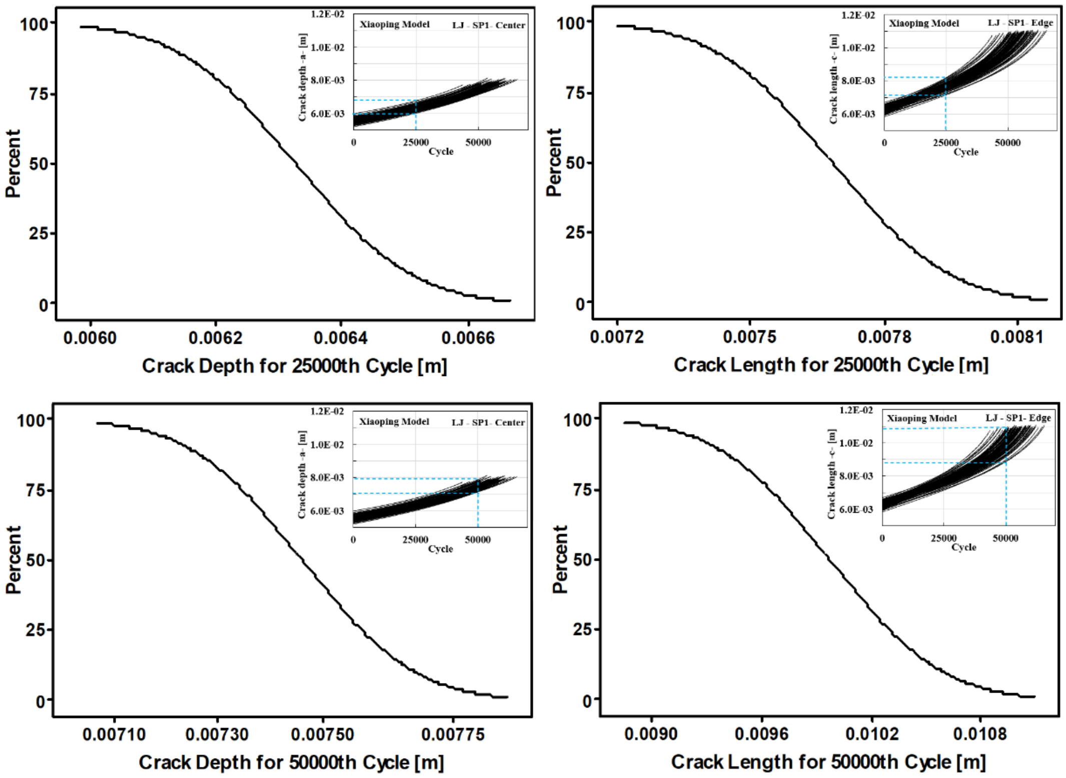

Figure 5.83. CDF for crack lengths under constant cycle load conditions (LJ specimen, SP1 loading spectrum, Xiaoping model)

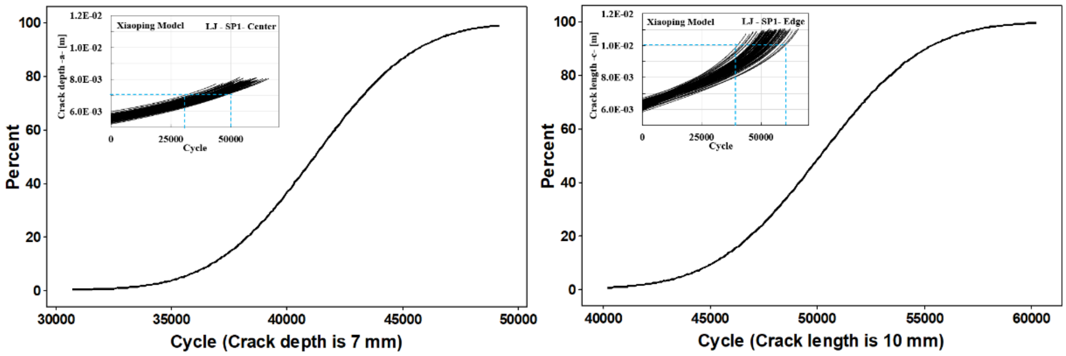

Figure 5.84. CDF for load cycles under constant crack length conditions (LJ specimen, SP1 loading spectrum, Xiaoping model)

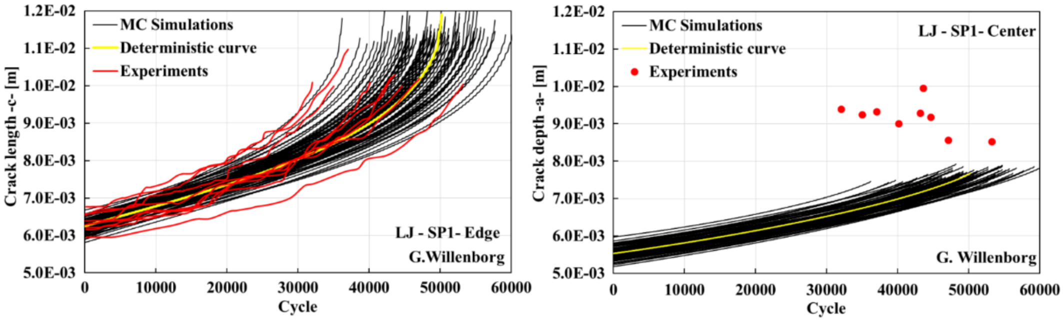

Figure 5.85. Probabilistic crack growth life curves and their comparison with the experiments (LJ specimen, SP1 loading spectrum, Generalized Willenborg model)

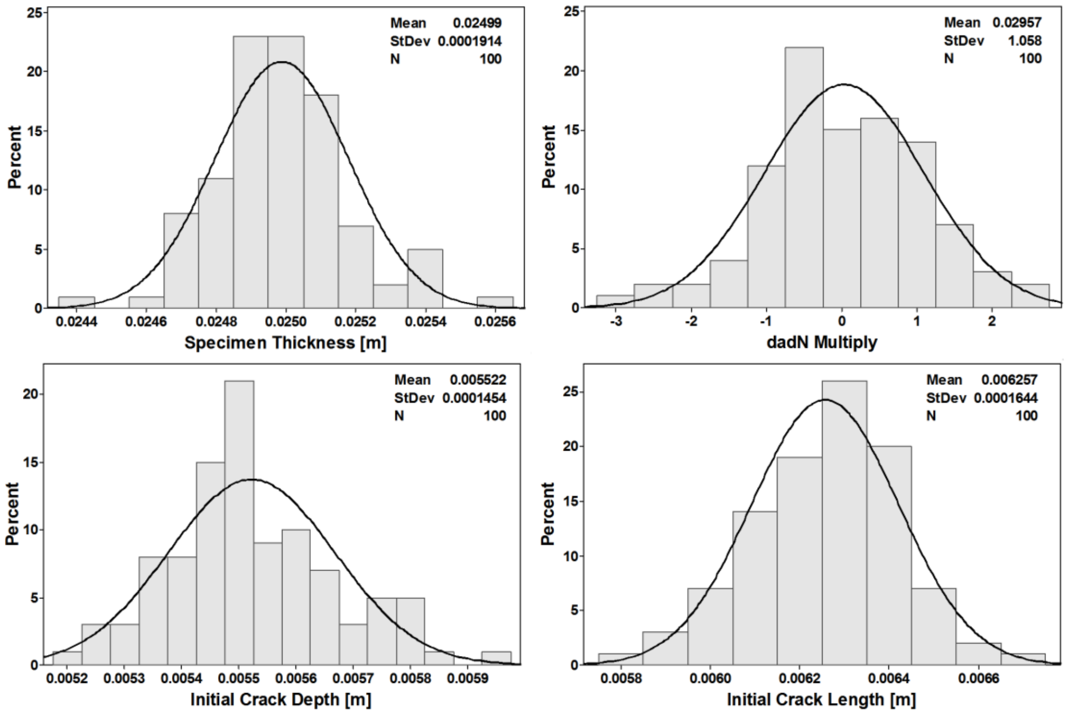

Figure 5.86. Distributions of the inputs used in crack growth life analysis (LJ specimen, SP1 loading spectrum, Generalized Willenborg model)

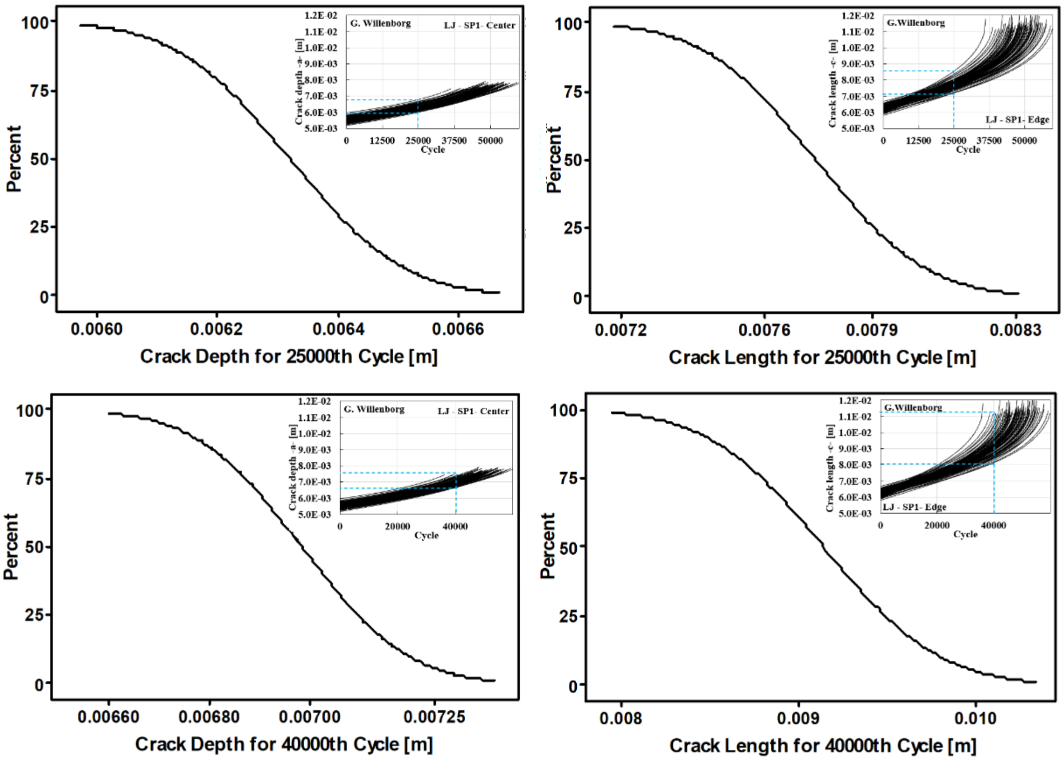

Figure 5.87. CDF for crack lengths under constant cycle load conditions (LJ specimen, SP1 loading spectrum, Generalized Willenborg model)

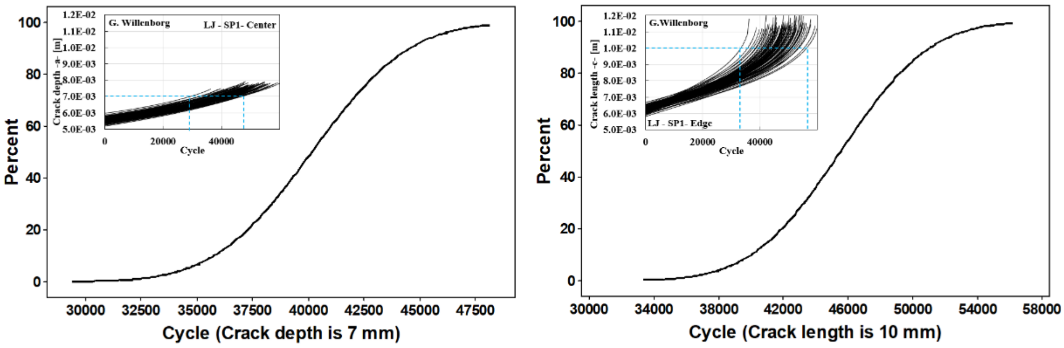

Figure 5.88. CDF for load cycles under constant crack length conditions (LJ specimen, SP1 loading spectrum, Generalized Willenborg model)

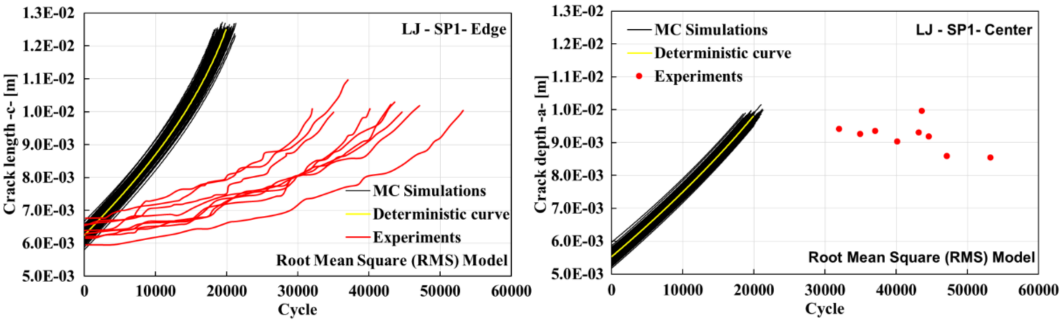

Figure 5.89. Probabilistic crack growth life curves and their comparison with the experiments (LJ specimen, SP1 loading spectrum, Root mean square model)

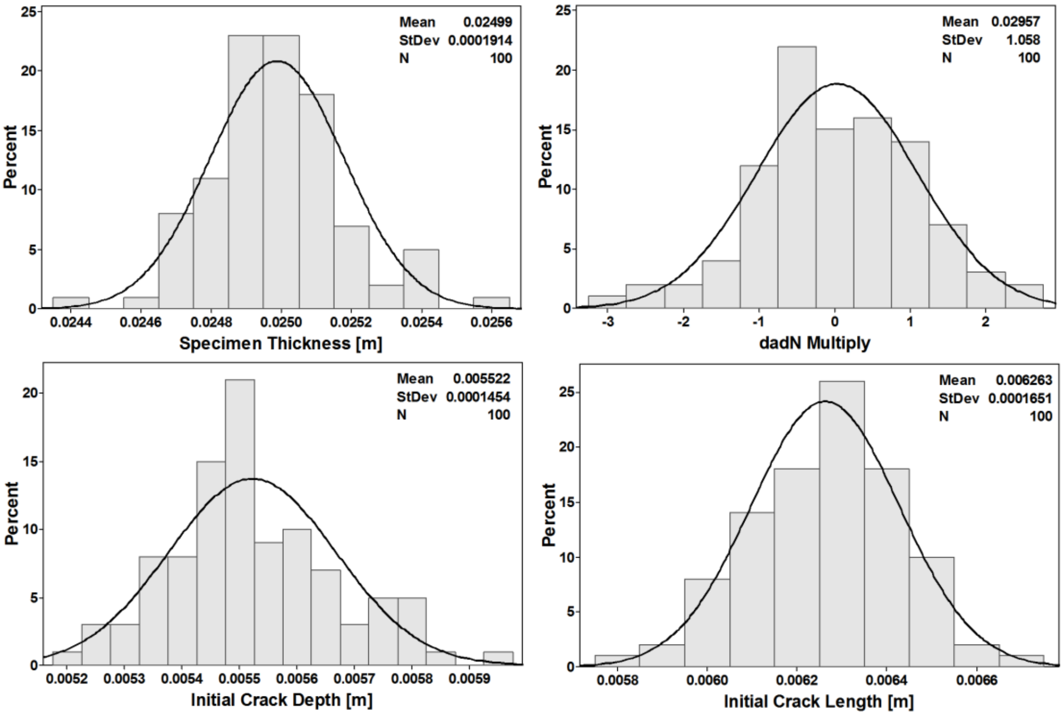

Figure 5.90. Distributions of the inputs used in crack growth life analysis (LJ specimen, SP1 loading spectrum, Root mean square model)

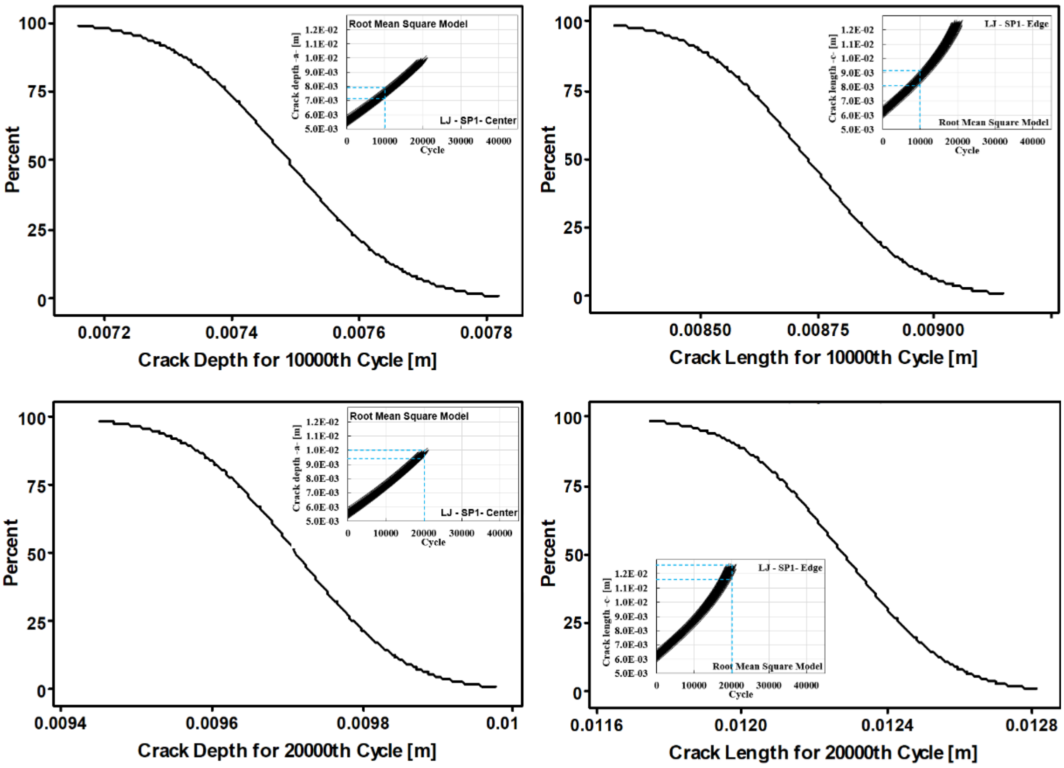

Figure 5.91. CDF for crack lengths under constant cycle load conditions (LJ specimen, SP1 loading spectrum, Root mean square model)

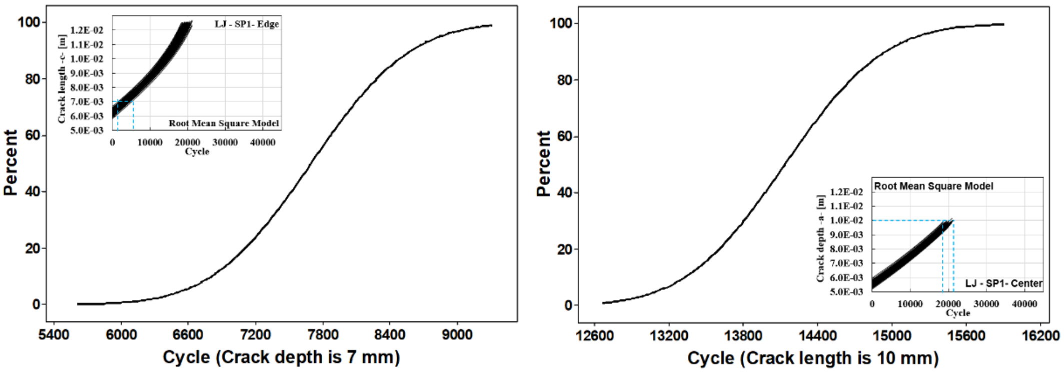

Figure 5.92. CDF for load cycles under constant crack length conditions (LJ specimen, SP1 loading spectrum, Root mean square model)

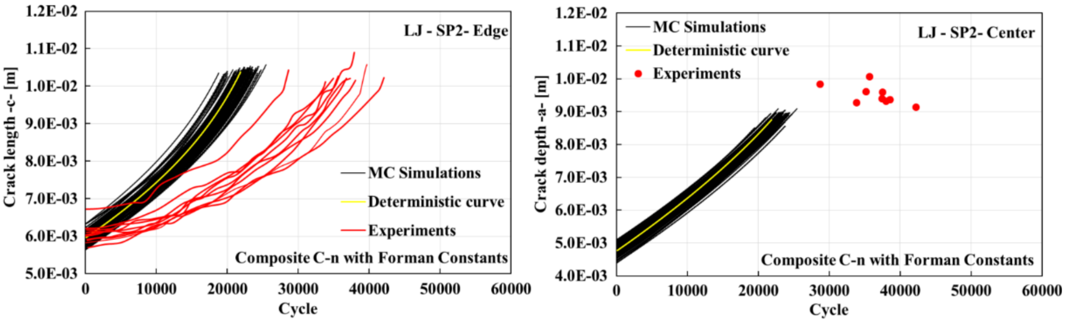

Figure 5.93. Probabilistic crack growth life curves and their comparison with the experiments (LJ specimen, SP2 loading spectrum, Composite C-n with Forman Constants)

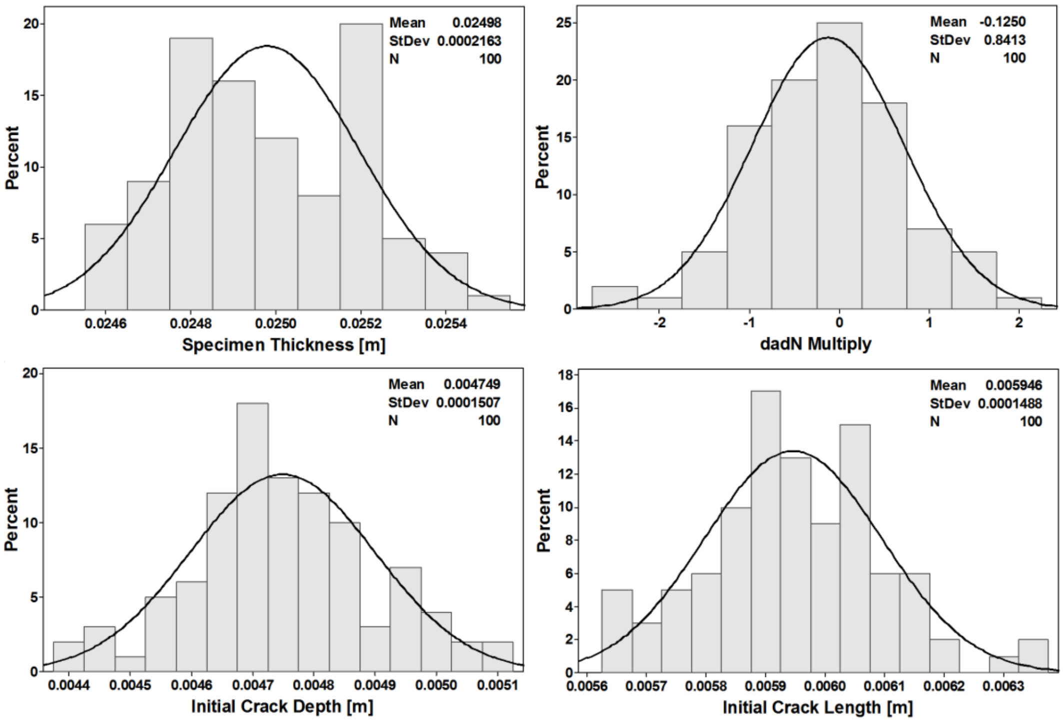

Figure 5.94. Distributions of the inputs used in crack growth life analysis (LJ specimen, SP2 loading spectrum, Composite C-n with Forman Constants)

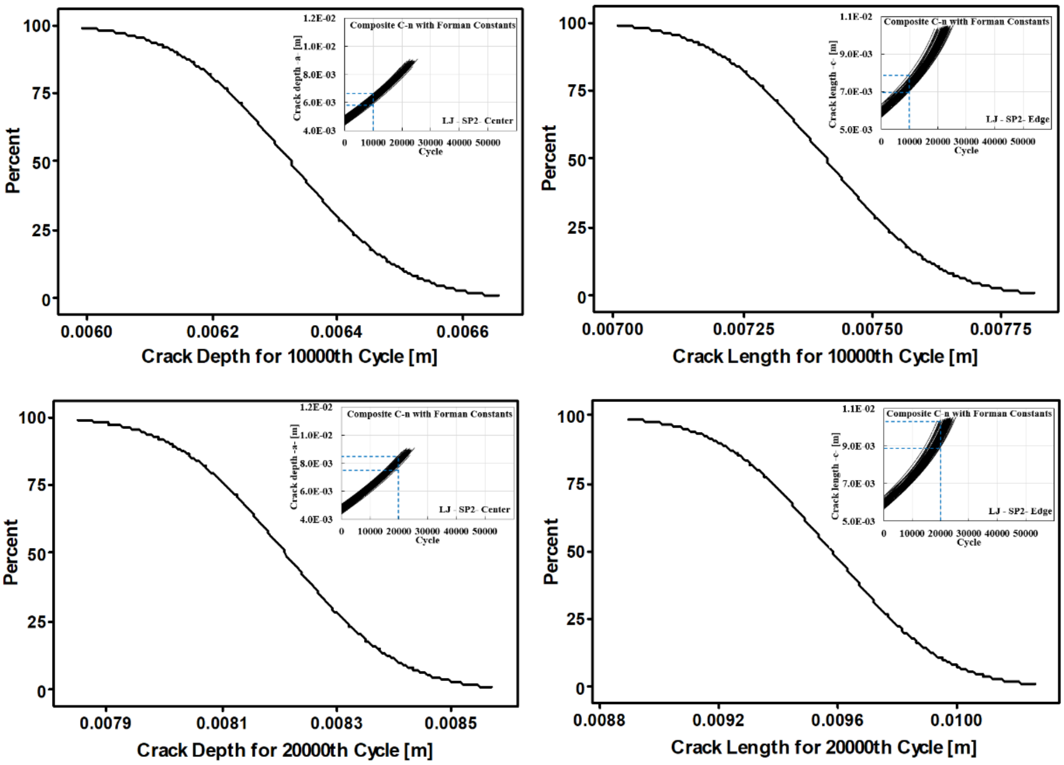

Figure 5.95. CDF for crack lengths under constant cycle load conditions (LJ specimen, SP2 loading spectrum, Composite C-n with Forman Constants)

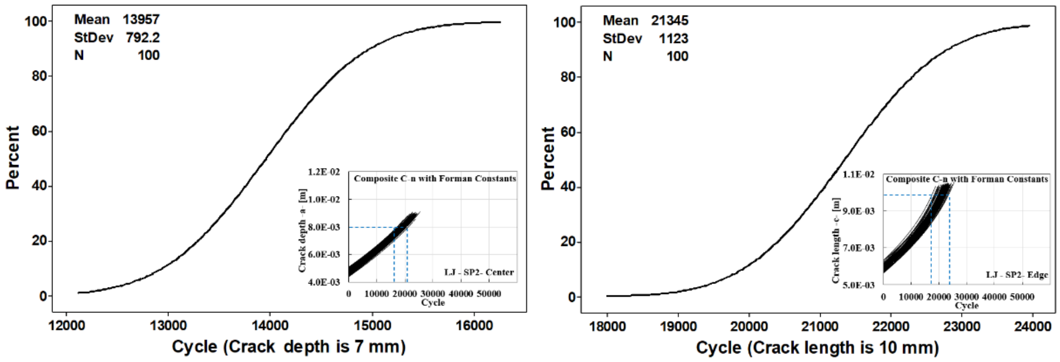

Figure 5.96. CDF for load cycles under constant crack length conditions (LJ specimen, SP2 loading spectrum, Composite C-n with Forman Constants)

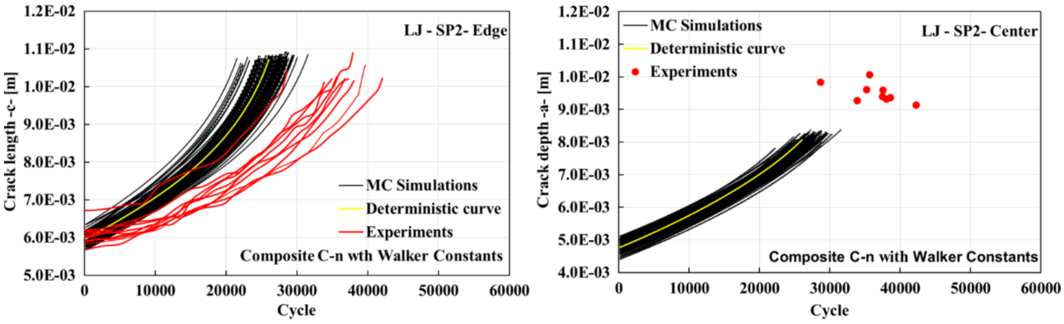

Figure 5.97. Probabilistic crack growth life curves and their comparison with the experiments (LJ specimen, SP2 loading spectrum, Composite C-n with Walker Constants)

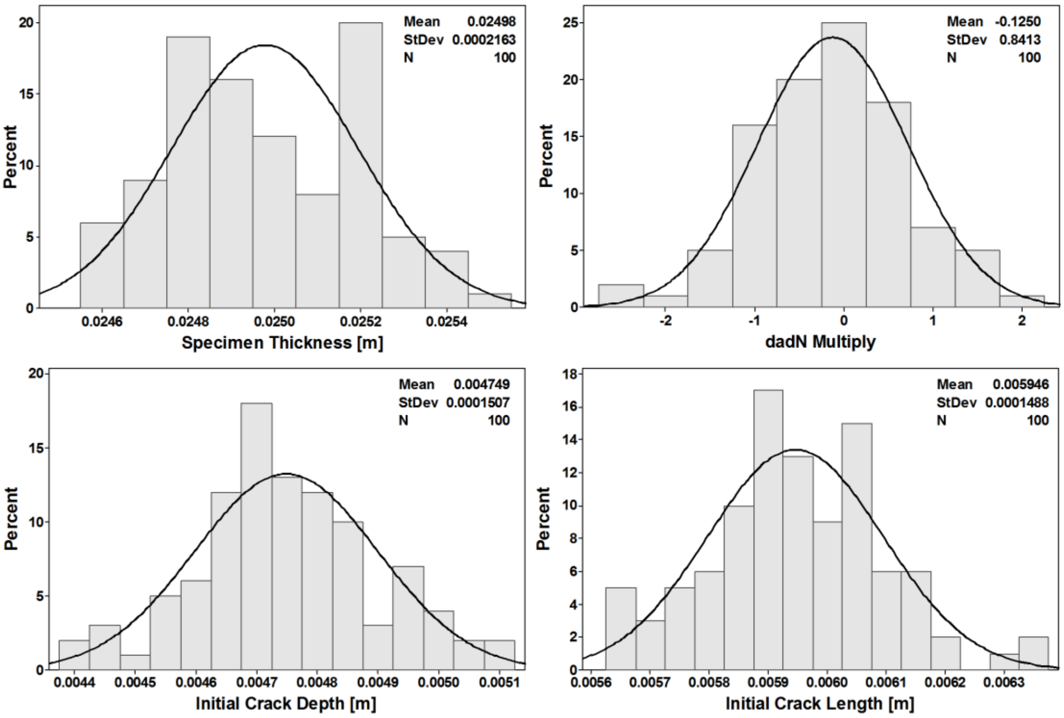

Figure 5.98. Distributions of the inputs used in crack growth life analysis (LJ specimen, SP2 loading spectrum, Composite C-n with Walker Constants)

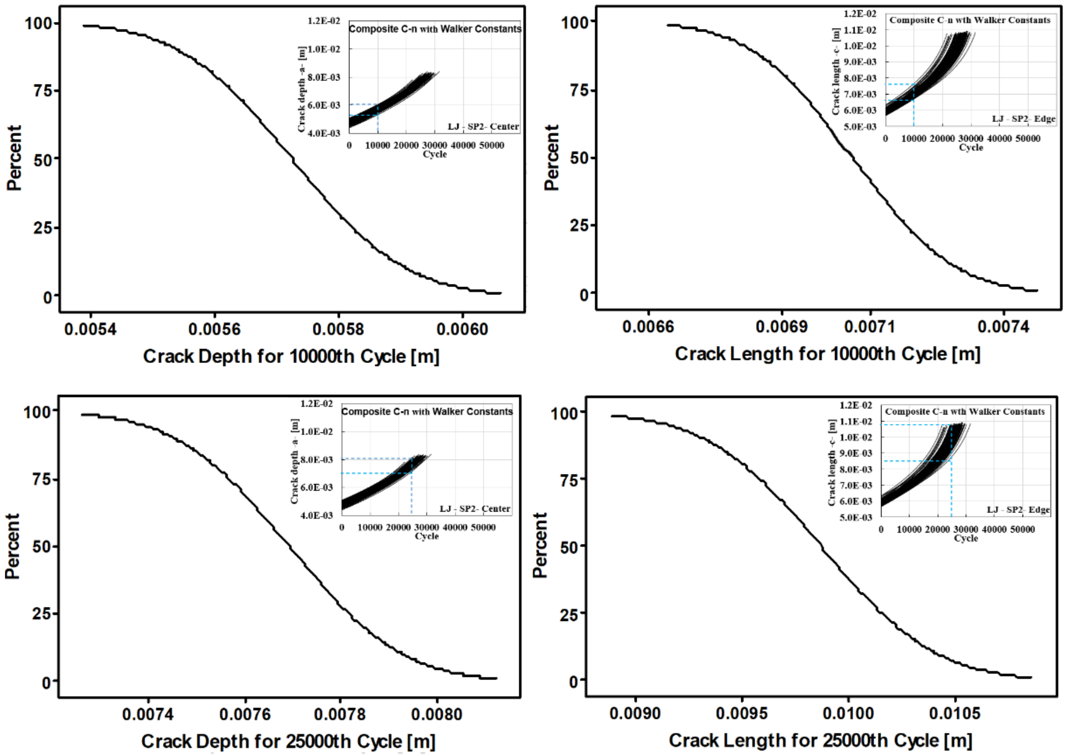

Figure 5.99. CDF for crack lengths under constant cycle load conditions (LJ specimen, SP2 loading spectrum, Composite C-n with Walker Constants)

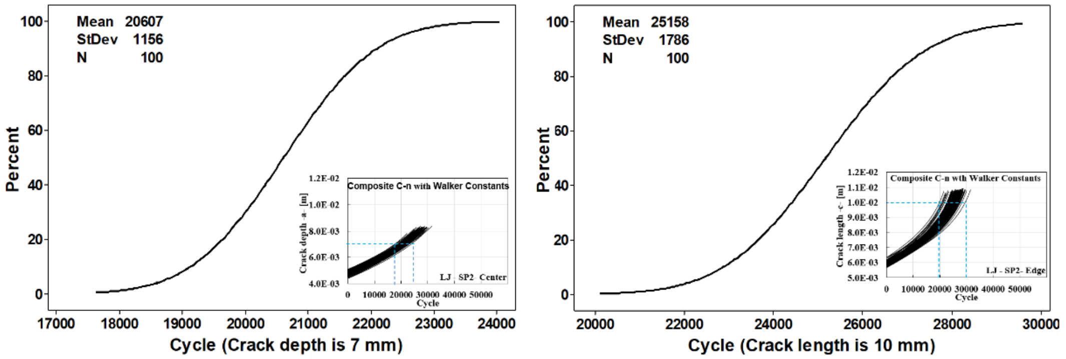

Figure 5.100. CDF for load cycles under constant crack length conditions (LJ specimen, SP2 loading spectrum, Composite C-n with Walker Constants)

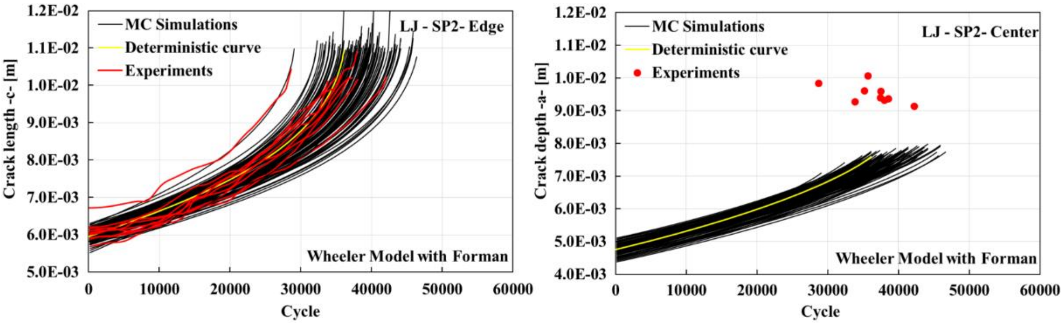

Figure 5.101. Probabilistic crack growth life curves and their comparison with the experiments (LJ specimen, SP2 loading spectrum, Wheeler model with Forman)

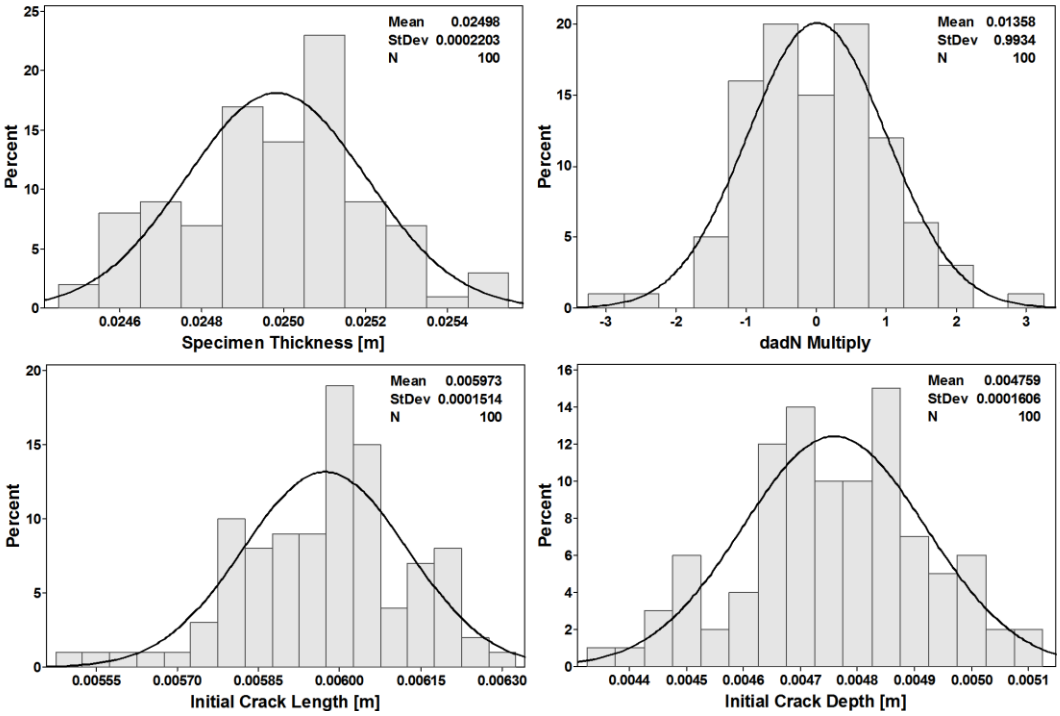

Figure 5.102. Distributions of the inputs used in crack growth life analysis (LJ specimen, SP2 loading spectrum, Wheeler model with Forman)

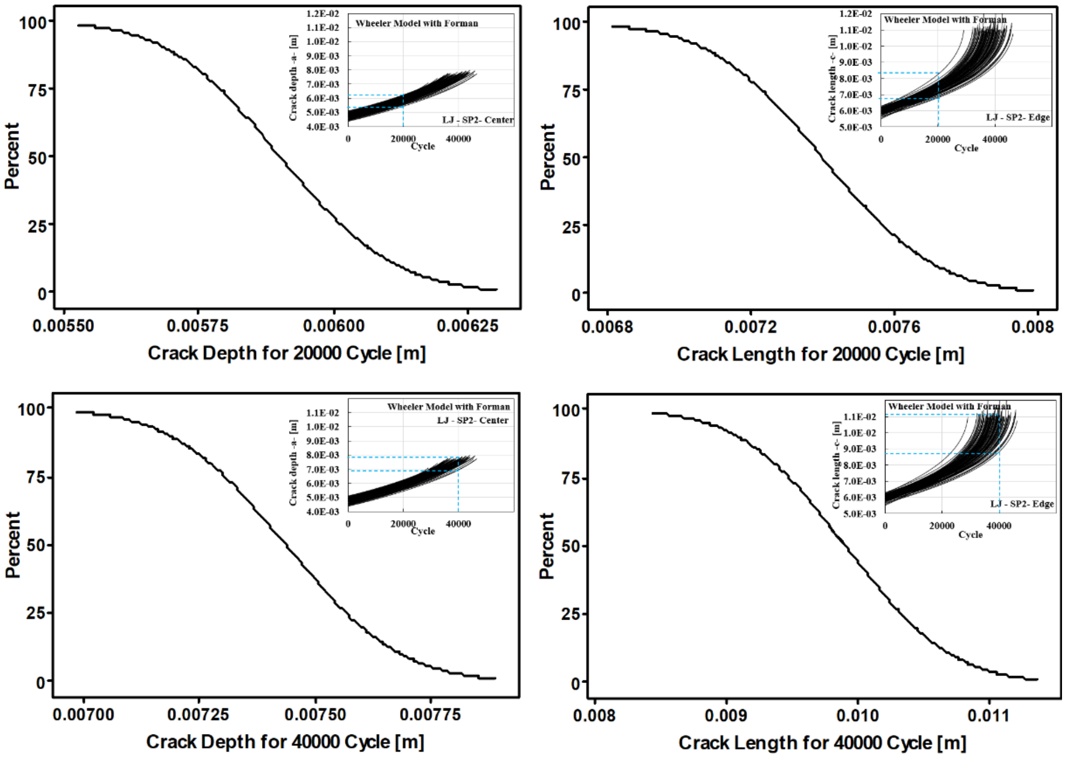

Figure 5.103. CDF for crack lengths under constant cycle load conditions (LJ specimen, SP2 loading spectrum, Wheeler model with Forman)

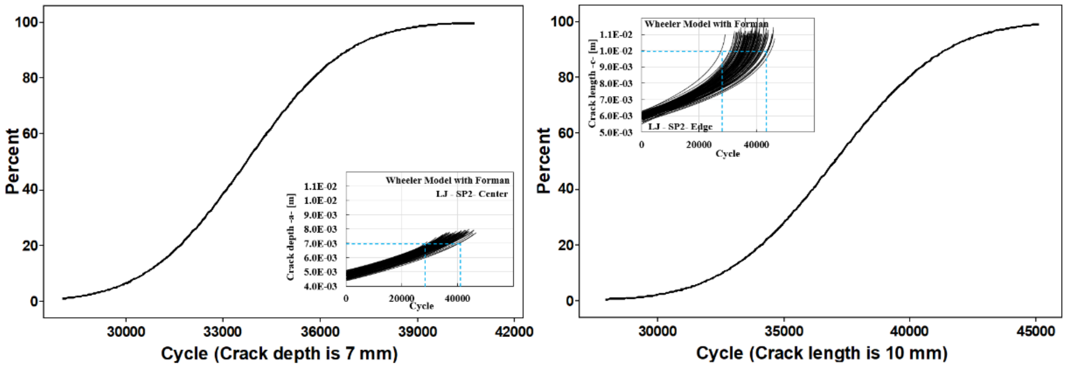

Figure 5.104. CDF for load cycles under constant crack length conditions (LJ specimen, SP2 loading spectrum, Wheeler model with Forman)

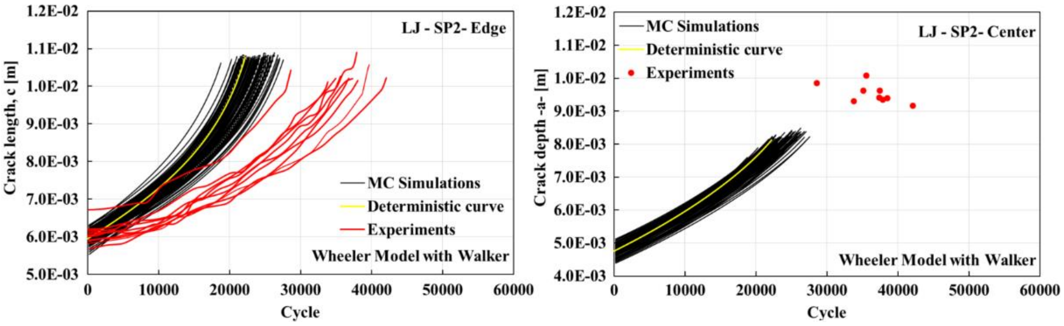

Figure 5.105. Probabilistic crack growth life curves and their comparison with the experiments (LJ specimen, SP2 loading spectrum, Wheeler model with Walker)

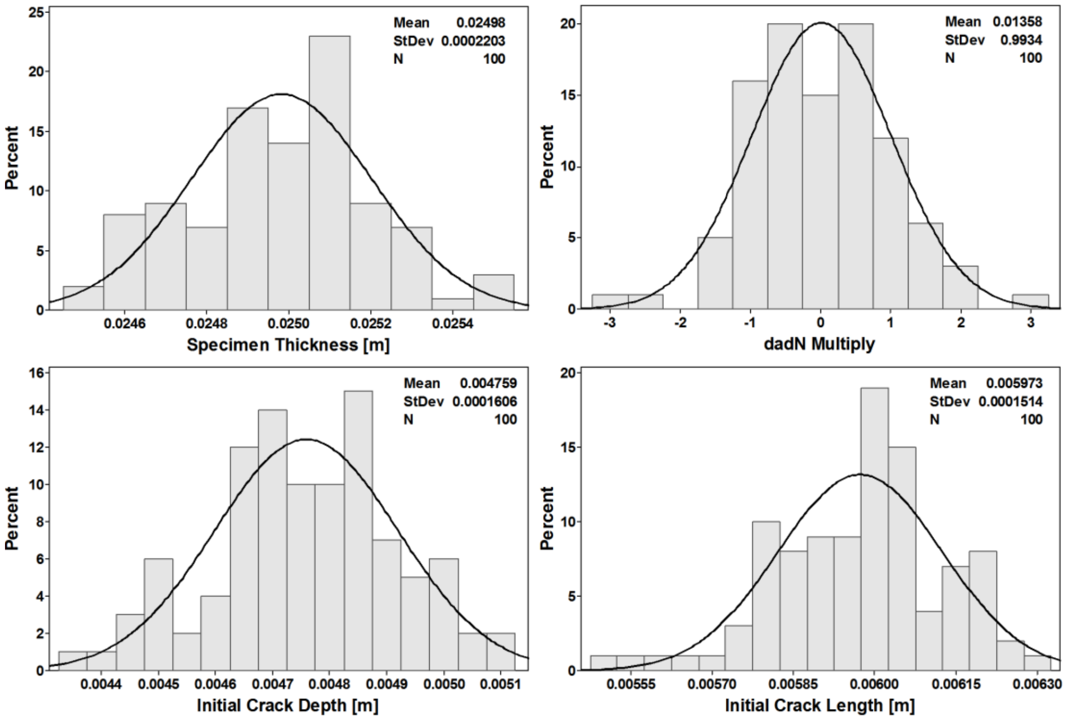

Figure 5.106. Distributions of the inputs used in crack growth life analysis (LJ specimen, SP2 loading spectrum, Wheeler model with Walker)

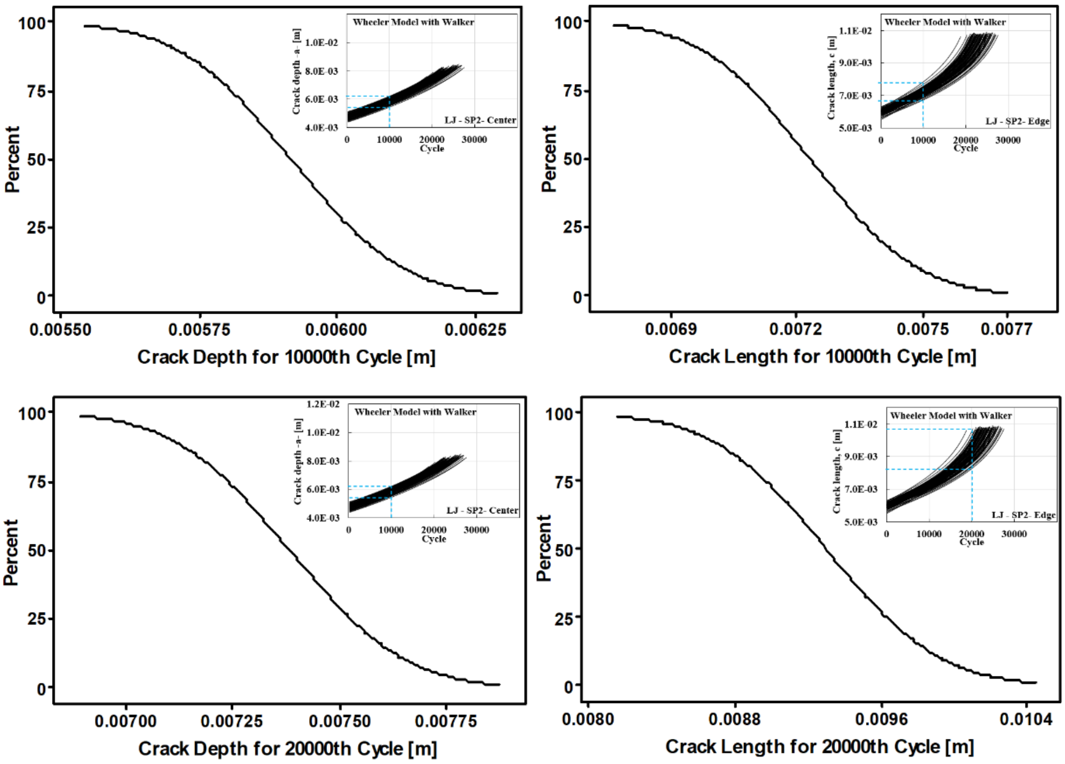

Figure 5.107. CDF for crack lengths under constant cycle load conditions (LJ specimen, SP2 loading spectrum, Wheeler model with Walker)

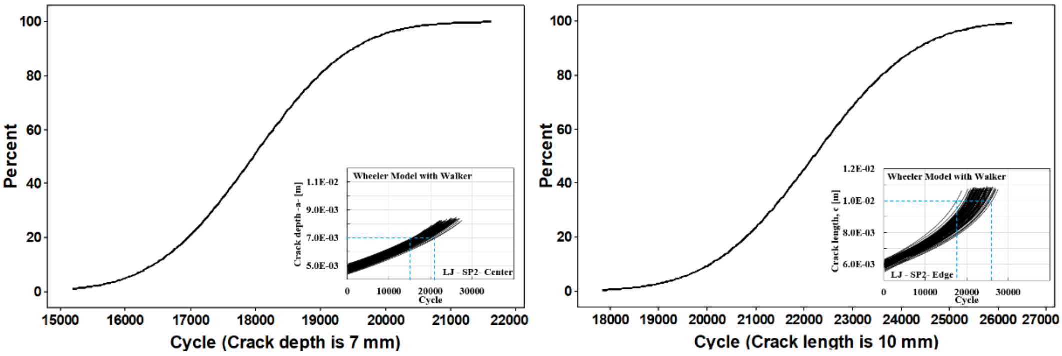

Figure 5.108. CDF for load cycles under constant crack length conditions (LJ specimen, SP2 loading spectrum, Wheeler model with Walker)

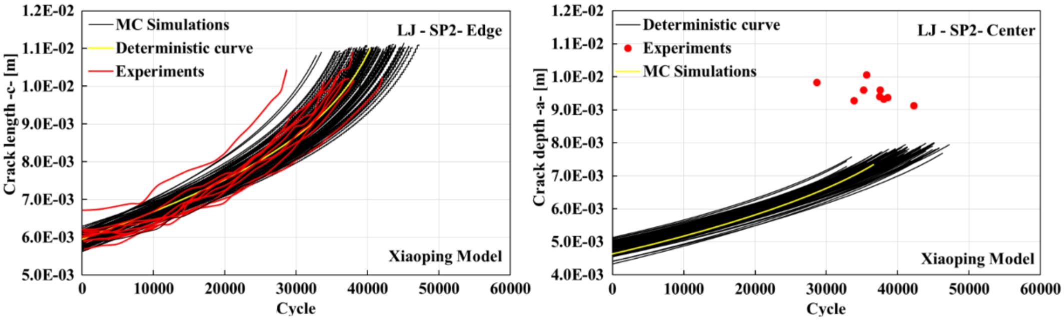

Figure 5.109. Probabilistic crack growth life curves and their comparison with the experiments (LJ specimen, SP2 loading spectrum, Xiaoping model)

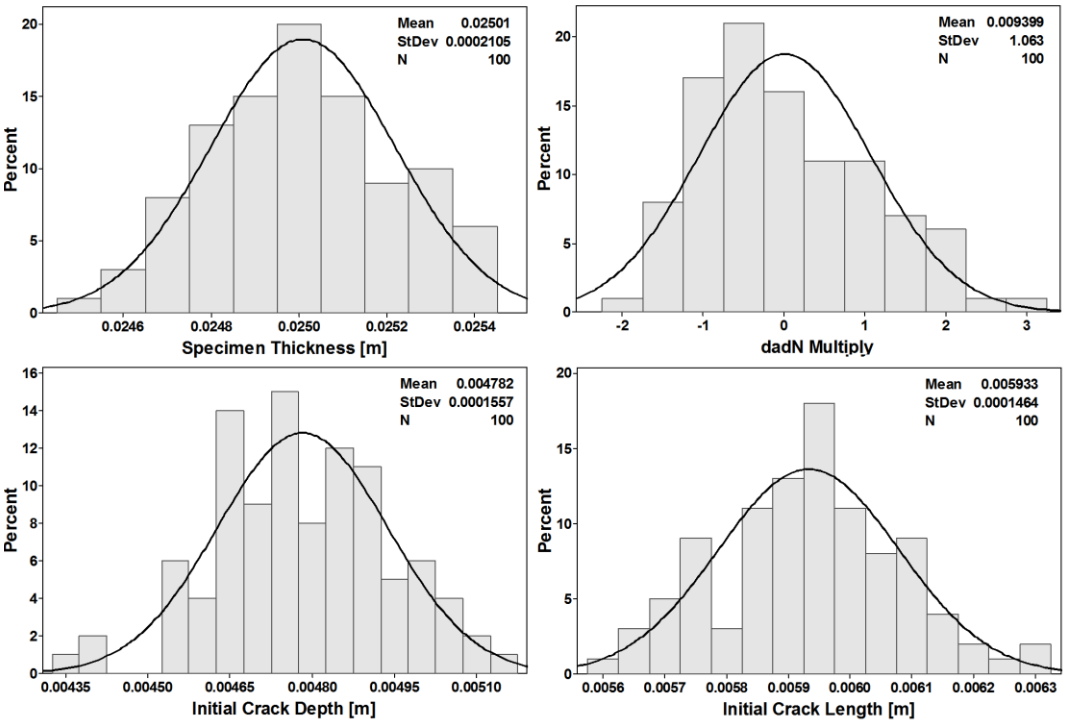

Figure 5.110. Distributions of the inputs used in crack growth life analysis (LJspecimen, SP2loading spectrum, Xiaoping model)

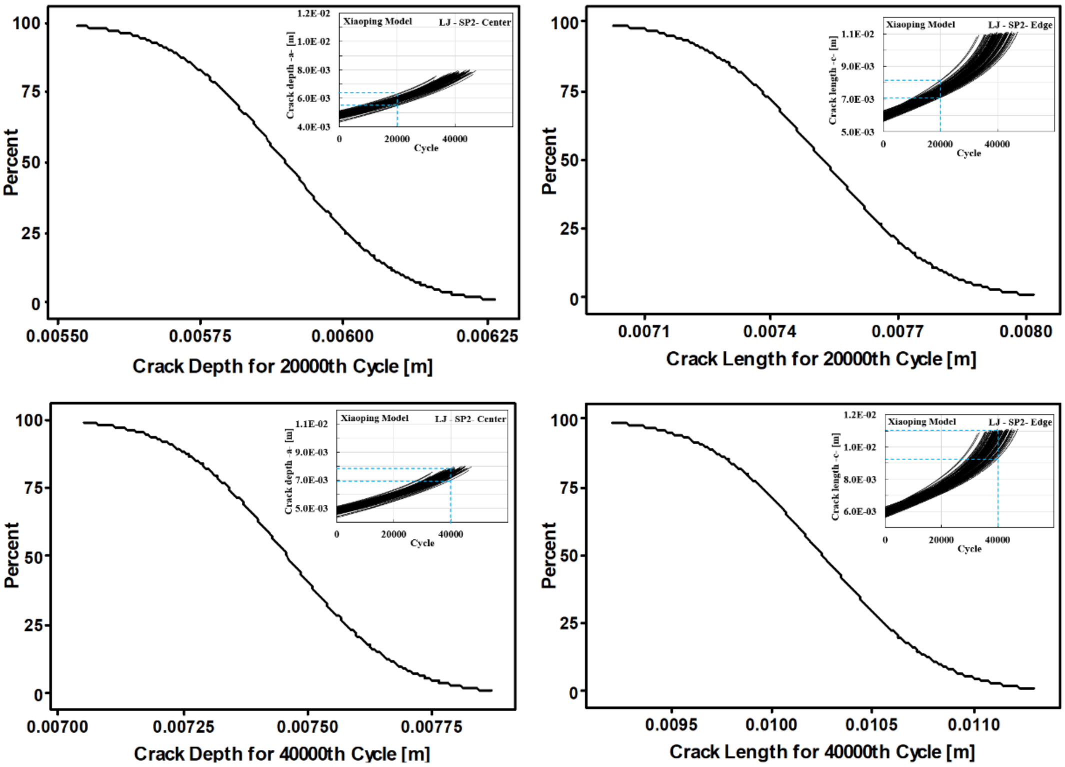

Figure 5.111. CDF for crack lengths under constant cycle load conditions (LJ specimen, SP2 loading spectrum, Xiaoping model)

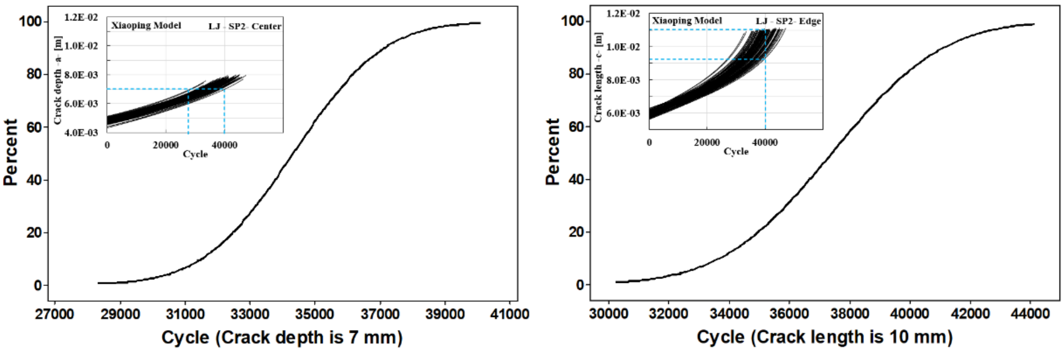

Figure 5.112. CDF for load cycles under constant crack length conditions (LJ specimen, SP2 loading spectrum, Xiaoping model)

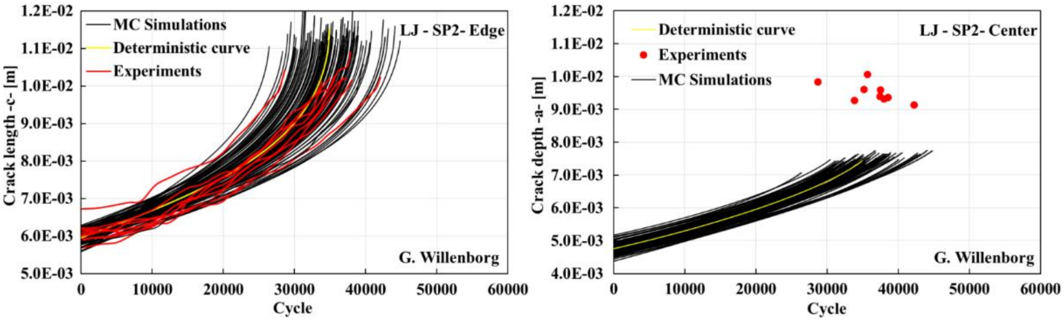

Figure 5.113. Probabilistic crack growth life curves and their comparison with the experiments (LJ specimen, SP2 loading spectrum, Generalized Willenborg model)

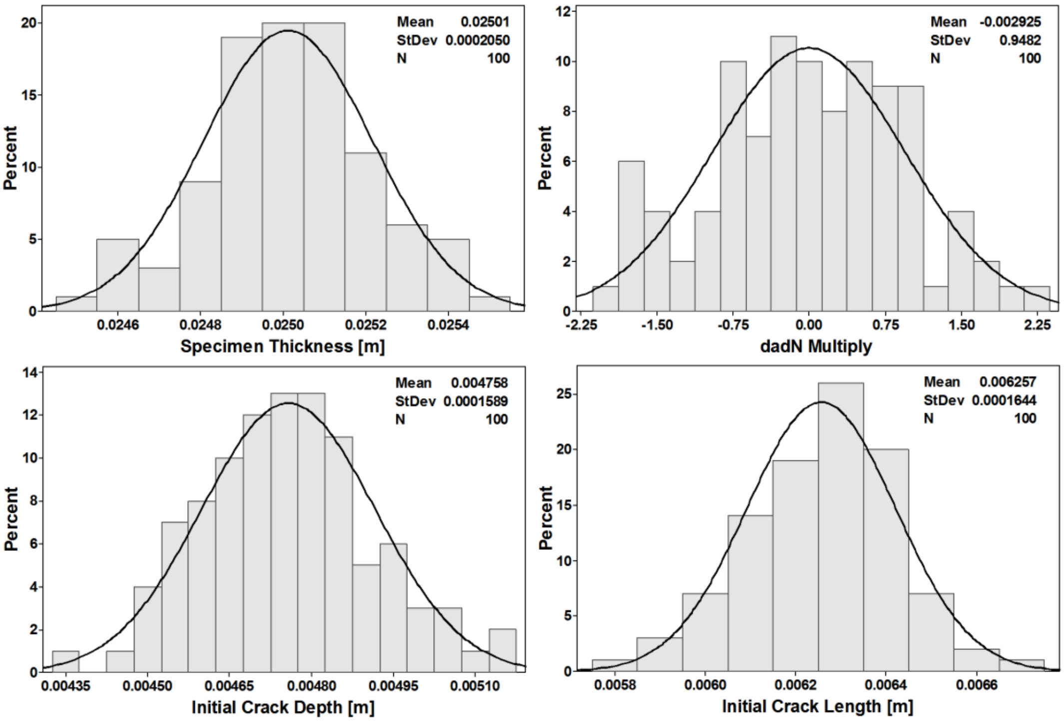

Figure 5.114. Distributions of the inputs used in crack growth life analysis (LJ specimen, SP2 loading spectrum, Generalized Willenborg model)

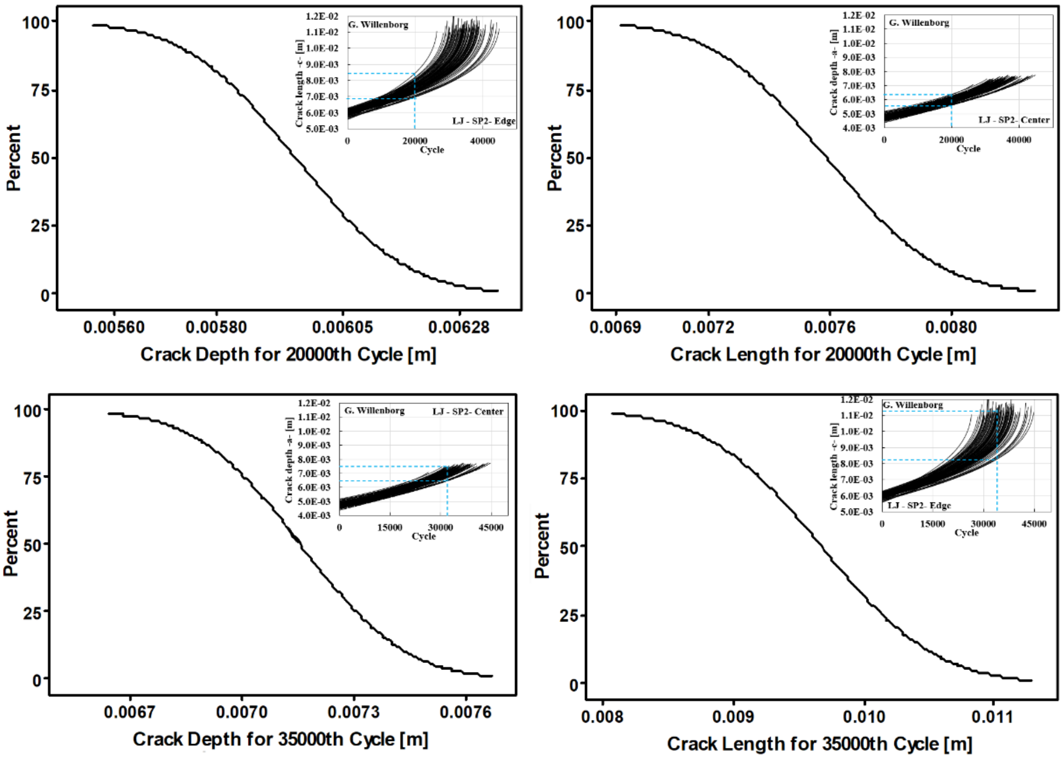

Figure 5.115. CDF for crack lengths under constant cycle load conditions (LJ specimen, SP2 loading spectrum, Generalized Willenborg model)

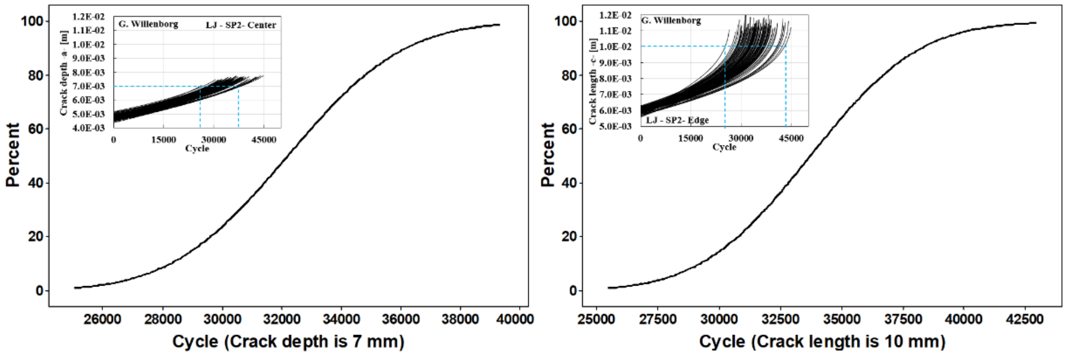

Figure 5.116. CDF for load cycles under constant crack length conditions (LJ specimen, SP2 loading spectrum, Generalized Willenborg model)

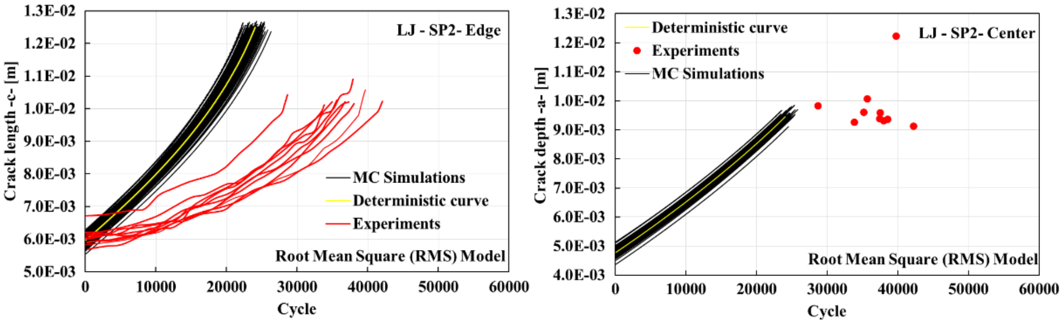

Figure 5.117. Probabilistic crack growth life curves and their comparison with the experiments (LJ specimen, SP2 loading spectrum, Root mean square model)

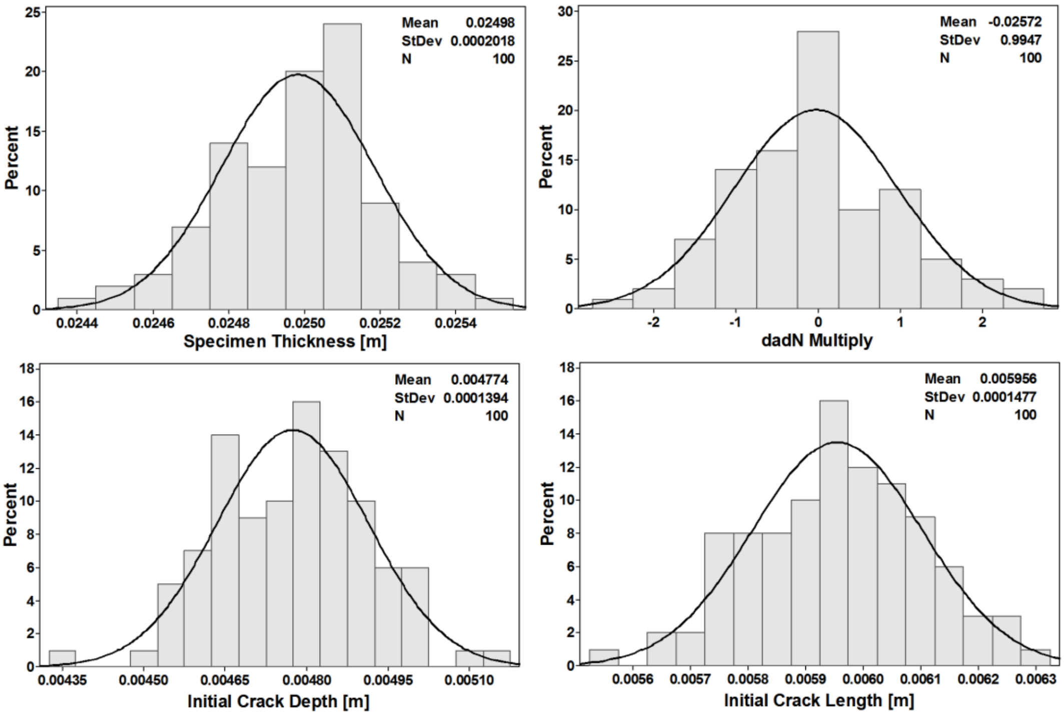

Figure 5.118. Distributions of the inputs used in crack growth life analysis (LJ specimen, SP2 loading spectrum, Root mean square model)

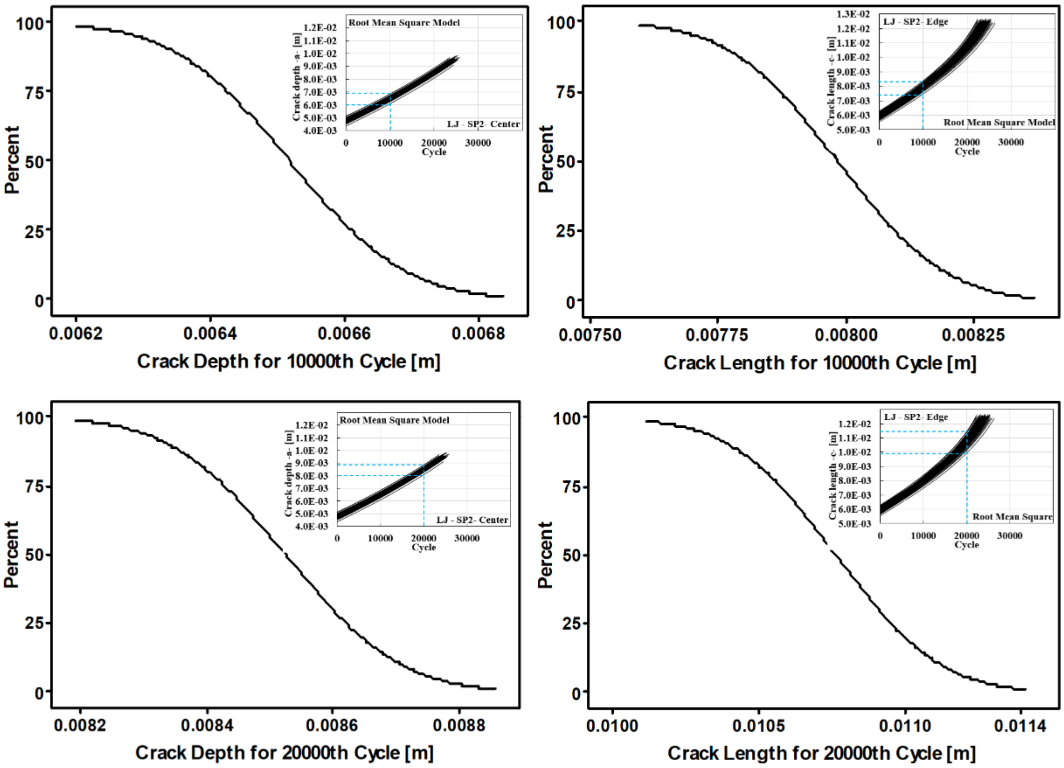

Figure 5.119. CDF for crack lengths under constant cycle load conditions (LJ specimen, SP2 loading spectrum, Root mean square model)

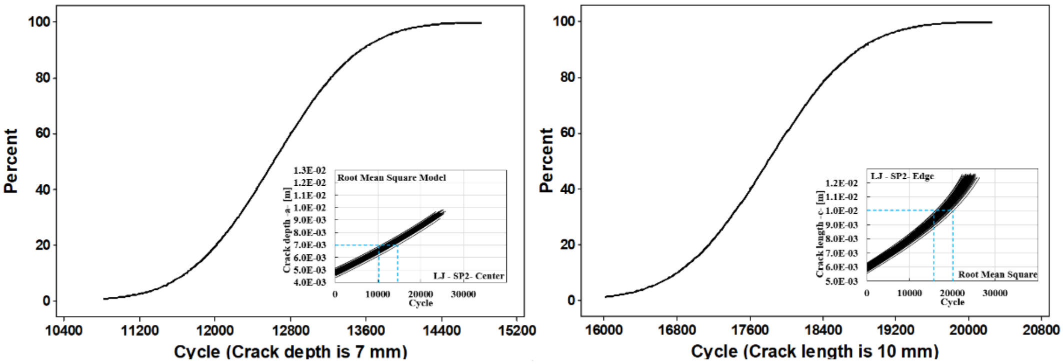

Figure 5.120. CDF for load cycles under constant crack length conditions (LJ specimen, SP2 loading spectrum, Root mean square model)

According to the results for 3-D crack propagation obtained by using different models, the results of the Wheeler model with Forman equation in Figure 5.101., Xiaoping model in Figure 5.109. and Generalized Willenborg Model in Figure 5.113. are close to experiments. As explained before, SOL Index was not used for three-dimensional crack propagation. In both two and three-dimensional crack propagation, the closest result to the experiments was obtained by the Wheeler model, using the Forman equation.

## 5.3. Verification Tests and Simulations for Three-Dimensional Crack Growth

In the previous sections, comparisons between the results of the experiments performed under two different random loading profiles (spectrum loading) and the crack propagation curves obtained from probabilistic two- and three-dimensional crack propagation simulations by using different models were presented. It is concluded that the use of Wheeler model for crack growth retardation gives better results with Forman equation in the estimation of two- and three-dimensional mode-I crack propagation life under random loading. The application of SOL index to determine the partial crack growth acceleration after overload for two-dimensional crack propagation problems under random loading was presented as a model improvement and verified by independent experimental results obtained from the literature.

Probabilistic analyses were performed using two different load spectrums for three-dimensional mode-I crack propagation and the results were compared with experiments. A new spectrum named as Spectrum-3 (SP3) has been used to verify the results, which was obtained by selecting a different part of the FALSTAFF spectrum than the SP2 spectrum. SP3 loading spectrum is given in Figure 5.111.

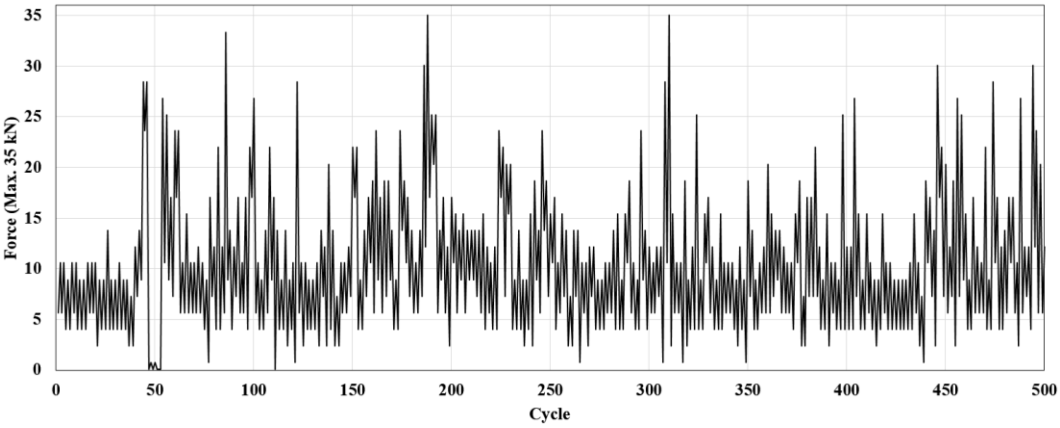

Figure 5.121. Partial FALSTAFF (Spectrum-3, SP3) loading profiles for LJ Specimen

In order to determine the variations in the crack propagation life curves, 10 tests were performed under Spectrum-3 by following the procedure described in Section 3.5. Details of the tests performed under SP3 are given in Table 5.2.

Table 5.2. Details of the 3-D FCG tests performed under Spectrum-3

| | | Precrack | | | Fatigure crack growth | | |
|---|---|---|---|---|---|---|---|
| Specimen Name | Specimen Type | Stress Ratio for precrack R | Max. Load for Precrack (kN) | $a_{(avg)}$ (mm) | Spectrum | Max. Load for FCG (kN) | Cycle |
| 20200702_01 | LJ | 0.1 | 17 | 5.943 | Spectrum 3 | 35 | 39176 |
| 20200703_01 | LJ | 0.1 | 17 | 5.805 | Spectrum 3 | 35 | 37888 |
| 20200703_02 | LJ | 0.1 | 17 | 6.215 | Spectrum 3 | 35 | 34797 |
| 20200706_01 | LJ | 0.1 | 17 | 5.840 | Spectrum 3 | 35 | 39717 |
| 20200706_02 | LJ | 0.1 | 17 | 5.800 | Spectrum 3 | 35 | 43104 |
| 20200707_01 | LJ | 0.1 | 17 | 6.075 | Spectrum 3 | 35 | 31586 |
| 20200707_02 | LJ | 0.1 | 17 | 5.868 | Spectrum 3 | 35 | 38782 |
| 20200708_01 | LJ | 0.1 | 17 | 5.890 | Spectrum 3 | 35 | 37284 |
| 20200708_02 | LJ | 0.1 | 17 | 6.275 | Spectrum 3 | 35 | 33014 |
| 20200709_01 | LJ | 0.1 | 17 | 5.908 | Spectrum 3 | 35 | 41137 |

After the experiments, Monte Carlo Simulations were performed, and the crack growth curves obtained by using different models are given in Figure 5.121. - Figure 5.149. in comparison with the experiments. The input and output distributions are also given for each model.

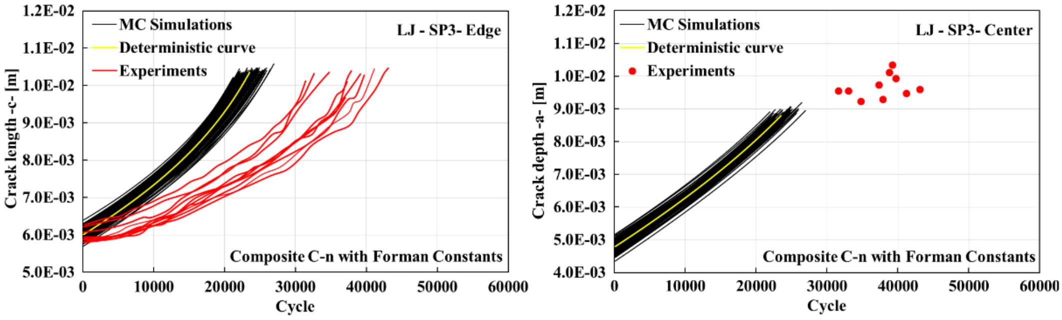

Figure 5.122. Probabilistic crack growth life curves and their comparison with the experiments (LJ specimen, SP3 loading spectrum, Composite C-n with Forman Constants)

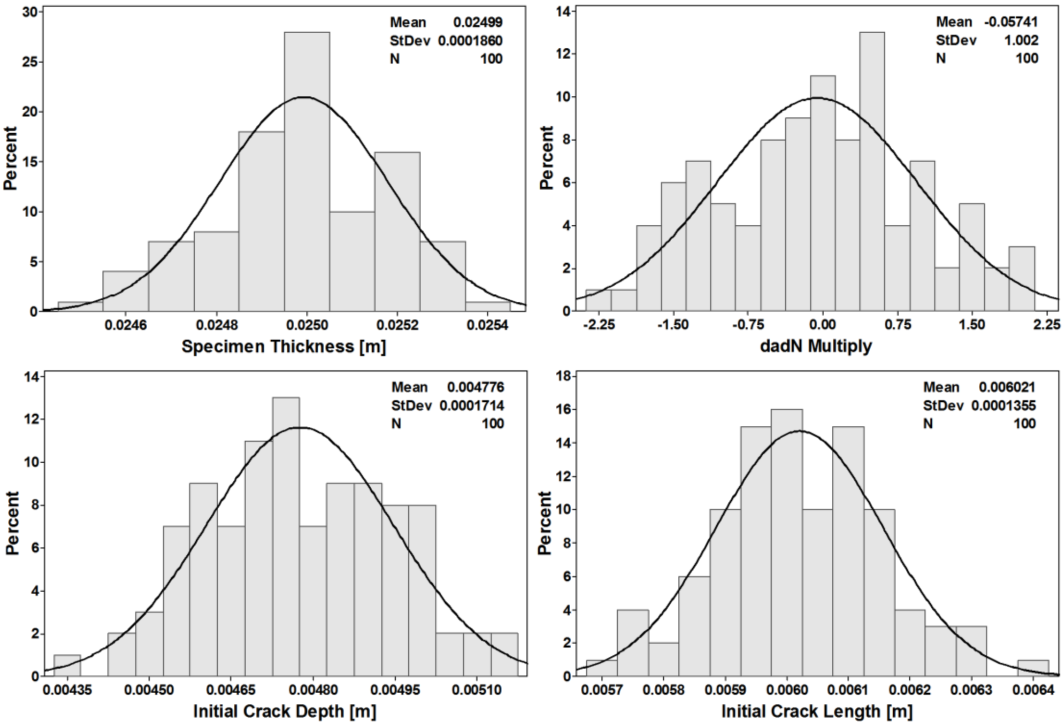

Figure 5.123. Distributions of the inputs used in crack growth life analysis (LJ specimen, SP3 loading spectrum, Composite C-n with Forman Constants)

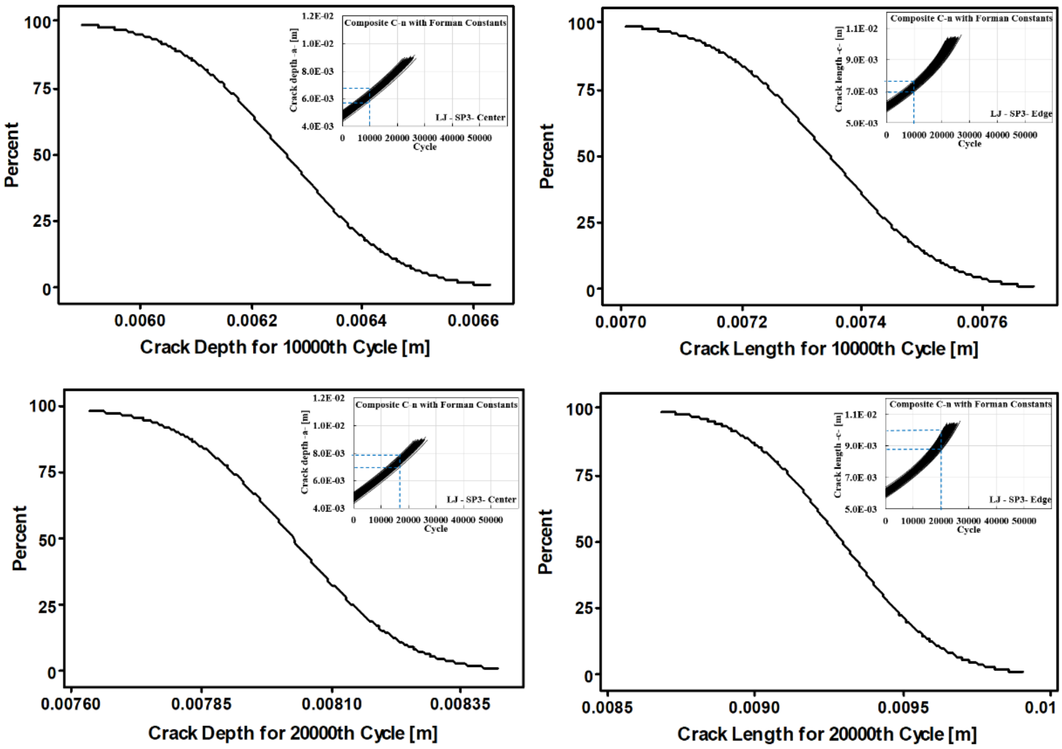

Figure 5.124. CDF for crack lengths under constant cycle load conditions (LJ specimen, SP3 loading spectrum, Composite C-n with Forman Constants)

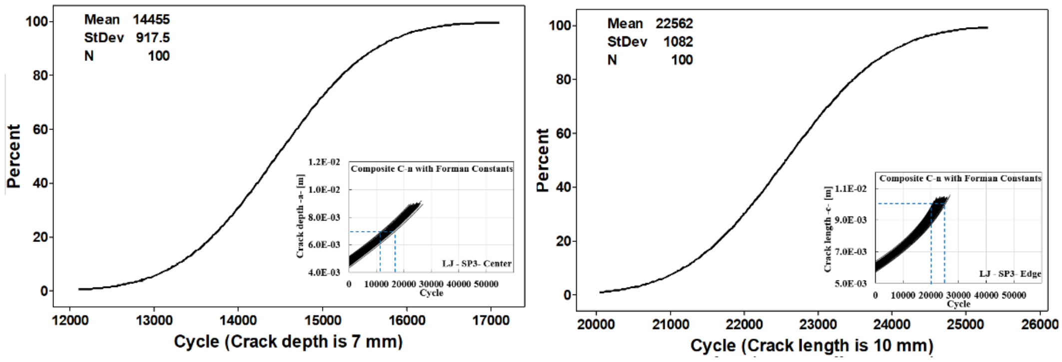

Figure 5.125. CDF for load cycles under constant crack length conditions (LJ specimen, SP3 loading spectrum, Composite C-n with Forman Constants)

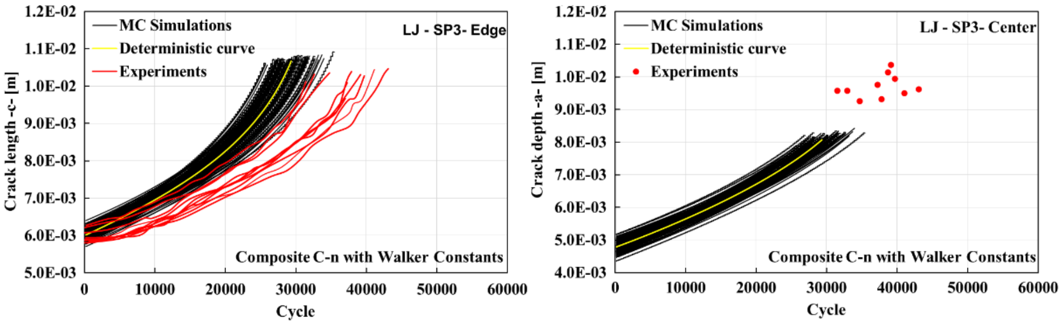

Figure 5.126. Probabilistic crack growth life curves and their comparison with the experiments (LJ specimen, SP3 loading spectrum, Composite C-n with Walker Constants)

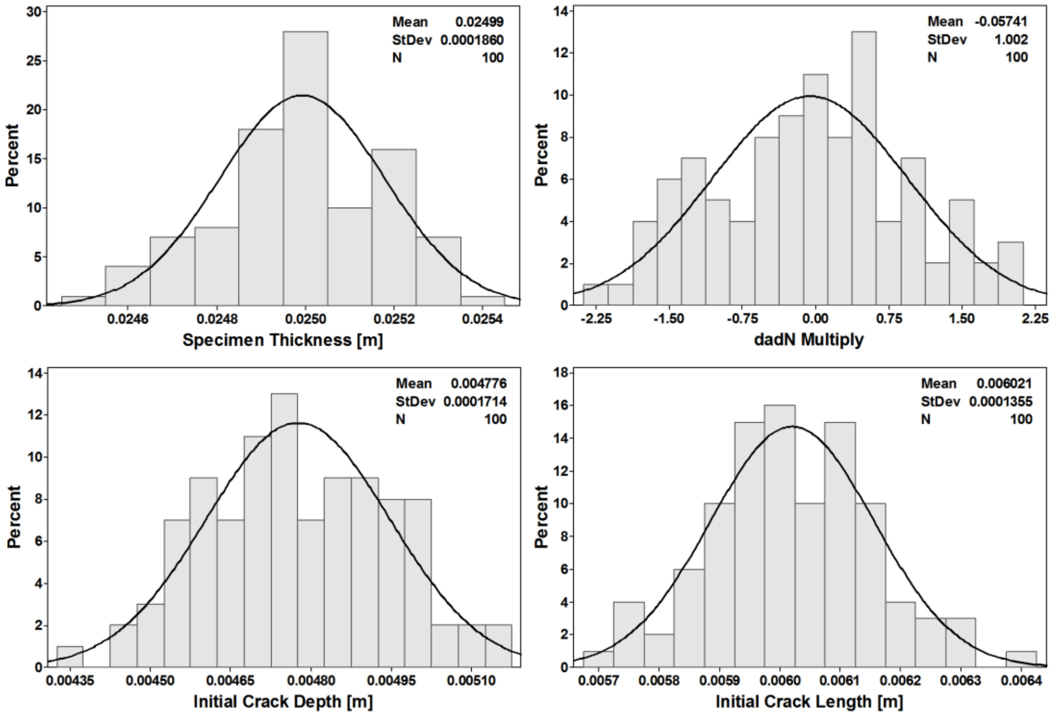

Figure 5.127. Distributions of the inputs used in crack growth life analysis (LJ specimen, SP3 loading spectrum, Composite C-n with Walker Constants)

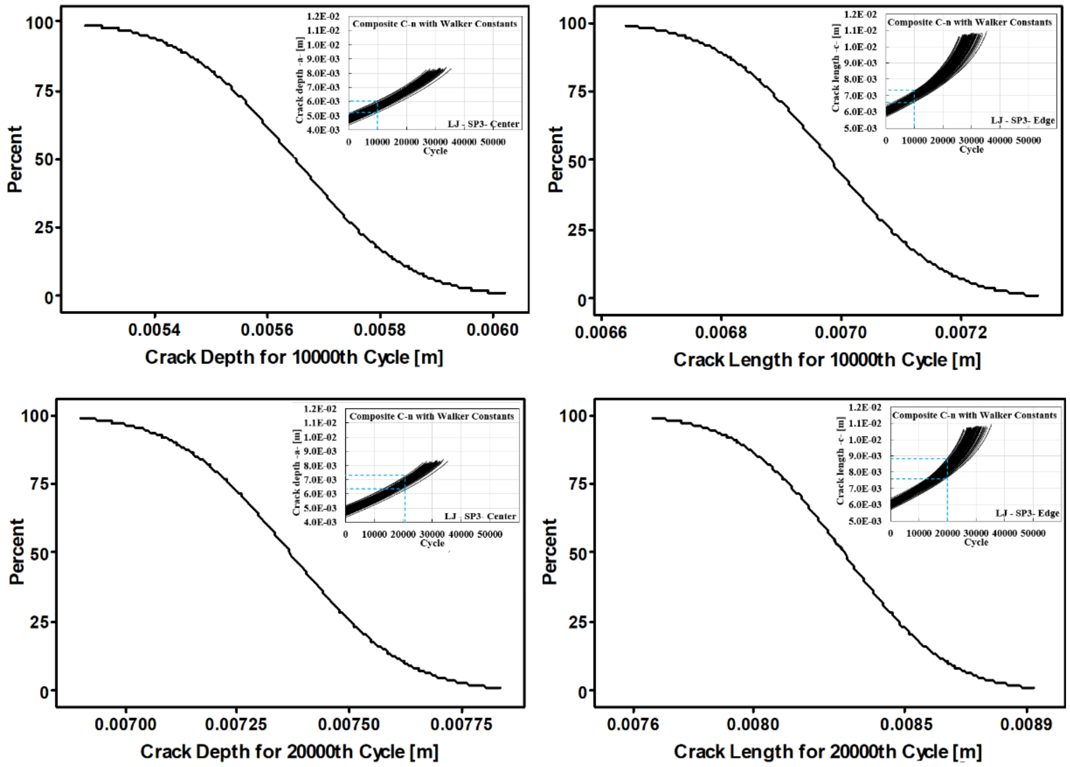

Figure 5.128. CDF for crack lengths under constant cycle load conditions (LJ specimen, SP3 loading spectrum, Composite C-n with Walker Constants)

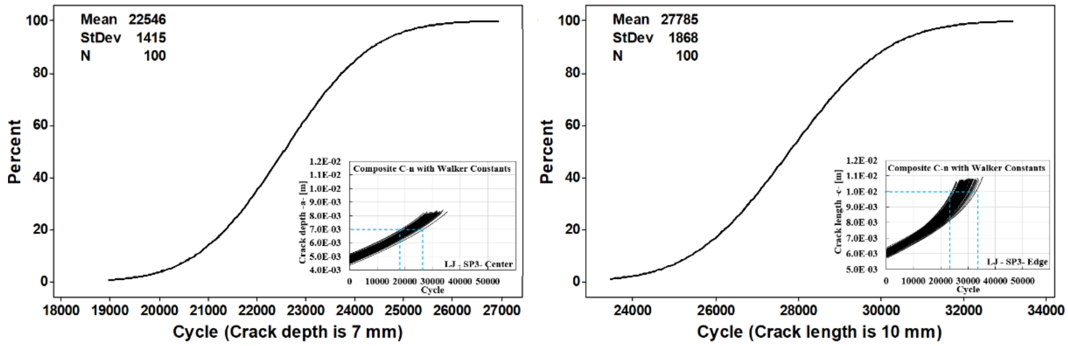

Figure 5.129. CDF for load cycles under constant crack length conditions (LJ specimen, SP3 loading spectrum, Composite C-n with Walker Constants)

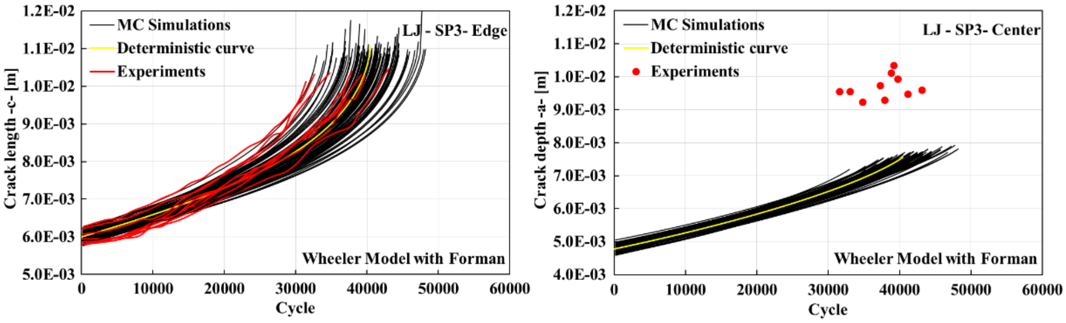

Figure 5.130. Probabilistic crack growth life curves and their comparison with the experiments (LJ specimen, SP3 loading spectrum, Wheeler model with Forman)

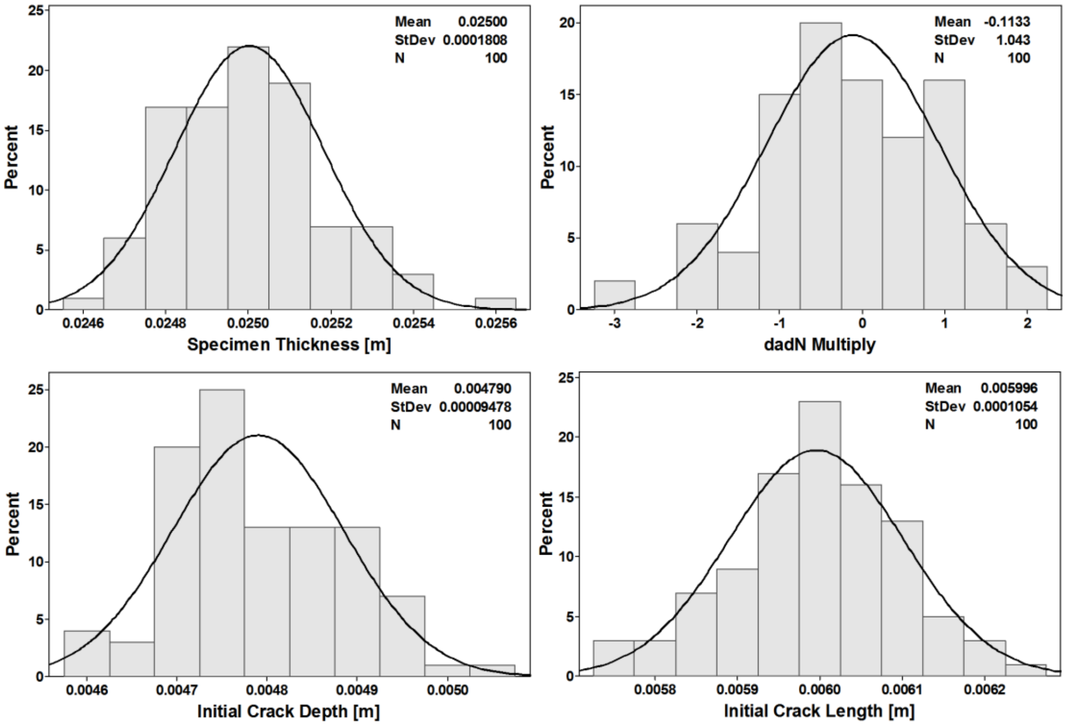

Figure 5.131. Distributions of the inputs used in crack growth life analysis (LJ specimen, SP3 loading spectrum, Wheeler model with Forman)

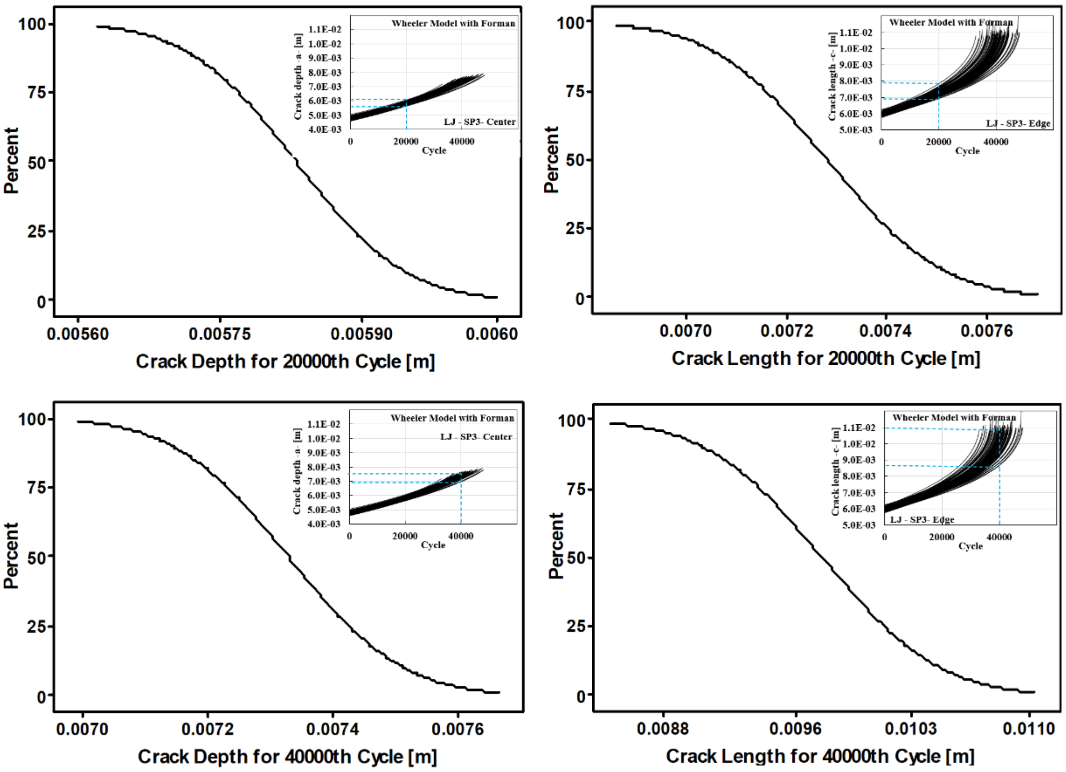

Figure 5.132. CDF for crack lengths under constant cycle load conditions (LJ specimen, SP3 loading spectrum, Wheeler model with Forman)

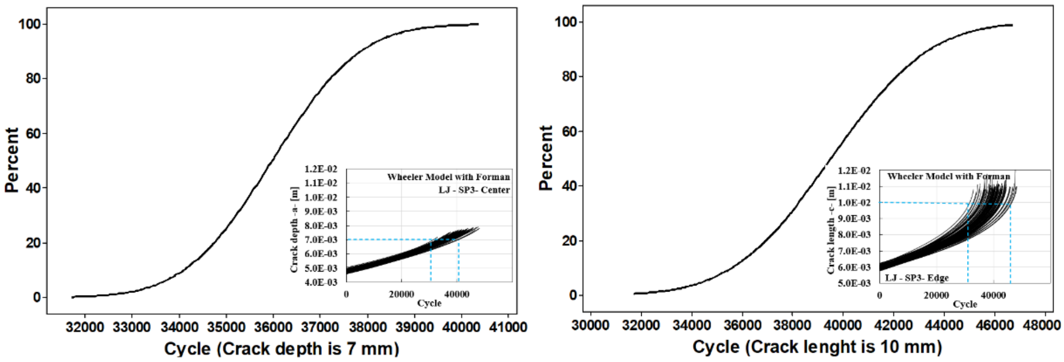

Figure 5.133. CDF for load cycles under constant crack length conditions (LJ specimen, SP3 loading spectrum, Wheeler model with Forman)

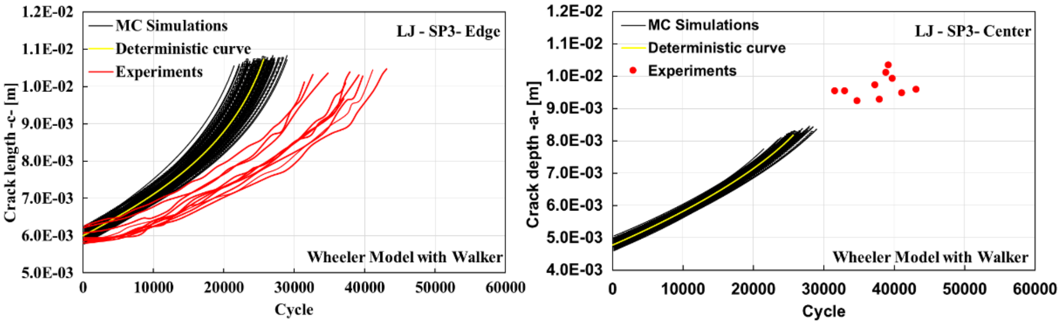

Figure 5.134. Probabilistic crack growth life curves and their comparison with the experiments (LJ specimen, SP3 loading spectrum, Wheeler model with Walker)

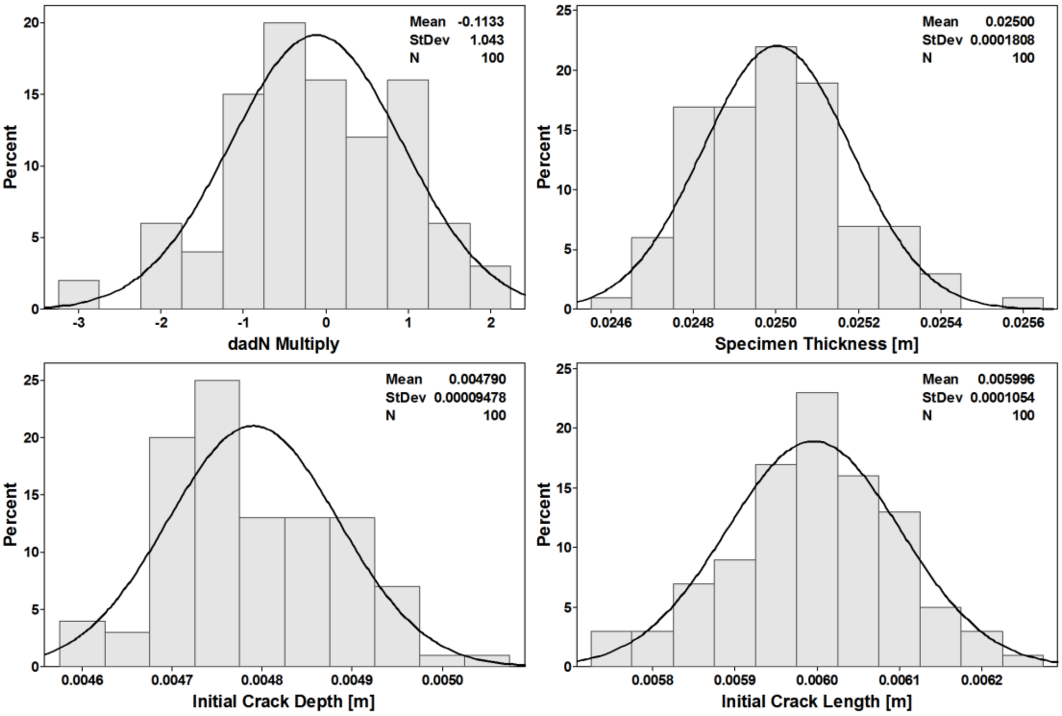

Figure 5.135. Distributions of the inputs used in crack growth life analysis (LJ specimen, SP3 loading spectrum, Wheeler model with Walker)

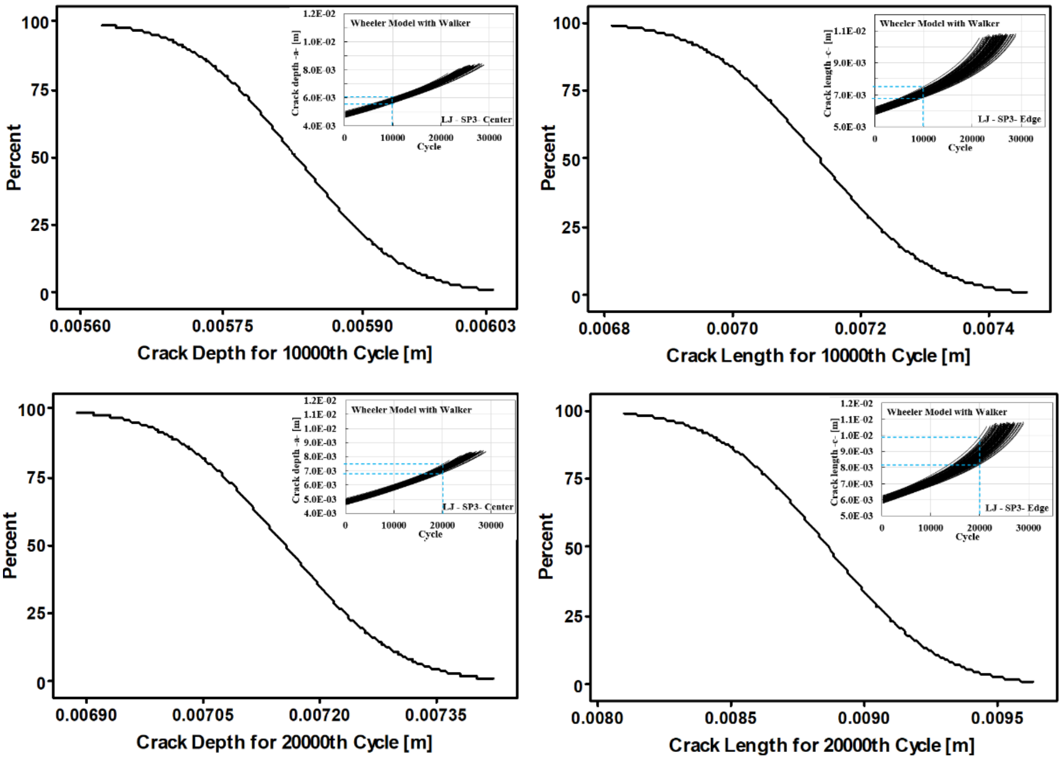

Figure 5.136. CDF for crack lengths under constant cycle load conditions (LJ specimen, SP3 loading spectrum, Wheeler model with Walker)

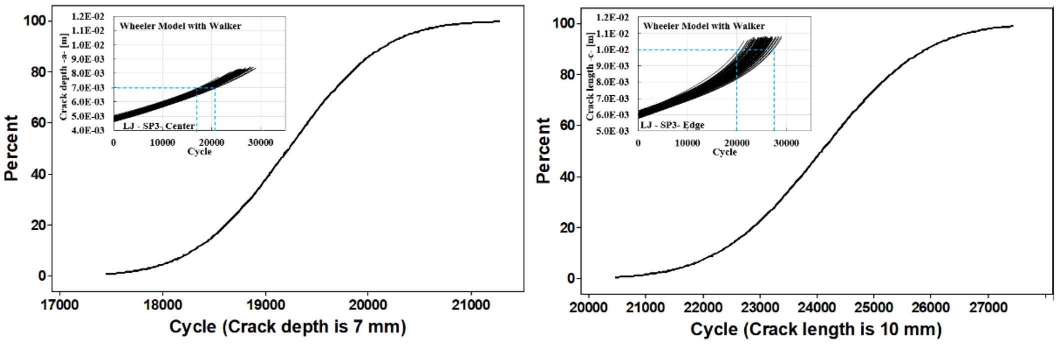

Figure 5.137. CDF for load cycles under constant crack length conditions (LJ specimen, SP3 loading spectrum, Wheeler model with Walker)

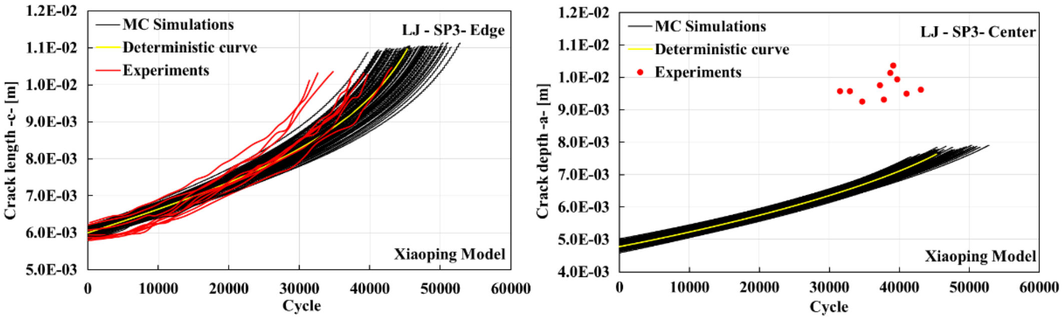

Figure 5.138. Probabilistic crack growth life curves and their comparison with the experiments (LJ specimen, SP3 loading spectrum, Xiaoping model)

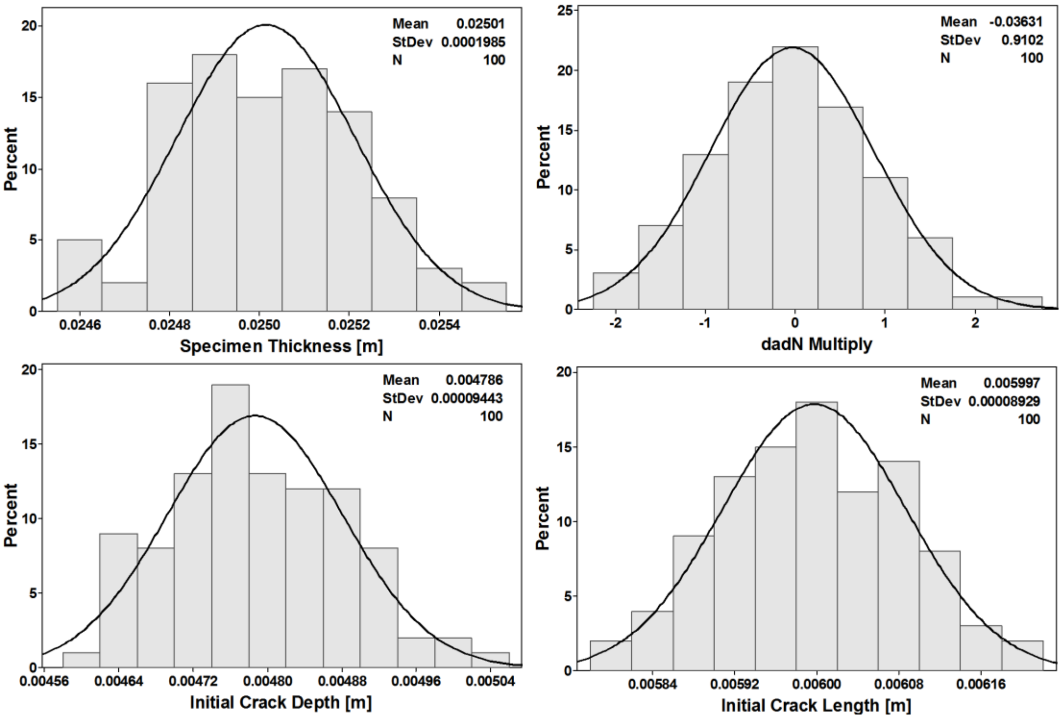

Figure 5.139. Distributions of the inputs used in crack growth life analysis (LJ specimen, SP3 loading spectrum, Xiaoping model)

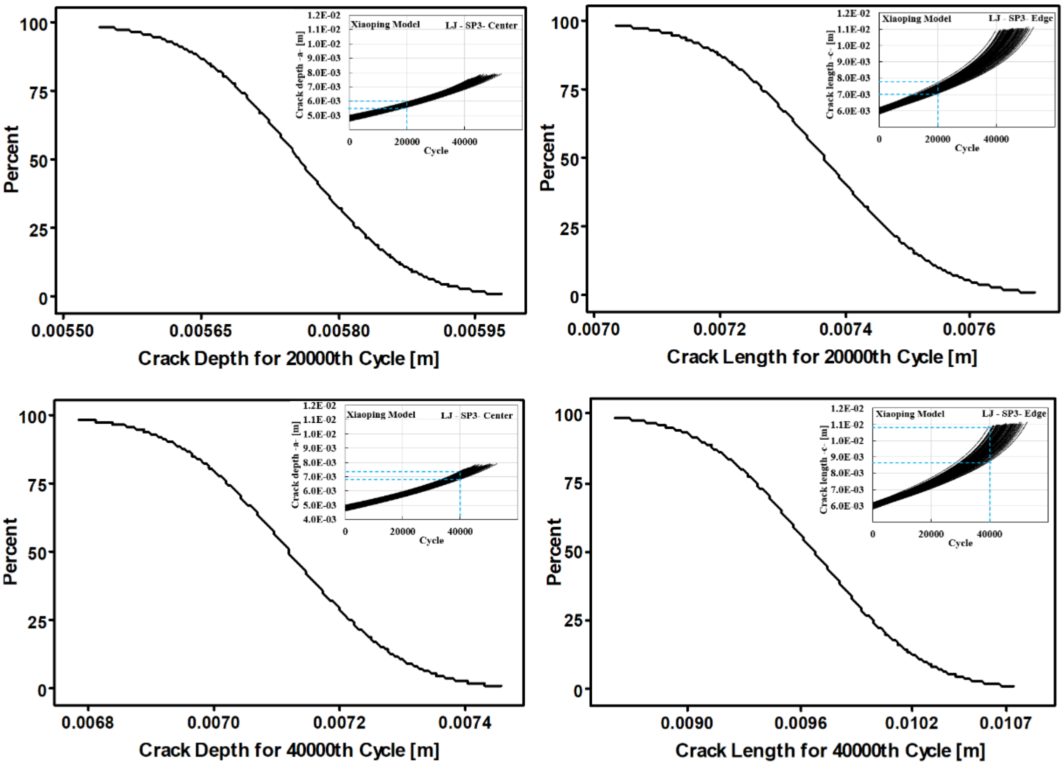

Figure 5.140. CDF for crack lengths under constant cycle load conditions (LJ specimen, SP3 loading spectrum, Xiaoping model)

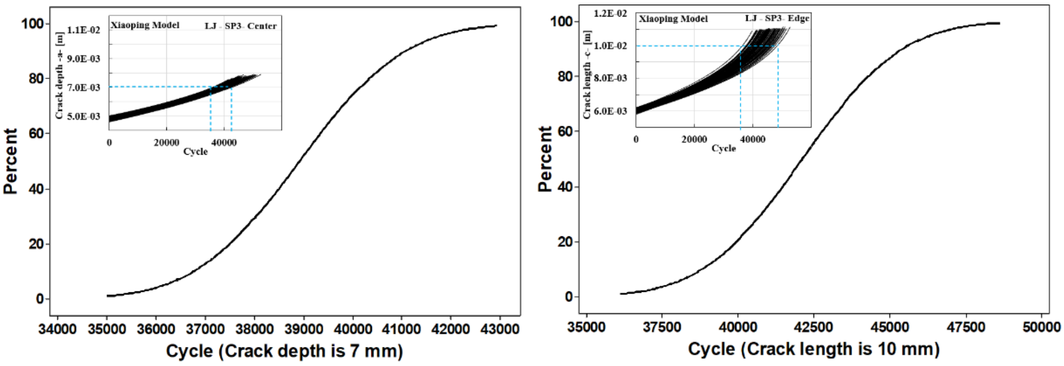

Figure 5.141. CDF for load cycles under constant crack length conditions (LJ specimen, SP3 loading spectrum, Xiaoping model)

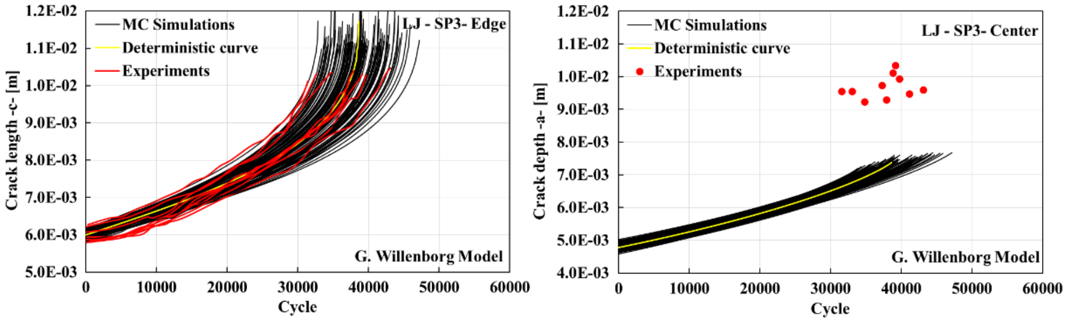

Figure 5.142. Probabilistic crack growth life curves and their comparison with the experiments (LJ specimen, SP3 loading spectrum, Generalized Willenborg model)

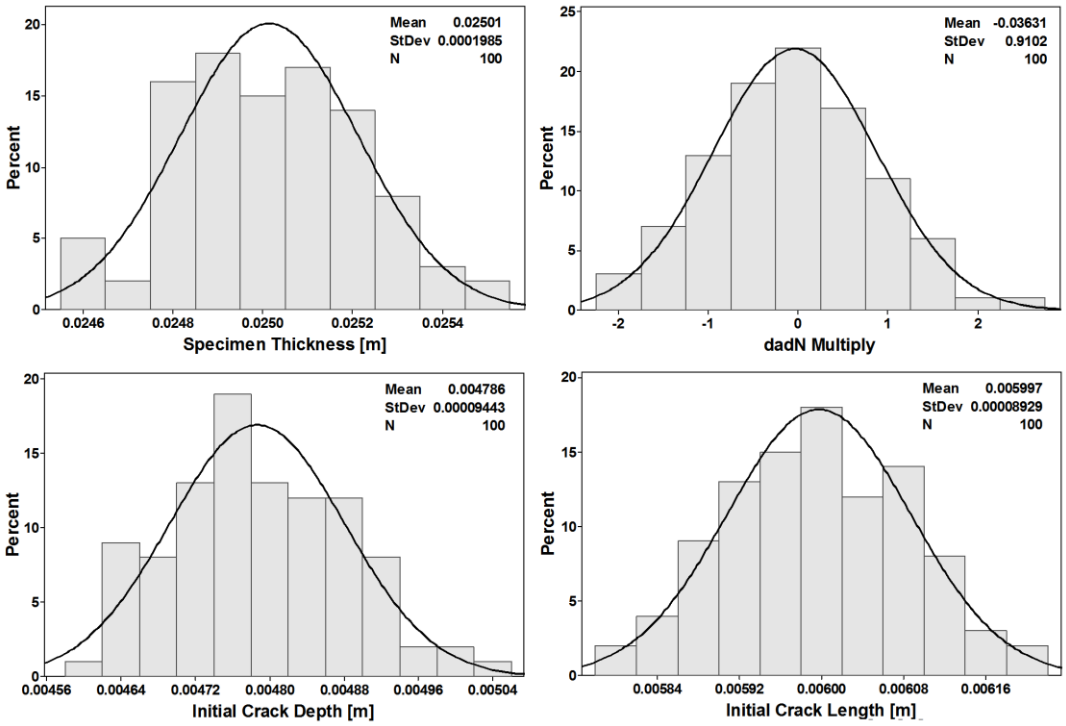

Figure 5.143. Distributions of the inputs used in crack growth life analysis (LJ specimen, SP3 loading spectrum, Generalized Willenborg model)

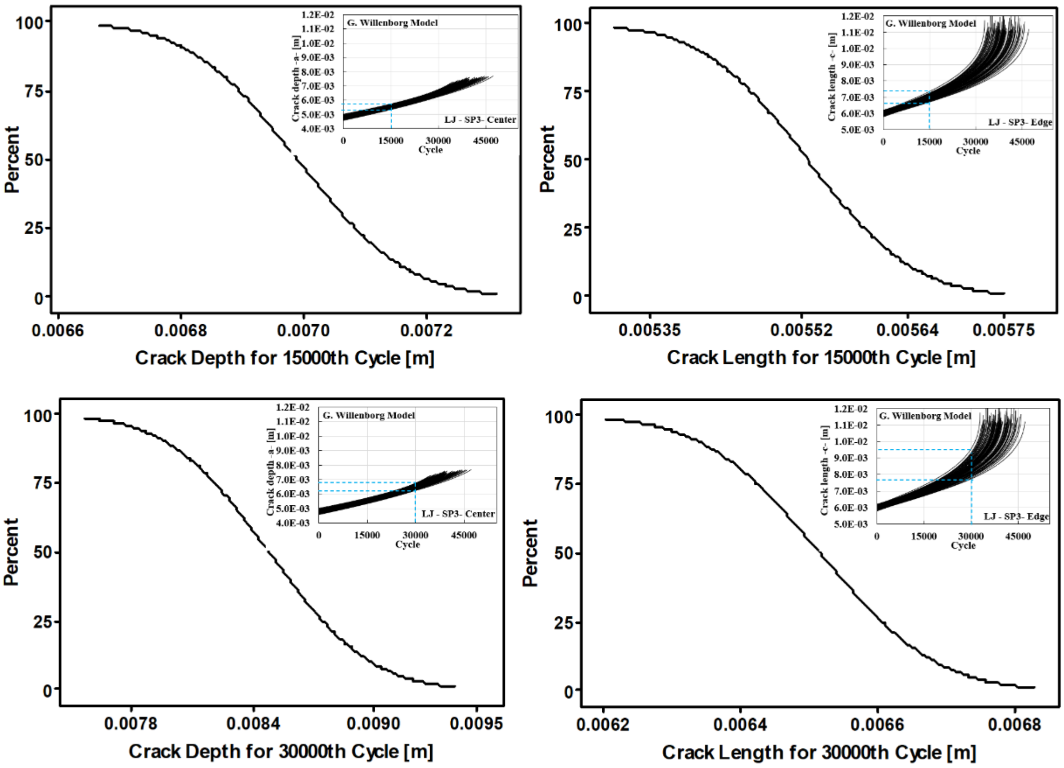

Figure 5.144. CDF for crack lengths under constant cycle load conditions (LJ specimen, SP3 loading spectrum, Generalized Willenborg model)

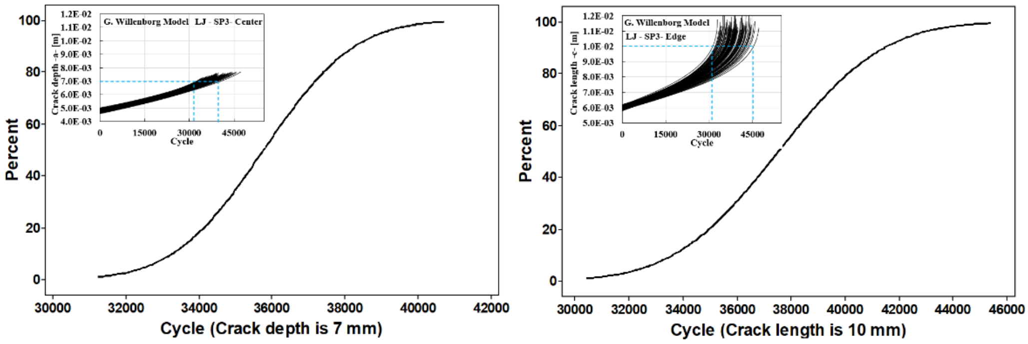

Figure 5.145. CDF for load cycles under constant crack length conditions (LJ specimen, SP3 loading spectrum, Generalized Willenborg model)

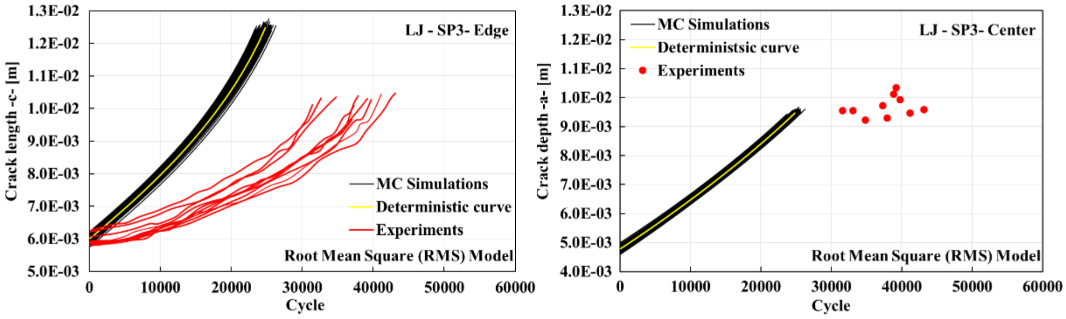

Figure 5.146. Probabilistic crack growth life curves and their comparison with the experiments (LJ specimen, SP3 loading spectrum, Root mean square model)

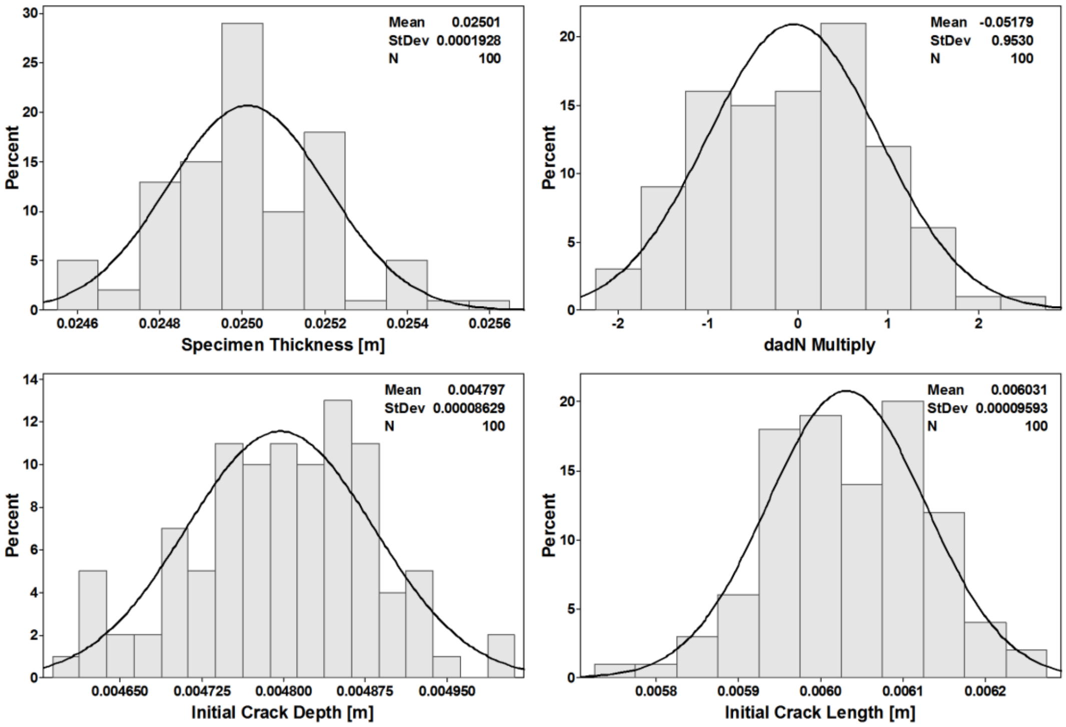

Figure 5.147. Distributions of the inputs used in crack growth life analysis (LJ specimen, SP3 loading spectrum, Root mean square model)

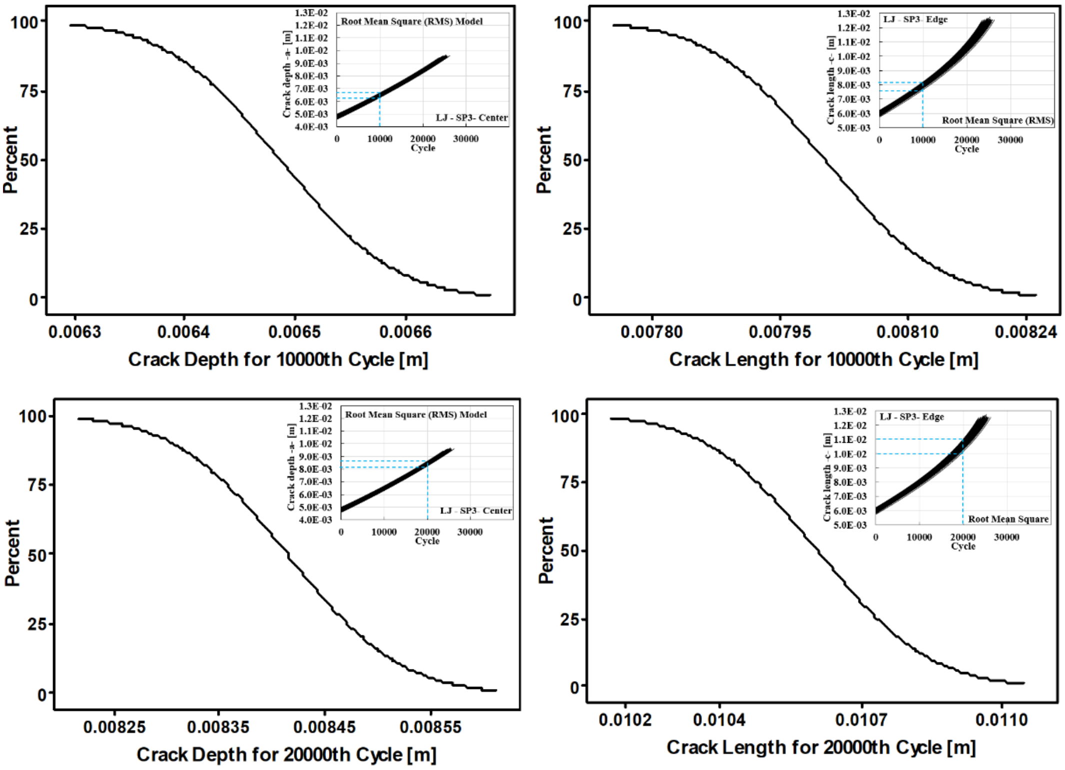

Figure 5.148. CDF for crack lengths under constant cycle load conditions (LJ specimen, SP3 loading spectrum, Root mean square model)

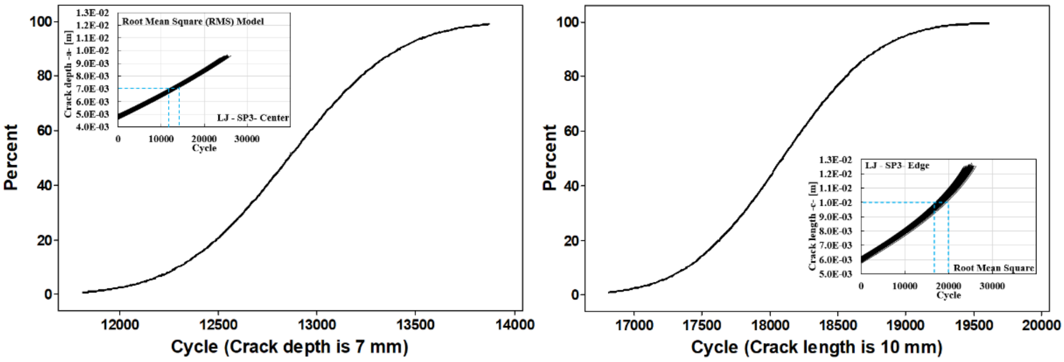

Figure 5.149. CDF for load cycles under constant crack length conditions (LJ specimen, SP3 loading spectrum, Root mean square model)

As can be seen from the graphs above, it has been confirmed that the probabilistic crack growth simulations performed under SP3 load spectrum by using the Wheeler model with Forman equation together, gives the closest results to the experiment, as it was under SP1 and SP2 load spectrums. In addition, Xiaoping and Generalized Willenborg models also showed good accordance with results of three-dimensional mode-I crack propagation tests, as it was the case under the SP1 and SP2 spectrums.

Developing a probabilistic method for three-dimensional crack propagation life estimation using FCPAS software is aimed in this study. A total of 61 two-dimensional crack propagation tests at 4 different strain rates under constant amplitude were performed to be used in probabilistic crack growth simulations. Thus, the variation in material properties affecting the crack propagation was determined. The crack propagation life was estimated by Monte Carlo simulation, taking into account the variability in material properties, load sensitivity, and geometric tolerances on the crack and specimen. In order to compare the predicted life interval, a total of 24 two-dimensional and 30 three-dimensional crack propagation tests were performed under random loading.

Wheeler [12] and Willenborg [13] models have been used by the studies in the literature to calculate variable amplitude crack growth, and researches have been conducted to improve these models. However, there is no generally accepted model in the literature for random amplitude loading. Models proposed by different authors in the literature do not obtain a close result for different load spectrums or materials. When different load spectrums are applied, the plasticity effect in the crack tip, generated by load interaction, changes. In a study published by ASTM [22], crack growth life was calculated by using 6 different models for the same load spectrum. According to the experimental results, the crack growth life was estimated in the range of 1 - 2.13 ($N_{pred}$ / $N_{test}$) times. One of the models in the study is Multi-Parameter Yield Zone [23] which includes 4 different empirical values obtained from the material and gives the closest life to the tests compared to other used models. It is seen that the results with Multi-Parameter Yield Zone model change between 0.97 - 1.18 ($N_{pred}$ / $N_{test}$) under different magnitude. Kermanitis A.T. and Pantelakis S.G [63] compared the results of their models containing material-related parameters such as material hardening with the experiments ($N_{pred}$ / $N_{test}$) in the ASTM reference [22] mentioned above, they obtained results in the range of 0.53 - 1.43. In the literature, additional parameters are used with the proposed models to explain the interaction effect between loads. X. Huang et al. [21] proposed additional coefficients to define the interaction effect between the loads and they calculated crack growth life close to the experimental results for a spectrum used in their study.

Coefficients' dependence on the material and experimental results make it difficult to apply a proposed model. In this dissertation, Spectrum Overload Index (SOL index) was used to improve a crack growth model in two-dimensional crack propagation. SOL index is easy to apply as it is a parameter derived directly from the load spectrum, regardless of the material and experimental results. In this study, close results with experiments were obtained by Forman with Wheeler Equation model for two-dimensional crack propagation using the SOL index with two different spectrums. However, due to the difference in crack propagation behavior, SOL index is not recommended for three-dimensional cracks. In three-dimensional cracks, the plane strain condition inside the specimen causes a constrain effect, and it decreases the crack growth rate in the test.

There is no standard specimen for three-dimensional crack propagation tests in the literature. In this study, a new specimen type is proposed, which can perform crack propagation tests without very high load values. Finite element analyzes were performed on the specimen and the results were verified by strain-gauge measurements. A transfer function has been obtained for the SIFs calculation in the specimen by DOE analysis. Close results to experiments were obtained on the proposed specimen using the Wheeler with Forman Eqn. model for three different spectrums. For other crack propagation models used, the difference between experiments and calculations changes. Compared to the studies in the literature, the ratio of calculated life to experimental results is at reasonable levels.

# CHAPTER 6. CONCLUSION AND FUTURE RESEARCH

## 6.1. Conclusion

This study aims to determine the variability in crack propagation life for three-dimensional mode-I fatigue crack propagation problems using the probabilistic fracture mechanics method. Initially, it is necessary to determine the material properties such as fracture toughness and fatigue crack propagation, which are obtained from standard fracture toughness and crack growth experiments using the Compact Tension (CT) specimen. A large number of crack propagation tests under different loading types were performed to determine the variability in the material properties. Therefore, approximately 10 tests were performed under each loading type, including spectrum loading. The effect of the overload ratio was investigated in the single overload tests. It was observed that when the overload ratio equals two, the crack growth life increases more than three times. Then block loading tests were performed, and the effect of the block overload period on crack growth life was investigated. In the case of a short cycle of block overload, the crack propagates slower than the case of single overload. If the block overload is applied for a long-time new plastic zone is created consequently, and it accelerates the crack growth.

The experimental results were compared with variable amplitude loading models in the literature, and an improved model was proposed for spectrum loading. Since the stress ratio is not included in the equation, the calculated results under random loading by only the Wheeler model represent an unrealistic condition. In the literature, some modifications to the Wheeler model were proposed to overcome this problem. In this dissertation, four different approaches have been used to define the crack growth behavior as a function of the stress ratio in the Wheeler model. The first of these approaches is to substitute the Paris-Erdogan C-n coefficients in the Wheeler model with the coefficients obtained by gathering the da/dN curves with Walker procedure. In other words, experiments with different stress ratios were combined on a curve with the Walker procedure, and crack propagation coefficients were obtained. Eventually, these coefficients were used directly in the Wheeler model. Secondly, the Forman fatigue crack growth coefficients are directly used in the Wheeler Model with a similar approach. As the third and fourth approaches, crack propagation life was estimated by substituting the Forman or Walker equation into the Wheeler model. Calculations were performed by using these approaches under different loading spectrums, and the obtained results from each model were plotted for the edge and center of the crack front, separately. It was found that Wheeler model with Forman equation gives the closest results to the experiment for two- and three-dimensional crack growth.

Since the plane stress condition is dominant on the sides of the specimens, the crack propagation rate at the edge is slower than it is at the center of the specimen. For this reason, the crack growth retardation effect was not applied in the center of the specimen. Crack tunneling, observed in crack propagation tests under variable amplitude loading, also supports this approach. Note that only the increasing load profiles were taken into account for counting the load profiles in spectrum loading, and the decreasing profiles were not used in the crack growth calculation since they do not physically open the crack surfaces.

In addition, an improved model, Spectrum Overload (SOL) Index, has been proposed for modeling two-dimensional crack propagation under random loading. SOL Index is a multiplier to SIF in the crack propagation equations, representing the weight of the peaks in the loading spectrum as a percentage. Some studies in the literature have been focused on the interaction between load profiles. However, these studies mostly try to explain the order of the profiles and the relation of each profile to its neighbors. An approach, such as SOL Index, which is calculated along the spectrum for the definition of crack growth behavior, has not been seen in the literature. Simulations performed with the SP1 and SP2 loading profiles show that the use of SOL Index is appropriate for 2-D crack propagation. But simulations without SOL index are closer to experimental results for three-dimensional crack propagation. Since propagation of a semi-elliptical surface crack towards the free surfaces is difficult, it is considered that the three-dimensional crack propagation rate is not as fast as the two-dimensional crack after the overload. As a result, as seen from the simulation results on the LJ specimen, the SOL index was not used in the three-dimensional mode-I crack propagation analysis.

The material properties data and crack propagation modeling experience with two-dimensional crack growth were utilized for three-dimensional crack growth. For three-dimensional crack growth experiments, a non-standard specimen with semi-elliptical cracks (modified LJ specimen) was designed by performing finite element analyzes in different geometries. An ellipsoid-shaped three-dimensional notch was created. Crack propagation tests were performed under different loading conditions after generating a pre-crack as the semi-elliptical surface crack around the notch. Transfer functions were obtained to calculate the SIF for different sizes and positions of the crack in the specimen by performing three-dimensional fracture analyses with combinations of aspect ratios and crack depth/length, so that crack propagation can be analyzed for any crack reasonable crack sizes and loading spectrum. An independent probabilistic crack propagation analysis code has been developed in FORTRAN that uses the SIF transfer function obtained for the specimen. Loading spectrum, material properties, initial crack size, and some geometric tolerances were defined as input distributions. This code also considers the modeling of the crack growth retardation effect caused by overload by using a selected model. Analyses are repeated by picking random values from the input distributions to calculate the crack propagation lives by employing the Monte Carlo probabilistic simulation method. The variations in the crack propagation curves were obtained as a result of the Monte Carlo simulation. For each load case, approximately 10 two- and three-dimensional crack propagation tests were performed in the laboratory. Then, the Monte Carlo simulations were run in the same conditions as the tests. The models were calibrated using the experimental results and were further verified by additional independent experiments. Thus, the probabilistic fatigue crack growth simulation capability, which is the main purpose of this study, was achieved.

To give a brief of the results obtained in this thesis;

- Parallel computation of element stiffness matrices and assembly into global stiffness matrix in FCPAS was performed to save solution time in fracture analyses.
- The positive parts of the load profiles were used to calculate stress ratio in spectrum loading.
- Spectrum Overload (SOL) Index has been proposed for modelling two-dimensional crack propagation under random loading.
- Wheeler model with Forman equation gives the closest results to the experiment for two- and three-dimensional crack growth.
- A new specimen was designed to investigate three-dimensional crack growth, and transfer functions were obtained to calculate the SIF.
- An in-house probabilistic crack propagation code was developed that considers the general loading spectrum and variabilities in the governing parameters.
- The variations in the crack propagation curves were obtained as a result of the Monte Carlo simulation.

## 6.2. Recommendations for Future Results

In this thesis, mode-I crack propagation life is subjected by using 2-D and 3-D linear elastic fracture mechanics principles. Probabilistic life estimation for mixed-mode crack propagation can be planned as future research. The plastic zone at the crack tip must be calculated, and its effect on crack propagation should be considered under mixed-mode for the mentioned study.

The scatters in material properties are more prominent for the studies in non-linear fracture mechanics. Probabilistic crack propagation studies can be performed for ductile materials or under high-temperature conditions. In this way, significant results can be obtained for engineering applications.

Prognostic health management and probabilistic fracture mechanics methods can be used together. It may be possible to obtain results in a smaller range by using update methods (Kalman filter, Bayesian updating, etc.) while performing probabilistic crack propagation life estimation during the experiment.

# REFERENCES

[1] Gdoutos, E. E. Fracture Mechanics: An Introduction, 2nd ed. Springer, 2005.

[2] Griffith, A. A. The phenomena of rupture and flow in solids. Trans. R. Soc. London. Ser. A, Contain. Pap. a Math. or Phys. Character, 221:582-593 (1921): 163-198,1921.

[3] Griffith, A. A. The theory of rupture, in Proc. of 1st International Congress of Applied Mechanics, Delft, , pp. 55–63, 1924.

[4] Irwin, G. R. Analysis of Stresses and Strains Near the End of a Crack Traversing a Plate. J. Appl. Mech., 24(3):361–364, 1957.

[5] Rice, J. R. A Path independent integral and the approximate analysis of strain concentration by notches and cracks, J. Appl. Mech., 35(2):379–386, 1968.

[6] Miedlar, P. C., Berens, A. P., Gunderson, A., Gallagher, J. P. Analysis and support initiative for structural technology (ASIST) delivery order 0016: USAF damage tolerant design handbook: guidelines for the analysis and design of damage tolerant aircraft structures., Dayton Univ oh Research Inst., 2002.

[7] Paris, P., Erdogan, F. A Critical analysis of crack propagation laws, J. Basic Eng., 85(4):528–533, 1963.

[8] Forman, R. G., Study of fatigue crack initiation from flaws using fracture mechanics theory, Eng. Fract. Mech., 4(2):333–345, 1972.

[9] Walker, K., The effect of stress ratio during crack propagation and fatigue for 2024-T3 and 7075-T6 aluminum. In Effects of Environment and Complex Load History on Fatigue Life. ASTM International, PA, USA:, 1–14, 1970.

[10] Newman, J. C., A crack-closure model for predicting fatigue crack growth under aircraft spectrum loading. In Methods and Models for Predicting Fatigue Crack Growth Under Random Loading, Chang, J. and Hudson C. M, (Eds); PA, USA: ASTM International, PA, USA, 1981.

[11] Elber, W., The significance of fatigue crack closure. In Damage Tolerance in Aircraft Structure. M. Rosenfeld, (Ed); ASTM International, PA, USA, 230–242, 1971.

[12] Wheeler, O. E., Spectrum loading and crack growth. J. Fluids Eng. Trans. ASME, 94(1):181–186, 1972.

[13] Willenborg, J., Engle, R. M., Wood, H. A., A crack growth retardation model using an effective stress concept. Tech. Memo. 71-1-FBR:1–22, 1971.

[14] Barsom, J., Fatigue crack growth under variable-amplitude loading in various bridge steels. In Fatigue Crack Growth Under Spectrum Loads, Wei, R. and Stephens, R. (Eds); ASTM International, PA, USA: pp. 217–232, 1976.

[15] Hudson, C., A root-Mean-Square Approach for Predicting Fatigue Crack Growth under Random Loading. In Methods and Models for Predicting Fatigue Crack Growth Under Random Loading, Chang, J. and Hudson C. M, (Eds); PA, USA: ASTM International, pp. 41–52, 1981.

[16] Manjunatha, C. M., Fatigue crack growth prediction under spectrum load sequence in an aluminum alloy by K*-RMS approach. Int. J. Damage Mech., 17(6):477–492, 2008.

[17] Sheu, B. C., Song, P. S., Hwang, S., Shaping Exponent In Wheeler Model Under a Single Overload. Eng. Fract. Mech., 51(1):135–143, 1995.

[18] Gallagher, J. P. A., generalized development of yield zone models. Air Force Flight Dynamics Lab Wright-Patterson AFB OH, 1974

[19] Meggiolaro, M. A., De Castro, J. T. P., An evaluation of Elber-type crack retardation models. SAE Tech. Paper 2001-01-4063, 2001.

[20] Zhang, S., Marissen, R., Schulte, K., Trautmann, K. K., Nowack, H., Schijve, J., Crack propagation studies on al 7475 on the basis of constant amplitude and selective variable amplitude loading histories. Fatigue Fract. Eng. Mater. Struct., 10(4):315–332, 1987.

[21] Huang, X., Torgeir, M., Cui, W., An engineering model of fatigue crack growth under variable amplitude loading. Int. J. Fatigue, 30(1):2–10, 2008.

[22] Hudson C. M, Chang, J. B. (eds), Methods and Models for Predicting Fatigue Crack Growth Under Random Loading., ASTM International, PA, USA, 1981.

[23] Johnson, W., Multi-parameter yield zone model for predicting spectrum crack growth. In Methods and Models for Predicting Fatigue Crack Growth Under Random Loading, Chang, J. and Hudson C. M, (Eds); PA, USA: ASTM International, pp. 85–102, 1981.

[24] Newman, J., A Crack-closure model for predicting fatigue crack growth under aircraft spectrum loading” In Methods and Models for Predicting Fatigue Crack Growth Under Random Loading, Chang, J. and Hudson C. M, (Eds); PA, USA: ASTM International, pp. 53–84, 1981.

[25] Chang, J., Szamossi, M., Liu, K.W., Random Spectrum Fatigue Crack Life Predictions With or Without Considering Load Interactions. In Methods and Models for Predicting Fatigue Crack Growth Under Random Loading, Chang, J. and Hudson C. M, (Eds); PA, USA: ASTM International, pp. 115–132, 1981.

[26] Wu, W. F., Ni, C. C., Probabilistic models of fatigue crack propagation and their experimental verification. Probabilistic Eng. Mech., 19(3):pp. 247–257, 2004.

[27] Yang, J. N., Manning, S. D., A simple second order approximation for stochastic crack growth analysis. Eng. Fract. Mech., 53(5):677–686, 1996.

[28] Annis, C., Probabilistic Life Prediction. In Probabilistic Aspects of Life Prediction, Johnson, W. and Hillberry, B. (Eds); ASTM International, PA, USA, pp. 3–14.

[29] Farahmand, B., Abdi, F., Probabilistic fracture toughness and fatigue crack growth rstimation resulting from material uncertainties. In Probabilistic Aspects of Life Prediction, Johnson, W. and Hillberry, B. (Eds) ASTM International, PA, USA: 61–74, 2004.

[30] Ayhan, A. O., Simulation of three-dimensional fatigue crack propagation using enriched finite elements. Comput. Struct., 89(9–10):801–812, 2011.

[31] Ayhan, A. O., Nied, H. F., Stress intensity factors for three-dimensional surface cracks using enriched finite elements. Int. J. Numer. Methods Eng., 54(6):899–921, 2002.

[32] Ayhan, A. O., Fracture and crack propagation analysis system - Phase 1, TUBITAK Project no: 108M283, 2008-2011.

[33] Yaren, M. F., Ayhan, A. O., Implementation of Parallel Computations on 3-D Enriched Finite Elements Used for Fracture Analyses. In Proceedings of the 5th International Conf. on Parallel, Distributed, Grid and Cloud Computing for Engineering Proc, P. Iványi, B.H.V. Topping, G. Várady, (Eds), Civil-Comp Press, UK, 2017.

[34] Ayhan, A. O., Nied, H. F., Finite element analysis of interface cracking in semiconductor packages. IEEE Trans. Components Packag. Technol., 22(4): 503–511, 1999.

[35] Ayhan, A. O., İriç, S., Demir, O., Yaren, M. F., Kurt, E., Fracture and crack propagation analysis system - Phase 3, TUBITAK Project no: 217M690, 2020.

[36] ASTM International, E399-12: Standard Test Method for Linear-Elastic Plane-Strain Fracture Toughness $K_{IC}$ of Metallic Materials. PA, USA, 2017.

[37] J. Pickle, D. Gullage, Analyzing digital images installation packages for windows and OS/X. https://www.umassk12.net/adi/, Access Date: 26.05.2021.

[38] ASTM International, E647-15: Standard Test Method for Measurement of Fatigue Crack Growth Rates. PA, USA, 2015.

[39] Zhao, T., Zhang, J., Jiang, Y., A study of fatigue crack growth of 7075-T651 aluminum alloy. Int. J. Fatigue, 30(7):1169–1180, 2008.

[40] Demir, O., Üç boyutlu karışık mod kırılma kriterlerinin sayısal ve deneysel olarak incelenmesi ve geliştirilmesi. Ph.D Dissertation in Sakarya University, 2016.

[41] Bergner, F., Zouhar, G., New approach to the correlation between the coefficient and the exponent in the power law equation of fatigue crack growth. Int. J. Fatigue, vol. 22, no. 3, pp. 229–239, 2000.

[42] Avram, J., Round Robin Fatigue Crack Growth Testing Results. Air force academy Colorado Springs Co Center for Aircraft Structural Life Extension 2006.

[43] Sander, M., Comparison of fatigue crack growth concepts with respect to interaction effects. In Proceedings of ECF (Vol. 15), 2004.

[44] MINITAB: Data Analysis, Statistical & Process Improvement Tools. Minitab Inc.

[45] Aicher, W., Branger, J., Dijk, V., G. M., E., J., H., De Jonge, J. B., ... & Schütz, W., Description of a fighter aircraft loading standard for fatigue evaluation FALSTAFF, 1976.

[46] Microsoft Excel, Microsoft Corporation, 2013, [Online]. https://office.microsoft.com/excel, Access Date: 26.05.2021.

[47] Song, P. S., Sheu, B. C., Chang, L., A modified Wheeler model to improve predictions of crack growth following a single overload. JSME International Journal Series A Solid Mechanics and Material Engineering, 44(1):117-122, 2001.

[48] Yuen, B. K. C., Taheri, F., Proposed modifications to the Wheeler retardation model for multiple overloading fatigue life prediction. Int. J. Fatigue, 28(12):1803–1819, 2006.

[49] Sander, M., Richard, H. A., Fatigue crack growth under variable amplitude loading Part II: Analytical and numerical investigations. Fatigue Fract. Eng. Mater. Struct., (29)4:303–319, 2006.

[50] Forman, R. G., Shivakumar, V., Mettu, S. R., Newman, J. C., Fatigue crack growth computer program NASGRO v3.0. Nasa-JSC-22267B, 2000.

[51] Porter, T. R., Method of analysis and prediction for variable amplitude fatigue crack growth. Eng. Fract. Mech., 4(4):717–736, 1972.

[52] Huang, X. P., Zhang, J. B., Cui, W. C., Leng, J. X., Fatigue crack growth with overload under spectrum loading. Theor. Appl. Fract. Mech. 44, (2):105–115, 2005.

[53] Dowling, N. E., Mechanical behavior of materials: engineering methods for deformation, fracture, and fatigue. 4th ed. Boston, MA: Pearson, 2012.

[54] Andresen, P. L., Ayhan, A., Catlin, G. M., Catlin, W. R., Development and the use of a lee james surface cracked specimen for evaluating chemistry and flow rate effects in realistic cracks. 2004. Access date: 26.05.2021. https://www.onepetro.org/conference-paper/NACE-04567.

[55] James, L. A., Wilson, W. K., Development of a surface-cracked specimen. Theor. Appl. Fract. Mech., 20(2):115–121, 1994.

[56] ANSYS Inc, ANSYS, Theory Manual V12. Canonsburg, PA, USA, 2009.

[57] Iriç, S., Ayhan, A. O., Dependence of fracture toughness on rolling direction in aluminium 7075 alloys. In Acta Physica Polonica A,.132(3):892–895, 2017.

[58] Campbell, F. C. (Ed.). Elements of metallurgy and engineering alloys. ASM International, 2008.

[59] Ayhan, A. O., Yaren, M. F., Effects of microstructural through-thickness non-uniformity and crack size on fatigue crack propagation and fracture of rolled Al-7075 alloy. Fatigue Fract. Eng. Mater. Struct., 43(9):2071–2084, 2020.

[60] Mcdonald, V., Daniewicz, S., An experimental study of the growth of surface flaws under cyclic loading. In Fatigue and Fracture Mechanics: Chona, R. (Ed) PA, USA: ASTM International, 32nd Volume, 381–396, 2002.

[61] ASM International, Atlas of Stress-Strain Curves, 2nd ed. OH, USA: ASM International, 2002.

[62] Chandler, R., Northrop, P., Documentation for file randgen.f. 2007, www.ucl.ac.uk/~ucakarc/work/randgen.html, Access Date: 25.05.2021.

[63] Kermanidis, A. T., Pantelakis, S. G., Fatigue crack growth analysis of 2024 T3 aluminium specimens under aircraft service spectra. Fatigue Fract. Eng. Mater. Struct., 24(10):699–710, 2001.

# RESUME

**Name Surname** **:** Mehmet Faruk YAREN

## EDUCATION

| **Degree** | **Institute** | **Year** |
|---|---|---|
| Doctor of Philosophy | Sakarya University / Institute of Natural Science / Computational Mechanics and Manufacturing | Ongoing |
| Master of Science | Sakarya University / Institute of Natural Science / Mechanical Engineering | 2014 |
| Bachelor S. | Trakya University / Faculty of Engineering and Architecture / Mechanical Engineering | 2011 |
| High School | Asfa Ahmet Mithat High School | 2007 |

## WORK EXPERIENCE

| **Years** | **Organisation** | **Position** |
|---|---|---|
| 2019-Ongoing | Sakarya University | Research Assistant |

## LANGUAGE

English

## PROJECTS and INDEXED PAPERS

**1.** Project: Fracture and Crack Propagation Analysis System – Phase- 3

**2.** Project: Fracture and Crack Propagation Analysis System – Phase- 2

**3.** Paper: Effects of microstructural through-thickness non-uniformity and crack size on fatigue crack propagation and fracture of rolled Al-7075 alloy

**4.** Paper: 3-D mode-I/III fatigue crack propagation: Comp. modeling & experiments

**5.** Paper: Expanded graphite–epoxy–flexible silica composite bipolar plates for PEM fuel cells